Technische Universität München

TUM School of Natural Sciences

Elucidation of the Redox-Active Mabiq Ligand Effect on Electrocatalytic Hydrogen Evolution Reaction

Gülen Ceren Tok

Vollständiger Abdruck der von der TUM School of Natural Sciences der Technischen Universität München zur Erlangung einer

Doktorin der Naturwissenschaften (Dr. rer. nat.)

genehmigten Dissertation.

Vorsitz: Prof. Dr. Tom Nilges

Prüfende der Dissertation: 1. Prof. Dr. Corinna R. Hess

2. Prof. Dr. Hubert A. Gasteiger

Diese Dissertation wurde am 25.03.2024 bei der Technischen Universität München eingereicht und durch die TUM School of Natural Sciences am 24.04.2024 angenommen.

Abstract

Using fossil raw materials as an energy resource or for material production poses significant environmental and climate problems today. Replacing fossil energies with renewable energies is part of the energy in full swing. In this context, hydrogen can be considered a promising alternative carbon-free fuel/energy carrier. The focus of this thesis is to utilize a cobalt complex coordinated by a macrocyclic biquinazoline (Mabiq) ligand ($[Co^{II}(Mabiq)(THF)](PF_6)$, Co_{Mbq}) as an electrocatalyst for H_2 release and to investigate the role of the redox-active ligand for HER pathways.

The first part addresses the onset potential for H_2 evolution and HER activity. Besides the detected H_2 evolution by Co_{Mbq}, the combined on-line electrochemical mass spectrometry (OEMS) and rotating ring disk electrode (RRDE) techniques denote a precatalytic process involving the formation of a protonated, two-electron-reduced intermediate. Further results indicate the presence of more than one intermediate in the system, and there might be a deactivation pathway for HER. Therefore, elucidating the inhibitory sites of the catalyst might assist the ligand modification to shut down the deactivation pathway.

The second part of the thesis is based on the characterization of the possible Co-Mabiq intermediates before H_2 evolution. Co-Mabiq complexes in various oxidation states exhibit distinct absorption bands. In this respect, bulk electrolysis and UV-Vis spectroscopy combined with quantum chemical calculations are employed, and the combined results provide an insight into two decoupled pathways forming two intermediates operating at different overpotentials for HER. This study shows how the various protonation sites of the redox-active ligand influence the activities of HER intermediates and how modifications to the ligand backbone may prevent the formation of the less active intermediates.

Kurzfassung

Die Verwendung fossiler Rohstoffe als Energiequelle stellt heutzutage ein großes Problem für die Umwelt sowie das Klima dar. Energiegewinnung aus erneuerbaren Quellen gewinnt daher immer mehr an Bedeutung. Wasserstoff kann in diesem Zusammenhang als ein vielversprechender, kohlenstofffreier, alternativer Energieträger betrachtet werden. Der Fokus dieser Arbeit liegt darin, einen Kobaltkomplex mit einem makrozyklischen Biquinazolin (Mabiq) Liganden ($[Co^{II}(Mabiq)(THF)](PF_6)$, Co_{Mbq}) als Elektrokatalysator für H_2 Produktion zu verwenden und die Rolle des redoxaktiven Liganden in der HER zu untersuchen.

Der erste Teil befasst sich mit dem Verhalten von Co_{Mbq} in der HER. Neben der Produktion von H_2 zeigt die Kombination von On-line elektrochemischer Massenspektrometrie (OEMS) und rotierender Ringelektroden- (RRDE) Messungen einen präkatalytischen Prozess an, der die Bildung eines protonierten und um zwei Elektronen reduzierten Intermediats beinhaltet. Weitere Ergebnisse indizieren mehr als nur ein Intermediat sowie einen Deaktivierungspfad für HER.

Der zweite Teil behandelt die Charakterisierung der, in die H_2 Entwicklung involvierten, möglichen Co-Mabiq Intermediate. Da Co-Mabiq Komplexe in verschiedenen Oxidationszuständen sehr distinkte Absorptionsbanden zeigen, wurde Bulk-Elektrolyse und UV-Vis Spektroskopie in Kombination mit quantenchemischen Berechnungen durchgeführt. Die kombinierten Ergebnisse zeigen zwei entkoppelte Pfade, die zu zwei verschiedenen Intermediaten führen, die bei unterschiedlichen Überpotentialen operieren. Diese Studie verdeutlicht wie die verschiedenen Protonierungsstellen des redoxaktiven Liganden die Reaktivitäten der HER-Intermediate beeinflussen.

Die Ergebnisse beider Studien können genutzt werden, um durch gezielte Modifikationen des Ligandenrückgrates die Bildung von weniger reaktiven/deaktivierenden Intermediaten zu verhindern.

Contents

List of Abbreviations

Abbreviation	Description
CE	Counter electrode
CECE	Chemical-electrochemical-chemical-electrochemical
CV	Cyclic voltammetry
DCM	Dichloromethane
DFT/MRCI	Density functional theory multi-reference configuration interaction
EC	Ethylene carbonate
ECEC	Electrochemical-chemical-electrochemical-chemical
EEC	Electrochemical-electrochemical-chemical
EECE	Electrochemical-electrochemical-chemical-electrochemical
EMC	Ethyl methyl carbonate
F	Faraday constant
Fc	Ferrocene
HER	Hydrogen evolution reaction
HOR	Hydrogen oxidation reaction
$LiBF_4$	Lithium tetrafluoroborate
$LiPF_6$	Lithium hexafluorophosphate
MeCN	Acetonitrile
Mt	Megaton
n	Number of electrons
OCV	Open-circuit voltage
PCET	Proton-coupled electron transfer
PEEK	Polyetheretherketone
PEIS	Potentiostatic electrochemical impedance spectroscopy
PTFE	Polytetrafluoroethene
R	Universal gas constant
RDE	Rotating disk electrode
RE	Reference electrode
RRDE	Rotating ring disk electrode

_____

T	Temperature
THF	Tetrahydrofuran
TOF	Turnover frequency
TON	Turnover number
UV-Vis	Ultraviolet-Visible
ω	Angular velocity
WE	Working electrode
η	Overpotential

1 Introduction

1.1 Hydrogen: Importance and Background

Climate change is one of the most critical problems that humankind faces, and the contribution of greenhouse gas emissions by human influence to climate change is undeniable. The Paris Agreement aims to limit global warming to 1.5 °C to avoid catastrophic outcomes for climate and the environment; however, there are concerns that the average global temperature might increase above 3 °C by 2100.[1] The most significant share of the greenhouse emission results from the energy industry, thus, the utility of alternative energy carriers is essential. Global energy demand is projected to increase significantly in the coming decades, and the energy demand has been carried out by the exploitation of fossil fuels like coal, oil, and natural gas. The energy generated by burning fossil fuels is used for transportation, electricity, and other industries. However, these sources are non-renewable, and their combustion results in the release of CO_2 into the Earth's atmosphere. It is estimated that roughly 80 % of manmade CO_2 and greenhouse gas emissions originate from fossil fuel combustion reaching the highest level (36 Gt) in 2021.[2] Coal is the largest source of CO_2 and greenhouse gas emissions. Recent reports[3, 4] show that 85 % of global energy is obtained from fossil fuels and renewable energy sources such as wind, solar, and biofuels, whereas hydroelectric sources constitute only 15 %. The energy consumption by source over the years (Figure 1.1) shows the high share of fossil fuels and the increase in the use of renewable sources over the last decade.
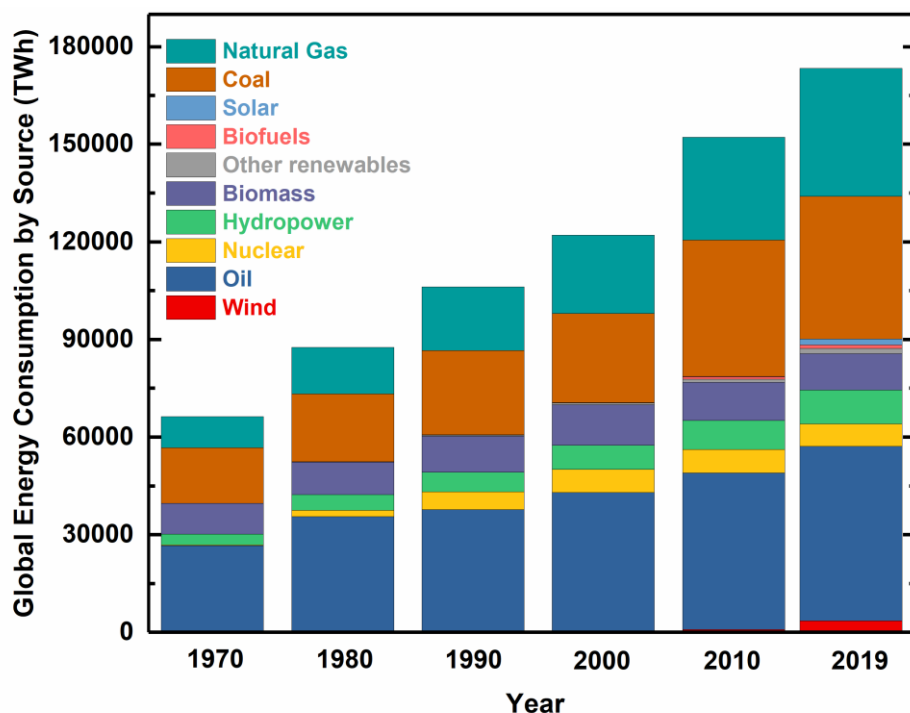
Figure 1.1: The energy consumption (TWh) by source over the years.

Overall, the adverse and irreversible effects of fossil fuels on the environment have promoted the search for clean alternate energy sources. In this context, hydrogen can be considered a promising alternative carbon-free fuel/energy carrier. Hydrogen can serve in the raw material industry or be used as a fuel for fuel cell-driven vehicles in the mobility sector. Regarding the raw material industry, calculations show that global demand by industry and oil refining for hydrogen is roughly 90 Mt in 2020, with more than 70 Mt used as pure hydrogen and less than 20 Mt mixed with carbon-containing gases in methanol production and steel manufacturing.[5] The growing demand for hydrogen, coupled with the need for CO_2 emission reduction, presents the issue that the energy required for fossil fuel cracking is environmentally unsustainable. Thus, hydrogen production from renewable energy sources such as light, water, or biomass would be an excellent pathway to generate energy, as it is environment friendly with negligible impact on the natural environment. In this context, hydrogen produced via electrochemical splitting of water has great potential due to the high current density and purity of the generated hydrogen. The catalyst choice is essential for electrolytic and/or photochemical systems to achieve efficient hydrogen production in terms of energy

_____

conversion and storage. Thus, the development of both heterogeneous and homogeneous catalysts for the hydrogen evolution reaction (HER) from water/acid and the hydrogen oxidation reaction (HOR) has received significant attention. [6-12] For the reactions to take place at meaningful rates for effective energy storage, energy beyond the thermodynamic potential needs to be applied, and in electrochemical systems, this is referred to as the overpotential (η). At the moment, platinum is an excellent catalyst displaying fast kinetics at low overpotentials. However, the low abundance and high cost of platinum bring obstacles to its comprehensive usage. Therefore, HER catalysts based on earth-abundant metals have been developed over the last decade, inspired partly by metalloenzyme cofactors.[13-16]

1.2 Hydrogenase and Biomimetic Hydrogenase Complexes

Hydrogenases are a diverse group of metalloenzymes that catalyze the hydrogen oxidation reaction and hydrogen evolution that occur in bacteria, archaea, and eukarya. The hydrogen evolution reaction occurs due to a hydride and a proton coupling during the enzymatic catalytic cycle. Hydrogenase with iron/nickel in the active site was first observed in anaerobically grown *Escherichia Coli* cells, which mediate the reversible reduction of dyes with H_2.[17] Based on the metal active center hydrogenase is classified as [NiFe], [FeFe], and [Fe] hydrogenase. As a characteristic feature of the [FeFe] hydrogenases, Fe ion is coordinated by highly unusual diatomic ligands like CO and CN^-, and the diiron moiety is covalently attached to a [4Fe4S]-cluster. Considering the [NiFe] hydrogenase class, a [Ni(cysteinate)$_4$] unit is linked via two of its cysteine ligands to an [Fe(CN)$_2$(CO)] unit (Figure 1.2), and the Ni-center plays a key role with hydride binding and redox activity.[14, 18, 19] In all hydrogenases the protein matrix involves some key compartments: (i) the ligand sphere to bind the active metal site, (ii) an optimized cage for the catalytic cycle, and (iii) electron transfer pathways between the active site and molecular surface.
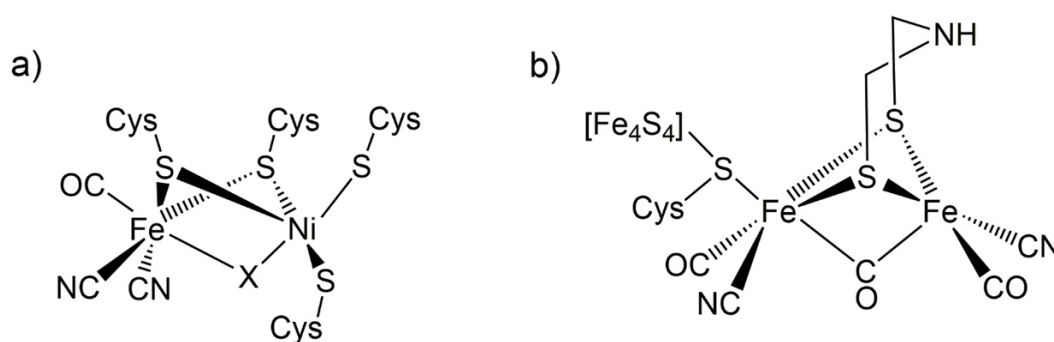

Figure 1.2: Chemical structures of the active sites of two types of hydrogenases: a) the [NiFe] hydrogenase and b) the [FeFe] hydrogenase. X referring to vacant or H.

The main function of hydrogenase is to supply energy to microorganisms through H_2 oxidation or evolution. These metalloenzymes exhibit significantly high rates of H_2 production (10^4 s^{-1}).[19, 20] In all hydrogenases, heterolytic coupling of a metal-bound hydride with a proton produces hydrogen. The [FeFe] hydrogenase is more active towards H_2 evolution; on the other hand, the [NiFe] hydrogenase shows

higher activity towards H_2 oxidation.[15, 20] In the catalytic cycle of [NiFe], several H_2 uptake mechanisms claim the enzyme cycles between formal Ni^{II} and Ni^{III}. Upon reduction of the active site, [NiFe] hydrogenase generates two different paramagnetic intermediates named unready and ready. Both states have formal Ni^{III} states, and they are inactive. Upon activation, unready and ready complexes generate the first catalytically active complex in the catalytic cycle containing a Ni^{II} species (Ni-S, Figure 1.3).[21, 22] Upon one electron and one proton addition to the resting diamagnetic Ni-S ($Ni^{II}Fe^{II}$), Ni–C is generated. In the last step, Ni–C is further reduced, and the protonation of the hydride ligand forms Ni–R, resulting in heterolytic H_2 evolution (Figure 1.3).[14, 22, 23] However, another study highlights the relevance of another possible intermediate, $Ni^{I}Fe^{II}$ electronic structure, suggesting a different oxidation state of Ni for H_2 release.[24] The proposed mechanism for [FeFe] hydrogenase has reached an agreement compared to [NiFe] hydrogenase, suggesting alternative intermediates for hydrogen evolution. In the [FeFe] hydrogenase case, the enzyme cycles between the formal Fe^{II} and Fe^{I}. In the initial state, the proximal iron side is Fe^{I} and the distal iron has a 2+ oxidation state. Upon reduction followed by proton transfer, the distal iron becomes Fe^{I}.[23, 25] In this proposed mechanism; the bridging amine reacting with an external proton results in intramolecular proton transfer from the bridging amine to the distal Fe, leading to H_2 evolution.[26-28]
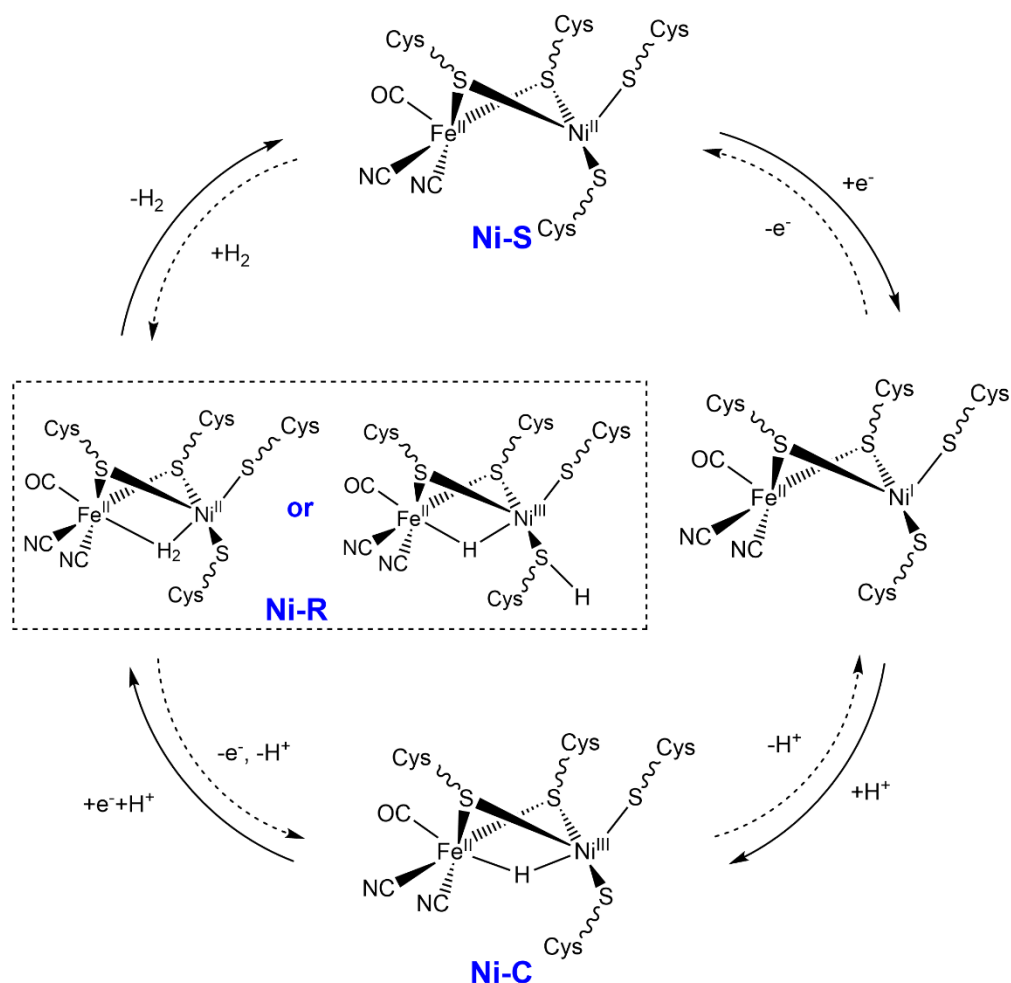
Figure 1.3: Catalytic mechanism for reversible H_2 evolution by [NiFe] hydrogenases, with the proposed structures for structurally uncharacterized Ni-R state.

It is important to understand the mechanism behind the hydrogenase to generate the structure and the function of the active site of the metalloenzymes that show peculiar reactivity toward H_2 production. For this purpose, many studies have been conducted to mimic the active sites of hydrogenase to develop efficient and economically affordable electrocatalysts for H_2 evolution. One of the key features of an efficient electrocatalyst[29] should involve a metal-center that can be reduced and oxidized at moderate potentials, and the d-block transition metals are more appealing than noble metals due to their lower cost and availability. Furthermore, the catalyst should consist of a coordination site for forming a metal-hydride bond, either vacant formed by reductive elimination of a ligand or involving a labile ligand. Lastly, the complex needs a basic group, which enables capturing and delivering protons to the immediate vicinity of the reactive center; this group is

referred to as a proton relay site. The H_2 evolution based on the transition metal-center follows either a homolytic or heterolytic pathway involving metal-hydride formation to release H_2 (Figure 1.4); however, there is still a debate about which pathway is preferred more in the reaction mechanism.[29-33] In the homolytic or bimetallic route, metal-hydride species ([M–H]) can react with another metal-hydride to release H_2 via reductive elimination. On the other hand, in the heterolytic or monometallic pathway, the metal-hydride requires further protonation to evolve H_2.
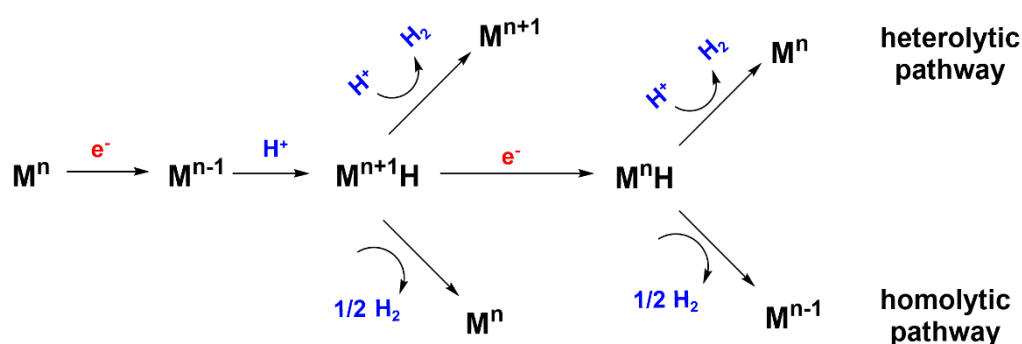

Figure 1.4: Illustration of heterolytic pathway (upper panel) and homolytic pathway (lower panel) for H_2 evolution based on a metal-center represented as M.

The development of biomimetic catalysts is based on generating the active sites of hydrogenases with Ni and/or Fe-centers. Many diverse mechanistic pathways towards HER and some factors affecting the activity, such as the acid strength and substituents on the active sites, have been displayed through the development of biomimetic catalysts originated from [FeFe] and [NiFe] hydrogenases.[34-36] Ogo and his coworkers develop the first dinuclear biomimetic NiFe complex catalyzing both H_2 evolution and oxidation[37], and the first NiFe complex that binds the hydride on the Ni-center shows the Ni^{II}–H is the crucial intermediate in the H_2 evolution catalytic cycle.[14] Although they give insightful information regarding the mechanism, they suffer from poor stability and large overpotentials for HER. All the dinuclear complexes given as examples in this section show overpotentials between 500 mV and 900 mV for HER; therefore, they are not beneficial in the applications. However, they are essential in comprehending HER.

Dubois and Bullock's groups extensively examine the reactivity of nickel and iron bis(diamine) complexes.[38-45] These catalysts are based on two diphosphine ligands in a distorted square planar geometry coordinated to the metal-center, and both ligands bear one or two pendant amine groups (Figure 1.5a). The synthesized form of the catalyst has a second coordination sphere function as a proton relay in amine form with proximity to the metal-center, and the second coordination sphere assists in the transfer of protons between the solution and the metal site in the catalytic HER and HOR. Moreover, pendant bases can stabilize the binding of small molecules such as H_2, which enhances the proton-couple electron transfer (PCET). Dubois *et al.* shed light on the effect of the coordination sphere on molecular electrocatalysis. [46, 47] The coordination spheres consist of three parts: (i) inner sphere, (ii) second sphere, and (iii) outer sphere. The inner coordination sphere is the ligands directly attached to the metal-center, affecting the properties of the metal-center, such as the presence of vacant sites. The second coordination sphere includes functional groups incorporated in the ligand that preferentially interact with substrates and metal-centers weakly or not, such as the pendant amine interacting with the H_2 molecule. Lastly, the outer coordination involves the remainder of the ligand and the solvent molecule surrounding the catalyst. In this case, the pendant amine in the second coordination sphere serves as an intramolecular proton acceptor, and the metal-center serves as a hydride acceptor. The study on the H_2 evolution mechanism suggests that the proton does not reside on the amine and transfers from N on the pendant amine to the Ni-center leading to rapid intramolecular exchange.[48] Ni-H forms after the intramolecular proton transfer to the Ni-center, and the second protonation occurs on the pendant amine base. In the final step of the HER mechanism, H_2 is produced by combining the metal-hydride with the proton on the amine site, and the original catalyst is regenerated for the subsequent cycles. The proposed HER mechanism based on pendant amine type of catalysts goes through the ligand-assisted metal-centered pathway. Furthermore, as expected, varying the basicity of the amino group, i.e., its ability to deliver protons, directly impacts turnover numbers (TONs). Comprehensive studies prove that the amines that are more basic disfavor the catalytic H_2 formation, leading to low turnover frequencies (TOFs), and surprisingly, switching from two amine groups to only one amine group per ligand

_____

improves the TOF for HER.[43, 48, 49] The latter result is attributed inactive conformations of the protonated forms of the complex with two amine groups per ligand. The catalyst, which consists of only one pendant amine in each ligand, prevents unproductive proton binding steps and leads to magnificent TOFs as 100,000 H_2 per second.[43] Overall, this type of catalyst shows very high activity towards HER and HOR by operating at low overpotentials, and they perform either in an aqueous or nonaqueous acidic environment.[42, 43]

a)

b)

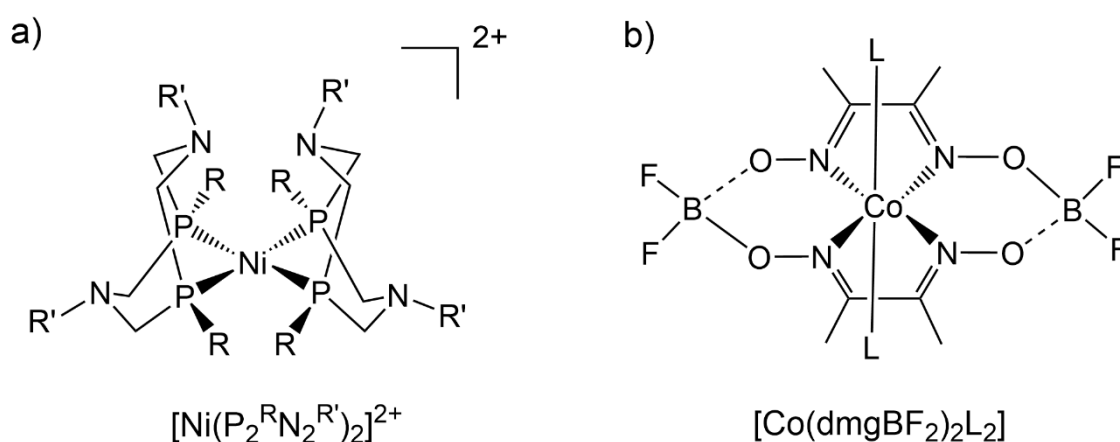$[Ni(P_2{}^RN_2{}^{R'})_2]^{2+}$

$[Co(dmgBF_2)_2L_2]$

Figure 1.5: Chemical structures of the selected examples of a) Ni bis(diamine), R: Ph and R':Ph, and b) cobaloxime, L: solvent.

Different transition metals have been examined to investigate the effect of the metal-center on the overpotential and activity toward the H_2 evolution. Cobalt stands out among first-row transition metals for its ability to support multiple oxidation states, adopt multiple coordination geometries depending on its surrounding ligands, and have high stability under catalytic conditions. One of the most studied classes of the H_2 evolution catalysts is the cobaloxime complexes inspired by B12 enzymes.[50] They are based on Co^{II} and Co^{III} centers consisting of two glyoximato equatorial ligands and two other *trans-axial* ligands (Figure 1.5b).[51-62] The substituents on the glyoxime ligand enable tuning of the complex's redox properties. For instance, stronger electron-withdrawing groups decrease the driving force for a reduction on the metal-center, leading to unfavorable protonation. Hu *et al.* and Dempsey *et al.* claimed that the cobaloxime type of complexes follow dominantly the homolytic pathway where the homolytic bond

cleavage of two Co–H species results in H$_2$ evolution and the heterolytic pathway takes place only in the presence of high acid concentrations.[53, 59, 63] In the proposed reaction mechanism, the Co^{III}-center is reduced to Co^{I}, which takes up a proton and forms Co^{III}–H. The resultant Co^{III}–H either directly leads to homolytic bond cleavage or is reduced to Co^{II}–H, reacting with an external proton to generate H$_2$. In this case, EEC (E: electrochemical reaction, C: chemical reaction, proton uptake in this context) or EECE are the pathway sequences to produce H$_2$. Various theoretical studies imply H$_2$ evolution occurs through a Co^{II}–H intermediate, and pathway sequence depends on the pK$_a$ of the system.[32, 33, 64] Despite the calculations suggesting the formation of Co^{III}–H, Co^{III}–H has still not been isolated in the catalytic cycle up to this date due its high reactivity. A study by Artero *et al.* claimed that HER activity is associated with ligand degradation, while the active species for H$_2$ evolution consists of Co-based nanoparticles formed on the electrode surface.[60] Furthermore, Lacy *et al.* proposed that the intermediate complex in the HER pathway is a Co-complex, which crystallizes as a dimer and exhibits monomer-dimer equilibrium in an organic solvent.[65] The NMR signal assigned as Co^{III}–H for Schrauzer's synthesized hydridocobaloxime is the cobalt trimer instead of Co^{III}–H.[65] Estes *et al.* also challenge the reliability of Co^{III}–H assignment in the cobaloxime system.[66] They propose that the ligand bears the reactive H atom instead of the Co-center. These collective thoughts still do not rule out the formation of Co^{III}–H as an intermediate in the HER mechanism; however, they encourage the consideration of ligand-based protonation schemes in HER mechanisms.

While various studies on metal-hydride formation have led to significant advances in designing efficient molecular catalysts evolving H$_2$, recent years have witnessed a growing interest in using ligands. This attention to ligands arises from the potential for alternate pathways facilitated by the coordination environment, which can result in enhanced catalytic activities.

1.3 Redox-active ligand-centered HER electrocatalysts

Redox-active ligands imply the non-innocent ligand framework that is capable of undergoing an oxidation reaction or a reduction reaction in the transition metal complexes. Ligand non-innocence and redox-active ligand descriptions might be understood as interchangeable terms; however, they differ in some ways.[67] Non-innocent complex conveys uncertainty to determine the oxidation states of the redox-active molecules and stating specific ligands as "suspects".[67-69] Ligands are innocent if the oxidation state of the central atom can be defined and the metal-center acts as the source or sink of electrons transferred.[70] Redox-active ligands can behave both in innocent or non-innocent ways.[69] Since the ligands can participate in the HER by acting as electron or proton storage sites or both, they can enhance the reaction kinetics, decrease the overpotential, and improve stability.[13, 71-80] Furthermore, the redox-active ligands can introduce new catalytic pathways to HER mechanisms by disrupting the electron density distribution within the catalyst. Instead of the metal-center, the electron density may be located on the ligand scaffold resulting in alternative mechanistic pathways. The alternative HER pathways involving redox-active ligands are ligand-assisted metal-centered, metal-assisted ligand-centered, or only ligand-centered mechanisms (Figure 1.6). Besides all the advantages, different effects related to the involvement of the redox-active moieties may be expected. The reduced state of the redox-active ligand may lead to undesired reactivity. For instance, they can react with electrophilic substrates, and the electron on the ligand might be trapped due to the formation of irreversible chemical bonds. Consequently, the deactivation or decomposition mechanisms may occur due to the redox-active moiety. Therefore, it is challenging to draw conclusions regarding the impact of the redox-active ligands, and understanding the effects of the different redox-active ligand systems can assist in developing more efficient electrocatalysts.
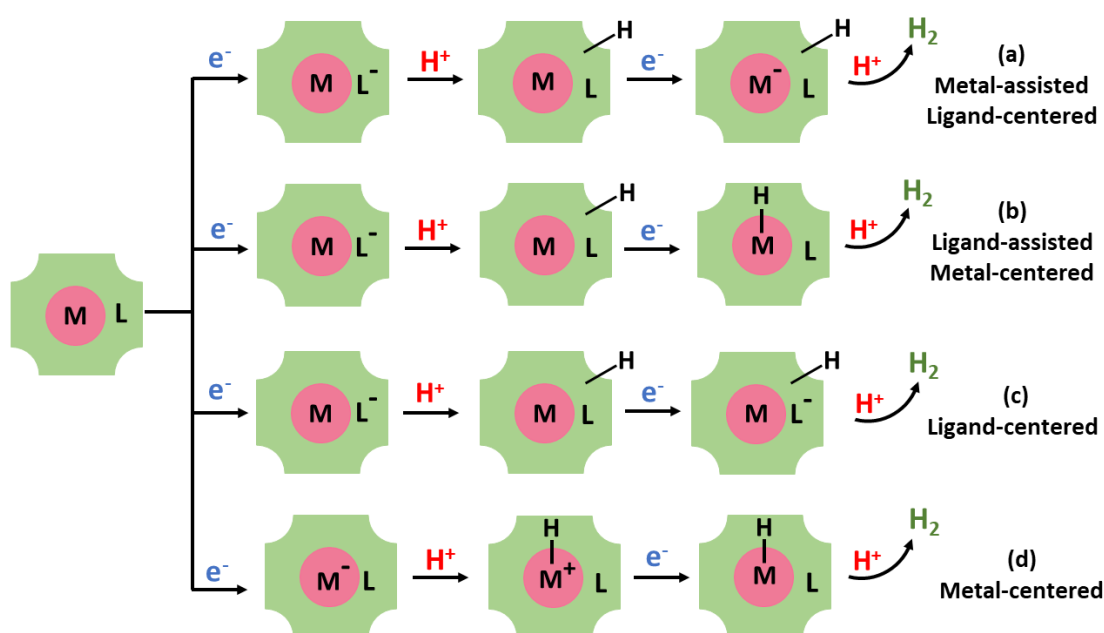
Figure 1.6: Various H_2 evolution pathways by metal complexes containing redox-active ligands. Reprinted with permission from Hess *et al.* [81]. Copyright 2024 American Chemical Society.

One example of compounds containing bidentate redox-active ligands is a dithiolate-based complex. Owing to its unique electronic properties, the electron density on metal-dithiolene complexes is delocalized over the metal-sulfur core, enabling electron storage on the ligand core, and stabilizing anionic oxidation species. In their studies, Mcnamara *et al.* and Das *et al.* showed that Co-centered dithiolene complexes can produce H_2 in photocatalytic and electrocatalytic ways.[6, 82] The electrocatalytic mechanism is proposed to be ECEC, and due to the similar energy levels of the frontier metal and the ligand-based orbitals, protonation may take place at either the metal-center or the ligand. Even though Co-based dithiolene complexes are more extensively studied, Fontcave *et al.* suggested using Mo and W-centers for oxo-dithiolene complexes as alternative metal-centers, and the theoretical calculations show that the ligand acts as a proton exchange site.[83] Based on all the intriguing research, Zarkadoulas *et al.* drew inspiration from the natural NiS_4 cluster of the active site of [NiFe] hydrogenase and investigated the complexes with Ni-centered bis-1,2-dithiolate ligands for H_2 evolution.[72] They claim the substituents with electron-donating ability on the dithiolene ring improve the HER activity, and the decomposition of the dithiolene complexes most probably depends on the acid strength on applied potentials.
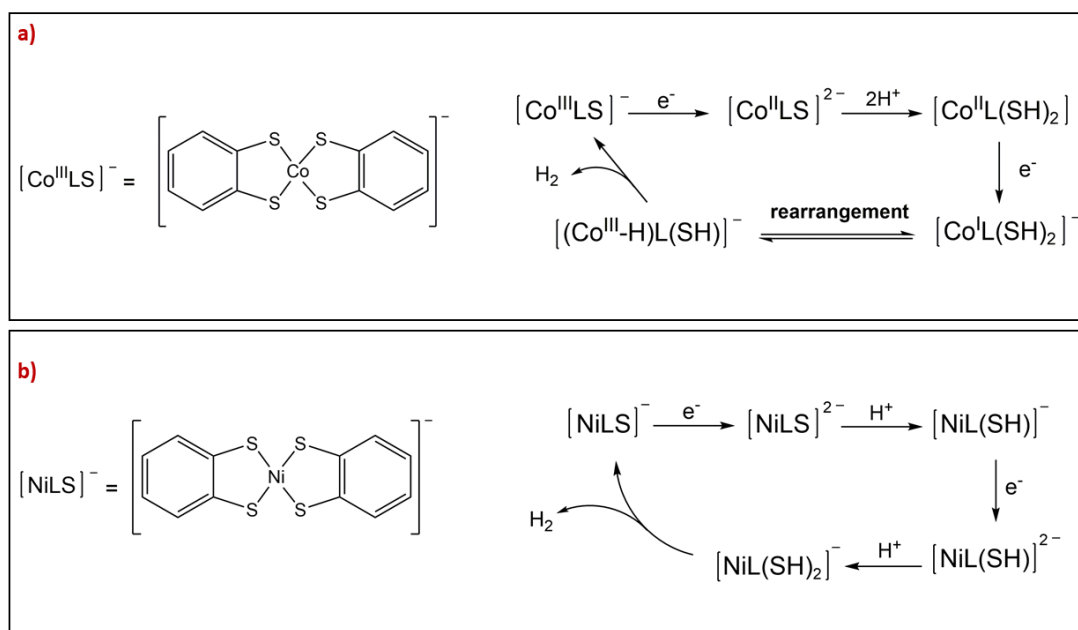
Figure 1.7: H$_2$ evolution pathways by a) Co- or b) Ni-centered dithiolate complexes.

The theoretical calculations on the dithiolate complexes reveal that reduction and protonation steps occur most likely at sulfur atoms (Figure 1.7).[72, 84, 85] To understand the effect of redox-active ligands, theoretical calculations are extensively used to investigate the mechanistic pathways of dithiolene ligands toward H$_2$ evolution. Theoretical calculations on the Co–dithiolene complexes for HER reported by Solis *et al.* and Panetier *et al.* showed that the reduction occurs on the Co-center and sulfur atoms are the protonation sites for H$_2$ evolution.[84, 86] In the report by Solis *et al.* varying electron-withdrawing substituents on the dithiolene ligands were examined and strongly electron-withdrawing groups on the ligand were less likely to have two protonated sulfur atoms. [84] The mechanistic pathway suggests that the protonation of the sulfur atom facilitates Co$^{II/I}$ reduction, which results in the generation of Co^{III}–H via intramolecular proton transfer by one of the S–H parts of the modified complex (Figure 1.7a). Another mechanistic pathway suggests that after two-electron reductions, the first generation of Co^{II}–H occurs, and the ligand-based protonation at a sulfur atom is essential to release H$_2$ as a last step.[86] In contrast to Co-dithiolene complexes, the protonation of the sulfur atoms is more likely than protonation on the Ni-center for Ni-dithiolate complexes, and it is proposed that both the protonation and reduction effects mainly occur on the

ligand framework (Figure 1.7b) due to the decreased contribution of the Ni orbitals. Koshiba *et al.* designed a Ni pyrazinedithiolene catalyst, which exhibits a relatively low overpotential (330-400 mV at pH 4–6) and high Faradaic efficiency toward HER.[87] With this specific ligand, it is proposed that the protonation and reduction occur on the ligand, and the Ni-center remains as Ni^{II} throughout the mechanism, which follows the ligand-centered PCET pathway. Although each dithiolene ligand system shows different reduction and protonation steps, the HER follows either the ligand-centered or the ligand-assisted metal-centered pathways that play a crucial role in the kinetics and activity.

Thompson *et al.* reported Al-centered pyridine complex, which includes a redox-active ligand assisting the HER in a non-aqueous environment.[76, 88] The mechanism of this redox-active complex suggests the involvement of two protonation events at the ligand that are followed by two electron reduction of the modified ligand to release H$_2$.[76] This complex is the first example for main group compounds involving molecular catalyst, which promotes only ligand centered pathway for HER. In another study, an Al-centered pyridine complex with low pK$_a$ values for the N-donor atoms undergoes the HER mechanism involving the ligand-centered pathway, whereby the pK$_a$ values of the ligand influence the reactivity with protons.[88] In the mechanism, the ligand is first reduced, and then the reduced ligand facilitates electron and proton transfer to release H$_2$. The results indicate that controlling the ligand's donor atom can tune the HER mechanism. In this specific system, the low pK$_a$ values of the ligand can enhance the ligand-based electron and proton transfer.
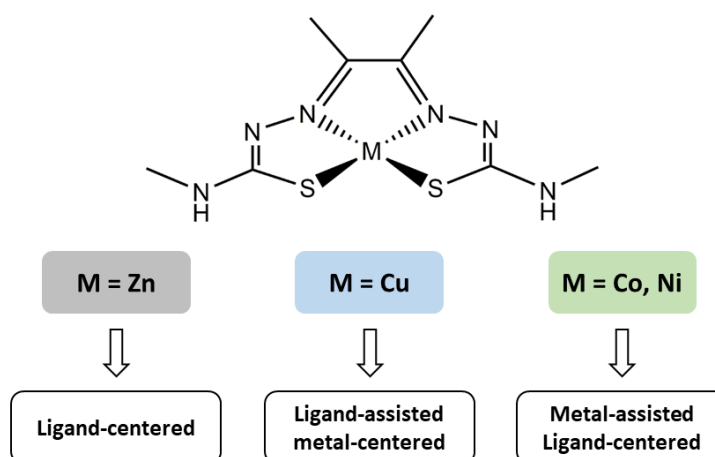
_____

Figure 1.8: Overview of transition metals with bis(thiosemicarbazone) ligand for HER

Bis(thiosemicarbazone) ligands derived from 1,2-diones are redox-active ligands and can coordinate with transition metals with low oxidation states through the N_2S_2 chelating site.[75, 79, 89-91] Owing to its ability to have multiple modification sites on the structure, these molecules attracted great attention. The coordination of redox-active bis(thiosemicarbazone) ligands with different transition metals can affect the HER pathways (Figure 1.8). The first reported bis(thiosemicarbazone) complex as an HER catalyst involves Zn as the metal-center (Figure 1.9a).[89] The kinetic parameters, including digital simulations, suggest that the catalytic cycle starts with the EC mechanism, proceeding with two hypothetical catalytic cycles. The first possible pathway (stated as 1, Figure 1.9a) involves homocoupling of the two modified complexes after the EC mechanism. The second one (stated as 2, Figure 1.9a) is based on the heterocoupling of the complex with the modified complex (an ECC step to the catalyst). Calculations suggest that protonation occurs on the hydrazine nitrogen within the complex, and the release of H_2 proceeds through ligand-centered radical coupling. Unlike the traditional catalysts evolving H_2 through metal-hydride, the non-transition metal-center combined with the thiosemicarbazone ligand restrains the activity on the ligand, and the high Lewis acidity of Zn^{II} in the structure reduces the overpotential by balancing the charge on the anionic ligand and enhancing protonation.

Cu[II] is another alternative as a metal-center for the bis(thiosemicarbazone) ligand, and Grapperhaus and his coworkers examined the Cu[II]-centered complex as an H_2 evolving electrocatalyst that operates via the metal-assisted ligand-centered pathway (Figure 1.9b).[79] The proposed HER pathway favors the CECE mechanism, and the initial chemical step involves the protonation of hydrazine nitrogen on the ligand followed by metal-centered reduction that yields a Cu[I]-center. In the mechanism, the third step involves protonating the opposing hydrazine nitrogen, and the Cu-center retains the +1 oxidation state. The final electrochemical step is based on the ligand-centered double-bond rearrangement within the complex, which promotes internal proton transfer. In the last step, a hydrogen atom or proton/hydride coupling leads to H_2 evolution and forms the initial complex. Thus, the H_2 evolution involves a metal-assisted ligand-centered path; in this context, the metal serves as an auxiliary redox site. Therefore, this system promotes electrocatalysts that function without metal-hydride formation for HER.
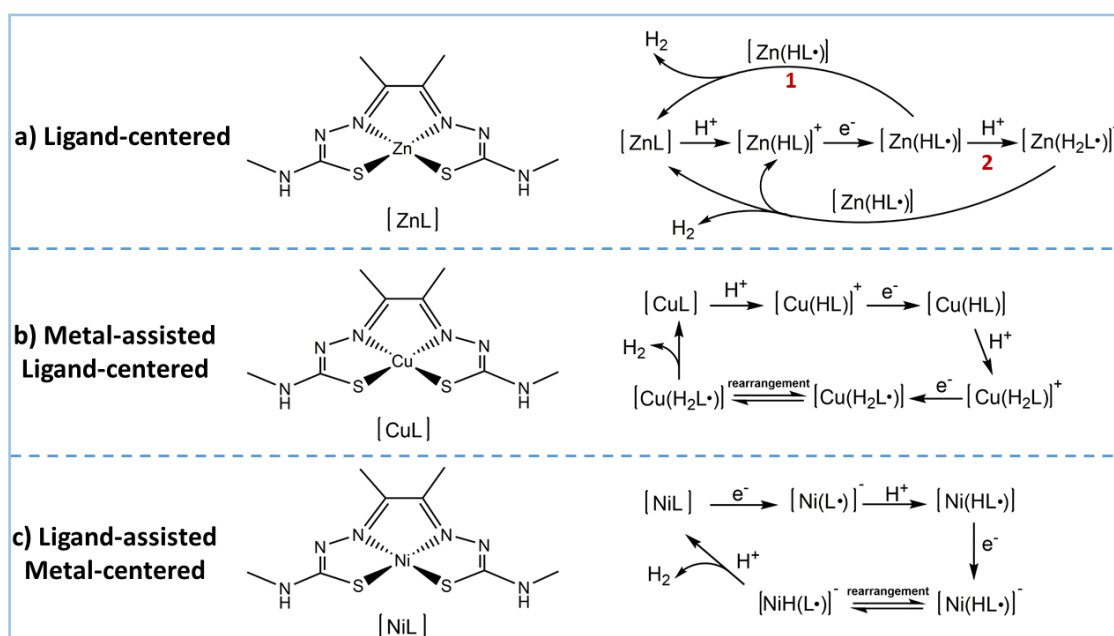

Figure 1.9: Three types of HER mechanisms with first-row transition metal coordinated bis(thiosemicarbazone) complexes: a) ligand-centered, b) metal-assisted ligand-centered, c) ligand-assisted metal-centered.

The studies involving Ni[II] coordinated bis(thiosemicarbazone) complexes revolve around the ligand-assisted metal-centered mechanism; however, they involve diverse electrochemical and chemical steps to evolve H_2.[75, 90] The computational studies by Orio and her coworkers claim the HER mechanism involves a PCET step

_____

on the ligand as the first reaction step and the protonation occurs on the hydrazino nitrogen.[75] The second step involves the reduction of the metal-center to Ni^I followed by Ni-centered protonation to generate H_2. Thus, the HER mechanism consists of PCET followed by an EC mechanism, and the metal-center is essential for H_2 evolution. Jain *et al.* proposed ECEC steps for the HER mechanism supported by computational investigations (Figure 1.9c).[90] In this study, the mechanism starts and continues the same as Orio and her coworkers determined; however, the metal-hydride is generated via an internal proton transfer instead of an external proton transfer. As a final step, the metal-hydride (Ni^{III}–H) complex reacts with an external proton source to evolve H_2. Straistari *et al.* assessed the HER mechanism of a Co coordinated bis(thiosemicarbazone) complex to understand the effect of the Co-center on H_2 evolution.[91] The results indicate that changing the metal-center to Co does not change the ligand-assisted metal-centered pathway and the ECEC sequence. According to Straistari's study, the Co^{III}–H and protonated ligand radical species generate H_2 in the HER mechanism like the Ni–bis(thiosemicarbazone) system. Overall, the thiosemicarbazone ligand shows a variety of HER mechanisms depending on the nature of the metal-center and proves that metal-hydride formation is not necessary to evolve H_2 at moderate potentials.
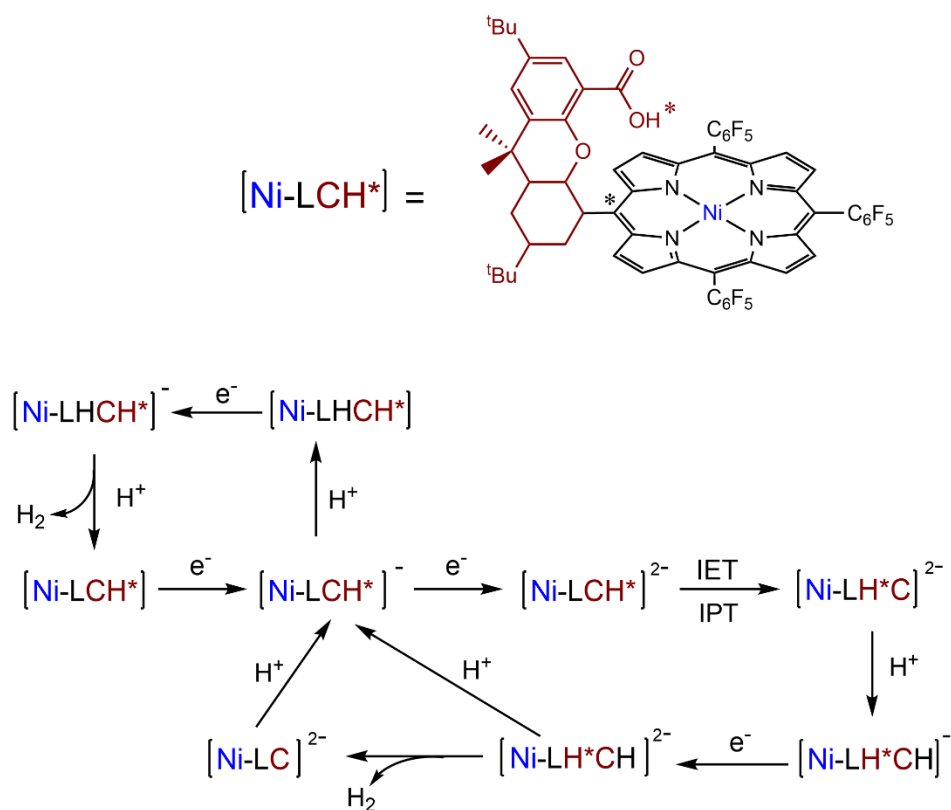
Figure 1.10: Proposed HER mechanism of Ni hangman porphyrin in different acidic media. C and L representing the hangman group and porphyrin ring, respectively. H with a red asterisk corresponding to the internally transferred proton on carboxylic acid and a black asterisk corresponding to the site that the internal proton transferred. IET and IPT on the mechanism standing for internal electron transfer and intramolecular proton transfer, respectively. Internal electron transfer affecting the Ni-center and all the other electron transfers on the mechanism involving the ligand.

Nocera and Hammes-Schiffer and their coworkers discovered the utility of the hangman active sites as pendant proton relays in governing PCET for H_2 evolution.[92-95] In the hangman structure, acidic or basic functional groups affixed to a xanthene or furan backbone are positioned over a redox-active macrocycle such as porphyrin, corrole, or salen. In these studies, a carboxylic acid group enhances an internal proton transfer to the metalloporphyrin, capable of electrochemical reduction. Furthermore, Solis *et al.* studied the influence of acid strength on the HER pathways for Ni (Figure 1.10) or Co coordinated hangman porphyrins.[93, 94] The H_2 evolution potential in the presence of a weak acid occurs above −1.8 V vs. ferrocene/ferrocenium (Fc/Fc⁺ potential). On the other hand, using a strong acid leads to H_2 evolution at −0.66 V vs. Fc/Fc⁺.[94] In the presence of a weak acid, the catalytic cycle begins with two reduction steps for Ni hangman porphyrins. The first reduction occurs on the Ni-center, and the second on the porphyrin ring. The

following step involves a PCET reaction by an internal ET and an intramolecular PT from the carboxylic acid to a *meso* carbon on the porphyrin. The subsequent step is the protonation of the hanging carboxylate group, followed by a reduction of the phlorin ring. Further reduction leads to H_2 evolution via self-elimination to the deprotonated complex or by reaction with the weak acid, and the formed complex at the end is the one-electron reduced of the initial Ni coordinated hangman porphyrin. However, the theoretical calculations on Co coordinated hangman porphyrins imply that Co^{III}–H formation is necessary for H_2 evolution in a weak acid.[93] In the presence of a strong acid for both Ni and Co coordinated hangman porphyrins, the catalytic cycle begins with a reduction step, affecting the metal-center that is followed by a proton transfer step via a direct protonation of the *meso* carbon from the acid source. The subsequent reduction occurs rapidly, forming the phlorin anion reacting with the acid to produce H_2. These studies imply that the protonation of phlorin ring is more favorable than metal-hydride formation in the presence of a strong acid, and the main contribution to H_2 evolution is the ligand framework. Moreover, the weak acid causes too many protonation and reduction steps in the catalytic cycle prior to H_2 evolution, leading to a higher overpotential for HER.

All the redox-active ligand systems mentioned in this chapter demonstrate that they play different roles during the HER. Several factors, such as the metal-center, active site, and proton source, contribute to tuning HER activity. There is still a debate on the conclusive effects of redox-active ligands, and open questions remain regarding how redox-active ligands may affect the catalytic mechanism. Drawing relevant comparisons between complexes is challenging since the redox moieties of the ligand frameworks in each system are different. In the past years, the redox-active macrocyclic biquinazoline (Mabiq) ligand system was investigated to comprehend the effect of the redox-active system in catalysis.[81, 96-100] Muller *et al.* first synthesized the Mabiq ligand (Mabiq = 2−4:6−8-bis(3,3,4,4-tetramethyldihydropyrrolo)-10−15-(2,2′-biquinazolino)-[15]- 1,3,5,8,10,14-hexaene-1,3,7,9,11,14-N_6, Figure 1.11), and different earth-abundant transitional metals were subsequently coordinated to the redox-active Mabiq ligand.[101-104]

Furthermore, bimetallic Mabiq complexes based on the monomeric metallic complex were generated to understand whether a second metal can improve the catalytic activities. The focus of this thesis is to investigate a monometallic Co coordinated Mabiq complex, [Co^{II}(Mabiq)(THF)](PF$_6$)], (Co$_{Mbq}$) as an electrocatalyst for H$_2$ evolution and to elucidate the HER mechanism. In the Results Section 3.1, we show electrochemical H$_2$ evolution by the Co$_{Mbq}$ complex for the first time and examine the activity as a function of the different acid concentrations. The Results Section 3.2 describes different techniques to explore the HER mechanism through the Co$_{Mbq}$ complex. Moreover, various proton sources were used for mechanistic studies, and theoretical calculations were applied to determine the possible reduction and protonation sites on the Co$_{Mbq}$ complex. Overall, these studies with Co$_{Mbq}$ show how various features of redox-active ligands can influence catalysis, and catalyst design plays a significant role in HER pathways.
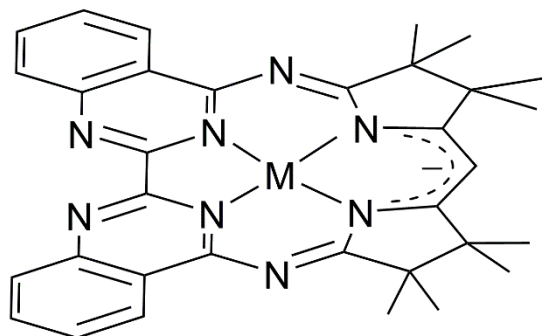

Figure 1.11: The structure of macrocyclic biquinazoline ligand (Mabiq), M in the structure representing the earth-abundant transition metals.

2 Experimental Methods

2.1 Synthesis of [Co(Mabiq)(THF)](PF$_6$)

In the course of this PhD project, the [Co(Mabiq)(THF)](PF$_6$) complex is generated and analyzed. Both HMabiq ligand and [Co(Mabiq)(THF)](PF$_6$) are synthesized as described in the literature.[102, 104] Upon the HMabiq generation in 5 steps, [Co(CH$_3$CN)$_6$](PF$_6$) (Scheme 2.1) is added to a suspension of HMabiq and trimethylamine in acetonitrile (MeCN) in an Argon–filled glovebox (O$_2$<0.1 ppm, H$_2$O<0.1 ppm, MBraun, Germany). After stirring overnight, the resultant mixture is filtered, and the crude product is dissolved in dichloromethane (DCM) and precipitated in hexane. As a last step, single crystals are obtained by slow diffusion of pentane into Co$_{Mbq}$ complex dissolved in tetrahydrofuran (THF). Elemental analysis is used to characterize the synthesized [Co^{II}(Mabiq)(THF)](PF$_6$).
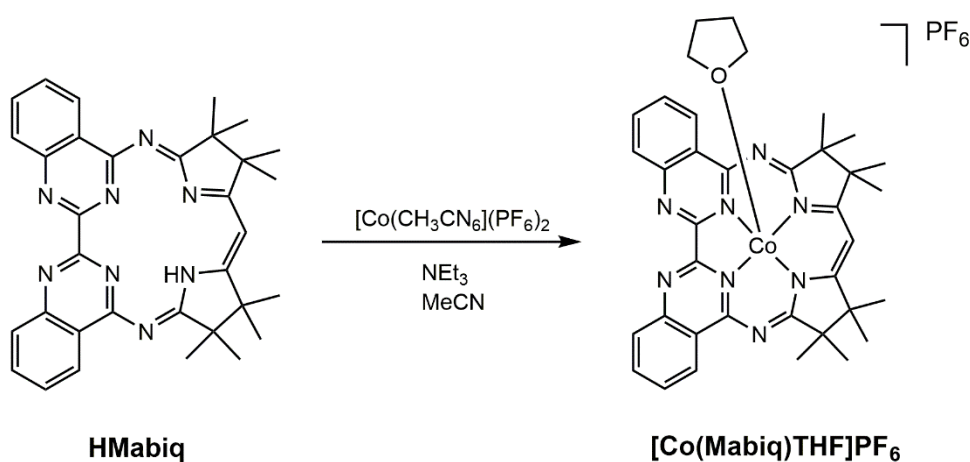
Scheme 2.1: Synthesis of [Co(Mabiq)(THF)](PF$_6$).

2.2 Cyclic voltammetry (CV)

Cyclic voltammetry (CV) is a powerful electroanalytical technique to examine the oxidation and reduction reactions of molecular species; it is a valuable tool to comprehend complex reactions.[105, 106] This method can mainly be used to investigate the electrochemical behavior of species diffusing to an electrode, interfacial phenomena at the electrode surface, and the bulk properties of the materials.[107] A CV is based on a linear potential sweep applied to a stationary electrode in an unstirred solution and the resulting current response is plotted against the potential. In general, the current is controlled by the rates of mass transfer, electron transfer, surface reactions, and chemical reactions following the electron transfer, such as protonation. In principle, mass transfer includes diffusion, migration, and convection as its main elements, but in a CV experiment with a stagnant electrolyte containing a large amount of a non-reacting salt next to a small amount of an electroactive species, diffusion is the only mass transport mode. This results in a time-dependent concentration gradient in the vicinity of the electrode surface. Figure 2.1 shows the triangular potential profile (panel a) and the typical current response (panel b) for a simple redox reaction ($A^{-\bullet} \leftrightarrow A + e^-$). Note that here, the US convention is used, where the negative potential is plotted on the y– and x– axes in panel a and panel b, respectively, and where cathodic currents are taken as positive currents. Starting the potential scan at E_i by going towards more negative potentials; initially, small capacitive currents are flowing until the equilibrium potential ($E^{0'}$) is reached; going towards $E^{0'}$, a faradaic reduction current starts to flow provided by $A + e^- \rightarrow A^{-\bullet}$ and the reduction takes place (Figure 2.1b). Going to more negative potentials, the reduction current increases until a current peak is reached, where the concentration of A near the surface of the electrode is depleted. Eventually, the growth of the so-called diffusion boundary slows down the transport of A to the electrode surface, leading to a decreasing reduction current. When the potential scan is reversed, i.e., when scanning to a positive direction, the reduction current further declines until the potential approaches $E^{0'}$, at which point the accumulated reduced species ($A^{-\bullet}$) are being oxidized, resulting in an anodic current peak.
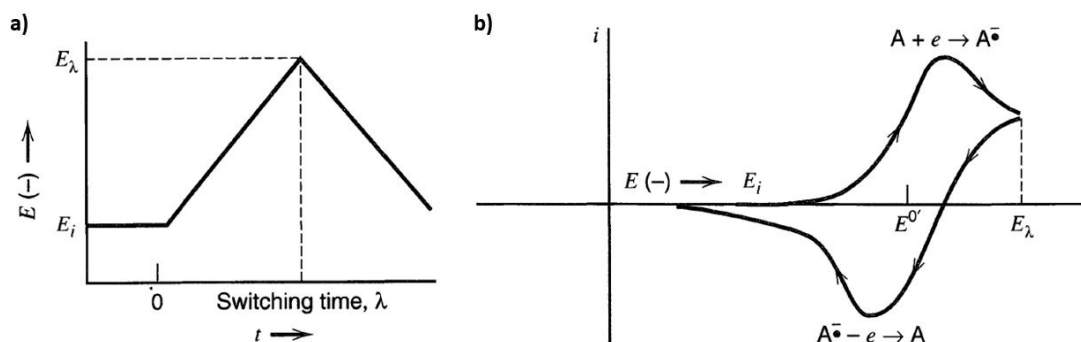
_____

Figure 2.1: a) Cyclic potential scan b) Resulting cyclic voltammogram (in US convention). Reprinted from Bard and Faulkner *et al.*[106]. Copyright 2024 John Wiley and Sons.

The Nernst equation is one of the most quoted equations that relates the half-cell potential to a redox reaction ($C_R \rightarrow C_o + e^-$) to the standard half-cell potential ($E^{0'}$) and the relative activities of the oxidized and reduced species at equilibrium. When the kinetics of the electron transfer is rapid, the concentration of oxidized and reduced species at the electrode surface ($C_{o,\,x=0}$; $C_{R,\,x=0}$, respectively) are assumed to be in equilibrium with the electrode potential, governed by the Nernst equation (Eq 2.1). In the Nernst equation, F is Faraday's constant (96485 C·mol^{-1}), R is the universal gas constant (8.314 J·mol^{-1}·K^{-1}), n is the number of electrons, and T is the temperature (K).

$$E \; = \; E^{0'} + \frac{RT}{nF}\ln\frac{C_o}{C_R} = E^{0'} + 2.3026\,\frac{RT}{nF}\log\frac{C_o}{C_R} \qquad \text{(Eq 2.1)}$$

If the redox process is chemically and electrochemically reversible, the potential difference between the anodic and cathodic current peak, *i.e.*, the peak-to-peak separation, is $2.3RT/nF$, corresponding to $59/n$ mV at 25°C.

In the course of this project, the CV technique was one of the first applied electrochemical techniques to address the possible generated intermediates of Co_{Mbq} in the presence of an acid source and an applied negative potential. During the PhD project, various concentrations of the proton source and acids with different pK$_a$ values were added to the Co_{Mbq} solution, and the potential was scanned to different cut-off values. For this purpose, CV measurements were performed in a four-neck, jacketed glass cell assembled and sealed inside the

_____

glovebox. The cell setup was adopted from previous studies described in detail in section 2.3.[108, 109]

2.3 Rotating (Ring) Disk Electrode (R(R)DE)

The rotating disk electrode (RDE) and rotating ring disk electrode (RRDE) are widely applied to investigate the reaction kinetics and transport properties of the electrochemical reaction systems. Diffusion and convection are two major mass transport processes in the RDE configuration. Based on the Nernstian diffusion boundary layer model, the electrolyte is conceptually divided into two regions. The first region, which is close to the surface of the electrode, is considered to form a stagnant in which diffusion is the only mode of mass transport. In the second region, far away from the electrode surface, it is considered that all species have a constant concentration, so that convection is the only mode of mass transport.[110, 111] The result is that for a rotating disk electrode, the thickness of the diffusion boundary layer remains constant, resulting in a steady-state mass transport limited current. By precisely controlling the rotation rate of the electrode, the RDE generates a well-defined mass transport limited flow of electrolyte species to the surface of the electrode.[106, 110] Since the flux of the solution towards the disk surface does not alter with the radial distance from the axis of rotation, mass transport at the disk is considered to be uniform across the disk, which is then referred to as uniformly accessible.
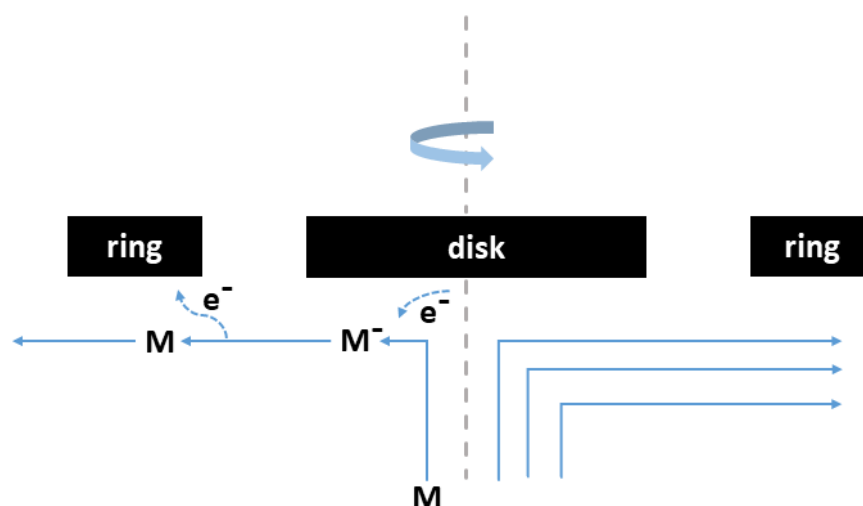

Figure 2.2: Schematic presentation of a planar RRDE electrode and the process occurring at the RRDE during the potential sweep. M: species in the bulk solution and M⁻: one electron reduced species.

The RDE setup consists of a central planar disk electrode embedded in a rod made of an electronic insulator material such as polytetrafluoroethylene (PTFE) or polyetheretherketone (PEEK), with an electrical brush employed to connect the electrode shaft and wire during electrode rotation. As the electrode rotates at a certain angular velocity of ω (rad/s), the centrifugal force causes the solution to flow toward the electrode (disk) surface, following a laminar flow pattern across the electrode surface and flushing out parallel to the disk surface (Figure 2.2). The current at the RDE assumes a steady state value when the angular velocity is fixed, in contrast to the transient in an unstirred solution where the current ultimately decays to zero. At the steady state, the concentration of the species close to the surface no longer depends on time. Under these conditions, an expression for the limiting current can be derived, known as the Levich equation (Eq .2.2):

$$i_{LC} = 0.62nFAD_O^{2/3}\omega^{1/2}v^{-1/6}C_O \qquad\qquad \text{(Eq 2.2)}$$

This equation applies to only mass-transfer-limited conditions an RDE. n stands for the number of electrons transferred, F for the Faraday constant (96485 C·mol^{-1}), A for the electrode surface area (in cm^2), D_o for the diffusion coefficient of the reacting species (in cm^2·s^{-1}), ω for angular velocity (rad·s^{-1}), v for the kinematic viscosity (cm^2·s^{-1}), and C_O for the concentration of the reacting species (mol·L^{-1}). Therefore, limiting current vs. $\omega^{1/2}$ for fast electron transfer kinetics can be determined by Eq .2.2 and is independent of overpotential (as long as it is sufficiently large).

Like an RDE, an RRDE consists of a central planar disk electrode imbedded into an insulator adding, however, a second working electrode in the form of a ring around the disk electrode. Both disk and ring electrodes in the RRDE setup are independently controllable. RRDE experiments are useful for studying multielectron processes, the kinetics of a slow electron transfer, and possible adsorption/desorption steps. The collection efficiency is one of the key characteristics of an RRDE that assists in identifying these processes. The collection efficiency quantitatively measures the amount of the reaction products or intermediates produced at the disk electrode, reaching the ring electrode. This factor allows for the analysis of the reaction mechanisms in catalytic reactions and is defined as the ratio of the absolute value of the ring current to the disk current obtained for a simple and fast redox reaction. If the reduction occurs on the disk

_____

surface, the ring should be kept at sufficiently positive potentials to re-oxidize the species that are reduced at the disk under mass transport limited conditions. By knowing the collection efficiency of a given RRDE, one can deduce the amount of reduced species that were reduced at the disk. The collection efficiency is normally between 20-40%, depending on the relative areas of the disk and ring electrode.

In this thesis, RDE and RRDE measurements were very valuable to examine the reaction mechanism prior to the HER using Co_{Mbq} as an electrocatalyst. Furthermore, the RDE concept was further employed for the bulk electrolysis experiments, which were designed to isolate the intermediate products prior to H_2 evolution. The disk was held at certain reductive potentials and rotated at a certain angular velocity to ensure high and defined mass transport rates from the solution to the electrode surface. All the experiments were conducted in an Ar filled glovebox due to the air sensitivity of Co_{Mbq}. In the cell setup, the working electrode consisted of a glassy carbon disk with a 5.0 mm diameter, surrounded by a glassy carbon ring with a 6.5 mm internal diameter and 7.5 mm external diameter. 1 M $LiBF_4$ in MeCN was used as a supporting electrolyte in the main compartment of the cell, which included the working electrode. A platinum wire, separated from the working electrode part via a glass fitting, was used as the counter electrode for the RDE and RRDE experiments. On the other hand, for bulk electrolysis experiments, a $LiFePO_4$ electrode was preferred as a counter electrode separated from the working electrode compartment via a glass fitting at the bulk electrolysis experiments. The reference electrode was separated via a Vycor frit from the working electrode for the RDE and bulk electrolysis experiments. While $Ag/AgNO_3$ (0.1 M $AgNO_3$ and 0.1 M $LiBF_4$ in MeCN) was chosen as a reference electrode for RDE experiments, Li metal in 1 M $LiPF_6$ in EC/EMC 3:7 (LP57) was used as a reference electrode for bulk electrolysis experiments.

2.4 On-Line Electrochemical Mass Spectrometry (OEMS)

The first goal of this PhD project was to prove that the Co_{Mbq} complex was an electrocatalyst for the H_2 evolution reaction. On-Line Electrochemical Mass Spectrometry (OEMS) is an insightful technique to monitor and quantify the evolved gaseous species during a reaction; therefore, this technique was employed to examine the H_2 evolution for Co_{Mbq}. The setup was developed by the Chair of Technical Electrochemistry at Technical University of Munich and is depicted schematically in Figure 2.3. It was described in detail in previous publications.[112,113] In brief, the setup consists of a custom-made electrochemical cell with a headspace volume of ~10 mL that is attached to a mass spectrometer via a capillary leak with a leak rate of ~$1x10^{-5}$ atm-cc s^{-1}(1 μL min^{-1}, Vacuum Technologies, United States). The quantification of H_2 (m/z = 2) was done by flushing the cell at the end of the measurement with a calibration gas containing 2000 ppm of the H_2 in argon.
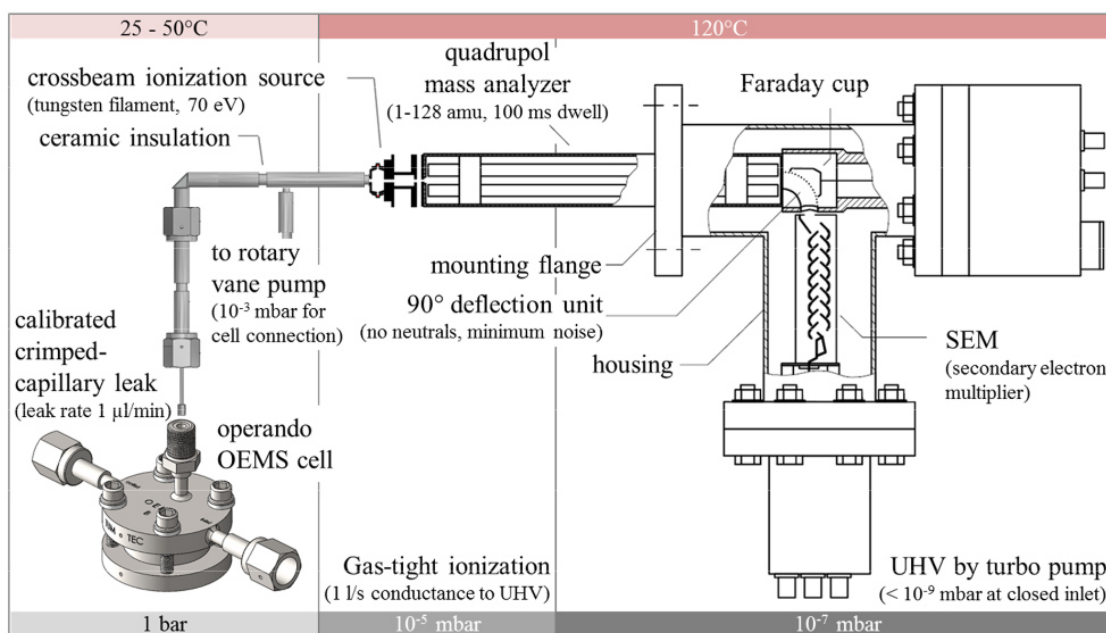

Figure 2.3: Schematic illustration of the OEMS setup. The figure is adapted with minor changes from Tsiouvaras *et al.*[112]. Copyright 2024 IOP Publishing.

In this PhD thesis, a two-compartment OEMS cell setup in which the counter electrode (lower compartment) part was separated from the working electrode part (upper compartment) that is connected via a capillary leak to the mass

_____

spectrometer. For this purpose, an aluminum edge-sealed lithium ion conducting glass ceramic ("Ohara glass", 1 inch diameter, thickness 150 μm) was used to separate two electrode compartments in the OEMS cell.[114] The lower compartment included a 17 mm diameter lithium counter electrode, a 22 mm glassfibre separator, and LP57 as electrolyte. The lithium ion conducting Ohara glass served as a diffusion barrier for gases and liquids between the two compartments. Thus, any gas evolution from the lower compartment cannot be detected. Only gas evolved in the upper compartment by Co_{Mbq} catalyst dissolved in 1 M $LiBF_4$ in MeCN in the presence of an acid source at the carbon paper working electrode (Freudenberg H1410, diameter 15 mm, thickness ~150 μm) was recorded by the mass spectrometer. H_2 evolved on the surface of the carbon paper during operation reached the mass spectrometer within seconds, while the diffusion of H_2 produced at the separator/carbon paper interface required at most a few minutes to transport H_2 into the cell headspace. Hence, the OEMS setup provides a significant advantage regarding response time. Chronoamperometry technique was applied to detect the onset potential for HER and quantify the maximum amount of released H_2.

2.5 Operando Transmission Ultraviolet-Visible (UV-Vis) Spectroscopy

Light absorption as a function of wavelength supplies information about electronic transitions happening in the material *via* ultraviolet-visible light (UV-Vis) spectroscopy. The energy difference within the occupied frequency range corresponds to the electronic states of atoms and molecules.[115, 116] In the case of isolated atoms, UV-Vis spectroscopy provides information about purely electronic transitions, and in the general case of molecules, rotational and vibrational motions are further excited by ground or excited states with their rotational and vibrational levels. The many transitions originating from the superposition of vibrational and rotational energy levels result in a broadened UV-Vis band.[116]

When light passes through a surface, it can be transmitted, reflected, or absorbed. Transmittance, absorbance, and extinction are frequently used terms for UV-Vis spectroscopy. The transmittance (T) (Eq 2.3) of a material refers to the part of the light that passes through the material. Absorption (A) (Eq 2.3) is the process where light intensity from the beam is decreased due to the transitions from the ground state to the excited state. Lastly, extinction refers to the entire loss of light upon passing through the material; it includes absorption, scattering, and reflection processes that lead to values higher than the absorption.

$$A = -logT = \frac{I}{I_0} \times 100 \qquad \text{(Eq 2.3)}$$

In Eq 2.3, *A* stands for absorbance, and *T* is for transmittance. I_0 represents the intensity of the incident light entering the sample, and *I* represents the intensity of this light emerging from the sample. These numerical values obtained from UV-Vis are applied to quantify the absorbance known as the Bouguer-Lambert-Beer law (Eq 2.4):

$$A = \varepsilon bc \qquad \text{(Eq 2.4)}$$

whereby ε (L·mol^{-1}·cm^{-1}) refers to the molar extinction coefficient, *b* to the path length of the sample in cm, and *c* (mol·L^{-1}) to the concentration of the light absorbing material.

UV-Vis theoretically enables the characterization of electronic transitions as either a direct and indirect transition or allowed and forbidden states. Investigations of solutions and crystals usually take place in transmission, whereas powder samples are often measured in diffuse reflection mode. In the catalysis field, UV-Vis spectroscopy is a commonly applied technique because the wavelength change on the absorption band allows for the characterization of any changes in the material. Many studies examine the shift in wavelength of the absorption band as a function of pH, temperature, solvent change, reaction with metal ions, and ligands.
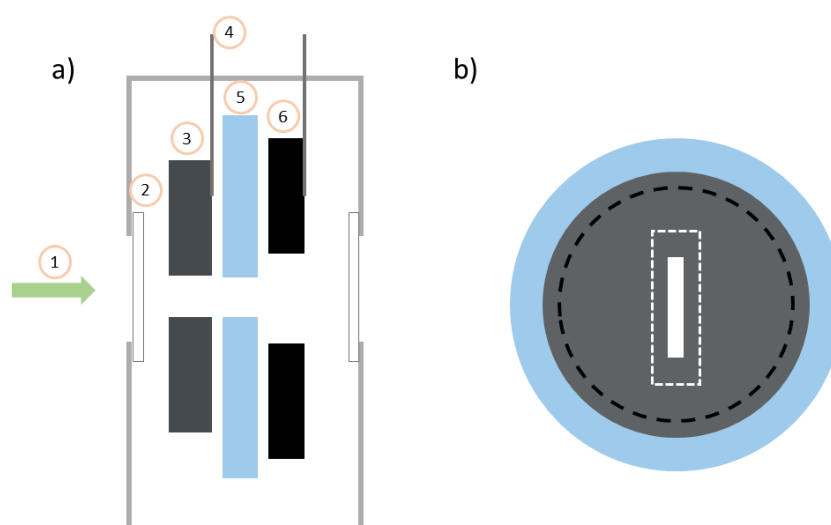

Figure 2.4: a) Operando UV-Vis spectroelectrochemical pouch-cell design: 1) incident UV-Vis beam, 2) quartz-glass (~165 µm), 3) carbon paper, working electrode (~150 µm), 4) Al or Ni current collector tab (~100 µm), 5) separator (80 µm = 4 layers of Celgard H2013), 6) chemically delithiated LFP, counter electrode (90 µm). b) Top view of working electrode (⌀ 15 mm, grey area) with a slit (1 mm×5 mm, white area), counter electrode (⌀ 14 mm, black dashed lined area) with a slit (3 mm×10 mm, white dashed line area) and separator (⌀ 18 mm, blue area) with a slit (1 mm×5 mm).

The setup based on a pouch-cell transmission spectroelectrochemical cell was developed by the Chair of Technical Electrochemistry at Technical University of Munich.[117] This special cell setup was employed for Li-S batteries and adopted over the course of this PhD study to screen the intermediates formed prior to H_2 evolution by Co_{Mbq}. In the cell setup, two quartz glass windows are sealed into the pouch case, and the small slits are cut into the separator, counter electrode, and working electrode to enable the transmission of the UV-Vis beam (see the design in Figure 2.4). The mechanistic insights prior to H_2 evolution by Co_{Mbq} gained

_____

significance since the first part of the study displayed that the Co_{Mbq} complex takes up protons and electrons to generate H_2 (see section 3.1). Due to the changes in the Co_{Mbq} complex, a change on the absorption bands was expected; thus, this spectroelectrochemical cell setup was employed (see section 3.3). Furthermore, bulk electrolysis combined with UV-Vis spectroscopy was applied to characterize the products generated during the bulk electrolysis (see section 3.2).

3 Results

This chapter presents the published work and unpublished results of the PhD thesis, which are grouped into three sections.

The first part (section 3.1), published as a peer-reviewed article, focuses on the H_2 evolution detection via the Co_{Mbq} complex in the presence of a proton source, applying various electrochemical techniques such as cyclic voltammetry, on-line electrochemical mass spectrometry (OEMS), and rotation ring disk electrode measurements (RRDE). OEMS analysis is utilized to investigate the onset potential of H_2 evolution and to quantify the evolved H_2 during the applied electrochemical procedure. RRDE is employed to examine the electron transfer steps prior to the H_2 evolution step.

The second part (see section 3.2.1), published as a peer-reviewed article, deals with the mechanistic insights of the Co_{Mbq} in the presence of a proton source as a function of the applied potential. The first part of this thesis revealed that the complex undergoes modification by electron and proton transfer to produce H_2. For this purpose, UV-Vis spectroscopy and bulk electrolysis methods are applied here with computational calculations to identify the intermediate complexes.

The last section (see section 3.2.2) shows unpublished work during this PhD study. Real-time monitoring of the intermediate complexes by operando transmission UV-Vis spectroscopy can give insight into HER mechanisms. However, problems due to the side reactions could not be resolved, so that this part was not published.

3.1 Electrocatalytic H$_2$ Evolution by the Co$_{Mbq}$ complex

The article "Electrocatalytic H$_2$ Evolution by the Co-Mabiq Complex Requires Tempering of the Redox-Active Ligand" was submitted in May 2019 and published online in July 2019 in the peer-viewed version of *ChemCatChem*. The main findings of the paper were presented as a poster by Gülen Ceren Tok at the 69th Annual Meeting of the International Society of Electrochemistry in Bologna, Italy in September 2018. A permanent link to this article can be found at: https://chemistry-europe.onlinelibrary.wiley.com/doi/abs/10.1002/cctc.201900953. To support the main article, additional information is provided in the Supporting Information, including details about the chemical stability of the Co$_{Mbq}$ complex in the presence of the acid source and the protonation step of the complex with applied potential.

This study aims to determine the onset potential for H$_2$ generation via Co$_{Mbq}$ as an electrocatalyst and examine the H$_2$ evolution mechanism catalyzed by this complex. The OEMS technique was explicitly established for Li-ion battery systems, and the cell components were adopted for this study. A two-compartment OEMS cell setup enables the detection of the gas evolution originating from the working electrode compartment. In this study, the working electrode compartment contains the Co$_{Mbq}$ complex and a proton source (*para*-cyanoanilinium, *p*CA), as well as a carbon paper (Freudenberg H1410) that serves as a working electrode. The chronoamperometric steps in the OEMS measurement revealed that Co$_{Mbq}$ evolves H$_2$ at an onset potential of −0.9 V vs. ferrocene/ferrocenium (Fc/Fc$^+$ potential, named as V$_{Fc}$), and the H$_2$ production increases exponentially. Alternating ratios of the catalyst and the proton source are applied to reach the maximum theoretical amount of H$_2$ generation at selected potentials; however, the results show that the amount of H$_2$ generated ranges between 48-62% of the theoretical amount of which, indicative of a possible deactivation of the catalyst. Another conclusion drawn from the OEMS measurements is that the catalyst may undergo activation prior to the catalysis since H$_2$ evolution is not observed until rather high overpotentials. Different chronoamperometric steps in OEMS measurement suggest that the redox events prior to the onset potential for H$_2$ generation lead to significant deactivation of the

_____

catalyst. The RRDE method is employed to further assess the redox events between −0.4 V_{Fc} and −0.85 V_{Fc}. To comprehend how many electrons are transferred at this redox step, firstly, Co_{Mbq} in the absence of *p*CA solution is evaluated by the RRDE technique using different rotation rates. The results prove that the obtained current with various rotation rates on the disk and ring agree with the Levich equation. In the presence of *p*CA, the initial redox event exhibits two electrons transferred to Co_{Mbq}. The redox event with increasing *p*CA concentration shifts to more positive potentials, indicating the likely proton-coupled electron transfer (PCET) process followed by electron transfer. The second protonation can not be ruled out; thus, the redox event between −04 V_{Fc} and −0.85 V_{Fc} refers to a precatalytic form of the catalyst and includes two electrons and at least one proton.

Author contributions

G.C.T. designed and conducted the CV, OEMS, RRDE, and UV-Vis experiments. A.T.S.F. assisted to design and employ the OEMS and RRDE experiments. G.C.T., A.T.S.F. and C.R.H. wrote the manuscript, and H.A.G. edited the manuscript. All the authors discussed the data and commented on the manuscript.

Electrocatalytic H$_2$ Evolution by the Co-Mabiq Complex Requires Tempering of the Redox-Active Ligand

G. Ceren Tok,[a, b] Anna T. S. Freiberg,[a] Hubert A. Gasteiger,*[a] and Corinna R. Hess*[b]

H$_2$ is a promising fuel for sustainable energy conversion and storage. The development of effective earth abundant H$_2$ evolution catalysts is integral to advancing hydrogen-based technologies. H$_2$ evolution by molecular complexes classically involves the formation of metal hydride intermediates. Recently, the use of redox-active ligands has emerged as an alternate strategy for electron and proton storage. Herein, we examine the electrocatalytic behavior of [Co^{II}(Mabiq)(THF)](PF$_6$) (**Co$_{Mbq}$**), containing a redox-active macrocyclic ligand, in acidic, organic media (using *para*-cyanoanilinium (*p*CA) as the proton source).

Cyclic voltammetry (CV) and Rotating Ring Disk Electrode (RRDE) voltammetry evidence a pre-catalytic process that leads to the formation of a protonated, two-electron reduced intermediate. This species evolves H$_2$ at potentials negative of -1.1 V$_{Fc}$, as confirmed by On-line Electrochemical Mass Spectrometry (OEMS). OEMS results further reveal a catalyst deactivation pathway. The electrochemical data denote the involvement of the redox-active Mabiq ligand in the hydrogen evolution reaction (HER), with implications for the use of such scaffolds in electrocatalytic complexes.

Introduction

The increasing demand for safe, clean and sustainable energy sources as an alternative to fossil fuels has prompted a strong interest in hydrogen-based technologies.[1] Hydrogen is an important candidate as a fuel for prospective electrochemical devices, such as proton exchange membrane fuel cells (PEM-FC).[2] H$_2$ can also be produced via photochemical water splitting, offering a promising approach to sustainable energy storage by solar fuel cells.[3] Both electrochemical and solar systems rely on the development of effective hydrogen evolution catalysts, including molecular complexes. With respect to electrochemical H$_2$ production, platinum is an excellent catalyst, exhibiting fast kinetics at low overpotentials. However, the low abundance and high cost of this noble metal[4] present significant obstacles for its comprehensive usage.[5] Hence, a number of earth-abundant HER catalysts have been developed over the last decade, inspired in part by metalloenzyme cofactors that carry out related redox and organometallic chemistry.[3a,c,6] Co and Ni complexes have demonstrated particular promise.[6a,b,7] However, molecular complexes still present several limitations.[3c] Key to improving the systems is a

detailed understanding of the factors that govern HER activity and overpotential.

The textbook mechanisms of H$_2$ formation by molecular complexes involve metal-hydride formation.[8] A correlation between the hydricity of metal complexes and reactivity has been established.[8–9] Recently, ligand-assisted and ligand-centered H$_2$ production pathways have attracted attention.[10] In such mechanisms, the metal site is not the exclusive protonation site, or is not involved at all. Amine and thiol groups, including in the hydrogenase active sites, readily take up protons that subsequently can be transferred to a metal-hydride to effect H$_2$ release.[6b,7c] Furthermore, redox-active ligands can store both protons and electrons.[11] Consequently, the ligands can act as reservoirs for hydrogen atoms or hydrides during the catalytic cycle. The H$_2$ evolution pathways of, e.g., pincer,[12] thiosemicarbazone,[10e,g,h] and thiolate[13] complexes are known to involve the redox-active scaffold. Proton relay sites and redox-active ligands are proposed to significantly enhance the kinetics of H$_2$ formation and decrease the HER overpotentials of metal complexes.[10c,g,h,12a,b,14] However, a redox non-innocent coordination environment also may result in non-productive pathways.[10f,15] The question remains whether the incorporation of redox-active ligands offers a strategy to overcome limitations of specific metal ions, and potentially allow a wider array of metal ions to be explored as electrocatalysts.
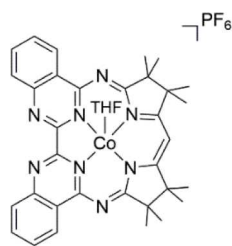
We herein describe studies on the H$_2$ evolution activity of a cobalt complex coordinated by the macrocyclic biquinazoline ligand, Mabiq (2-4:6-8-bis(3,3,4,4-tetramethyldihydropyrrolo)-10-15-(2,2′-biquinazolino)-[15]-1,3,5,8,10,14-hexaene-1,3,7,9,11,14-N$_6$).[16] Mabiq is redox-active, capable of storing electrons on each of its diketiminate and bipyrimidine units.[17] An electron transfer series of Co-Mabiq complexes was previously reported, which exemplify ligand-centered reduction among the formally 'low valent' compounds.[17b] We have previously shown that the reaction of protons with [Co^{II}(Mabiq$^{••}$)]$^-$ – containing the two electron reduced Mabiq ligand – leads to the formation of [Co

[a] G. C. Tok, A. T. S. Freiberg, Prof. Dr. H. A. Gasteiger
Chair of Technical Electrochemistry
Chemistry Department and Catalysis Research Center
Technical University of Munich
Lichtenbergstr. 4, Garching bei Munich (Germany)
E-mail: hubert.gasteiger@tum.de
[b] G. C. Tok, Prof. Dr. C. R. Hess
Chemistry Department and Catalysis Research Center
Technical University of Munich
Lichtenbergstr. 4, Garching bei Munich (Germany)
E-mail: corinna.hess@tum.de

Supporting information for this article is available on the WWW under https://doi.org/10.1002/cctc.201900953

This manuscript is part of the Special Issue dedicated to the Women of Catalysis.

Scheme 1. The structure of [Co^{II}(Mabiq)(THF)](PF$_6$) (**Co$_{Mbq}$**).

Figure 1. Cyclic voltammograms of **Co$_{Mbq}$** in 0.1 M LiBF$_4$/MeCN; conducted with a glassy carbon electrode in the RRDE set-up; 100 mV/s; under Ar atmosphere. Solid blue trace: 1 mM **Co$_{Mbq}$**; orange solid trace: 1 mM **Co$_{Mbq}$** plus 10 mM *p*CA. The dashed grey trace shows the CV of 10 mM *p*CA only, for comparison.

(MabiqH$_2$)], in which the macrocycle effectively stores H$_2$ on the bipyrimidine moiety.[18] Here, we report for the first time that [Co^{II}(Mabiq)(THF)](PF$_6$), **Co$_{Mbq}$** (Scheme 1), acts as an electrocatalyst for H$_2$ evolution. The HER by **Co$_{Mbq}$** was examined using a combination of electrochemical methods that provide initial insight into the mechanism and the role of the redox-active ligand.

Results and Discussion

The Co-Mabiq complexes adopt formal metal oxidation states of $0 \rightarrow +3$,[17b,18] encompassing the full range of oxidation states invoked in metal-based HER pathways. We therefore reasoned that the compounds also might act as electrocatalysts for H$_2$ evolution. However, the 'low-valent' Co-Mabiq compounds contain reduced ligand forms. The 'Co^{II}' complex was best described as [Co^{II}(Mabiq$^{\cdot}$)], with spin density localized on the diketiminate portion of the Mabiq ligand. The doubly reduced 'Co^{0}' form is in actuality a Co^{II} containing, ligand biradical complex, in which the bipyrimidine moiety also is reduced. The electronic structures of both complexes were previously established by spectroscopic and DFT computational methods.[17b,18] We questioned how the unique electronic structures might impact their reactivity.

The ability of the Co-Mabiq complex to act as an electrocatalyst for the HER was first investigated by cyclic voltammetry (CV) with **Co$_{Mbq}$**, using *para*-cyanoanilinium (*p*CA) as a proton source. In the absence of acid, the CV of **Co$_{Mbq}$** ([**Co$_{Mbq}$**] = 1 mM, in 0.1 M LiBF$_4$/MeCN) exhibits three reversible redox events (Figure 1, blue line) with cathodic peak potentials at $E_{p,c} =$ 0.08 V, −0.76 V and −1.56 V vs Fc$^{+/0}$ (V$_{Fc}$), which correspond to the *formal* Co$^{III/II}$, Co$^{II/I}$ and Co$^{I/0}$ couples, respectively. Upon addition of ten equivalents of *p*CA (pK$_a$ = 7 in acetonitrile),[19] a series of new redox waves emerge (Figure 1, orange line), at $E_{p,c} = $ −0.51 V$_{Fc}$ and −1.06 V$_{Fc}$, whereas the original Co$^{II/I}$ couple is no longer present. The closely spaced set of reductions positive of the original Co$^{II/I}$ couple coincide with only a modest current increase, suggesting the absence of H$_2$ evolution, as proven by OEMS (vide infra). However, the significant current increase negative of appx. −0.9 V$_{Fc}$ is indicative of electrocatalytic H$_2$ evolution, again consistent with the OEMS data shown below. The onset potential lies appx. 0.5 V$_{Fc}$ positive of the Co$^{I/0}$ couple, and therefore is unlikely to stem from the direct reactivity of the Co^{0} form. The control experiment using 10 mM *p*CA alone confirms that proton reduction from the acid
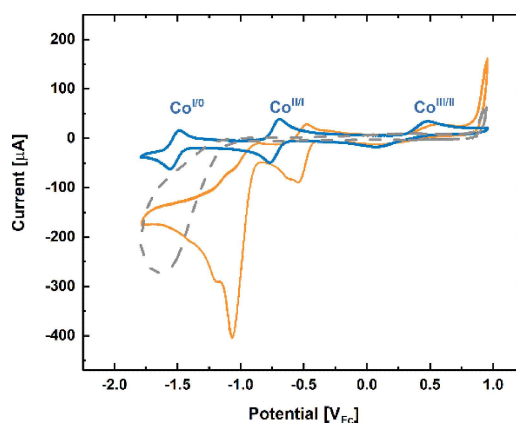
in the absence of a catalytic species, i.e. on a bare glassy carbon surface, only occurs at more negative potentials, namely negative of appx. −1.1 V$_{Fc}$, with a cathodic peak potential of $E_{p,c} = $ −1.65 V$_{Fc}$ (Figure 1, grey dashed line). The electrocatalytic behavior of **Co$_{Mbq}$** toward protons is in contrast to that of e.g. the well-studied cobaloximes, which exhibit onset potentials for HER already positive of the Co$^{II/I}$ couples.[20] The emergence of new redox events preceding catalysis in our system further suggests that hydrogen evolution may involve an 'activation' step with modification of **Co$_{Mbq}$**. We note that no change in the absorption spectrum is observed upon addition of 10 equivalents of *p*CA to a solution of the divalent **Co$_{Mbq}$** in MeCN (Figure S1), indicating that any modification to the Co–Mabiq complex occurs only after cathodic reduction. A rinse test experiment confirms that no complex is adsorbed on the electrode.[21]

On-line Electrochemical Mass Spectrometry (OEMS) experiments were performed to verify electrocatalytic H$_2$ evolution, and to establish the HER onset potential. In particular, we wanted to confirm that the redox process at $E_{p,c} = $ −1.06 V$_{Fc}$ corresponds to H$_2$ formation, and to determine whether any hydrogen might already be generated in the prior reduction steps between −0.4 and −0.85 V$_{Fc}$. To our knowledge, the OEMS set-up used here has not been applied previously to the study of homogeneous H$_2$ evolution electrocatalysts. This unique system permits hydrogen to be quantified at ppm-levels, with a fast response time, and to be monitored throughout the electrochemical experiment.[22]

Figure 2 depicts the amount of H$_2$ (m/z = 2) evolved vs. the applied potential in experiments using 4 mM **Co$_{Mbq}$** and 40 mM *p*CA (**Co$_{Mbq}$**/*p*CA) in 0.1 M LiBF$_4$/MeCN. The theoretical amount of H$_2$ that can be produced under these conditions, assuming 100% conversion of the total amount of added acid by the catalyst, is 2.8 µmol. An open circuit voltage (OCV) step was initially applied to the system (from −2 to 0 h), after which the potential was decreased by 100 mV every 30 min, from
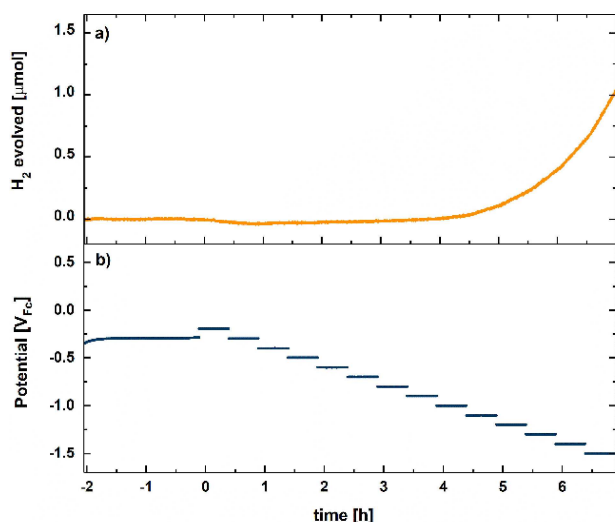
Figure 2. OEMS data for the mixture of 4 mM Co_{Mbq} and 40 mM pCA (Co_{Mbq}/pCA), using a carbon fiber paper as the working electrode and Li metal as counter and reference electrodes (sealed by a Li-ion conducting glass ceramic from the working electrode compartment). a) The amount of H_2 (m/z = 2) evolved at varying potentials. b) After the OCV step (-2 h to 0 h), the chronoamperometry (CA) steps were initiated and the potential was decreased by 100 mV from -0.2 V_{Fc} to -1.5 V_{Fc}, every 30 min.

-0.2 to -1.5 V_{Fc} (Figure 2b), and mass spectra were recorded throughout (Figure 2a). Two important conclusions can be drawn from the OEMS data (Figure 2). Firstly, Co_{Mbq} clearly evolves H_2, with an onset potential of -0.9 V_{Fc}, after which H_2 production increases exponentially with increasing overpotential. Secondly, although significant cathodic charge flows at potentials positive of $-0.9 V_{Fc}$ – both during the CV (orange line in Figure 1) and during the chronoamperometric (CA) steps in the OEMS experiment (Figure S2b) – hydrogen evolution is not observed until the potential is decreased to below $-0.9 V_{Fc}$; a further indication that the catalyst may undergo activation prior to catalysis.

The rate of H_2 evolved per hour at each potential (Figure 3b, red squares), and the percent H_2 generated (Figure 3b, blue squares) by Co_{Mbq}/pCA, was determined from the OEMS data. The values for percent H_2 are additive and represent the total amount of hydrogen accumulated at each potential, referenced to the theoretical H_2 amount corresponding to 100 % acid conversion. For comparison, the CV of Co_{Mbq}/pCA under standard conditions (1 mM Co_{Mbq}, 10 mM pCA; glassy carbon electrode in the RRDE set-up) is shown in Figure 3a. The total amount of H_2 produced by Co_{Mbq} at the end of the experiment was only 38 % (i.e., 1.05 µmol of the possible 2.8 µmol, Figure 2a).

The experimental conditions were subsequently adjusted to determine whether the maximum theoretical amount of H_2 could be generated using alternate ratios of Co_{Mbq} and pCA, and by applying a potential at which H_2 can be evolved for a longer time. Accordingly, the potential was held at -1.1 V_{Fc} for 20 hours after the OCV step. A moderate rate of H_2 evolution by Co_{Mbq} is observed at the selected potential, whereas the background hydrogen generated due to reduction of pCA at
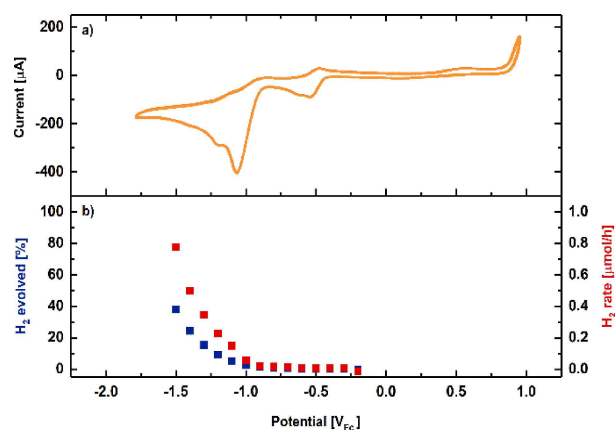

Figure 3. a) CV of Co_{Mbq}/pCA under standard conditions (1 mM Co_{Mbq}) with 10 mM pCA; glassy carbon electrode; 100 mV/s scan rate. b) OEMS data for 4 mM Co_{Mbq} with 40 mM pCA (Co_{Mbq}/pCA) in 0.1 M LiBF$_4$/MeCN). The amount of H_2 was determined at each potential according to the experiment shown in Figure 2. The percent H_2 (blue squares) represents the accumulated amount at each potential; rate of H_2 evolved at each potential is depicted by the red squares.

carbon is expected to be minimal in comparison (see Figure 1). Solutions containing Co_{Mbq}:pCA concentrations of 8 mM:40 mM (Figure 4, blue line), 8 mM:80 mM (Figure 4, green line) and 4 mM:40 mM (Figure 4, orange line) were employed. Based on the amount of added electrolyte, the maximum theoretical amount of H_2 which can be evolved is 2.8 µmol for 40 mM pCA, and 5.6 µmol for 80 mM pCA. OEMS data also were collected for a 40 mM pCA solution without catalyst (Figure 4a, red line) as a control experiment. As depicted by the CA experiments at -1.1 V_{Fc} in Figure 4a, a substantial amount of H_2 is evolved within the first 10 minutes after the potential is applied. Values

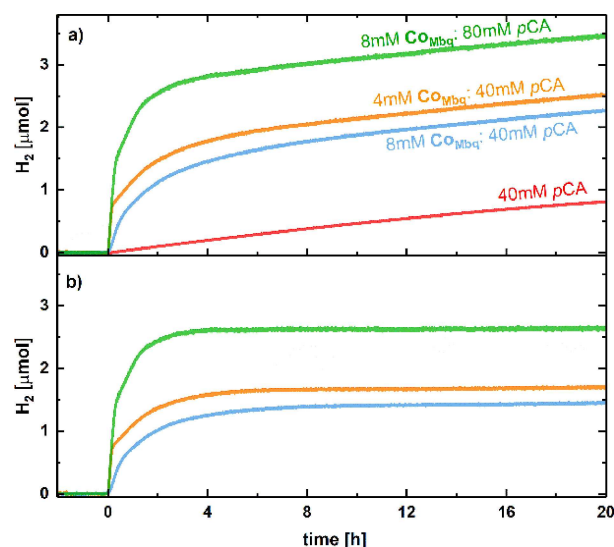**Figure 4.** OEMS data analysis for varied Co_{Mbq}:pCA concentrations. After the two hour OCV step, the potential was held at -1.1 V_{Fc} for 20 h. a) Co_{Mbq}:pCA = 8 mM:80 mM (green), 4 mM:40 mM (orange), 8 mM:40 mM (blue) and 40 mM pCA only (red); b) plot of Co_{Mbq}:pCA data from which the 40 mM pCA curve has been subtracted.

for the turnover number (TON) and turnover frequency (TOF) can only be quantitatively evaluated by product analysis (here OEMS) during the initial time period following a potential step into the HER-active region. This is based on the fact that for short reaction times, changes in the concentration of the reactants (catalyst and acid in this case) are negligible, so that rates can be obtained at well-defined concentrations (a ubiquitously used concept in heterogeneous catalysis). Thus, over a sufficiently short initial time period, the reaction rate must remain constant as long as catalyst degradation over the chosen time period can be considered negligible. Using this concept, we can obtain the TOF and TON values at -1.1 V_{Fc}, over an initial time period of 4 minutes of H_2 evolution data shown in Figure 4b (as shown in Figure S5, the H_2 evolution rate is indeed constant over this time period). The thus determined TON values over a period of 4 minutes at -1.1 V_{Fc} for Co_{Mbq}:pCA = 8 mM:40 mM and 8 mM:80 mM are 0.4 and 2, respectively (see section 5 of the Supporting Information for details). The corresponding TOFs are 6 h^{-1} and 32 h^{-1}, respectively, indicating a roughly 5-fold increase when doubling the acid concentration. In general, the literature reports an increase of the TOF with acid concentration,[23] which is consistent at least qualitatively with our TOF data. It should be noted that the calculated TON and TOF values are based on the maximum amount of Co_{Mbq} that could have been utilized within the first four minutes of the CA step. However, the effective catalyst concentration in the activated state cannot accurately be determined, and the calculated TON and TOF values represent lower estimates.

After appx. two hours, the increase in H_2 over time is comparable to that of the control experiment using pCA alone, which indicates that unreacted pCA remains in solution and is slowly and continuously reduced to H_2 at the carbon electrode. This becomes more obvious by subtracting the background H_2 evolution (i.e., in the absence of Co_{Mbq}, red line in Figure 4a) from the raw data in Figure 4a, clearly showing that the Co_{Mbq}-catalyzed H_2 evolution ceases after appx. 4 hours for the examined Co_{Mbq}:pCA concentrations (Figure 4b). Based on the final amount of H_2 obtained in the background-corrected data, the amount of H_2 generated by Co_{Mbq} ranges from 48–62%. The fact that only ~50% of the possible amount of H_2 is evolved, is indicative of time-dependent or turnover-dependent deactivation of the Co_{Mbq} catalyst. After four hours, no active catalyst remains in solution and only background H_2 formation at the carbon electrode is observed.

A further OEMS measurement was carried out (using 4 mM Co_{Mbq}: 40 mM pCA) to examine at which stage catalyst deactivation occurs. Following the two hour OCV step, the potential was first held at -0.8 V_{Fc} for 8 hours where no H_2 evolution occurs (see Figure 3b), after which a potential of -1.1 V_{Fc} was applied for 12 hours (Figure 5, blue trace). The latter potential is near the onset potential for H_2 evolution (see Figure 3b). After this 12 hour period, 1.25 μmol H_2 have been produced (see blue line in Figure 5). This is ca. 50% less than the amount of H_2 produced after 12 hours at -1.1 V_{Fc} in the absence of the preceding 8 hour hold at -0.8 V_{Fc} (2.5 μmol H_2, see orange line in Figure 5). We therefore conclude that
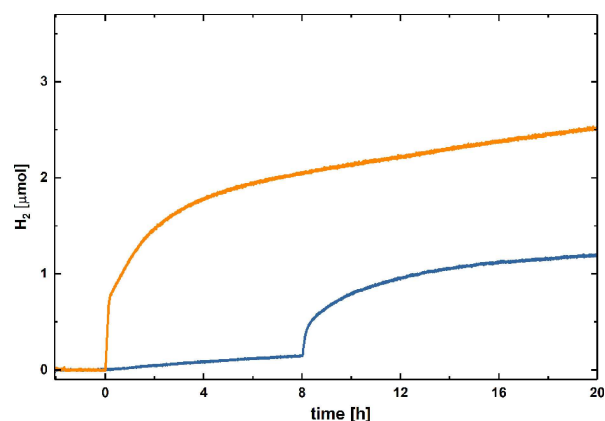

Figure 5. OEMS data analysis for Co_{Mbq} with pCA (4 mM Co_{Mbq} with 40 mM pCA). After the two hours OCV step, the potential was held either directly at -1.1 V_{Fc} for 20 h (orange), or a potential of -0.8 V_{Fc} was first applied for 8 h, followed by further reduction at -1.1 V_{Fc} for 12 h (blue).

deactivation of the catalyst already can occur during the initial redox events observed in the CV between ca. -0.5 and -0.85 V_{Fc} (Figure 1). A significant part of the deactivation is therefore not correlated with the H_2 evolution mechanism.

As noted above, the OEMS results unequivocally establish that the redox processes between -0.4 V_{Fc} and -0.85 V_{Fc} (orange line in Figure 1) do not coincide with H_2 formation. However, the uptake of at least one proton is inferred. The redox features between -0.4 V_{Fc} and -0.85 V_{Fc} are dissimilar in shape and potential from the original $Co^{II/I}$ features in the absence of pCA. The first redox event shifts to more positive potential with increasing [pCA], in accord with the Nernst equation (Figure S3), and consistent with a proton-coupled electron transfer process. The behavior of the second reduction is more ambiguous, such that additional proton transfer associated with the second reduction cannot be excluded. The electrochemical events in this region correspond to formation of protonated HER intermediates or pre-catalytic species.

Rotating ring disk electrode (RRDE) methods were employed to further assess the nature of these initial redox processes. In the RRDE experiments, the glassy carbon disk serves as the site of reduction, while reduced products are reoxidized at the glassy carbon ring (with rotation). The ring potential was set to 0.5 V_{Fc}. Hydrogen is not oxidized by glassy carbon at this potential, such that there is no current contribution from H_2 oxidation, but only from the molecular catalyst depending on the disk potential.

RRDE experiments were first performed with solutions of 1 mM Co_{Mbq} in 0.1 M LiBF$_4$/MeCN (Figure 6) in the absence of the proton source. At potentials negative of -0.65 V_{Fc}, the reduction of Co_{Mbq} to 'Co^I' occurs, reaching a diffusion-limited current negative of appx. -0.8 V_{Fc} (yellow marked area in Figure 6). This is evidenced by the fact that the current plateau value at -55 μA at 200 rpm approximately doubles to -107 μA at a four-fold higher rotation rate of 800 rpm, in accord with the Levich Equation (1).
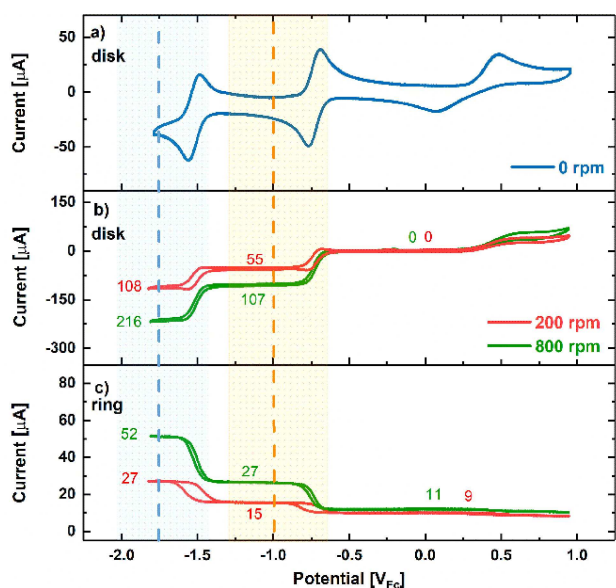
Figure 6. RRDE data for 1 mM **Co_Mbq** using glassy carbon disk and ring working electrodes; 100 mV/s scan rate; a) CV recorded at the disk at 0 rpm plotted vs. the raw voltage (i.e., without iR-correction, which would be negligible for such small currents). b) and c) Current collected on the disk and ring, respectively, at 200 rpm (red) and 800 rpm (green) plotted vs. the iR-free voltage. The ring potential was held at 0.5 V_Fc.

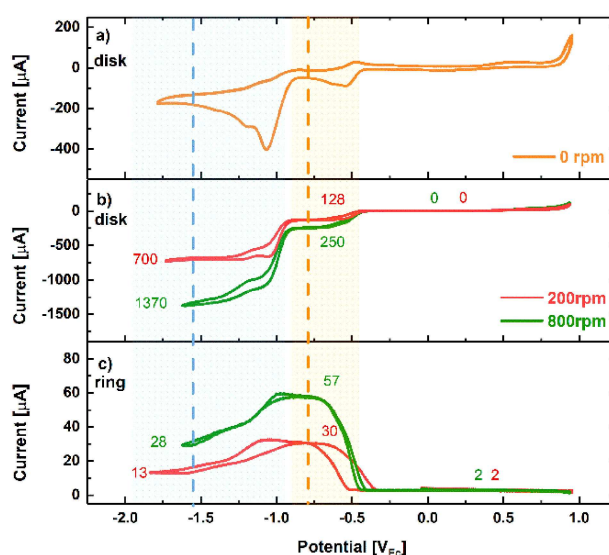**Figure 7.** RRDE data for **Co_Mbq** with pCA (1 mM **Co_Mbq** with 10 mM pCA) using glassy carbon disk and ring working electrodes; 100 mV/s scan rate. a) CV recorded at the disk at 0 rpm, plotted vs. raw voltage. b) and c) Current collected on the disk and ring, respectively, at 200 rpm (red) and 800 rpm (green) plotted vs. iR-free voltage. The ring potential is held at 0.5 V_Fc.

$$i_{lim} = 0.62 A n F D^{2/3} v^{-1/6} C \sqrt{w} \tag{1}$$

As the potential decreases below ca. -1.45 V_Fc, the **Co_Mbq** complex undergoes an overall two-electron reduction to the 'Co⁰' complex (i.e., $n = 2$ in Eq. 1), evidenced by the approximately two-fold higher currents of the subsequent current plateau negative of ca. -1.6 V_Fc (108 µA and 216 µA at 200 and 800 rpm, respectively; see blue marked area in Figure 6). For these RRDE experiments, the ring electrode was held at $+0.5$ V_Fc, where a fraction of the **Co_Mbq** complex reaching the ring can be oxidized to the Co^III complex, leading to the positive ring currents at potentials positive of -0.5 V_Fc (Figure 6c). The 'Co^I' and 'Co⁰' species produced at the disk electrode in the yellow and blue marked potential regions, respectively, will also be re-oxidized at the disk electrode, which results in the expected positive deflections of the ring currents in these regions.

Upon the addition of 10 mM pCA to the 1 mM **Co_Mbq** solution, two current plateaus again are observed in the RRDE experiment. Both regions (likewise marked in yellow and blue in Figure 7) are shifted positively by approximately 0.5 V, consistent with the positive potential shift observed for the CVs in Figure 1. The current plateaus in the yellow marked region in Figure 7 (i.e., positive of -0.9 V_Fc, where no H₂ evolution is detected by OEMS; Figure 3b) yield diffusion-limited currents of -128 µA (200 rpm) and -250 µA (800 rpm). These values are approximately double those observed without pCA (Figure 6). The data clearly indicate that at the more positive potentials (yellow area in Figure 7), two electrons are transferred overall to **Co_Mbq**. Since in the presence of pCA the oxidation of the divalent **Co_Mbq** to the Co^III form at the ring potential of $+0.5$ V_Fc

is very slow (indicated by the very weak Co^III oxidation feature in Figure 7b and by the near-zero ring current at potentials positive of 0 V_Fc), the ring current response in the first reduction plateau can be analyzed quantitatively. Based on the ring collection efficiency of N_c = 24 % (see Experimental Section), the ring current of 30 µA at 200 rpm would correspond to a disk current of -125 µA (i.e., -1×30 µA/0.24), if the species produced by an overall two-electron reduction at the disk electrode could be re-oxidized reversibly. This value is in good agreement with the experimentally obtained disk current of -128 µA at 200 rpm. The data clearly indicate the high reversibility of the reductive events at the disk electrode in the yellow marked potential region. A similarly good agreement is obtained at 800 rpm (i.e., -1×57 µA/0.24 = 238 µA, which is close to the disk current of -250 µA). In summary, in the first reduction step in the presence of pCA (yellow marked region in Figure 7), a total of two electrons are transferred reversibly (at least within the $\sim$1 s time-scale for the transport of products formed at the disk to the ring electrode) to **Co_Mbp**.

A large increase in the disk current is observed negative of -0.9 V_Fc for solutions of **Co_Mbq** containing 10 mM pCA (i.e., in the blue marked area in Figure 7), consistent with the onset and increase of H₂ evolution observed by OEMS (Figure 3b). Interestingly, the ring current in the blue region decreases by about a factor of two, which can have two possible reasons: 1) The re-oxidation of the active catalyst proceeds only by a one-electron transfer, rather than by a two-electron transfer observed at higher potentials (i.e., in the yellow region); and/or, 2) A portion of the active catalyst also is deactivated in the blue marked potential region within the $\sim$1 s time-scale of the transport of the active species from the disk to the ring electrode. The latter can be ruled out on the basis of the OEMS

data (Figure 5), which shows that deactivation of the catalyst occurs in the time frame of hours in both regions and would therefore not interfere with the RRDE analysis, where the reactions are probed within a few seconds.

The RRDE data reveals that **Co$_{Mbq}$** is reduced by two electrons in the yellow marked region, and the uptake of at least one proton during this process was established. The nature of this protonated reduced intermediate remains an open question. Our previous studies revealed that the reaction of the two-electron reduced 'Co^0' complex resulted in the formation of [Co(MabiqH$_2$)], in which a formal equivalent of H$_2$ was added across a C−N bond of the bipyrimidine unit.[18] The hydrogenated species thus offered one possibility for the identity of the pre-activated intermediate. Hence, we examined the electrochemical behavior of the isolated [Co(MabiqH$_2$)]. In the absence of acid, the CV of 1 mM [Co(MabiqH$_2$)] (Figure 8,
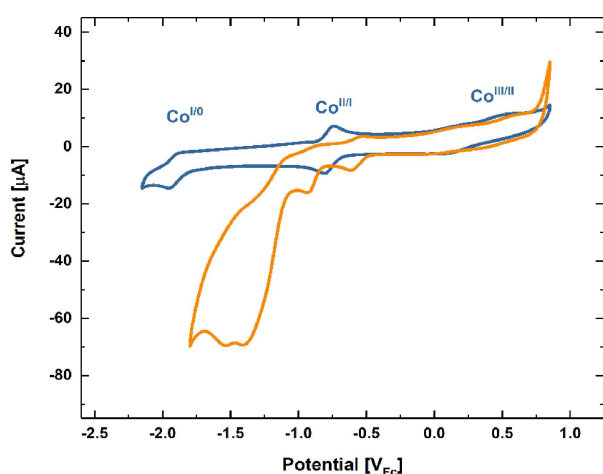

Figure 8. Cyclic voltammograms of [Co(MabiqH$_2$)] in 0.1 M LiBF$_4$/MeCN; conducted with a glassy carbon electrode in the glass cell set-up; 100 mV/s; Ar atmosphere. Solid blue trace: 1 mM [Co(MabiqH$_2$)]; orange solid trace: 1 mM [Co(MabiqH$_2$)] plus 10 mM pCA.

blue line) shows three reversible redox events at E$_{p,c}$ = 0.08 V$_{Fc}$, −0.8 V$_{Fc}$ and −1.9 V$_{Fc}$ that again correspond to the formal Co$^{III/II}$, Co$^{II/I}$ and Co$^{I/0}$ couples, respectively. The first two redox potentials are only moderately shifted with respect to the analogous couples of **Co$_{Mbq}$**. However, the 'Co$^{I/0}$' couple occurs at a potential greater than 300 mV negative of the **Co$_{Mbq}$** 'Co$^{I/0}$' couple. This behavior is consistent with reduction of the bipyrimidine moiety upon addition of the second electron to **Co$_{Mbq}$**. Since the bipyrimidine unit of [Co(MabiqH$_2$)] is hydrogenated, reduction of the complex becomes more difficult. The formation of the 'Co^I' species, on the other hand, involves reduction of the opposing diketiminate group. The similar potentials in the CVs of both **Co$_{Mbq}$** and [Co(MabiqH$_2$)] for the Co$^{II/I}$ couple suggest that in the latter complex, reduction also is ligand centered and likewise involves the diketiminate group.

The CV of 1 mM [Co(MabiqH$_2$)] in the presence of 10 mM pCA in 0.1 M LiBF$_4$/MeCN exhibits several new redox waves at E$_{p,c}$ = −0.6 V$_{Fc}$, −0.9 V$_{Fc}$, −1.4 V$_{Fc}$ and −1.53 V$_{Fc}$ (Figure 8, orange

line). The data yields two important outcomes regarding formation of the intermediate in the **Co$_{Mbq}$**/pCA system. First, the original Co$^{II/I}$ couple of [Co(MabiqH$_2$)] at −0.8 V$_{Fc}$ (Figure 8, blue line) shifts to positive potentials in the presence of pCA, exhibiting the same behavior as **Co$_{Mbq}$** upon addition of acid (Figure 1, orange line). This redox potential likewise is dependent on the concentration of acid, indicative of a proton coupled event (Figure S4). The positive potential shift denotes that the hydrogenated [Co(MabiqH$_2$)] can still be modified in a similar manner as **Co$_{Mbq}$**. Therefore, uptake of the first proton by both complexes, coincident with formation of the activated form, is unlikely to occur at the bipyrimidine moiety of the Mabiq ligand. Secondly, the large current increase at −1.4 V$_{Fc}$ (Figure 8, orange line) signifies that H$_2$ evolution occurs at potentials significantly more negative than for **Co$_{Mbq}$**, and at a potential that also coincides with proton reduction at the bare glassy carbon electrode (Figure 1, grey dash line). Thus, the non-hydrogenated **Co$_{Mbq}$** is a better catalyst with regard to HER, and [Co(MabiqH$_2$)] does not appear to be an intermediate in the reaction.

The combined electrochemical data provide insight into the HER pathways available to the Co-Mabiq complex. The OEMS data show that no hydrogen is produced during the initial redox processes. However, these steps correlate with the uptake of two-electrons and at least one proton to form a pre-catalytic intermediate ([Co(MabiqH)]^0 in Scheme 2). However, a two-electron reduction of [Co^{II}(Mabiq)(THF)](PF$_6$) followed by proton transfer to the metal center (i.e. protonation of the 'Co^0' form to generate a Co^{II}-H species, according to an EEC (E: electrochemical, C: chemical) mechanism) is not consistent with our data. A stable Co^{II}-H species was not produced upon reaction of the two electron reduced [Co(Mabiq)(NaOEt$_2$)]$_2$ complex with acid.[18] Furthermore, we have ruled out the resultant hydrogenated [Co(MabiqH$_2$)] form as an intermediate. Given the redox activity of the Mabiq ligand, and based on the large potential difference between the activation step and the Co$^{I/0}$ couple, at least one proton is expected to be taken up by the ligand. The data suggest that proton transfer occurs after addition of the first electron – i.e. upon reaction of the Co^I form – corresponding to an electrochemical-chemical-electrochemical ECE mechanism. This is consistent with the positive shift in potential with increasing acid concentration (Figure S3). Further protonation following the second reduction, according to an ECEC mechanism, also is a possibility.

Further reduction of the pre-catalytic complex is required to evolve H$_2$ at potentials negative of ca. −0.9 V$_{Fc}$. The addition of a third electron is needed for H$_2$ release by the Ni-containing

$$[Co^{II}(Mabiq)]^+ + e^- + H^+ \longrightarrow [Co(MabiqH)]^+$$
Co$_{Mbq}$

$$[Co(MabiqH)]^+ + e^- \longrightarrow [Co(MabiqH)]^0$$
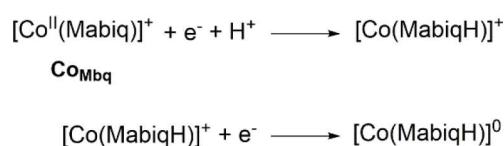
Scheme 2. Proposed ECE pathway for formation of pre-catalytic species. Further protonation in the second step, in accord with an ECEC mechanism, is possible and may occur either at the metal center or the ligand.

hangman porphyrins, which similarly acquire a proton at the ligand backbone.[10f] A similar mechanism may be operational in our system. Alternatively, Mabiq protonation in the pre-catalytic step may render the ligand less nucleophilic, potentially facilitating a metal-based catalytic cycle at lower potentials. Reduction and protonation of redox active ligands preceding metal hydride formation has been observed in Ni-thiosemicarbazone complexes.[10d,h] In our system, a second proton transfer in an ECEC pathway also could involve the metal center.

The low H_2 yields obtained at varied molar ratios of **Co$_{Mbq}$**: pCA in the OEMS additionally denote formation of both active and inactive species in our system. A substantial amount of the complex already is deactivated in the first reductive events corresponding to the yellow marked region of the **Co$_{Mbq}$**/pCA RRDE data (Figure 7). The identity of the active and deactivated intermediates is still unclear, but our data implicate a protonated diketiminate group. Potentially the pre-catalytic complex becomes protonated at multiple sites, with only one form corresponding to a productive intermediate. Indeed, the spin density of the 'Co^{II}' complex, [Co^{II}(Mabiq$^{\cdot}$)], is fully delocalized over the diketiminate moiety and the imine units connecting the bipyrimidine.[17b] Each of the doubly bonded carbon atoms offers a potential protonation site; attack at a diketiminate carbon atom was observed in porphyrin complexes.[10f,15a] Studies are currently ongoing to characterize the pre-catalytic complex, and to elucidate further details of the HER.

Conclusions

The current studies reveal, for the first time, that [Co^{II}(Mabiq)(THF)](PF$_6$) acts as an electrocatalyst for H_2 evolution. The data clearly point to the formation of a pre-catalytic form of the complex, and implicate protonation of the Mabiq ligand in this process. Several researchers have touted the advantages of redox-active ligands for catalysis, and a growing number of HER catalysts are being designed to include such functionalities. However, in our case, the redox-active Mabiq unit seems to initially act as a hydride sink. Consequently, at least three electrons are required for H_2 release by the complex, and H_2 evolution occurs at a significant overpotential with respect to the formal Co$^{II/I}$ reduction potential of **Co$_{Mbq}$**. The catalytic onset occurs below the Co$^{II/I}$ couple, even using the relatively strong acid, pCA. Our studies demonstrate that redox-active organic groups are not always advantageous for catalysis, and caution should be exercised in molecular catalyst design. However, the use of redox-active ligands for proton coupled electron transfer processes should not be discounted. These molecules have proven effective in other systems. The Mabiq ligand also may be optimized to overcome the current limitations, and a viable pathway for H_2 release is available from the Co-Mabiq pre-catalyst. Identification of the inhibitory sites will facilitate ligand modifications to shut down the deactivation pathway, thereby allowing us to harness the rich redox and coordination chemistry of this molecule for effective catalysis.

Experimental Section

Chemicals were purchased from Sigma-Aldrich unless otherwise noted. Acetonitrile (MeCN) was dried by passage over activated alumina columns (MBraun), deoxygenated prior to use, and subsequently stored over molecular sieves (3 Å). The water content in MeCN was <1 ppm as determined by Karl Fischer titration. Lithium tetrafluoroborate (LiBF$_4$; BASF, Germany) was used as the supporting electrolyte salt in all electrochemical experiments. Ferrocene was purified by sublimation. H(Mabiq), [Co^{II}(Mabiq)(THF)] (PF$_6$) and [Co(MabiqH$_2$)] were synthesized as previously described.[18] p-cyanoanilinium tetrafluoroborate (pCA) was synthesized according to literature procedure.[24]

On-line Electrochemical Mass Spectrometry (OEMS) -OEMS measurements were conducted in a two-compartment cell separated by Al-sealed lithium-ion conducting Ohara glass (LICGC^{TM}, 1 inch diameter, thickness 150 μm).[25] The Li-ion conducting glass served as a diffusion barrier for gases and liquids between the two compartments. Hence, any gas evolution at the Li metal counter electrode (diameter 17 mm) cannot be detected by the mass spectrometer. Only gas evolved by **Co$_{Mbq}$**, in acidic media, at the carbon paper working electrode (Freudenberg H1410, diameter 15 mm, thickness ca. 150 μm) was recorded by the mass spectrometer. The two compartment-cell was assembled in a glovebox (Ar, MBraun, Germany, <1 ppm of H_2O and O_2). Prior to use, all cell components were dried in a vacuum oven for at least 6 h at 70 °C. Glass fiber separator sheets (glass microfiber filter #691, from VWR, Germany) were punched (22 mm diameter) and subsequently dried in a glass oven (Büchi, Switzerland) under dynamic vacuum for at least 12 h at 300 °C. Two separators were used for each measurement, sandwiching the Li–Ion conducting glass. As an electrolyte, LP57 (1 M LiPF$_6$ in EC:EMC (3:7 wt/wt), <20 ppm H_2O, BASF, Germany) was used in the counter electrode compartment and 140 μl of **Co$_{Mbq}$**/pCA in MeCN, 0.1 M LiBF$_4$, was used in the working electrode compartment. The experimental set-up is such that the electrochemical reaction is constrained to occur within a ca. 150 μm thick electrolyte-filled carbon paper electrode, so that the H_2 evolved on the surface of the carbon paper reaches the MS within ca. 1 second, while the diffusion of H_2 produced at the separator/carbon paper interface will require at most a few minutes to transport H_2 into the cell head-space, where it can be detected by the MS (for a conservatively chosen hydrogen diffusion coefficient of only 10^{-6} cm^2/s). Therefore, this thin-film set-up offers a significant advantage in terms of response time, if compared to most of the commonly used bulk electrolysis systems with electrolyte film thicknesses more like on the order of 1 cm (at 1 cm thickness, the diffusional time constant would be on the order of 1 day). The cell was connected to the OEMS and subsequently flushed with Ar for two minutes.

Prior to all experiments, AC impedance measurements were recorded to determine the resistance due to the Ohara glass. The cell potential was held at open circuit voltage (OCV) for 2 hours to obtain a good signal extrapolation for the MS baseline correction in the data treatment. Three different chronoamperometry experiments (CA) were carried out for this study, in which either: 1) the potential was decreased by 100 mV every 30 min starting from −0.2 V to −1.5 V vs Fc$^{+/0}$ (V$_{Fc}$); 2) the potential was maintained at −1.1 V$_{Fc}$ for 20 h; 3) the potential was held at −0.8 V$_{Fc}$ for 8 hours after which a potential of −1.1 V$_{Fc}$ was applied for 12 hours. The potential hold at −0.8 V$_{Fc}$ was chosen based on the **Co$_{Mbq}$**:pCA results. The gas evolved during impedance, OCV and CA steps was recorded in all cases. All mass signals were normalized to the ^{36}Ar isotope ion current. The resultant ion current signals were converted to ppm by using a calibration gas containing 2000 ppm of H_2, O_2, CO and CO_2 in Ar (Westfalen, Germany). The conversion of

ppm to the total moles of H_2 evolved during the experiment was determined from the cell volume and ideal gas law.[22]

Rotating Ring Disk Electrode (RRDE) and cyclic voltammetry (CV)- RRDE and CV measurements were performed in a four-neck, jacketed glass cell assembled and sealed inside the glovebox. The cell configuration was adopted from previous studies.[26] The PEEK shroud working electrode includes a glassy carbon disk with 5.0 mm diameter, surrounded by a glassy carbon ring with 6.5 mm internal diameter and 7.5 mm external diameter (Pine Research Instrumentation, Durham, NC). Before usage, the working electrode was polished with 1.0 μm and 0.05 μm alumina suspensions (Buehler, Düsseldorf, Germany), and cleaned by sonication in ultrapure water. The electrode was subsequently dried for 12 h in a vacuum oven (Thermo Scientific, USA) at 70 °C. For the CV measurements, a potential was applied only to the glassy carbon disk working electrode, while a potential was applied to both the disk and ring electrodes for RRDE measurements. A platinum wire, separated via a glass fitting was used as the counter electrode. Ag/AgNO$_3$ (0.1 M AgNO$_3$ and 0.1 M LiBF$_4$ in MeCN) was used as the reference electrode, separated via a Vycor 3535 frit (Advanced Glass & Ceramics, Holden, MA).[26a]

The electrochemical cell – which consisted of a working electrode screwed onto a PEEK shaft, the reference and counter electrodes, a glass bubbler and the four-neck glass vessel – was assembled in the glovebox. Upon removal from the glovebox, the working electrode rod was connected to the rotator, and the glass bubbler was connected to an Ar line. The cell was continuously flushed with Ar to ensure a constant overpressure inside the cell and prevent atmospheric contamination. Prior to the RRDE measurements, impedance measurements were carried out to record the Ohmic resistance between the working and reference electrode. The impedance measurement was performed with a SP300 potentiostat (BioLogic, Grenoble, France). All other measurements were recorded with an AFCBP1 bipotentiostat (Pine Research Instrumentation) controlled with Aftermath software. All potentials were reported with reference to an internal standard of Fc$^{+/0}$. RRDE and CV measurements were conducted at 100 mV/s scan rate. RRDE measurements were recorded at 200 rpm and 800 rpm, whereas CV measurements were recorded at 0 rpm. In this study, since the current on the CV is not high compared to the current values obtained from RRDE, only the RRDE results are affected by IR-drop, hence the potentials are IR corrected.

The RRDE collection efficiency value was calibrated using the ferrocene (Fc)/ferrocenium (Fc$^+$) redox couple, by comparison of the Fc oxidation disk currents to the Fc$^+$ reduction ring currents. The collection efficiency, N$_c$, the absolute ratio of ring to disk current, can be described by Equation (2).[27] The calibrated N$_c$ value of the RRDE electrode was 24%.

$$N_c = -\frac{I_{ring}}{I_{disk}} \tag{2}$$

Alternatively, CV measurements (corresponding to data in Figure 8 and Figure S3) were performed in a 5-neck glass cell inside the glovebox. Two glassy carbon electrodes (3 mm diameter, PalmSens, Houten, Netherlands) were employed as the working and counter electrodes. Before use, electrodes were polished with 1.0 μm and 0.05 μm alumina suspensions (Buehler, Düsseldorf, Germany). The same reference electrode system as described for the RRDE experiments was employed. The CV measurements were recorded with a VMP3 multichannel potentiostat (BioLogic, Grenoble, France). The measurements were conducted at 100 mV/s; the results were not affected by IR-drop.

[1] a) N. S. Lewis, D. G. Nocera, *Proc. Natl. Acad. Sci. USA* **2007**, *104*, 20142–20142; b) V. Artero, *Nat. Energy* **2017**, *2*; c) V. Artero, *Nat. Energy* **2017**, *2*, 17131.

[2] a) O. Gröger, H. A. Gasteiger, J.-P. Suchsland, *J. Electrochem. Soc.* **2015**, *162*, A2605–A2622; b) A. Veziroglu, R. Macario, *Int. J. Hydrogen Energy* **2011**, *36*, 25–43; c) W. Vielstich, H. A. Gasteiger, H. Yokokawa, *Handbook of fuel cells: fundamentals technology and applications: advances in electrocatalysis, materials, diagnostics and durability, Vol. 5*, John Wiley & Sons, **2009**.

[3] a) S. Berardi, S. Drouet, L. Francas, C. Gimbert-Surinach, M. Guttentag, C. Richmond, T. Stoll, A. Llobet, *Chem. Soc. Rev.* **2014**, *43*, 7501–7519; b) J. Willkomm, K. L. Orchard, A. Reynal, E. Pastor, J. R. Durrant, E. Reisner, *Chem. Soc. Rev.* **2016**, *45*, 9–23; c) J. R. McKone, N. S. Lewis, H. B. Gray, *Chem. Mater.* **2013**, *26*, 407–414.

[4] H. A. Gasteiger, S. S. Kocha, B. Sompalli, F. T. Wagner, *Appl. Catal. B* **2005**, *56*, 9–35.

[5] O. T. Holton, J. W. Stevenson, *Platinum Met. Rev.* **2013**, *57*, 259–271.

[6] a) J. R. McKone, S. C. Marinescu, B. S. Brunschwig, J. R. Winkler, H. B. Gray, *Chem. Sci.* **2014**, *5*, 865–878; b) W. Lubitz, H. Ogata, O. Rudiger, E. Reijerse, *Chem. Rev.* **2014**, *114*, 4081–4148; c) G. N. Schrauzer, *Acc. Chem. Res.* **1968**, *1*, 97–103; d) V. Firpo, J. M. Le, V. Pavone, A. Lombardi, K. L. Bren, *Chem. Sci.* **2018**, *9*, 8582–8589; e) B. Kandemir, L. Kubie, Y. Guo, B. Sheldon, K. L. Bren, *Inorg. Chem.* **2016**, *55*, 1355–1357.

[7] a) N. Queyriaux, R. T. Jane, J. Massin, V. Artero, M. Chavarot-Kerlidou, *Coord. Chem. Rev.* **2015**, *304–305*, 3–19; b) D. Brazzolotto, M. Gennari, N. Queyriaux, T. R. Simmons, J. Pecaut, S. Demeshko, F. Meyer, M. Orio, V. Artero, C. Duboc, *Nat. Chem.* **2016**, *8*, 1054–1060; c) R. M. Bullock, M. L. Helm, *Acc. Chem. Res.* **2015**, *48*, 2017–2026; d) V. Artero, M. Chavarot-Kerlidou, M. Fontecave, *Angew. Chem. Int. Ed.* **2011**, *50*, 7238–7266; *Angew. Chem.* **2011**, *123*, 7376–7405.

[8] E. S. Wiedner, M. B. Chambers, C. L. Pitman, R. M. Bullock, A. J. Miller, A. M. Appel, *Chem. Rev.* **2016**, *116*, 8655–8692.

[9] K. M. Waldie, A. L. Ostericher, M. H. Reineke, A. F. Sasayama, C. P. Kubiak, *ACS Catal.* **2018**, *8*, 1313–1324.

[10] a) J. W. Jurss, R. S. Khnayzer, J. A. Panetier, K. A. El Roz, E. M. Nichols, M. Head-Gordon, J. R. Long, F. N. Castellano, C. J. Chang, *Chem. Sci.* **2015**, *6*, 4954–4972; b) T. J. Sherbow, J. C. Fettinger, L. A. Berben, *Inorg. Chem.* **2017**, *56*, 8651–8660; c) G.-G. Luo, H.-L. Zhang, Y.-W. Tao, Q.-Y. Wu, D. Tian, Q. Zhang, *Inorg. Chem. Front.* **2019**, *6*, 343–354; d) R. Jain, A. A. Mamun, R. M. Buchanan, P. M. Kozlowski, C. A. Grapperhaus, *Inorg. Chem.* **2018**, *57*, 13486–13493; e) A. Z. Haddad, B. D. Garabato, P. M. Kozlowski, R. M. Buchanan, C. A. Grapperhaus, *J. Am. Chem. Soc.* **2016**, *138*, 7844–7847; f) B. H. Solis, A. G. Maher, D. K. Dogutan, D. G. Nocera, S. Hammes-Schiffer, *Proc. Natl. Acad. Sci. USA* **2016**, *113*, 485–492; g) A. Z. Haddad, S. P. Cronin, M. S. Mashuta, R. M. Buchanan, C. A. Grapperhaus, *Inorg. Chem.* **2017**, *56*, 11254–11265; h) T. Straistari, J. Fize, S. Shova, M. Réglier, V. Artero, M. Orio, *ChemCatChem* **2017**, *9*, 2262–2268.

[11] R. H. Crabtree, *New J. Chem.* **2011**, *35*, 18–23.

[12] a) O. R. Luca, S. J. Konezny, J. D. Blakemore, D. M. Colosi, S. Saha, G. W. Brudvig, V. S. Batista, R. H. Crabtree, *New J. Chem.* **2012**, *36*, 1149–1152; b) K. E. Rosenkoetter, M. K. Wojnar, B. J. Charette, J. W. Ziller, A. F. Heyduk, *Inorg. Chem.* **2018**, *57*, 9728–9737; c) V. Lyaskovskyy, B. de Bruin, *ACS Catal.* **2012**, *2*, 270–279.

[13] A. Z. Haddad, D. Kumar, K. Ouch Sampson, A. M. Matzner, M. S. Mashuta, C. A. Grapperhaus, *J. Am. Chem. Soc.* **2015**, *137*, 9238–9241.

[14] a) E. J. Thompson, L. A. Berben, *Angew. Chem. Int. Ed.* **2015**, *54*, 11642–11646; *Angew. Chem.* **2015**, *127*, 11808–11812; b) M. Nippe, R. S. Khnayzer, J. A. Panetier, D. Z. Zee, B. S. Olaiya, M. Head-Gordon, C. J. Chang, F. N. Castellano, J. R. Long, *Chem. Sci.* **2013**, *4*, 3934–3945.

[15] a) B. H. Solis, A. G. Maher, T. Honda, D. C. Powers, D. G. Nocera, S. Hammes-Schiffer, *ACS Catal.* **2014**, *4*, 4516–4526; b) C. Costentin, J. M. Saveant, C. Tard, *Proc. Natl. Acad. Sci. USA* **2018**, *115*, 9104–9109.

[16] E. Muller, G. Bernardinelli, A. Vonzelewsky, *Inorg. Chem.* **1988**, *27*, 4645–4651.

[17] a) P. Banerjee, A. Company, T. Weyhermuller, E. Bill, C. R. Hess, *Inorg. Chem.* **2009**, *48*, 2944–2955; b) E. V. Puttock, P. Banerjee, M. Kaspar, L. Drennen, D. S. Yufit, E. Bill, S. Sproules, C. R. Hess, *Inorg. Chem.* **2015**, *54*, 5864–5873.

[18] M. Kaspar, P. J. Altmann, A. Pothig, S. Sproules, C. R. Hess, *Chem. Commun.* **2017**, *53*, 7282–7285.

[19] A. M. Appel, S. J. Lee, J. A. Franz, D. L. DuBois, M. R. DuBois, B. Twamley, *Organometallics* **2009**, *28*, 749–754.

[20] P.-A. Jacques, V. Artero, J. Pécaut, M. Fontecave, *Proc. Natl. Acad. Sci. USA* **2009**, *106*, 20627–20632.

[21] N. Kaeffer, A. Morozan, J. Fize, E. Martinez, L. Guetaz, V. Artero, *ACS Catal.* **2016**, *6*, 3727–3737.

[22] N. Tsiouvaras, S. Meini, I. Buchberger, H. A. Gasteiger, *J. Electrochem. Soc.* **2013**, *160*, A471–A477.

[23] a) V. Artero, J. M. Saveant, *Energy Environ. Sci.* **2014**, *7*, 3808–3814; b) C. Costentin, J.-M. Savéant, *ChemElectroChem* **2014**, *1*, 1226–1236; c) E. S. Rountree, B. D. McCarthy, T. T. Eisenhart, J. L. Dempsey, *Inorg. Chem.* **2014**, *53*, 9983–10002.

[24] A. M. Appel, D. L. DuBois, M. R. DuBois, *J. Am. Chem. Soc.* **2005**, *127*, 12717–12726.

[25] M. Metzger, B. Strehle, S. Solchenbach, H. A. Gasteiger, *J. Electrochem. Soc.* **2016**, *163*, A798–A809.

[26] a) Q. He, Y. Gorlin, M. U. M. Patel, H. A. Gasteiger, Y.-C. Lu, *J. Electrochem. Soc.* **2018**, *165*, A4027–A4033; b) Y.-C. Lu, Q. He, H. A. Gasteiger, *J. Phys. Chem. C* **2014**, *118*, 5733–5741.

[27] A. J. Bard, L. R. Faulkner, J. Leddy, C. G. Zoski, *Electrochemical methods: fundamentals and applications, Vol. 2*, Wiley New York, **1980**.

CHEM**CAT**CHEM

Supporting Information

Electrocatalytic H$_2$ Evolution by the Co-Mabiq Complex Requires Tempering of the Redox-Active Ligand

G. Ceren Tok, Anna T. S. Freiberg, Hubert A. Gasteiger,* and Corinna R. Hess*This manuscript is part of the Special Issue dedicated to the Women of Catalysis.

Supporting Information

for

Electrocatalytic H$_2$ evolution by the Co-Mabiq complex requires tempering of the redox-active ligand

G. Ceren Tok,[a, b] Anna T. S. Freiberg,[a] Hubert A. Gasteiger*[a] and Corinna R. Hess*[b]

[a]   G. C. Tok, A. T. S. Freiberg, Prof. Dr. H. A. Gasteiger
        Chair of Technical Electrochemistry, Chemistry Department and Catalysis Research Center
        Technical University of Munich
        Lichtenbergstr. 4, Garching b. Munich, Germany
        E-mail: hubert.gasteiger@tum.de

[b]   G.C. Tok, Prof. Dr. C.R. Hess
        Chemistry Department and Catalysis Research Center
        Technical University of Munich
        Lichtenbergstr. 4, Garching b. Munich, Germany
        E-mail: corinna.hess@ch.tum.de

Table of Contents

1. Absorption spectra of 1 mM Co$_{Mbq}$ with 10 mM pCA
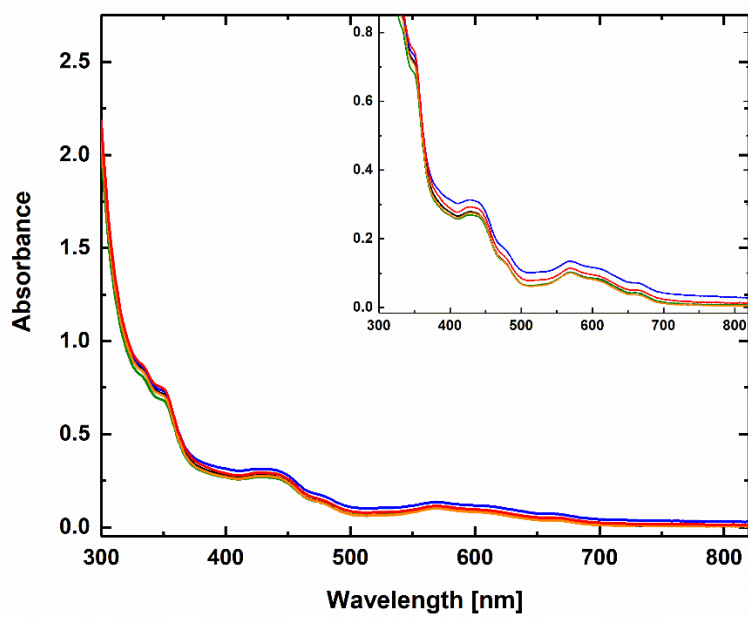
Figure S1. Absorption spectra obtained upon reaction of [Co^{II}(Mabiq)(THF)](PF$_6$) (**Co$_{Mbq}$**, 4 mM) with 40 mM pCA in 0.1 M LiBF$_4$/MeCN for reaction times of 1h (black), 3h (blue), 5h (green), 11h (orange), and 25h (red).

The spectra indicate that **Co$_{Mbq}$** does not react with pCA.

2. Charge flow at varied potentials
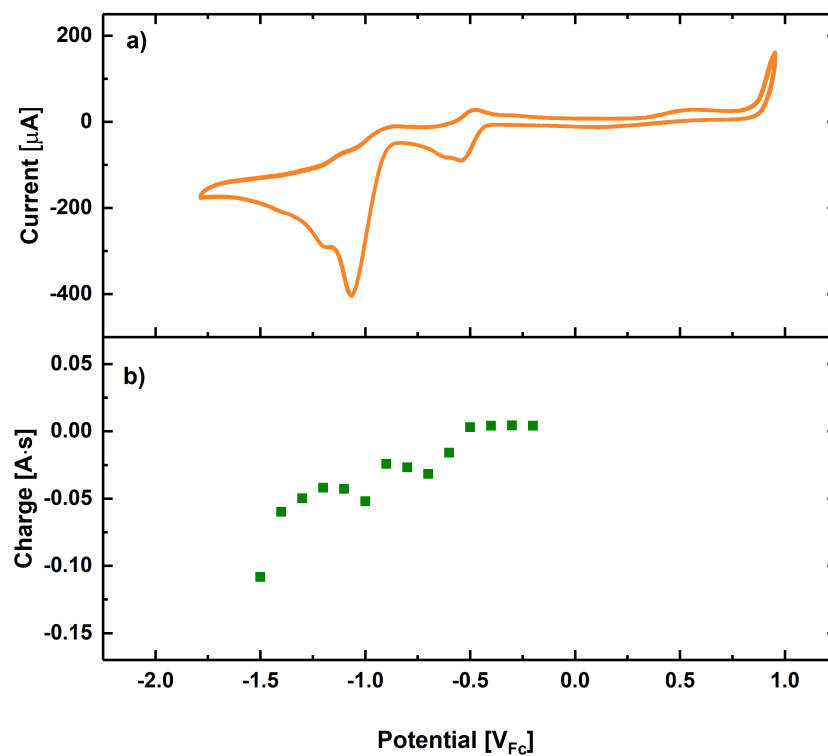
Figure S2. a) CV of 1 mM **Co$_{Mbq}$** with 10 mM *p*CA in 0.1 M LiBF$_4$/MeCN; glassy carbon electrode; 100 mV/s scan rate in a glass cell. b) Charge vs. potential for OEMS experiments with 4 mM **Co$_{Mbq}$** and 40 mM pCA; 0.1 M LiBF$_4$/MeCN in a two-compartment OEMS cell. The potential was decreased by 100 mV every 30 min, and the charge was calculated from the current measured at each potential over the course of 0.5 h each

3. CVs of Co$_{Mbq}$ with varied [pCA]

The CV of 1 mM **Co$_{Mbq}$** with 10 mM pCA suggests that two different redox steps take place between −0.4 and −0.75 V$_{Fc}$. Varying equivalents of pCA were added to a 1 mM **Co$_{Mbq}$** solution to determine which step(s) is proton dependent. The reduction at −0.52 V$_{Fc}$ shifts to positive potentials at higher pCA concentrations, while protonation at the reduction at −0.61 V$_{Fc}$ cannot be excluded due to the unambiguous features of the second reduction upon addition of pCA (Figure S3). The *Nernst* potential shift was calculated to determine the agreement between the calculated and experimental results (Eqn. *3*).

Figure S3. CVs of 1 mM **Co$_{Mbq}$** with 10 mM (orange), 30 mM (blue), 50 mM (green), and 70 mM (red) pCA in 0.1 M LiBF$_4$/MeCN; glassy carbon electrode (3 mm); 100 mV/s scan rate, in a glass cell.
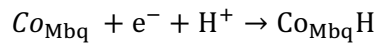
$$Co_{Mbq} + e^- + H^+ \rightarrow Co_{Mbq}H$$

$$E = E^0 - \frac{RT}{zF} \ln \frac{[red]}{[ox]} \qquad (3)$$

According to the Nernst equation given above, where,

R = gas constant, 8.314 J K^{-1} mol^{-1}

T = temperature in Kelvin, 298.15 K

Z = number of electrons transferred, 1 electron (assumed)

F = Faraday constant, 96485.33 C mol^{-1}

The potential difference for a proton dependent process is given by:

$$\Delta E_{[pCA_2]-[pCA_1]} = -\frac{RT}{zF} \ln \left\{ \frac{[red_2]}{[ox_2]} \frac{[ox_1]}{[red_1]} \right\} , \quad [pCA_2] > [pCA_1]$$

$$[ox_1] = [pCA_1][Co_{Mbq}]$$

$$[ox_2] = [pCA_2][Co_{Mbq}]$$

$$[red_1] = [red_2] = [Co_{Mbq}H]$$

The concentration of **Co_{Mbq}** is known (1 mM) and is the same for each acid concentration used. We assume that the concentration of the reduced species also is the same at each acid concentration. Hence, the following equation applies:

$$\Delta E_{[pCA_2]-[pCA_1]} = -\frac{RT}{zF}\ln\left\{\frac{[ox_1]}{[ox_2]}\right\}$$

If all assumptions are correct, the potential shifts calculated between 10 mM and 30 mM pCA, 10 mM and 50 mM pCA, 10 mM and 70 mM pCA are ~28, 41 and 50 mV respectively. In Figure S3, the theoretical calculated potential shifts between different pCA concentrations are represented as dashed lines. The reduction peak potential ($E_{p,c}$) using 10 mM pCA (orange dash line) serves as the reference potential. The blue, green and red dash lines represent the calculated potential differences between 10 mM and 30 mM pCA, 10 mM and 50 mM pCA, and 10 mM and 70 mM pCA. The calculated values reasonably match with the experimental reduction peak potentials. Therefore, we conclude that the first step involves first an electrochemical reduction, then a chemical reaction (EC) i.e., protonation, whereas we cannot resolve whether the second step only involves an electrochemical reduction (E) or electrochemical reduction followed by chemical reaction (EC).

4. CVs of [Co(MabiqH₂)] with varied [*p*CA]

The CV of 1 mM [Co(MabiqH₂)] with 10 mM *p*CA suggests that protonation also coincides with the reduction at −0.6 V_{Fc}. Varying equivalents of *p*CA were added to a 1 mM [Co(MabiqH₂)] solution to determine whether the reduction is in fact proton dependent. The *Nernst* potential shift was calculated to determine the agreement between the calculated and experimental results (Eqn. *4*).
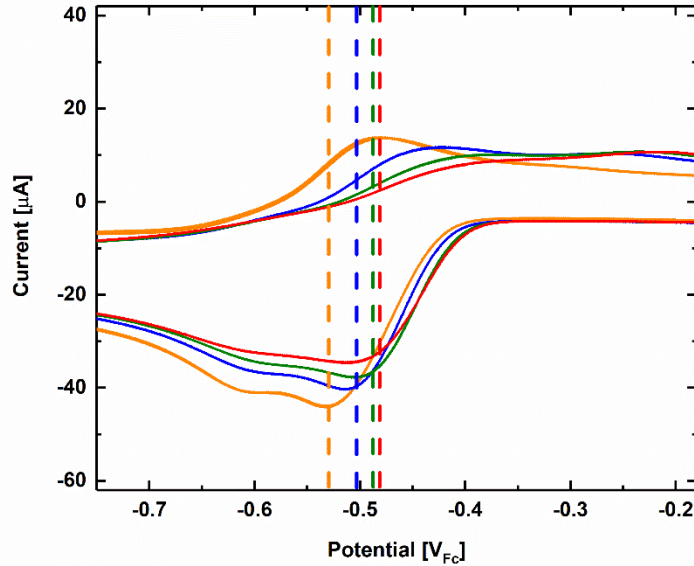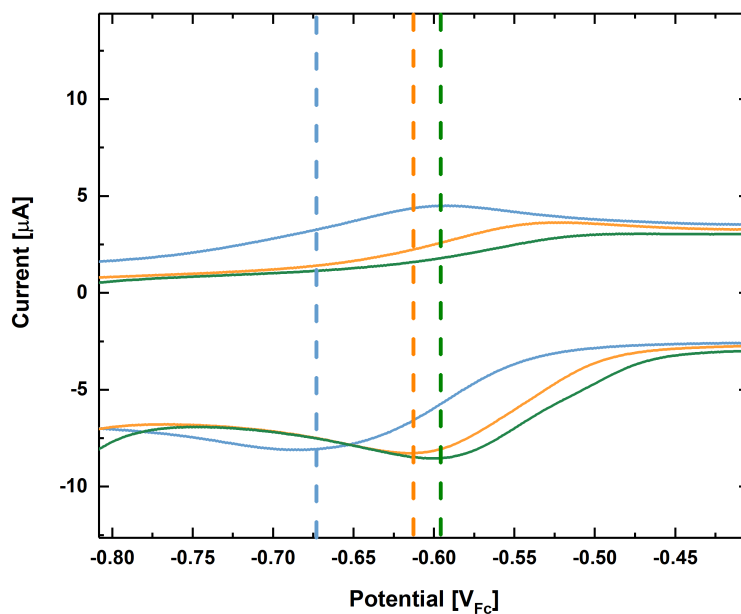

Figure S4. CVs of 1 mM [Co(MabiqH₂)] with 1 mM (blue), 10 mM (orange) and 20 mM (green) *p*CA in 0.1 M LiBF₄/MeCN; glassy carbon electrode (3 mm); 100 mV/s scan rate, in a glass cell.
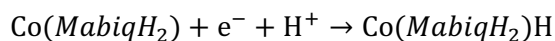
$$\text{Co}(MabiqH_2) + \text{e}^- + \text{H}^+ \rightarrow \text{Co}(MabiqH_2)\text{H}$$

$$E = E^0 - \frac{RT}{zF} \ln \frac{[red]}{[ox]} \qquad (3)$$

According to the Nernst equation given above, where,

R = gas constant, 8.314 J K⁻¹ mol⁻¹

T = temperature in Kelvin, 298.15 K

Z = number of electrons transferred, 1 electron (assumed)

F = Faraday constant, 96485.33 C mol⁻¹

The potential difference for a proton dependent process is given by:

$$\Delta E_{[pCA_2] - [pCA_1]} = -\frac{RT}{zF} \ln \left\{ \frac{[red_2]}{[ox_2]} \frac{[ox_1]}{[red_1]} \right\} , \quad [pCA_2] > [pCA_1]$$

$$[ox_1] = [pCA_1][\text{Co}(MabiqH_2)]$$

$$[ox_2] = [pCA_2][\text{Co}(MabiqH_2)]$$

$$[red_1] = [red_2] = [Co(MabiqH_2)H]$$

The concentration of [Co(MabiqH$_2$)] is known (1 mM) and is the same for each acid concentration used. We assume that the concentration of the reduced species also is the same at each acid concentration. Hence, the following equation applies:

$$\Delta E_{[pCA_2]-[pCA_1]} = -\frac{RT}{zF}\ln\left\{\frac{[ox_1]}{[ox_2]}\right\}$$

If all assumptions are correct, the potential shifts calculated between 1 mM and 10 mM *p*CA, 1 mM and 20 mM *p*CA, are ~60 and 77 mV respectively. In Figure 4, the theoretical calculated potential shifts between different *p*CA concentrations are represented as dashed lines. The reduction peak potential (E$_{p,c}$) using 1 mM *p*CA (blue dash line) serves as the reference potential. The orange and green dash lines represent the calculated potential differences between 1 mM and 10 mM *p*CA and 1 mM and 20 mM *p*CA. The calculated values reasonably match with the experimental reduction peak potentials. Therefore, we conclude that the first step involves first an electrochemical reduction, then a chemical reaction (EC) i.e., protonation.

5. Estimated Turn-over Number (TON) and Turn-over Frequency (TOF)

Lower estimates for the TON and TOF values for Co_{Mbq}:pCA 8 mM:80 mM and 8 mM:40 mM were calculated from the OEMS data shown in Figure 4b of the main text. The TOF values were determined from the data obtained at potentials of −1.1 V_{Fc} over the first four minutes of the CA step (Figure S5), where concentration gradients for the thin-layer electrode design are negligible, so that kinetic reaction rates can be obtained without interference from of mass transport resistance.
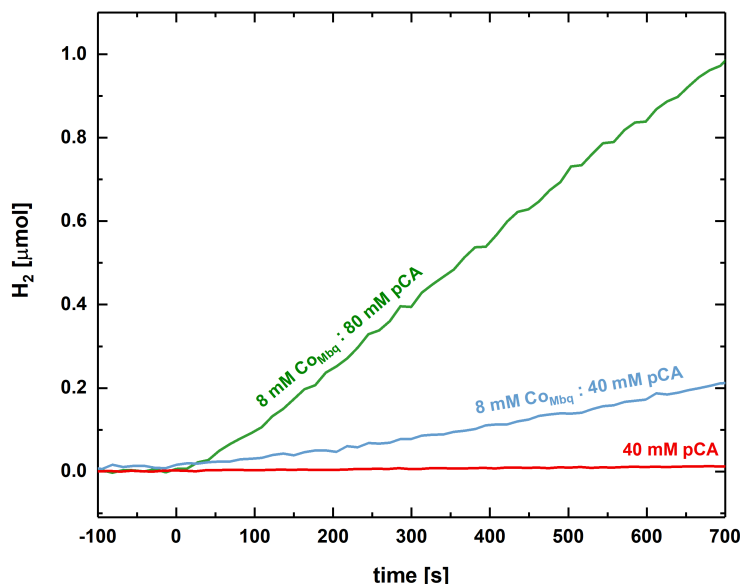

Figure S5. OEMS data analysis for Co_{Mbq}:pCA. After a two hour OCV step, the potential was stepped to −1.1 V_{Fc} for 20 h. Only 100 s of OCV step and 700 s of CA step are shown in the figure above. Co_{Mbq}:pCA = 8 mM:80 mM (green), 8 mM:40 mM (blue) and 40 mM pCA only (red).

The 40 mM pCA data (no catalyst, red trace, Figure S4) does not contribute to H_2 evolution during the CA step, within the time period examined. The 8 mM Co_{Mbq} used in this experiment corresponds to 1.12 μmol. However, with a porosity of 81%, the carbon paper can soak up approx. 22 μL of the 140 μL solution present in the OEMS cell; hence the maximum amount of accessible Co_{Mbq} is 0.18 μmol for the short time analyzed herein. Using this value, lower estimates of the TON (Eqn. *4*) for Co_{Mbq}:pCA : 8 mM:40 mM and 8 mM:80 mM over the initial 4 minutes were determined as 0.4 and 2, respectively. TOF (Eqn. *5*) values over the initial 4 minutes at −1.1 V_{Fc} for Co_{Mbq}:pCA : 8 mM:40 mM and 8 mM:80 mM were determined to be 6 and 32 h^{-1}, respectively, indicating that the TOF increases substantially with acid concentration. These values were determined as follows:

- For the total electrolyte volume of 140 μL, 8 mM Co_{Mbq} corresponds to 1.12 μmol (total). Considering that only 22 μl of the solution are utilized during this short time period (i.e., only the amount of electrolyte contained within the porous electrode), the amount of catalyst which is electrochemically active equates to 0.18 μmol for 8 mM Co_{Mbq}. Thus, the turnover number can be determined as

$$TON = \frac{amount\ of\ product}{amount\ of\ catalyst} \tag{4}$$

  The lower estimates of the TON for Co_{Mbq}:pCA = 8 mM:80 mM and 8 mM:40 mM are thus 2.1 (from 0.38 μmol$_{H2}$ / 0.18 μmol$_{catalyst}$) and 0.4 (from 0.07 μmol$_{H2}$ / 0.18 μmol$_{catalyst}$).

- The TOF frequency over the initial 4 minutes at −1.1 V_{Fc} can now be calculated from the above determined TON values:

$$TOF = \frac{TON}{time} \tag{5}$$

  This yields minimum TOF values of 32 h^{-1} (from 2.1/0.66 h) for Co_{Mbq}:pCA = 8 mM:80 mM and of 6 h^{-1} (from 0.4/0.66 h) for Co_{Mbq}:pCA = 8 mM:40 mM.

3.2 Elucidation of the Formation of the Precatalytic Complex

3.2.1 Employing bulk electrolysis technique and computational methods

The article "H_2 Evolution from Electrocatalysts with Redox-Active Ligands: Mechanistic Insights from Theory and Experiment vis-à-vis Co-Mabiq" was submitted in April 2021 and published online in July 2021 in the peer-viewed version of *Inorganic Chemistry*. The main findings of the paper were presented by Gülen Ceren Tok at the PRiME Meeting of the Electrochemical Society (online) in October 2020. A permanent link to this article can be found at: https://pubs.acs.org/doi/10.1021/acs.inorgchem.1c01157. To support the main article, additional information is provided in the Supporting Information, including the pH-dependent potential corrections, the CV results for various acid concentration with the catalyst, TD-DFT absorption spectra of intermediates, and calculated energy levels of intermediates.

The study shown in Chapter 3.1 implied that the precatalytic step likely involves the activation and deactivation of the Co_{Mbq} complex. Based on these findings, a mechanism involving two electrons and at least one proton transfer was proposed. Thus, this part of the research focuses on the characterization of the intermediates formed at the precatalytic step, employing a series of spectroelectrochemical experiments and the calculation of the absorption spectra of possible intermediates. Firstly, bulk electrolysis with an RRDE cell setup is applied to generate the precatalytic intermediate. The generated product is analyzed using UV-Vis spectroscopy, and a prominent new band appears that does not resemble any previously synthesized Co-Mabiq complexes. Furthermore, the cyclic voltammetry recorded upon generation of the intermediates after the bulk electrolysis displays the shift of the H_2 evolution potential from $-1.1\,V_{Fc}$ to $-1.32\,V_{Fc}$, which is associated with the intermediate that shows the new absorption band. These results indicate two intermediate products: 1) a stable intermediate with higher overpotentials toward H_2 evolution and 2) a more elusive intermediate

with lower overpotentials toward H_2 generation. To assist the characterization of the formed intermediates, varied pK_a value acids are employed since the strength of the proton source influences the reaction mechanism and the protonation sites. The findings reveal that using a weaker proton source results in a further reduction; then, the protonation takes place; thus, a different reaction mechanism occurs, likely leading to the generation of different intermediates. Experimental results provide insightful information regarding the formed intermediates; however, the isolation of the intermediates in order to characterize them in more detail could not be accomplished. Therefore, thermodynamics calculations are conducted to specify the favorable protonation sites. Two electrons and one proton transfer to the Co_{Mbq} complex forms a protonated diketiminate site as the most stable intermediate and a protonated imine site as the thermodynamically least stable intermediate. Moreover, absorption spectra are calculated using the DFT/MRCI method to identify possible intermediates. Combining the calculated absorption spectra and the thermodynamic calculations implies that the intermediate that evolves H_2 at -1.32 V_{Fc} is likely the diketiminate site protonated Co_{Mbq} complex and that the imine site protonation leads to lower overpotential towards H_2 evolution; however, due to its limited stability, the activity at -1.1 V_{Fc} disappears in time. The possible degradation mechanisms of the latter product are discussed in the publication. Possible HER mechanisms are further proposed in this study. The findings of this study exhibit how the multiple protonation sites of the non-innocent ligands affect the reaction mechanisms and the design of the catalysts, and their solution environment plays a significant role in influencing the metal-centered, ligand-centered, and ligand/metal-assisted pathways.

Author contributions

G.C.T. conducted the experimental section involving CV, bulk electrolysis, and UV-Vis experiments. S.R. carried out the computational section including thermodynamic calculations and DFT/MRCI. L.R. assisted in writing the experimental section. A.T.S.F. facilitated the designing of the spectroelectrochemical experiments. G.C.T., S.R., R.V.R., and C.R.H. wrote the manuscript, and A.T.S.F. assisted in the writing. G.C.T. and S.R. contributed equally

_____

to this work as co-shared first authors. All the authors discussed the data and commented on the manuscript.

H₂ Evolution from Electrocatalysts with Redox-Active Ligands: Mechanistic Insights from Theory and Experiment vis-à-vis Co-Mabiq

G. Ceren Tok,[∥] Sebastian Reiter,[∥] Anna T. S. Freiberg, Leonhard Reinschlüssel, Hubert A. Gasteiger, Regina de Vivie-Riedle,* and Corinna R. Hess*

Read Online

ACCESS | Metrics & More | Article Recommendations | SI Supporting Information

ABSTRACT: Electrocatalytic hydrogen production via transition metal complexes offers a promising approach for chemical energy storage. Optimal platforms to effectively control the proton and electron transfer steps en route to H₂ evolution still need to be established, and redox-active ligands could play an important role in this context. In this study, we explore the role of the redox-active Mabiq (Mabiq = 2−4:6−8-bis(3,3,4,4-tetramethlyldihydropyrrolo)-10−15-(2,2-biquinazolino)-[15]-1,3,5,8,10,14-hexaene1,3,7,9,11,14-N₆) ligand in the hydrogen evolution reaction (HER). Using spectro-electrochemical studies in conjunction with quantum chemical calculations, we identified two precatalytic intermediates formed upon the addition of two electrons and one proton to [Co^II(Mabiq)(THF)](PF₆) (**Co_Mbq**). We further examined the acid strength effect on the generation of the intermediates. The generation of the first intermediate, **Co_Mbq-H¹**, involves proton addition to the bridging imine-nitrogen atom of the ligand and requires strong proton activity. The second intermediate, **Co_Mbq-H²**, acquires a proton at the diketiminate carbon for which a weaker proton activity is sufficient. We propose two decoupled H₂ evolution pathways based on these two intermediates, which operate at different overpotentials. Our results show how the various protonation sites of the redox-active Mabiq ligand affect the energies and activities of HER intermediates.
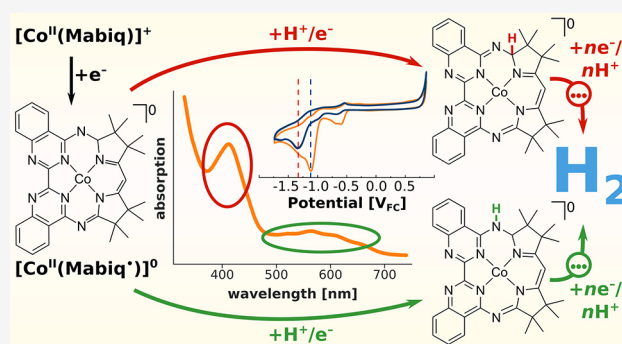
■ INTRODUCTION

As an appealing fuel for electrochemical devices and solar fuel systems, H₂ has sparked widespread efforts to develop effective molecular catalysts for its production—with an emphasis on earth-abundant transition metal complexes.[1−4] While proton reduction is seemingly simple, the design of complexes that can effectively manage the series of electron transfer (ET) and proton transfer (PT) events presents significant challenges. These steps can either occur sequentially or concertedly (proton coupled electron transfer, PCET), whereby the concerted pathway can circumvent high energy intermediates and coincides with diminished overpotentials.[5−7] In H₂ evolution catalyzed by transition metal complexes, both reduction and protonation can occur solely at the metal center, such that the metal hydricity must be tuned for both favorable hydride formation and release.[8,9] However, the use of ligands that can take part in the chemistry has garnered significant attention, since alternate pathways promoted by the coordination environment could result in enhanced activities.[10,11]

Ligands can participate in the H₂ evolution reaction (HER) in a number of ways, acting as proton or electron storage sites, or both.[10−17] The hydrogenases[18] have inspired the design of complexes with proton relay sites that can mediate proton movement between the acid and the second coordination sphere. For example, the pendant amine groups of the well-studied Ni-diphosphine complexes facilitate rapid transfer of the ligand-bound proton to the Ni−H, thereby affecting rapid electrocatalytic rates.[13,19] Hangman porphyrins, containing pendant carboxylic acid groups, also utilize this strategy—but these complexes further highlight the entanglement of redox noninnocent ligands in such processes.[20,21] As a consequence of accumulated electron density on the porphyrin, a ligand-centered pathway for H₂ evolution becomes available. Synergistic interactions between the metal and ligand offer various routes for the HER among complexes containing redox-active ligands. Cu-thiosemicarbazone complexes operate via metal-assisted ligand-centered pathways (Scheme 1a), in
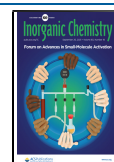
Scheme 1. Varying H$_2$ Evolution Pathways by Metal Complexes Containing Redox-Active Ligands

which reduction of the copper center is required for the addition of the second proton, yet both PT and H$_2$ release occur at the ligand.[22] In contrast, Co-dithiolene complexes exemplify ligand-assisted metal-centered pathways (Scheme 1b): while a conventional metal hydride is generated, both reduced and protonated dithiolene intermediates are additionally produced during the catalytic cycle.[12,14,23,24] In Ni-thiosemicarbazones[16,25,26] as well as Rh-cyclopentadiene complexes,[27,28] M−H and L−H tautomerism underlies H$_2$ production. Finally, several complexes with redox-active ligands evolve H$_2$ via purely ligand-centered pathways (Scheme 1c).[17,29]

Adding to the complexity of the HER is that the intermediates and catalytic pathways can differ substantially among metal complexes based on the same or similar ligands. As noted above, thiosemicarbazone complexes operate via all of the aforementioned metal-assisted ligand-centered (Scheme 1a), ligand-as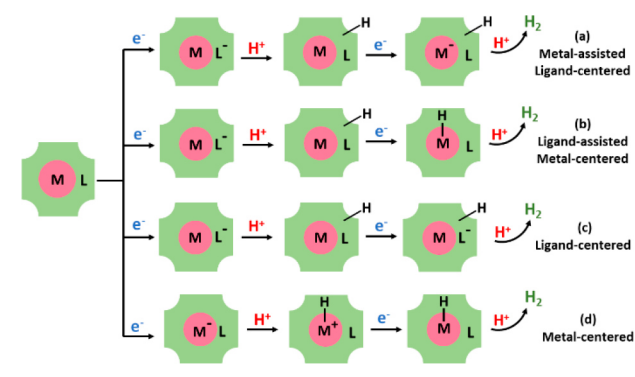sisted metal-centered (Scheme 1b), and ligand-centered (Scheme 1c) mechanisms, depending on the nature of the metal ion.[22,25,29] Ligand modifications, and/or the geometry of a complex, can likewise affect the catalytic pathways.[12,14,30] The mechanisms of many systems also can be switched by changes to the reaction conditions: changes in the acid strength affect the degree of ligand participation in the HER by metal hangman porphyrins, Rh-Cp, Fe-azadithiolate, and Co-polypyridyl complexes.[20,21,27,28,31,32]

There have been several excellent reviews that provide a more detailed overview on the topic of noninnocent ligands in H$_2$ evolution catalysts,[10,11,33] and significant progress has been made in the effective use of redox active ligands and proton relay sites for catalysis. However, while it is clear that "there is more than one way to skin a cat" when it comes to the HER, less clear are the types of motifs that support the different pathways or an overarching strategy for promoting the different pathways. Each of the above-mentioned systems is unique and affected by different conditions.[34,35] Saveant[36] highlighted competing factors concerning the use of proton relays, and the factors that allow such functional groups to provide a "boosting effect" for catalysis. Redox-active ligands similarly offer a powerful synergistic tool. However, further studies are required before one can effectively control PT and ET steps in such systems and design optimized motifs.

We have been investigating the H$_2$ evolution activity of a cobalt-Mabiq complex, [Co^{II}(Mabiq)(THF)](PF$_6$) (Mabiq = 2−4:6−8-bis(3,3,4,4-tetramethyldihydropyrrolo)-10−15-(2,2-biquinazolino)-[15]-1,3,5,8,10,14-hexaene1,3,7,9,11,14-N$_6$).[35] We will subsequently abbreviate the corresponding cationic

complex [Co^{II}(Mabiq)]$^+$ as **Co$_{Mbq}$**. The redox activity of the macrocyclic ligand was previously established; both the diketiminate and bipyrimidine moieties[37] of the Mabiq can store electrons. Our prior studies showed that H$_2$ evolution by **Co$_{Mbq}$** is preceded by the formation of an intermediate, which is likely generated upon protonation of the reduced Mabiq ligand. These studies also suggested that there is a competing pathway in operation, which leads to catalyst deactivation. We hypothesized that the Mabiq ligand could be protonated at multiple sites and that the various protonated **Co$_{Mbq}$** species displayed differing H$_2$ evolution activities. Therefore, understanding the reactivity of the **Co$_{Mbq}$** complex and its pathways can provide further insight into ET and PT steps at redox-active ligands.

In the present work, we employ spectro-electrochemical studies in conjunction with quantum chemical calculations, to identify the precatalytic intermediate and to gain greater insight into the requirements for H$_2$ evolution by **Co$_{Mbq}$**. We show that **Co$_{Mbq}$** can generate more than one intermediate upon cathodic activation depending on the acidic media employed. The H$_2$ evolution overpotential differs significantly between the two intermediates, underscoring the role of the ligand protonation sites on the **Co$_{Mbq}$** H$_2$ evolution mechanisms.

RESULTS

Two Intermediates in the Precatalytic Step. In our previous study,[35] we demonstrated that H$_2$ evolution by **Co$_{Mbq}$** in the presence of *para*-cyanoanilinium (*p*CA, pK_a = 7, pH = 4.85 in acetonitrile (MeCN), see section pH-Dependent Potential Correction, Supporting Information) occurs at a cathodic peak potential ($E_{p,c}$) of ca. −1.1 V vs Fc$^{+/0}$ (V$_{Fc}$). This potential is 300 mV cathodically shifted vs the [Co^{II}(Mabiq)]$^+$/[Co^{II}(Mabiq$^•$)]^0 couple in the absence of acid (see Figure 1 inset). In addition, a series of redox events were observed at $E_{p,c}$= −0.58 V$_{Fc}$, which correspond to the addition of two electrons and at least one proton, according to
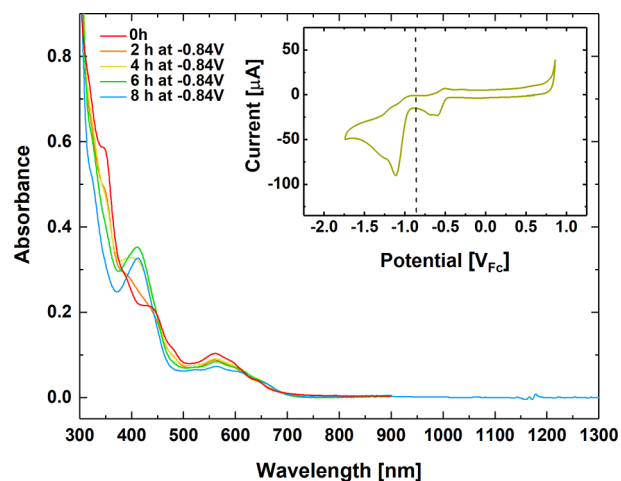
Figure 1. Spectral evolution of 0.2 mM **Co$_{Mbq}$** in the presence of 2 mM *p*CA in 0.1 M LiBF$_4$/MeCN in time during bulk electrolysis. Red trace, 0 h-prior to bulk electrolysis; orange trace, 2 h; yellow trace, 4 h; green trace, 6 h; blue trace, 8 h of bulk electrolysis. Inset graph: Cyclic voltammogram of 0.2 mM **Co$_{Mbq}$** plus 2 mM *p*CA in 0.1 M LiBF$_4$/MeCN, conducted with a glassy carbon electrode in the RDE setup, at 100 mV/s, under an Ar atmosphere. The vertical dashed black line indicates the applied potential for bulk electrolysis.

an electrochemical−chemical−electrochemical (ECE) mechanism (a subsequent protonation, with an electrochemical−chemical−electrochemical−chemical (ECEC) mechanism could not be excluded). No change in the absorption spectrum was observed upon the addition of pCA to a solution of the divalent $\mathbf{Co_{Mbq}}$ complex, further indicating that any modification to $\mathbf{Co_{Mbq}}$ occurs only after cathodic reduction.[35]

On the basis of our findings, we proposed a mechanism in which the reduction and protonation processes involved the Mabiq ligand (see Scheme 2). In the current study, we set out

Scheme 2. Proposed ECE pathway for formation of the precatalytic species. Possible protonation sites studied in this work are color-coded and assigned distinct labels. The candidate protonation sites were derived from the spin density of the $[\mathbf{Co^{II}(Mabiq^\bullet)}]^0$ species, calculated with DFT

$[\mathbf{Co^{II}(Mabiq)}]^+$ $[\mathbf{Co^{II}(Mabiq^\cdot)}]^0$

$\mathbf{Co_{Mbq}}$

- $\mathbf{Co_{Mbq}\text{-}H^{DK1}}$
- $\mathbf{Co_{Mbq}\text{-}H^{DK2}}$
- $\mathbf{Co_{Mbq}\text{-}H^{Im}}$
- $\mathbf{Co_{Mbq}\text{-}H^{Co}}$

Two intermediates $\mathbf{Co_{Mbq}\text{-}H^1}$ and $\mathbf{Co_{Mbq}\text{-}H^2}$ *out of four candidates*

$\mathbf{H_2}$
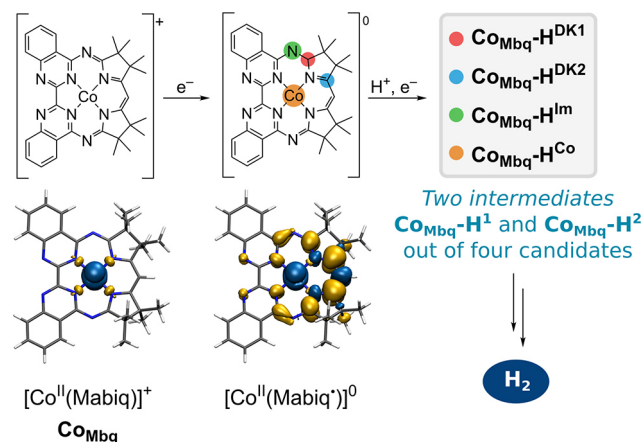
to characterize the intermediate through a series of spectroelectrochemical experiments. The distinctive spectroscopic features of the electron transfer series of Co-Mabiq compounds[37,38] are advantageous in this regard. The previously isolated $[\mathrm{Co(MabiqH_2)}],[38]$ which results from protonation of the two electron reduced $[\mathbf{Co^{II}(Mabiq^{\bullet\bullet})}]^-$, is inconsistent with the ECE pathway, and was previously ruled out as an intermediate.[35] However, given the electronic structure of the one electron reduced $[\mathbf{Co^{II}(Mabiq^\bullet)}]^0$ species, several protonation sites still could be envisioned (Scheme 2). Depending on the extent of metal ion involvement, the resultant protonated precatalytic species could contain either a $\mathrm{Co^I}$, $\mathrm{Co^{II}}$ or $\mathrm{Co^{III}}$ center.

To generate the precatalytic intermediate, we now carried out bulk electrolysis in an RDE setup, using 0.2 mM $\mathbf{Co_{Mbq}}$ in the presence of 2 mM pCA (Co/pCA = 1:10; 0.1 M LiBF$_4$/MeCN), at a potential of −0.84 V$_{Fc}$ (see Figure 1, vertical line in inset graph). An 80% conversion of $\mathbf{Co_{Mbq}}$ (for details, see Experimental Section, eq 1) to a precatalytic species referred to as $\mathbf{Co_{Mbq}\text{-}H^2}$ was achieved following 8 h of applied potential. The spectral evolution of the Co/pCA solution over this period shows a slight alteration in the band shape and position of the $[\mathbf{Co^{II}(Mabiq)}]^+$ transitions in the 500−700 nm region. Furthermore, a prominent new band, with λ_{max} = 411 nm, appears after 4 h. The final spectrum of the Co/pCA solution after 8 h of bulk electrolysis does not resemble any of the previously synthesized $[\mathbf{Co^{III}(Mabiq)}]^{2+}$, $[\mathbf{Co^{II}(Mabiq^\bullet)}]^0$, $[\mathbf{Co^{II}(Mabiq^{\bullet\bullet})}]^-$, or $[\mathbf{Co(MabiqH_2)}]$ compounds.[37,38] Notably, no new features are observed in the near IR region; transitions in this region are indicative of the one-electron

reduced Mabiq ligand. However, the sharp, intense transition at 411 nm in the final product spectrum suggests that the ligand has been modified. The final species generated at the end of the bulk electrolysis experiment features the distinctive 411 nm band and corresponds to one precatalytic species, for now denoted as $\mathbf{Co_{Mbq}\text{-}H^2}$. Comparison of the absorption spectrum at the end of bulk electrolysis with quantum chemical calculations indicate that this species is protonated at the diketiminate site $\mathbf{CoMbq\text{-}H^{DK1}}$; see section Calculated Absorption Spectra Identify the Intermediates. We note that comparison of the spectra after 6 and 8 h of bulk electrolysis shows a slight decrease of the absorbance around 411 nm that might stem from a decrease in a broader background feature. This could correspond to the generation of more than one intermediate in the bulk electrolysis experiment, which is consistent with the lack of an isosbestic point in the spectral evolution. The proportion of the two species seems to be time dependent.

The behavior of the bulk electrolysis product with respect to $\mathrm{H_2}$ evolution was subsequently examined by cyclic voltammetry (CV). The CV of $\mathbf{Co_{Mbq}\text{-}H^2}$ shows several important differences from the CV of the initial $\mathbf{Co_{Mbq}}/p$CA solution. A redox event at −0.63 V$_{Fc}$ (blue trace Figure 2) is still present,
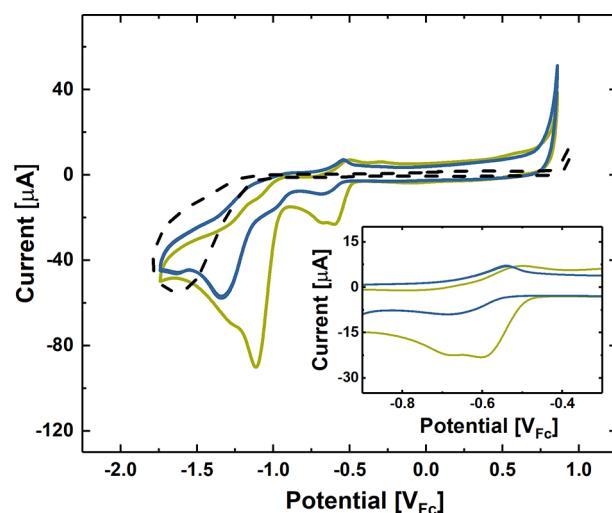
Figure 2. Cyclic voltammograms (including inset graph) of 0.2 mM $\mathbf{Co_{Mbq}}$ plus 2 mM pCA in 0.1 M LiBF$_4$/MeCN; solid green trace, prior to bulk electrolysis; solid blue trace, after bulk electrolysis, conducted with a glassy carbon electrode in the RDE setup, at 100 mV/s, under an Ar atmosphere. The dashed black trace shows the CV of 2 mM pCA on the glassy carbon disk only.

albeit of lower current magnitude—roughly 1/5 compared to the CV prior to bulk electrolysis. Considering the incomplete conversion of $\mathbf{Co_{Mbq}}$ to $\mathbf{Co_{Mbq}\text{-}H^2}$ during bulk electrolysis (roughly 80%), we assign the redox event in this region after bulk electrolysis to residual $\mathbf{Co_{Mbq}}$. Any current observed below −0.84 V$_{Fc}$ (just after the formation of the precatalytic species) stems from $\mathrm{H_2}$ evolution by the electrochemically formed intermediates. Hence, a change in the CV in this lower potential region correlates with a change in the intermediate formed. Indeed, the CV after bulk electrolysis displays only a minor reduction feature at −0.98 V$_{Fc}$, which we attribute to the same catalytic $\mathrm{H_2}$ evolution event occurring at −1.1 V$_{Fc}$ before bulk electrolysis, but with a significantly reduced contribution to the overall $\mathrm{H_2}$ evolution pathway. The predominant current

increase instead occurs at -1.32 V_{Fc}. This event was also observed in the CV of the initial Co_{Mbq}/pCA solution, as a shoulder to the primary catalytic process. Therefore, Co_{Mbq}-H^2, the species characterized by the 411 nm absorption band, facilitates H_2 evolution at -1.32 V_{Fc} and is generated on the time scale of the electrocatalytic CV experiments. Its formation accounts for the loss of activity that we previously observed in the OEMS studies when we examined H_2 evolution after 8 h of applied potential at -1.1 V_{Fc}.[35] The fact that Co_{Mbq}-H^2 does not evolve H_2 at -1.1 V_{Fc} again indicates that there is a second but elusive intermediate, which we refer to as Co_{Mbq}-H^1. The theoretical investigations presented later in this article will show that this species is most likely protonated at the imine site $CoMbq$-H^{Im}.

The combined data thus demonstrate that the initial proton coupled reduction processes at -0.63 V_{Fc} give rise to two distinct intermediates and that two competing pathways for H_2 evolution are available to the complex (Scheme 3). One of

Scheme 3. Formation of the Two Precatalytic Species Based on Competing ECE Pathways

Co_{Mbq} — $2e^- + H^+$ —⟨ Co_{Mbq}-H^1 HER at -1.1 V_{Fc}

                  Co_{Mbq}-H^2 HER at -1.32 V_{Fc}
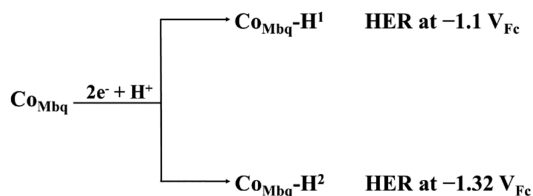
these intermediates Co_{Mbq}-H^1, represents the active species that evolves H_2 at -1.1 V_{Fc}. The other intermediate, Co_{Mbq}-H^2, is not inactive, as we had initially presumed based on OEMS studies. Rather, as noted above, Co_{Mbq}-H^2 requires a larger overpotential to affect H_2 production.

The fact that catalysis is observed at -1.1 V_{Fc} in the beginning of the bulk electrolysis, yet Co_{Mbq}-H^2 is the dominant species present after 8 h of applied potential resulting in H_2 evolution around -1.32 V_{Fc}, implies that Co_{Mbq}-H^1 is formed from Co_{Mbq} but is not stable over the time period of the bulk electrolysis.

Generation of Intermediates Depends on Acid Strength. We subsequently carried out electrochemical studies in the presence of a weaker acid, *para*-bromoanilinium (pBrA, pK_a = 9.43, pH = 6.06 in MeCN; see section pH-dependent potential correction, Supporting Information)[39,40] to examine whether the acid strength would affect the distribution of the two postulated intermediates. As previously noted, the acid strength can have a significant influence on the mechanism and led to the formation of varied intermediates in the HER pathway of other molecular catalysts.[31,32,34]

The CV of 0.2 mM Co_{Mbq} in the presence of 2 mM pBrA (Co/pBrA = 1:10; 0.1 M LiBF$_4$/ MeCN) displays similar features to that of the Co/pCA solution: a series of precatalytic redox events are followed by catalytic H_2 evolution at more negative potentials (Figure 3b). [The precatalytic steps are anodically shifted as expected for a proton dependent process. Analysis of the current magnitudes before and after bulk electrolysis indicated conversion between Co_{Mbq}-H^2 and Co_{Mbq} may not be fully reversible. See the SI for further details of the analysis.] A small wave is still observed at -1.1 V_{Fc}, the predominant H_2 evolution potential for Co/pCA (green trace, Figure 3a). After the 8 h of applied potential at

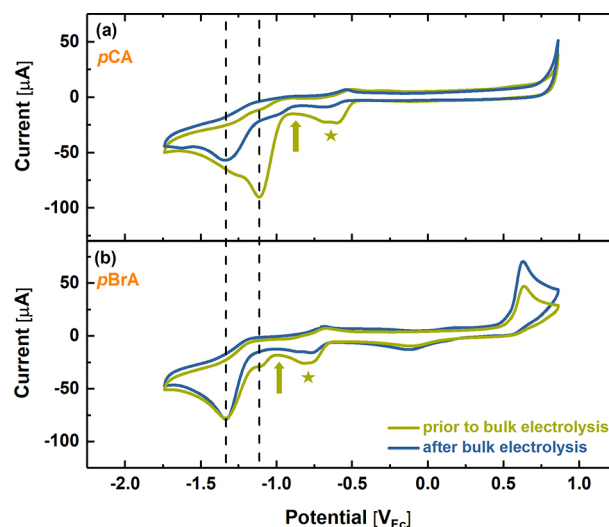**Figure 3.** Cyclic voltammograms of 0.2 mM Co_{Mbq} plus 2 mM (a) pCA or (b) pBrA in 0.1 M LiBF$_4$/MeCN; green trace, prior to bulk electrolysis; blue trace, after bulk electrolysis, conducted with a glassy carbon electrode in the RDE setup, at 100 mV/s, under an Ar atmosphere. The vertical dashed lines are positioned at -1.32 V_{Fc} and -1.1 V_{Fc}, respectively. The arrows represent the applied potentials for bulk electrolysis experiments. The stars indicate cathodic peak potentials for the precatalytic step.

-0.95 V_{Fc}—the potential of the precatalytic process in the case of Co/pBrA—the shoulder at -1.1 V_{Fc} completely disappears (blue trace, Figure 3b). Interestingly, H_2 evolution by the $Co/$ pBrA solution occurs at -1.32 V_{Fc} (green trace, Figure 3b), which coincides with the potential for H_2 evolution by the Co_{Mbq}-H^2 intermediate identified in the Co/pCA experiments. The catalytic process at -1.32 V_{Fc} is observable both before and after bulk electrolysis with the same current magnitude. Therefore, Co_{Mbq}-H^2 is generated in the presence of both pBrA and pCA. However, the formation of and H_2 evolution from Co_{Mbq}-H^2 dominate using pBrA as a proton source. The formation of Co_{Mbq}-H^1 appears to be negligible with the weaker acid, suggesting that pBrA is not strong enough to protonate the site that leads to this species, such that no significant H_2 evolution is observed at -1.1 V_{Fc}. The combined Co/pCA and Co/pBrA data further signify that two competing pathways for H_2 evolution are available, which are dependent on the acid strength. Nevertheless, after 8 h of applied potential, the more stable Co_{Mbq}-H^2 intermediate accumulates with both pCA and pBrA, and only the pathway for H_2 production at higher overpotentials is available.

The nature of the intermediates was further examined by absorption spectroscopic studies in conjunction with bulk electrolysis of a Co/pBrA solution carried out for 8 h of applied potential at -0.95 V_{Fc}—just below the activation region for the weaker acid (vertical line, inset, Figure 4a). In Co/pBrA, Co_{Mbq}-H^2 is unquestionably produced, as evidenced by the appearance of the distinctive absorbance at 411 nm (Figure 4). This species emerges earlier (solid blue line, Figure 4a) in comparison to its evolution with Co/pCA. The characteristic absorbance bands of Co_{Mbq} between 500 and 600 nm are unaltered (solid blue line and dashed black line, Figure 4c), indicative of residual Co_{Mbq} in the solution, which is consistent with the 60% conversion of Co_{Mbq} to Co_{Mbq}-H^2 after 8 h of applied potential in Co/pBrA (see Experimental Section, eq 1).
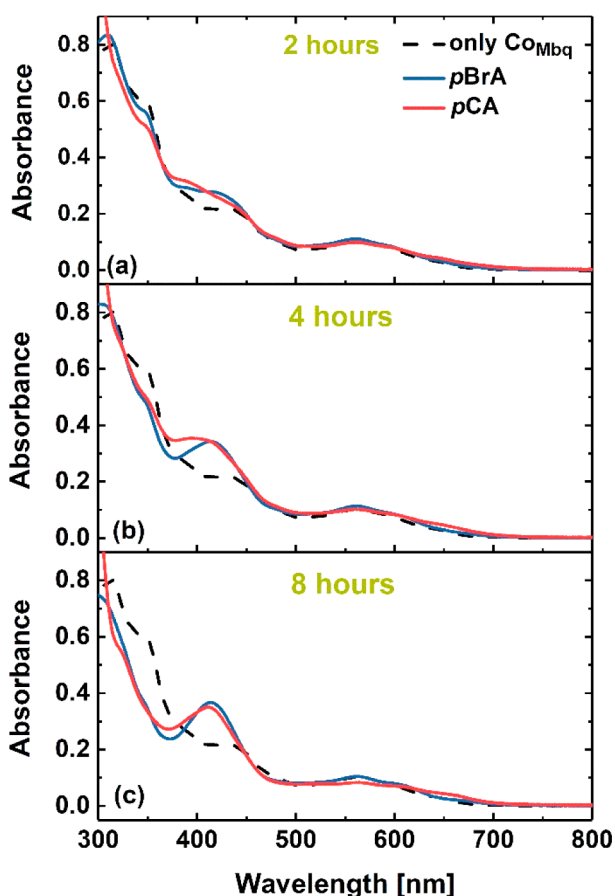
Figure 4. UV−vis absorption spectra of 0.2 mM Co_{Mbq} in the presence of 2 mM pBrA (Co/pBrA) or pCA (Co/pCA) in 0.1 M LiBF$_4$/MeCN in time during bulk electrolysis at potentials of −0.95 V$_{Fc}$ or −0.84 V$_{Fc}$, respectively. (a) 2 h, (b) 4 h, (c) 8 h of potential hold. Dashed black line, 0.2 mM Co_{Mbq}; solid red trace, Co/pCA; solid blue trace, Co/pBrA.

Figure 5. Cyclic voltammograms of 0.2 mM Co_{Mbq} plus 2 mM (a) pCA, (b) pBrA, or (c) pAn in 0.1 M LiBF$_4$/MeCN; blue trace, 0.2 mM Co_{Mbq} in the absence of acid source; orange trace, in the presence of acid source; conducted with a glassy carbon electrode in the RDE setup, at 100 mV/s, under an Ar atmosphere. For the CV in the absence of acid, the redox couples of Co_{Mbq} are assigned as follows: $[Co^{III}(Mabiq)]^{2+}/[Co^{II}(Mabiq)]^+$, $E_{P,c}$ = 0.08 V; $[Co^{II}(Mabiq)]^+/[Co^{II}(Mabiq^{\bullet})]^0$, −0.76 V; $[Co^{II}(Mabiq^{\bullet})]^0/[Co^{II}(Mabiq^{\bullet\bullet})]^-$, −1.56 V$_{Fc}$.

The lower conversion of Co_{Mbq} to Co_{Mbq}-H^2 in Co/pBrA compared to Co/pCA partly explains the differences in absorbance between 500 and 600 nm in the respective spectra, as well as the higher current observed in the activation region in the CV after bulk electrolysis. The final products generated after electrolysis with either acid have virtually the same absorption intensity at 411 nm. However, the additional absorbance bands in the pCA experiment, blue-shifted from the Co_{Mbq}-H^2 associated absorbance at 411 nm, can be correlated to the Co_{Mbq}-H^1 intermediate since Co_{Mbq}-H^1 is dominant at the beginning of the bulk electrolysis with pCA based on the CV but not generated in any appreciable amount using pBrA. Thus, both the CV and spectroscopic data further evidence that *two* intermediates, Co_{Mbq}-H^1 and Co_{Mbq}-H^2, arise from protonation of two distinct Mabiq sites, with differing pK_a's.

Acid Strength Influence on the Mechanism. Electrochemical studies in the presence of *para*-anisidinium (pAn; pK_a = 11.86, pH = 7.28 in MeCN)[39,40] were carried out to further assess the acid strength effect on the HER. Figure 5 compares the CVs of Co_{Mbq} in the absence of acid[35] with the CVs obtained upon the addition of the three different acids—pCA, pBrA, and pAn. The additional oxidation features above 0 V$_{Fc}$ originate from the acid source itself. In the presence of both pCA (orange trace, Figure 5a) and pBrA (orange trace, Figure

5b), the precatalytic event is anodically shifted compared to the $[Co^{II}(Mabiq)]^+/[Co^{II}(Mabiq^{\bullet})]^0$ couple. In the presence of pAn, two one-electron redox events are again observed prior to H$_2$ evolution. However, the first reduction occurs at a potential that is identical to that of the $[Co^{II}(Mabiq)]^+/[Co^{II}(Mabiq^{\bullet})]^0$ couple, while the following reductive event is 160 mV cathodically shifted. To verify the proton dependency of the processes, CVs were recorded at varied pAn concentration (Figure S1, Supporting Information). From the calculated theoretical potential shift based on the Nernst equation (eq S4, Supporting Information) and the experimentally observed [pAn]-dependent potential shifts, we confirm that only the second reduction feature at −0.95 V$_{Fc}$ is proton-dependent. The redox events preceding H$_2$ evolution are therefore consistent with an EEC mechanism, rather than the ECE process observed for the two stronger acids. The proton activity of pAn is not high enough to protonate the one electron reduced form of Co_{Mbq}, and protonation only becomes feasible after the addition of the second electron. H$_2$ evolution also requires further reduction of the complex

and an even higher overpotential ($E_{cat} = -1.48$ V_{Fc}). Since the present study was focused on resolving the ECE mechanism available to $\mathbf{Co_{Mbq}}$, we did not characterize the Co/pAn intermediates further. Nevertheless, the studies with pAn clearly demonstrate the effect of acid strength on the Co-Mabiq catalyzed HER—the proton source affects the formation of precatalytic intermediates and can alter the order of PT and ET steps.

On the basis of the experimental results, we conclude that two intermediates are generated in the electrocatalytic H_2 evolution pathway using acids with pK_a's in the range of 7.0 to 9.43, $\mathbf{Co_{Mbq}}\text{-}\mathbf{H^1}$ and $\mathbf{Co_{Mbq}}\text{-}\mathbf{H^2}$ (Scheme 4). However, over

Scheme 4. $\mathbf{Co_{Mbq}}$ Mechanisms and Initially Formed Intermediates in Different Acidic Media
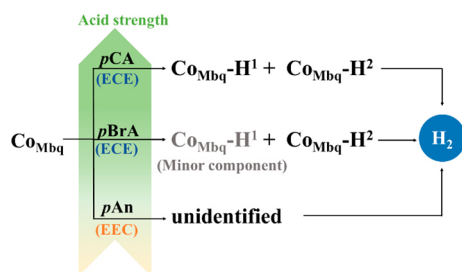
time, any $\mathbf{Co_{Mbq}}\text{-}\mathbf{H^1}$ generated in the reaction with pCA also is depleted. $\mathbf{Co_{Mbq}}\text{-}\mathbf{H^2}$ features a distinctive 411 nm absorption band and is associated with a higher overpotential for H_2 evolution. Attempts to crystallize or otherwise experimentally characterize this intermediate were unsuccessful. Consequently, we performed quantum chemical calculations to examine the relative energies and spectroscopic properties of possible protonation products and thereby identify $\mathbf{Co_{Mbq}}\text{-}\mathbf{H^1}$ and $\mathbf{Co_{Mbq}}\text{-}\mathbf{H^2}$. The computational studies focused on both the protonated one- and two-electron reduced species.

Thermodynamics Calculations Specify Favorable Protonation Sites. We started our theoretical investigation with protonation of the $[Co^{II}(Mabiq^\bullet)]^0$ complex, in accord with the established mechanism for the precatalytic event, where the first proton transfer coincides with the first electron transfer. On the basis of the electronic structure of $[Co^{II}(Mabiq^\bullet)]^{0,37}$ we identified four molecular sites where protonation is likely to occur (Figure 6)—one on the metal center and three on the ligand. We subsequently examined the reduced forms of these species, corresponding to the ECE mechanism determined from the experimental studies, and the products of the above-described bulk electrolysis studies. We denote each of the calculated candidate structures with a unique name (Figure 6) and assign a structure to the experimentally determined intermediates $\mathbf{Co_{Mbq}}\text{-}\mathbf{H^1}$ and $\mathbf{Co_{Mbq}}\text{-}\mathbf{H^2}$ at the end of the theoretical investigation.

We first optimized the structures of the four cations and the corresponding reduced intermediates, as well as that of pCA in its protonated (pCA) and deprotonated form (D-pCA) at the CAM-B3LYP level of theory (see Computational Details) and calculated the Gibbs free energies of protonation ΔG_{prot} as the difference between reactant and product free energies G:

$$\Delta G_{prot} = (G_{D\text{-}pCA} + G_{intermediate})$$
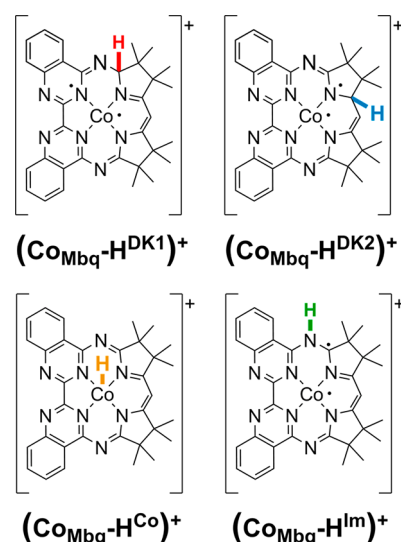$$- (G_{pCA} + G_{[Co^{II}(Mabiq^\bullet)]^0}) \quad (2)$$

Figure 6. Structures of investigated intermediates after the addition of one proton to the one-electron reduced $[Co^{II}(Mabiq^\bullet)]^0$, referred to by the "+" superscript. Subsequent reduction of these intermediates will be referred to without the "+" superscript in the following sections.

Table 1. Calculated Gibbs Free Reaction Energies for the Protonation of $[Co^{II}(Mabiq^\bullet)]^0$ with pCA (ΔG_{prot}) to Form Four Different Cationic Species, and for the Subsequent Reduction of the Cations (ΔG_{red}) to Yield Neutral Intermediates

cation	ΔG_{prot} [kJ/mol]	intermediate	ΔG_{red} [kJ/mol]
$(\mathbf{Co_{Mbq}}\text{-}\mathbf{H^{DK1}})^+$	−14.7	$\mathbf{Co_{Mbq}}\text{-}\mathbf{H^{DK1}}$	−517.5
$(\mathbf{Co_{Mbq}}\text{-}\mathbf{H^{DK2}})^+$	−26.7	$\mathbf{Co_{Mbq}}\text{-}\mathbf{H^{DK2}}$	−527.1
$(\mathbf{Co_{Mbq}}\text{-}\mathbf{H^{Co}})^+$	−42.2	$\mathbf{Co_{Mbq}}\text{-}\mathbf{H^{Co}}$	−360.6
$(\mathbf{Co_{Mbq}}\text{-}\mathbf{H^{Im}})^+$	−108.9	$\mathbf{Co_{Mbq}}\text{-}\mathbf{H^{Im}}$	−299.1

Analogously, the Gibbs free energies of reduction ΔG_{red} were calculated as the difference between the optimized cationic and neutral species (Table 1). The neutral diketiminate products $\mathbf{Co_{Mbq}}\text{-}\mathbf{H^{DK1}}$ and $\mathbf{Co_{Mbq}}\text{-}\mathbf{H^{DK2}}$ are significantly more stable (~200 kJ/mol) than the other two investigated species. Thus their formation is thermodynamically favored upon the addition of two electrons and one proton to $\mathbf{Co_{Mbq}}$. However, considering only the protonation step after the initial one-electron reduction of $\mathbf{Co_{Mbq}}$ (i.e direct protonation of $[Co^{II}(Mabiq^\bullet)]^0$), we observe the opposite trend. Here, the imine site ($\mathbf{Co_{Mbq}}\text{-}\mathbf{H^{Im}}$) is favored for protonation, followed by the cobalt center ($\mathbf{Co_{Mbq}}\text{-}\mathbf{H^{Co}}$). The diketiminate-based products have extraordinarily high protonation energies. The reason for this is the strong structural distortion and the breaking of ligand aromaticity introduced by protonation at any of the diketiminate sites (Figure S2, Supporting Information).

The opposite trends for the thermodynamics of protonation and reduction allow us to draw conclusions about the coupling of the two steps in the reaction mechanism: If the proton addition is strongly coupled to the first electron added to $\mathbf{Co_{Mbq}}$, forming $[Co^{II}(Mabiq^\bullet)]^0$, the protonation step becomes a limiting factor, and the most stable cation $(\mathbf{Co_{Mbq}}\text{-}\mathbf{H^{Im}})^+$ may be formed as a side product. A strong acid would be beneficial for this reaction pathway as the one electron reduced form $[Co^{II}(Mabiq^\bullet)]^0$ can be readily stabilized by proton addition. On the other hand, if the

proton addition is strongly coupled to the second electron in the ECE activation process, we expect formation of the most stable reduced intermediate, i.e., one (or both) of the diketiminate products. The CV data in Figure 3 show the apparent dissociation of EC and E mechanisms in the precatalytic process with the stronger acid, *p*CA, i.e., the two electron addition steps are well enough separated in potential to generate two distinct reduction peaks in the current profile of the CV. The separation of the ECE mechanism is not observed with the weaker acid, *p*BrA, however, leading only to one broad reduction event in the precatalytic step. The weak acid is not able to protonate the imine site and can therefore not stabilize the cation, which leads to direct formation of the most stable protonated and two electron reduced intermediate: one of the diketiminate products. Therefore, only one species, **Co$_{Mbq}$-H^2**, is formed with the weaker acid *p*BrA, while the stronger acid *p*CA initially leads to **Co$_{Mbq}$-H^1**, which disappears over time.

Calculated Absorption Spectra Identify the Intermediates. Excited states of Co-Mabiq complexes are an especially challenging problem for most computational methods. Time-dependent density functional theory (TD-DFT) is widely used to compute excited states of transition metal complexes[41−45] due to its comparably low cost and its ability to include electron correlation, depending on the chosen functional. We performed initial test calculations for the [Co^{II}(Mabiq$^•$)]^0 species using the CAM-B3LYP functional (Figure S3, Supporting Information) and found that reliable band assignment to the experimental spectra was not possible with TD-DFT, due to the strong multiconfigurational character of the open-shell singlet ground state. Therefore, we decided to use the DFT/MRCI method,[46−51] which combines a multi-reference configuration interaction (MRCI) ansatz with orbitals derived from a ground state DFT calculation, thereby ideally recovering both dynamic and static electron correlation at a feasible cost. DFT/MRCI has proven to produce highly accurate absorption spectra for molecules and complexes with either closed-shell or single-open-shell ground states.[46] On the downside, open-shell ground states with more than one unpaired electron, as is the case for most of the investigated Co-Mabiq complexes, are known to pose a particular challenge.[46]

Using a large basis set with diffuse functions in the DFT part of the calculation helped to overcome some of the issues and made it possible to compute an absorption spectrum for [Co^{II}(Mabiq$^•$)]^0, where the relevant experimental bands are unambiguously reproduced (Figure 7). All bands have strong metal contributions originating from the d$_{xz}$, d$_{yz}$, and d$_{z2}$ orbitals. Below 450 nm, doubly excited states start to dominate. The calculated absorption lines between 500 and 600 nm are red-shifted compared to the measurement, but the double-peak absorption is clearly visible. Both peaks correspond to d−π transitions from the d$_{xz}$ and d$_{yz}$ orbitals of the metal to the ligand. Though the oscillator strength of the band at 411 nm is quantitatively too small, we argue that the basic band structure is reproduced well enough to use this method for predicting which intermediates are formed in the experiments.

We therefore calculated DFT/MRCI absorption spectra for the four possible species after the addition of two electrons and one proton to [Co^{II}(Mabiq)]$^+$ (Figure 8). Protonation at the cobalt center (**Co$_{Mbq}$-H^{Co}**) produces a strong and broad absorption band around 411 nm but also leads to absorption in
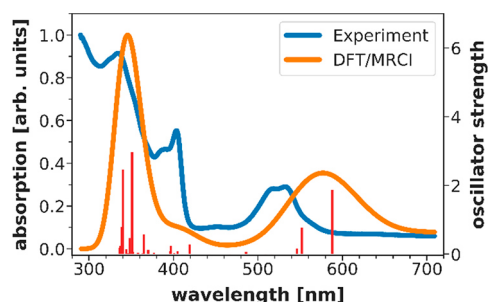

Figure 7. DFT/MRCI spectrum of [Co^{II}(Mabiq$^•$)]^0 in comparison to the synthesized [Co^{II}(Mabiq$^•$)]^0 absorption spectrum.[37] The line spectrum was convoluted with Gaussians with fwhm = 0.24 eV. The convoluted spectrum was normalized such that the highest absorption is one.

the red and NIR spectral region beyond 700 nm. As this is not observed experimentally (Figure 1), we conclude that the metal is not protonated at this stage of the reaction, in agreement with conclusions from the previous study.[35] Out of the four computed spectra, the one for **Co$_{Mbq}$-H^{DK1}** agrees best with the experimental spectrum. It explains the rising absorption band at 411 nm, which is blue-shifted by ∼30 nm in the calculations, as well as the shoulder at 340 nm and parts of the absorption after 600 nm. The other diketiminate product **Co$_{Mbq}$-H^{DK2}** also shows an absorption line at 411 nm, but the oscillator strength is much lower than for **Co$_{Mbq}$-H^{DK1}**. Since the rest of the spectral profile agrees well with the experimental spectrum, and **Co$_{Mbq}$-H^{DK2}** is also the thermodynamically most stable product, closely followed by **Co$_{Mbq}$-H^{DK1}**, we do not rule out the formation of both diketiminate products at this point. That said, our calculated absorption spectra indicate **Co$_{Mbq}$-H^{DK1}** as the main product **Co$_{Mbq}$-H^2** after bulk electrolysis.

For the spectrum of **Co$_{Mbq}$-H^{Im}**, the maximum number of 50 electronic states that could be calculated with the DFT/MRCI program prevented going below 504 nm. The corresponding cation spectrum (Figure S4, Supporting Information) shows no significant absorption at 411 nm, indicating that **Co$_{Mbq}$-H^{Im}** is not the final product after two-electron−one-proton addition to [Co^{II}(Mabiq)]$^+$. However, both the cation (**Co$_{Mbq}$-H^{Im}**)$^+$ and the reduced species **Co$_{Mbq}$-H^{Im}** exhibit broad absorption bands in the 500−600 nm region. Experimentally, absorption in this spectral range does not change during bulk electrolysis in the presence of *p*BrA, but it decreases over time in the presence of *p*CA. The spectral profile of the measured absorption bands fits that of the isolated **Co$_{Mbq}$** complex, indicating that residues of the reactant are present in the final reaction mixture. However, this does not explain why the band decreases only with *p*CA. Since the CV results indicate the presence of another intermediate, **Co$_{Mbq}$-H^1**, which evolves H$_2$ at −1.1 V and only forms in the presence of *p*CA, we attribute part of the absorbance between 500 and 600 nm in the presence of *p*CA to the imine-protonated species. Therefore, the **Co$_{Mbq}$-H^1** species corresponds to the product arising from protonation of the imine group, **Co$_{Mbq}$-H^{Im}**.

According to our DFT calculations (Table 1), protonation at the imine site yields the thermodynamically most stable cation but the least stable reduced product. Therefore, we investigated a side reaction with *p*CA, where the cation (**Co$_{Mbq}$-H^{Im}**)$^+$ forms initially and then slowly transforms to the more stable **Co$_{Mbq}$-H^{DK1}** product upon reduction, decreasing
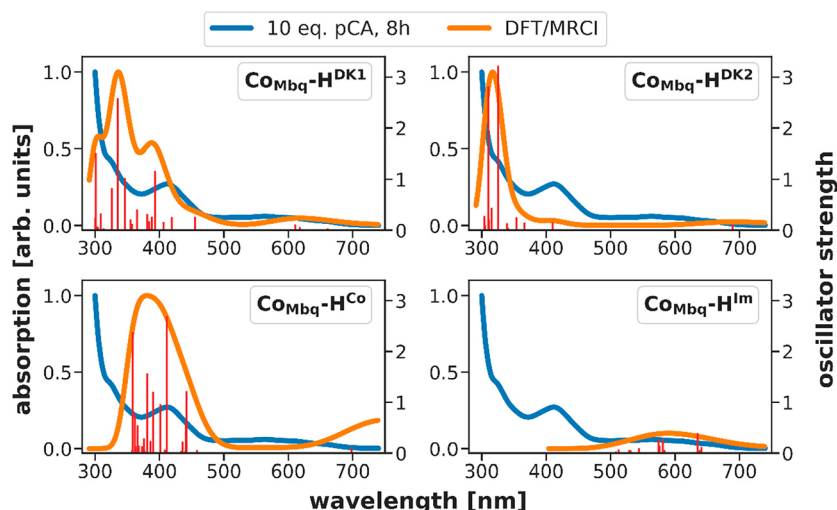
Figure 8. DFT/MRCI spectra obtained for the four investigated species after the addition of two electrons and one proton to $[Co^{II}(Mabiq)]^+$ in comparison to the experimentally obtained spectrum after 8 h of bulk electrolysis in the presence of 10 equiv of pCA. The highest excited state for $\mathbf{Co_{Mbq}\text{-}H^{Im}}$ that could be calculated with the DFT/MRCI method is located at 504 nm. Line spectra were convoluted with Gaussians with fwhm = 0.24 eV. Convoluted spectra were normalized such that the highest absorption is one, except for $\mathbf{Co_{Mbq}\text{-}H^{Im}}$ which was normalized to 0.1 to reflect the low oscillator strength in that spectral region.

the absorbance around 500−600 nm over time. However, the calculated free energy activation barrier of 162 kJ/mol seems too high for this process to occur under experimental conditions. From this, we conclude that two decoupled reaction pathways are possible in the presence of pCA, one leading to the species protonated at the diketiminate site, the other one leading to the imine-protonated intermediate.

To test how well the two intermediates can explain the experimental absorption spectrum, we fitted a linear combination of the calculated spectra for $\mathbf{Co_{Mbq}\text{-}H^{DK1}}$ and $\mathbf{Co_{Mbq}\text{-}H^{Im}}$ to the experimental spectrum after bulk electrolysis with pCA (Figure 9). The majority of the experimental spectrum is
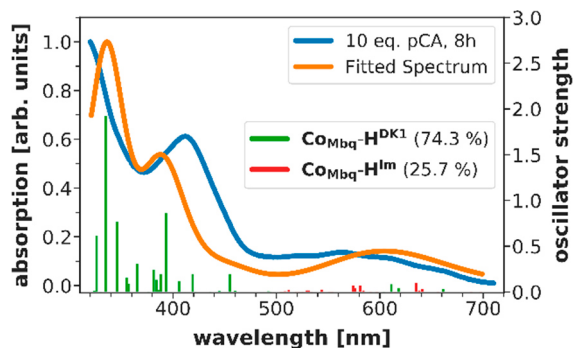

Figure 9. Fitted absorption spectrum composed of a linear combination of DFT/MRCI spectra of the diketiminate product $\mathbf{Co_{Mbq}\text{-}H^{DK1}}$ and the imine product $\mathbf{Co_{Mbq}\text{-}H^{Im}}$ in comparison to the experimentally obtained spectrum after 8 h of bulk electrolysis in the presence of 10 equiv of pCA. The fit was conducted in the range 320−700 nm.

explained by $\mathbf{Co_{Mbq}\text{-}H^{DK1}}$, underscoring that $\mathbf{Co_{Mbq}\text{-}H^{DK1}}$ is an important intermediate in the reaction mechanism. As expected, the absorption beyond 500 nm can be partly attributed to the $\mathbf{Co_{Mbq}\text{-}H^{Im}}$ species. As the rest of the 500−600 nm bands fit the measured spectrum of $\mathbf{Co_{Mbq}}$, the relative contribution of $\mathbf{Co_{Mbq}\text{-}H^{Im}}$ to the fit given in Figure 9 is an upper bound to the real share of $\mathbf{Co_{Mbq}\text{-}H^{Im}}$ in the spectrum.

DISCUSSION

Precatalytic Species. The combined experimental and computational studies point to the formation of two intermediates in the precatalytic ECE processes, $\mathbf{Co_{Mbq}\text{-}H^{DK1}}$ and $\mathbf{Co_{Mbq}\text{-}H^{Im}}$. The persistent precatalytic complex after 8 h of applied potential, using either pCA or pBrA, is $\mathbf{Co_{Mbq}\text{-}H^{DK1}}$. This compound acquires a proton at the diketiminate carbon and effectively describes a ligand-based hydride. In contrast, the formation of $\mathbf{Co_{Mbq}\text{-}H^{Im}}$ involves the reduction of both the ligand and the metal center, such that this species is best described as $[Co^I(MabiqH^{\bullet})]^0$. The proton is added to the bridging imine-nitrogen atom of the Mabiq ligand. The generation of significant amounts of $\mathbf{Co_{Mbq}\text{-}H^{Im}}$ requires a stronger acid, and this species is nevertheless depleted over time.

The reason for the loss of $\mathbf{Co_{Mbq}\text{-}H^{Im}}$ is not clear. However, three mechanisms could account for the loss of $\mathbf{Co_{Mbq}\text{-}H^{Im}}$ (Scheme 5): (i) There may be an indirect conversion to $\mathbf{Co_{Mbq}\text{-}H^{DK1}}$ via the original $\mathbf{Co_{Mbq}}$ complex. A homolytic pathway of H_2 evolution via the reaction of two $\mathbf{Co_{Mbq}\text{-}H^{Im}}$ molecules to form the one-electron reduced $[Co^{II}(Mabiq^{\bullet})]^0$ complex is unlikely, since no H_2 evolution above the pCA background was observed at -0.8 V_{Fc} in our earlier study.[35] (ii) The chemical instability of the $\mathbf{Co_{Mbq}\text{-}H^{Im}}$ intermediate could result in a completely deactivated form of the catalyst. The ratio of catalytic currents at -1.1 V_{Fc} and -1.32 V_{Fc} in the CV prior to bulk electrolysis cannot be used to determine the $\mathbf{Co_{Mbq}\text{-}H^{Im}}/\mathbf{Co_{Mbq}\text{-}H^{DK1}}$ ratio, as the turnover numbers for the two intermediates are unknown. It could be that only a minor portion of $\mathbf{Co_{Mbq}}$ is converted to $\mathbf{Co_{Mbq}\text{-}H^{Im}}$, despite significant H_2 evolution at -1.1 V_{Fc}. Therefore, the degradation of $\mathbf{Co_{Mbq}\text{-}H^{Im}}$ might not be observable in the absorption spectrum. Finally, (iii) one can envision a mechanism for interchange of the two intermediates—e.g., an equilibrium or comproportionation process—that allows for the accumulation of $\mathbf{Co_{Mbq}\text{-}H^{DK1}}$ over time in the presence of pCA with applied potential. The bridging imine groups of the Mabiq ligand correspond to the most favorable protonation sites in the one electron reduced Co-Mabiq complex, ($\mathbf{Co_{Mbq}\text{-}}$

Scheme 5. Possible Loss Channels of the Co_{Mbq}-H^{Im} Intermediate[a]
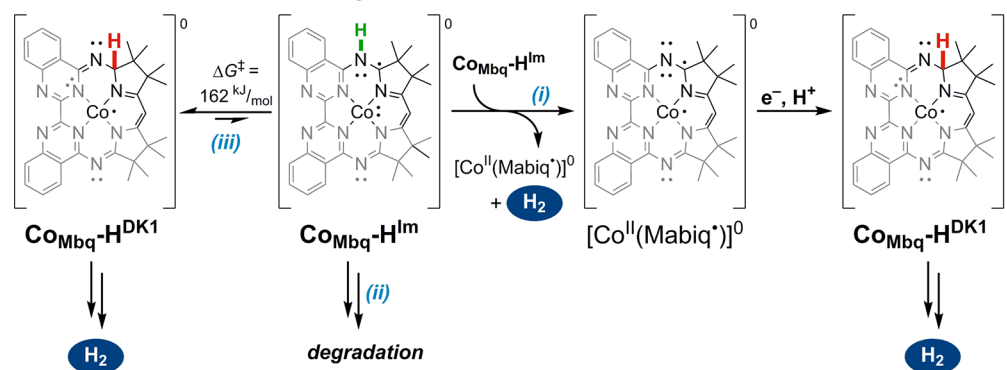
[a]Indirect conversion to Co_{Mbq}-H^{DK1} via pathway i would involve H_2 evolution at -0.8 V_{Fc}, which is not observed experimentally. Chemical degradation via ii or direct conversion via pathway iii could be alternative options, though the latter is unlikely due to the high kinetic barrier.

Scheme 6. Possible HER Pathways Involving the Co_{Mbq}-H^{DK1} (Top Pathway) and Co_{Mbq}-H^{Im} (Bottom Pathway) Intermediates[a]
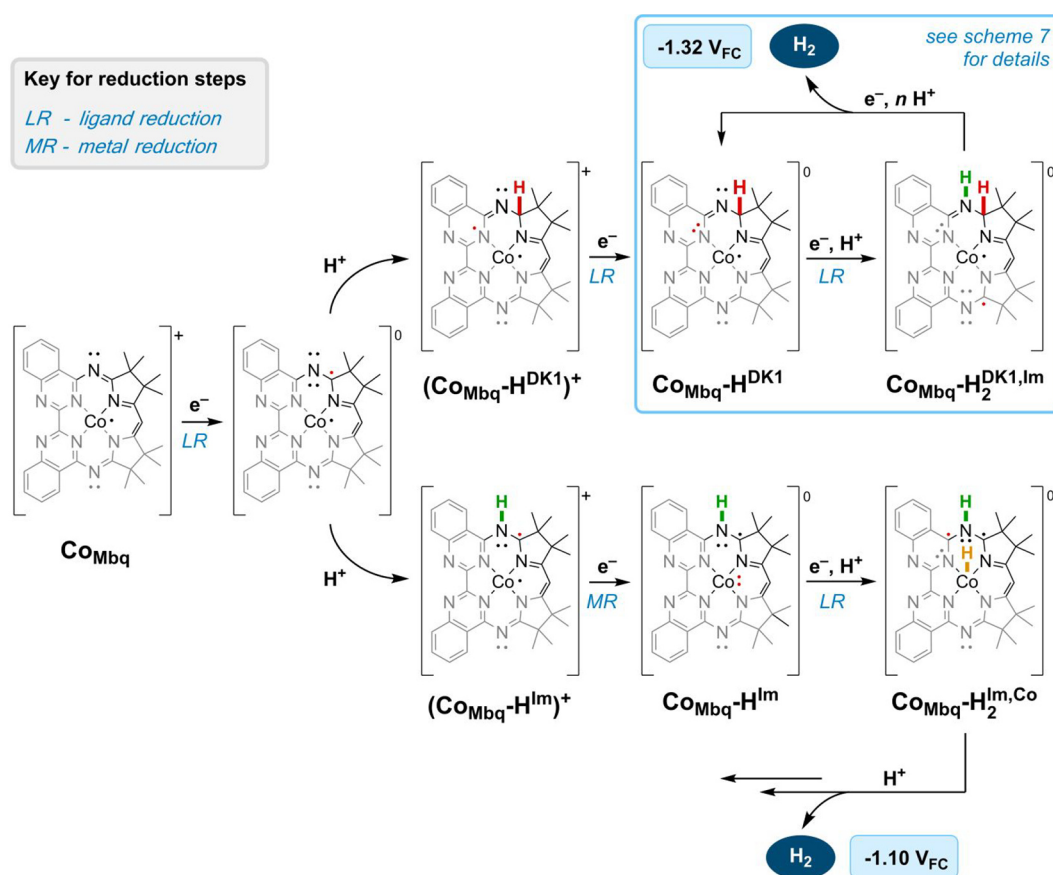
[a]The positions of the unpaired electron are based on DFT-derived spin densities (see Scheme 2 and Figure 10) and only show one of many possible resonance forms. Newly added electrons are highlighted in red in each reduction step.

$H^{Im})^+$. Among the protonated two-electron reduced forms we investigated, Co_{Mbq}-H^{Im} was associated with the highest energy. Indeed, intramolecular PT has been established for the HER mechanism of the Cu-thiosemicarbazone complexes.[22] However, as noted above, the computational results indicate that the barrier for conversion between Co_{Mbq}-H^{Im} and Co_{Mbq}-H^{DK1} is too large. This calculation, however, only signifies that the direct conversion of both intermediates after two-electron–one-proton addition is unlikely. An interchange between the cationic species or from one cationic species to a

fully activated form (i.e., $(Co_{Mbq}$-$H^{Im})^+$ to Co_{Mbq}-H^{DK1}) might still be feasible. Our evidence currently supports formation of the two intermediates via two decoupled pathways, though the experimentally observed disappearance of Co_{Mbq}-H^{Im} over time is not understood yet from a mechanistic point of view.

HER by Co_{Mbq}. H_2 evolution by the modified cobalt complexes produced in the precatalytic processes clearly still requires further reduction and protonation of Co_{Mbq}-H^{Im} or Co_{Mbq}-H^{DK1}, and we therefore also considered the subsequent HER mechanisms (Scheme 6).
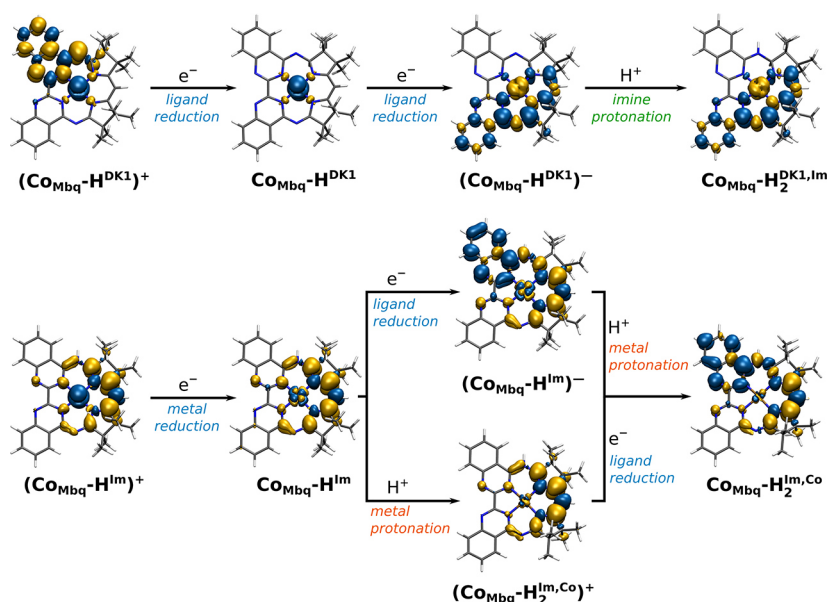
Figure 10. Broken-symmetry DFT derived spin density plots for the intermediates generated in an (EC)EE mechanism from **Co$_{Mbq}$**, [Co^{II}(Mabiq)]$^+$.

Scheme 7. Proposed Pathways for H$_2$ Evolution from Co$_{Mbq}$-H^{DK1}[a]
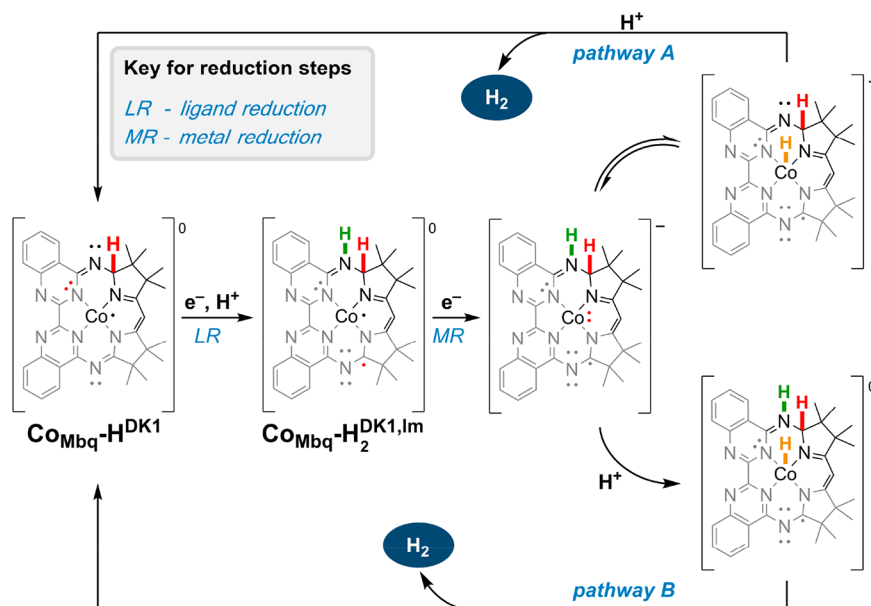
[a]The positions of the unpaired electron are based on DFT-derived spin densities (see Figure 10) and only show one of many possible resonance forms. Newly added electrons are highlighted in red in each reduction step.

The electronic structures of the two precatalytic complexes are highly distinctive. As noted, **Co$_{Mbq}$-H^{Im}** is a low-valent Co(I) complex, whereas **Co$_{Mbq}$-H^{DK1}** consists of a cobaltous ion coordinated to Mabiq-H. The differing oxidation states of the metal center will impact the ensuing ET and PT steps and further ligand participation in these processes. Although we have not established the order of these events, the electronic structures of the anionic species (**Co$_{Mbq}$-H^{DK1}**) or (**Co$_{Mbq}$-H^{Im}**)$^-$, generated upon the addition of another electron to the two intermediates (Figure 10), are informative in considering possible HER pathways. According to the DFT derived Merz−Singh−Kollman (MK) charges (Table S2, Supporting Information), (**Co$_{Mbq}$-H^{Im}**)$^-$ contains a low-valent, almost

neutral Co atom coordinated to a ligand anion. In the unrestricted formalism, the spins on the ligand are paired, while the broken-symmetry DFT solution, which is about 29 kJ/mol more stable, predicts a ligand biradical. By design, the broken-symmetry DFT approach overly delocalizes spin densities to arrive at the most stable wave function.[52] The true spin situation of the ligand can thus be debated, but in light of the unfavorable charge distribution, we deem formation of this intermediate unlikely in the absence of a proton. On the other hand, direct protonation of **Co$_{Mbq}$-H^{Im}** would lead to formation of a metal-hydride, the cationic (**Co$_{Mbq}$-H$_2$^{Im,Co}**)$^+$. We have not seen any evidence for a metal hydride species after bulk electrolysis at −0.84 V$_{Fc}$. Thus, we

propose that the first step in the HER from Co_{Mbq}-H^{Im} instead involves a PCET process; metal-hydride formation coincides with electron addition to generate the neutral Co_{Mbq}-$H_2^{Im,Co}$ (bottom pathway Figure 10). Once again, the broken-symmetry solution predicts biradical character for the ligand in Co_{Mbq}-$H_2^{Im,Co}$, while the unrestricted calculation yields a closed-shell ligand. The metal center is oxidized (MK charge 1.21), while the corresponding negative charge is spread across the Mabiq-ligand (sum of MK charges −1.04) and the Co-bound hydride ion (MK charge −0.17). This species may be further protonated to release H_2 (Scheme 6, bottom path).

The reduction in the calculated (Co_{Mbq}-H^{DK1}) species again occurs at the ligand. In this case, prediction of a H_2 evolution mechanism is more complex. This species has high negative charge density at the bridging imine group, making this a likely protonation site, though a route involving protonation of the second diketimine again offers a possibility. We speculate that H_2 evolution necessitates formation of the low-valent Co(I) species and subsequent metal protonation. However, even here a number of scenarios can be envisioned. For example, assuming involvement of a protonated imine-N, both direct protonation of a resultant metal-hydride (Scheme 7, pathway B, bottom) and a ligand-assisted pathway as established for Ni-thiosemicarbazone complexes (Scheme 7, pathway A, top),[16,25] can be envisioned.

Further studies are warranted to verify our proposed mechanisms. However, the suggested HER pathways already provide an explanation for the differing overpotentials for H_2 evolution from Co_{Mbq}-H^{Im} and Co_{Mbq}-H^{DK1}. The former complex already contains a reduced Co(I) center—the protonated imine appears to enable reduction of the cobalt ion at lower overpotentials. The formation of a low-valent cobalt species would thus readily support a metal-hydride pathway. However, at least three electrons are accumulated on the ligand in the pathways involving Co_{Mbq}-H^{DK1} before reduction of the metal center becomes favorable. Consequently, the redox-active ligand can also accumulate multiple protons. The higher overpotential for H_2 from Co_{Mbq}-H^{DK1} suggests that Mabiq acts as a hydride "sink," and access to an effective metal-centered HER pathway from this species requires additional electron transfer steps and thus also a higher energy input.

In our system, the formation of Co_{Mbq}-H^{Im} and the HER at lower overpotential is promoted by stronger acids. The effect of acid strength was also investigated for H_2 evolution by the hangman porphyrins.[20,21] In this system, stronger acids also allowed for H_2 evolution from a metal-hydride intermediate, whereas using the weaker acids, the HER occurred via a ligand-centered pathway that also required additional electron and transfer steps. Therefore, our suggested pathways are consistent with the acid strength effects observed in other systems.

CONCLUSION

The Co-Mabiq complex is one of several compounds in which the redox-active ligand engages in the PT and ET steps associate with H_2 evolution. However, a number of features are noteworthy and distinctive in the Mabiq system and provide general insight into the contribution of such ligands to the HER. In this regard, our studies also highlight how modern theoretical methods that can treat chemically relevant systems can greatly contribute to the understanding of experimental results. In particular, we point out the vital role of the

computationally affordable DFT/MRCI method in bridging the gap between multireference quantum chemistry and experiments. The computational studies contribute to our understanding of the nature of proton and electron storage sites, and the degree of PCET affects the energy and activity of intermediates.

The energetically low-lying π^* orbitals of the extended Mabiq π-bonded framework can readily accept electrons. The one-electron reduction potential for Co_{Mbq} in the absence of acid ($E_{p,c} = -0.8$ V_{Fc}) is thus fairly high in comparison to the *formal* $Co^{II/I}$ couples of Co-porphyrin (−1.08 V_{Fc}),[53] diothiolene (−1.49 V vs SCE),[12] and many cobaloxime[54] catalysts. In accord with previous findings,[55] coupling of a proton to the reduction process shifts the potential to more positive values. In fact, the addition of the second electron to the protonated Co-Mabiq compound also becomes highly favorable, with <150 mV separation between the proton-coupled precatalytic one- and two-electron reductions, regardless of the acid. Therefore, proton and electron storage by Mabiq—and by redox-active ligands in general—clearly can be an advantage for accessing reduced forms. However, the hydride equivalent that is added to Co_{Mbq} in the precatalytic steps is not readily released at this stage. Nevertheless, the potentials for catalytic H_2 evolution by Co_{Mbq} are also comparable to many redox-active ligand systems.[21,25]

The Co-Mabiq complex offers a metal- and multiple ligand-protonation sites. Consequently, the studies with Co_{Mbq} uniquely demonstrate how various features of noninnocent ligands can influence catalysis. The formation of the two distinct precatalytic intermediates, Co_{Mbq}-H^{Im} and Co_{Mbq}-H^{DK1}, is dependent on the acid strength. The two species can both evolve H_2 but have dissimilar electronic structures and operate at different potentials. Co_{Mbq}-H^{DK1} represents a ligand hydride—further reduction of this species remains ligand centered, and H_2 evolution requires a higher overpotential. In contrast, metal-centered reduction is favored for (Co_{Mbq}-H^{Im})$^+$—the ensuing H_2 evolution from Co_{Mbq}-H^{Im} involves metal protonation and occurs at lower energy. The implication is that pathways involving reduced metal centers, and thus metal-hydride species, may offer a more effective strategy for H_2 evolution. In this regard, the protonated imine of Co_{Mbq}-H^{Im} may further aid catalysis by serving as a proton relay site, whereas a similar role for the carbon bound hydrogen of Co_{Mbq}-H^{DK1} is unlikely.

Catalyst design clearly plays a significant role in effecting the metal, ligand-based, and ligand/metal-assisted HER pathways. In our system, modifying the Mabiq ligand on the diketimine unit may suppress the formation of Co_{Mbq}-H^{DK1} and promote H_2 evolution via Co_{Mbq}-H^{Im}. Select metals coordinated to the outer bipyrimidine also could alter the electronic structure in favor of metal-centered pathways. Overall, there is still a way to go in optimizing the metal−ligand synergies for efficient H_2 evolution. However, the mechanistic insights provided in this work shed further light on some of the competing factors to consider in the use of redox-active ligands for these processes and provide starting points for targeted ligand optimizations in future studies.

■ EXPERIMENTAL DETAILS

All chemicals were purchased from Sigma-Aldrich unless otherwise noted. Acetonitrile (MeCN) was dried by passage over activated alumina columns and stored over activated 3 Å molecular sieves. The water content in MeCN was determined to be below 1 ppm by Karl

Fischer titration. As a supporting electrolyte salt, lithium tetrafluoroborate ($LiBF_4$; BASF, Germany) was used in all cyclic voltammetry and bulk electrolysis experiments. $[Co^{II}(Mabiq)(THF)](PF_6)$[38] and the selected proton sources p-cyanoanilinium, p-bromoanilinium, and p-anisidinium were synthesized according to the literature procedure.[40,56]

Bulk Electrolysis and Cyclic Voltammetry (CV). Bulk electrolysis and CV measurements were conducted in a four-neck jacketed cell that was previously employed by our group,[35,57] and the cell was assembled in the glovebox (Ar, MBraun, Germany, < 0.1 ppm of H_2O and O_2.) The PEEK shroud working electrode includes a glassy carbon disk with a 5.0 mm diameter, surrounded by a glassy carbon ring with a 6.5 mm internal diameter and 7.5 mm external diameter (Pine Research Instrumentation, Durham, NC). For both bulk electrolysis and the CV measurements, a potential was applied only to the glassy carbon disk working electrode. Prior to usage, the working electrode was polished with 1.0 and 0.05 μm alumina suspensions (Buehler, Düsseldorf, Germany) and cleaned by sonication in ultrapure water. The electrode was subsequently dried for 12 h in an oven at 70 °C. A $LiFePO_4$ (BASF, Germany) electrode was employed as a counter electrode, which was separated from the working electrode part via a glass fitting. Li metal (Rockwood, USA) in 1 M $LiPF_6$ in EC/EMC 3:7, LP57 (BASF, Germany), was used as the reference electrode, separated via a Vycor 3535 frit (Advanced Glass & Ceramics, Holden, MA).

During the cell assembly, the working electrode rod was connected to the rotator, which was beneficial for the bulk electrolysis experiments. All measurements were recorded with an SP300 potentiostat (BioLogic, Grenoble, France). All potentials were recorded vs the $Li^{+/0}$ scale, and the potential scale conversion from $Li^{+/0}$ to $Fc^{+/0}$ was carried out experimentally by recording the $Fc^{+/0}$ redox couple in 0.1 M $LiBF_4$/MeCN with a Li reference electrode. The CV and bulk electrolysis experiments were recorded at 0 and 800 rpm, respectively.

At the end of the bulk electrolysis experiments, the conversion of Co_{Mbq} in the presence of the acid source (n, mole of the complex) was calculated according to eq 1, based on the number of electrons transferred (z), Faraday constant (F), and charge (Q).

$$Q = zFn \tag{1}$$

Q is the integrated area on current vs the time graph of Co/pCA or $Co/pBrA$; z represents two electrons (based on the ECE mechanism of precatalytic step); F is the Faraday constant, 96485.33 C mol^{-1}.

UV–Vis Absorption Spectroscopy. During the bulk electrolysis experiment, every 2 h, 100 μL aliquots were removed from the bulk solution and diluted with 2.7 mL of acetonitrile in the spectrophotometer cuvettes. Due to the possible air sensitivity of the samples, airtight far-UV quartz cuvettes (Starna GmbH, Germany) were used. Prior to usage, the cuvettes were cleaned and dried overnight in an oven at 70 °C and subsequently transferred into the glovebox. After the sample preparation in the glovebox, UV–vis spectra of samples at varied time intervals were recorded using a Cary 60 UV–vis spectrophotometer (Agilent Technologies, USA) for regions up to 900 nm wavelength, and the near IR region between 900 and 1300 nm was recorded with a UV-3600 Plus spectrophotometer (Schimadzu, Japan).

Computational Details. Geometry optimizations and thermodynamic analyses were carried out with *Gaussian 16*,[58] using the range-separated CAM-B3LYP[59] density functional. The optimized structures were identified as energy minima by the absence of imaginary vibrational frequencies. The transition state between Co_{Mbq}-H^{Im} and Co_{Mbq}-H^{DK1} was verified by its single imaginary vibrational frequency and by computing the reaction path toward the reactant and product. In all geometry optimizations, the broken symmetry DFT ansatz was used after testing the starting wave function for internal instabilities (keyword *stable = opt*), though the calculation converged to the closed-shell solution for $(Co_{Mbq}$-$H^{Co})^+$. The 6-31+G(d) basis set[60−63] was employed for all elements except cobalt. Here, the LANL2[63] pseudopotential replaced the inner core electrons [$1s^2 2s^2 2p^6$], leaving the outer core and valence shells to be described with the

corresponding double-ζ basis LANL2-DZ.[63] Implicit solvent effects were described by the polarizable continuum model (PCM) with standard parameters for acetonitrile.[64] Thermodynamic corrections to the electronic energies were computed in the harmonic approximation for a temperature of 298.15 K and a pressure of 1.0 atm.

TD-DFT absorption spectra were computed at the same level of theory as the geometry optimizations to assess the suitability of the method. However, due to the multiconfigurational nature of the complex, we eventually switched to the DFT/MRCI method[46−49,51] using the R2018 Hamiltonian.[51] Other common multiconfigurational methods, such as CASSCF or CASPT2, are computationally expensive, especially considering the extensive system of π electrons, and require careful selection of the active space. Multireference configuration interaction (MRCI) methods based on Hartree–Fock orbitals typically suffer from a lack of dynamical correlation and often require long expansions of high excitations.[46] DFT/MRCI is supposed to combine the best of both worlds—the description of dynamical correlation by DFT and the recovery of static correlation typical for multireference methods—all while keeping the computational effort at a feasible level. In contrast to CASSCF, there is no active space of carefully selected orbitals. Instead, a reference space of excited configurations is iteratively optimized, thereby removing any bias associated with manual orbital selection.

In preliminary test calculations for $[Co^{II}(Mabiq^\bullet)]^0$, a large and flexible basis set with diffuse functions emerged to be essential for a large enough configuration space to approximate the experimental spectrum. However, the size of the basis set is limited by technical constraints. To reconcile these conditions, we reduced the number of basis functions by replacing the methyl groups of the Mabiq ligand, which are unlikely to participate in any of the excitations we were interested in, with hydrogen atoms. The unrestricted DFT reference was calculated with *Orca 4.2.1*,[65,66] using the BHLYP[67,68] functional with the def2-TZVPD[69,70] all-electron basis set on the cobalt center and def2-SVPD[69,70] on all other atoms. The def2-TZVPD/C[71] and def2/JK[72] auxiliary basis sets were used within the resolution-of-the-identity formalism for coulomb and exchange integrals[73] (RI-JK) on all atoms. The only exception was Co_{Mbq}-H^{Im}, where def2-SVP/C was the largest feasible basis set for the subsequent MRCI step. Symmetry was turned off, and a final SCF convergence threshold of 10^{-7} E_h (keyword *SCFCONV7*) was used throughout with a 590-point Lebedev integration grid (keyword *Grid6*). Solvation effects were taken into account by means of the C-PCM model[74,75] with default parameters for acetonitrile. The resulting unrestricted molecular orbitals were transformed to a set of quasi-restricted orbitals[76] and used as input to the DFT/MRCI program. The reference space was iteratively optimized, increasing the number of excited states in each iteration until either the technical limit of 50 excited states or an excited state energy of 300 nm was reached. In any case, one final iteration was performed to ensure that the leading configurations of all excited states were contained in the reference space. The obtained line spectra were convoluted with Gaussians (fwhm = 0.24 eV). Convoluted spectra depicted in this work were normalized such that the highest absorption is one.

Visualizations of molecular structures and spin densities were created with VMD 1.9.3.[77]

■ ASSOCIATED CONTENT

Ⓢ Supporting Information

The Supporting Information is available free of charge at https://pubs.acs.org/doi/10.1021/acs.inorgchem.1c01157.

Details of pH-dependent potential correction; current response of the pre-catalytic step after the bulk electrolysis; CVs of Co_{Mbq} with varied p-anisidinium concentrations; visualization of structural distortions upon protonation of $[Co(Mabiq^\bullet)]$; TD-DFT absorption spectrum of $[Co^{II}(Mabiq^\bullet)]$; DFT/MRCI spectrum of $(Co_{Mbq}$-$H^{Im})^+$; additional spin density plots; calculated energy levels of intermediates; electrostatic

potential and atomic charges for $(Co_{Mbq}-H_2^{Im,Co})^+$ and $Co_{Mbq}-H_2^{Im,Co}$; and Cartesian coordinates of optimized geometries (PDF)

■ AUTHOR INFORMATION

Corresponding Authors

Regina de Vivie-Riedle − *Department of Chemistry, Ludwig-Maximilians-Universität München, 81377 München, Germany;* ⊙ orcid.org/0000-0002-7877-5979; Email: Regina.de_Vivie@cup.uni-muenchen.de

Corinna R. Hess − *Department of Chemistry and Catalysis Research Center, Technical University of Munich, 85748 Garching, Germany;* ⊙ orcid.org/0000-0002-9607-9184; Email: corinna.hess@ch.tum.de

Authors

G. Ceren Tok − *Department of Chemistry and Catalysis Research Center, Technical University of Munich, 85748 Garching, Germany*

Sebastian Reiter − *Department of Chemistry, Ludwig-Maximilians-Universität München, 81377 München, Germany;* ⊙ orcid.org/0000-0001-7381-4222

Anna T. S. Freiberg − *Department of Chemistry and Catalysis Research Center, Technical University of Munich, 85748 Garching, Germany; Present Address: Forschungszentrum Jülich GmbH, Helmholtz Institute Erlangen-Nürnberg for Renewable Energy, Cauerstrasse 1, 91058 Erlangen, Germany;* ⊙ orcid.org/0000-0002-7885-7632

Leonhard Reinschlüssel − *Department of Chemistry and Catalysis Research Center, Technical University of Munich, 85748 Garching, Germany*

Hubert A. Gasteiger − *Department of Chemistry and Catalysis Research Center, Technical University of Munich, 85748 Garching, Germany;* ⊙ orcid.org/0000-0001-8199-8703

Complete contact information is available at:
https://pubs.acs.org/10.1021/acs.inorgchem.1c01157

Author Contributions

‖The manuscript was written through contributions of all authors. All authors have given approval to the final version of the manuscript. G.C.T. and S.R. contributed equally.

Notes

The authors declare no competing financial interest.

■ ABBREVIATIONS

CV, cyclic voltammetry; DFT, density functional theory; ECE, electrochemical−chemical−electrochemical; ECEC, electrochemical−chemical−electrochemical−chemical; ET, electron transfer; MRCI, multireference configuration interaction; OEMS, online electrochemical mass spectrometry; PCET, proton coupled electron transfer; PT, proton transfer; RRDE, rotating ring disk electrode; TD-DFT, time-dependent density functional theory

■ REFERENCES

(1) McKone, J. R.; Lewis, N. S.; Gray, H. B. Will Solar-Driven Water-Splitting Devices See the Light of Day? *Chem. Mater.* **2014**, *26* (1), 407−414.

(2) Berardi, S.; Drouet, S.; Francas, L.; Gimbert-Surinach, C.; Guttentag, M.; Richmond, C.; Stoll, T.; Llobet, A. Molecular artificial photosynthesis. *Chem. Soc. Rev.* **2014**, *43* (22), 7501−7519.

(3) Brazzolotto, D.; Gennari, M.; Queyriaux, N.; Simmons, T. R.; Pecaut, J.; Demeshko, S.; Meyer, F.; Orio, M.; Artero, V.; Duboc, C. Nickel-centred proton reduction catalysis in a model of [NiFe] hydrogenase. *Nat. Chem.* **2016**, *8* (11), 1054−1060.

(4) McNamara, W. R.; Han, Z.; Alperin, P. J.; Brennessel, W. W.; Holland, P. L.; Eisenberg, R. A cobalt-dithiolene complex for the photocatalytic and electrocatalytic reduction of protons. *J. Am. Chem. Soc.* **2011**, *133* (39), 15368−15371.

(5) Hammes-Schiffer, S. Controlling Electrons and Protons through Theory: Molecular Electrocatalysts to Nanoparticles. *Acc. Chem. Res.* **2018**, *51* (9), 1975−1983.

(6) Huynh, M. H. V.; Meyer, T. J. Proton-Coupled Electron Transfer. *Chem. Rev.* **2007**, *107* (11), 5004−5064.

(7) Warren, J. J.; Tronic, T. A.; Mayer, J. M. Thermochemistry of Proton-Coupled Electron Transfer Reagents and its Implications. *Chem. Rev.* **2010**, *110* (12), 6961−7001.

(8) McKone, J. R.; Marinescu, S. C.; Brunschwig, B. S.; Winkler, J. R.; Gray, H. B. Earth-abundant hydrogen evolution electrocatalysts. *Chem. Sci.* **2014**, *5* (3), 865−878.

(9) Wiedner, E. S.; Chambers, M. B.; Pitman, C. L.; Bullock, R. M.; Miller, A. J.; Appel, A. M. Thermodynamic Hydricity of Transition Metal Hydrides. *Chem. Rev.* **2016**, *116* (15), 8655−8692.

(10) Das, A.; Hessin, C.; Ren, Y.; Desage-El Murr, M. Biological concepts for catalysis and reactivity: empowering bioinspiration. *Chem. Soc. Rev.* **2020**, *49* (23), 8840−8867.

(11) Luo, G.-G.; Zhang, H.-L.; Tao, Y.-W.; Wu, Q.-Y.; Tian, D.; Zhang, Q. Recent progress in ligand-centered homogeneous electrocatalysts for hydrogen evolution reaction. *Inorg. Chem. Front.* **2019**, *6* (2), 343−354.

(12) Solis, B. H.; Hammes-Schiffer, S. Computational study of anomalous reduction potentials for hydrogen evolution catalyzed by cobalt dithiolene complexes. *J. Am. Chem. Soc.* **2012**, *134* (37), 15253−15256.

(13) Fernandez, L. E.; Horvath, S.; Hammes-Schiffer, S. Theoretical Analysis of the Sequential Proton-Coupled Electron Transfer Mechanisms for H2 Oxidation and Production Pathways Catalyzed by Nickel Molecular Electrocatalysts. *J. Phys. Chem. C* **2012**, *116* (4), 3171−3180.

(14) Letko, C. S.; Panetier, J. A.; Head-Gordon, M.; Tilley, T. D. Mechanism of the electrocatalytic reduction of protons with diaryldithiolene cobalt complexes. *J. Am. Chem. Soc.* **2014**, *136* (26), 9364−9376.

(15) Rosenkoetter, K. E.; Wojnar, M. K.; Charette, B. J.; Ziller, J. W.; Heyduk, A. F. Hydrogen-Atom Noninnocence of a Tridentate [SNS] Pincer Ligand. *Inorg. Chem.* **2018**, *57* (16), 9728−9737.

(16) Straistari, T.; Fize, J.; Shova, S.; Réglier, M.; Artero, V.; Orio, M. A Thiosemicarbazone-Nickel(II) Complex as Efficient Electrocatalyst for Hydrogen Evolution. *ChemCatChem* **2017**, *9* (12), 2262−2268.

(17) Thompson, E. J.; Berben, L. A. Electrocatalytic Hydrogen Production by an Aluminum(III) Complex: Ligand-Based Proton and Electron Transfer. *Angew. Chem., Int. Ed.* **2015**, *54* (40), 11642−11646.

(18) Lubitz, W.; Ogata, H.; Rudiger, O.; Reijerse, E. Hydrogenases. *Chem. Rev.* **2014**, *114* (8), 4081−4148.

(19) DuBois, D. L. Development of molecular electrocatalysts for energy storage. *Inorg. Chem.* **2014**, *53* (8), 3935−3960.

(20) Solis, B. H.; Maher, A. G.; Dogutan, D. K.; Nocera, D. G.; Hammes-Schiffer, S. Nickel phlorin intermediate formed by proton-coupled electron transfer in hydrogen evolution mechanism. *Proc. Natl. Acad. Sci. U. S. A.* **2016**, *113* (3), 485−492.

(21) Solis, B. H.; Maher, A. G.; Honda, T.; Powers, D. C.; Nocera, D. G.; Hammes-Schiffer, S. Theoretical Analysis of Cobalt Hangman Porphyrins: Ligand Dearomatization and Mechanistic Implications for Hydrogen Evolution. *ACS Catal.* **2014**, *4* (12), 4516−4526.

(22) Haddad, A. Z.; Cronin, S. P.; Mashuta, M. S.; Buchanan, R. M.; Grapperhaus, C. A. Metal-Assisted Ligand-Centered Electrocatalytic Hydrogen Evolution upon Reduction of a Bis(thiosemicarbazonato)-Cu(II) Complex. *Inorg. Chem.* **2017**, *56* (18), 11254−11265.

(23) Panetier, J. A.; Letko, C. S.; Tilley, T. D.; Head-Gordon, M. Computational Characterization of Redox Non-Innocence in Cobalt-Bis(Diaryldithiolene)-Catalyzed Proton Reduction. *J. Chem. Theory Comput.* **2016**, *12* (1), 223−230.

(24) Zarkadoulas, A.; Field, M. J.; Papatriantafyllopoulou, C.; Fize, J.; Artero, V.; Mitsopoulou, C. A. Experimental and Theoretical Insight into Electrocatalytic Hydrogen Evolution with Nickel Bis(aryldithiolene) Complexes as Catalysts. *Inorg. Chem.* **2016**, *55* (2), 432−444.

(25) Jain, R.; Mamun, A. A.; Buchanan, R. M.; Kozlowski, P. M.; Grapperhaus, C. A. Ligand-Assisted Metal-Centered Electrocatalytic Hydrogen Evolution upon Reduction of a Bis(thiosemicarbazonato)-Ni(II) Complex. *Inorg. Chem.* **2018**, *57* (21), 13486−13493.

(26) Barrozo, A.; Orio, M. Unraveling the catalytic mechanisms of H2 production from thiosemicarbazone nickel complexes. *RSC Adv.* **2021**, *11* (9), 5232−5238.

(27) Johnson, S. I.; Gray, H. B.; Blakemore, J. D.; Goddard, W. A., 3rd Role of Ligand Protonation in Dihydrogen Evolution from a Pentamethylcyclopentadienyl Rhodium Catalyst. *Inorg. Chem.* **2017**, *56* (18), 11375−11386.

(28) Quintana, L. M.; Johnson, S. I.; Corona, S. L.; Villatoro, W.; Goddard, W. A., 3rd; Takase, M. K.; VanderVelde, D. G.; Winkler, J. R.; Gray, H. B.; Blakemore, J. D. Proton-hydride tautomerism in hydrogen evolution catalysis. *Proc. Natl. Acad. Sci. U. S. A.* **2016**, *113* (23), 6409−6414.

(29) Haddad, A. Z.; Garabato, B. D.; Kozlowski, P. M.; Buchanan, R. M.; Grapperhaus, C. A. Beyond Metal-Hydrides: Non-Transition-Metal and Metal-Free Ligand-Centered Electrocatalytic Hydrogen Evolution and Hydrogen Oxidation. *J. Am. Chem. Soc.* **2016**, *138* (25), 7844−7847.

(30) Papanikolaou, M. G.; Elliott, A.; McAllister, J.; Gallos, J. K.; Keramidas, A. D.; Kabanos, T. A.; Sproules, S.; Miras, H. N. Electrocatalytic hydrogen production by dinuclear cobalt(II) compounds containing redox-active diamidate ligands: a combined experimental and theoretical study. *Dalton Trans.* **2020**, *49* (44), 15718−15730.

(31) Queyriaux, N.; Sun, D.; Fize, J.; Pécaut, J.; Field, M. J.; Chavarot-Kerlidou, M.; Artero, V. Electrocatalytic Hydrogen Evolution with a Cobalt Complex Bearing Pendant Proton Relays: Acid Strength and Applied Potential Govern Mechanism and Stability. *J. Am. Chem. Soc.* **2020**, *142* (1), 274−282.

(32) Aster, A.; Wang, S.; Mirmohades, M.; Esmieu, C.; Berggren, G.; Hammarstrom, L.; Lomoth, R. Metal vs. ligand protonation and the alleged proton-shuttling role of the azadithiolate ligand in catalytic H2 formation with FeFe hydrogenase model complexes. *Chem. Sci.* **2019**, *10* (21), 5582−5588.

(33) Costentin, C.; Saveant, J. M.; Tard, C. Ligand "noninnocence" in coordination complexes vs. kinetic, mechanistic, and selectivity issues in electrochemical catalysis. *Proc. Natl. Acad. Sci. U. S. A.* **2018**, *115* (37), 9104−9109.

(34) Maher, A. G.; Liu, M.; Nocera, D. G. Ligand Noninnocence in Nickel Porphyrins: Nickel Isobacteriochlorin Formation under Hydrogen Evolution Conditions. *Inorg. Chem.* **2019**, *58* (12), 7958−7968.

(35) Tok, G. C.; Freiberg, A. T. S.; Gasteiger, H. A.; Hess, C. R. Electrocatalytic H2 Evolution by the Co-Mabiq Complex Requires Tempering of the Redox-Active Ligand. *ChemCatChem* **2019**, *11* (16), 3973−3981.

(36) Saveant, J. M. Proton Relays in Molecular Catalysis of Electrochemical Reactions: Origin and Limitations of the Boosting Effect. *Angew. Chem., Int. Ed.* **2019**, *58* (7), 2125−2128.

(37) Puttock, E. V.; Banerjee, P.; Kaspar, M.; Drennen, L.; Yufit, D. S.; Bill, E.; Sproules, S.; Hess, C. R. A Series of [Co(Mabiq)Cl2-n] (n = 0, 1, 2) Compounds and Evidence for the Elusive Bimetallic Form. *Inorg. Chem.* **2015**, *54* (12), 5864−5873.

(38) Kaspar, M.; Altmann, P. J.; Pothig, A.; Sproules, S.; Hess, C. R. A macrocyclic 'Co(0)' complex: the relevance of ligand non-innocence to reactivity. *Chem. Commun.* **2017**, *53* (53), 7282−7285.

(39) Kaljurand, I.; Kütt, A.; Soovali, L.; Rodima, T.; Mäemets, V.; Leito, I.; Koppel, I. A. Extension of the Self-Consistent Spectrophotometric Basicity Scale in Acetonitrile to a Full Span of 28 pKa Units: Unification of Different Basicity Scales. *J. Org. Chem.* **2005**, *70* (3), 1019−1028.

(40) Appel, A. M.; Pool, D. H.; O'Hagan, M.; Shaw, W. J.; Yang, J. Y.; Rakowski DuBois, M.; DuBois, D. L.; Bullock, R. M. [Ni(PPh2NBn2)2(CH3CN)]2+ as an Electrocatalyst for H2 Production: Dependence on Acid Strength and Isomer Distribution. *ACS Catal.* **2011**, *1* (7), 777−785.

(41) Adamo, C.; Barone, V. Inexpensive and accurate predictions of optical excitations in transition-metal complexes: the TDDFT/PBE0 route. *Theor. Chem. Acc.* **2000**, *105* (2), 169−172.

(42) Hay, P. J. Theoretical Studies of the Ground and Excited Electronic States in Cyclometalated Phenylpyridine Ir(III) Complexes Using Density Functional Theory. *J. Phys. Chem. A* **2002**, *106* (8), 1634−1641.

(43) Petit, L.; Adamo, C.; Russo, N. Absorption Spectra of First-Row Transition Metal Complexes of Bacteriochlorins: A Theoretical Analysis. *J. Phys. Chem. B* **2005**, *109* (24), 12214−12221.

(44) Andruniów, T.; Jaworska, M.; Lodowski, P.; Zgierski, M. Z.; Dreos, R.; Randaccio, L.; Kozlowski, P. M. Time-dependent density functional theory study of cobalt corrinoids: Electronically excited states of methylcobalamin. *J. Chem. Phys.* **2008**, *129* (8), 085101.

(45) Pastore, M.; Mosconi, E.; De Angelis, F.; Grätzel, M. A Computational Investigation of Organic Dyes for Dye-Sensitized Solar Cells: Benchmark, Strategies, and Open Issues. *J. Phys. Chem. C* **2010**, *114* (15), 7205−7212.

(46) Marian, C. M.; Heil, A.; Kleinschmidt, M. The DFT/MRCI method. *Wiley Interdiscip. Rev.: Comput. Mol. Sci.* **2019**, *9* (2), No. e1394.

(47) Grimme, S.; Waletzke, M. A combination of Kohn-Sham density functional theory and multi-reference configuration interaction methods. *J. Chem. Phys.* **1999**, *111* (13), 5645−5655.

(48) Kleinschmidt, M.; Marian, C. M.; Waletzke, M.; Grimme, S. Parallel multireference configuration interaction calculations on mini-β-carotenes and β-carotene. *J. Chem. Phys.* **2009**, *130* (4), 044708.

(49) Lyskov, I.; Kleinschmidt, M.; Marian, C. M. Redesign of the DFT/MRCI Hamiltonian. *J. Chem. Phys.* **2016**, *144* (3), 034104.

(50) Heil, A.; Marian, C. M. DFT/MRCI Hamiltonian for odd and even numbers of electrons. *J. Chem. Phys.* **2017**, *147* (19), 194104.

(51) Heil, A.; Kleinschmidt, M.; Marian, C. M. On the performance of DFT/MRCI Hamiltonians for electronic excitations in transition metal complexes: The role of the damping function. *J. Chem. Phys.* **2018**, *149* (16), 164106.

(52) Neese, F. Prediction of molecular properties and molecular spectroscopy with density functional theory: From fundamental theory to exchange-coupling. *Coord. Chem. Rev.* **2009**, *253* (5−6), 526−563.

(53) Lee, C. H.; Dogutan, D. K.; Nocera, D. G. Hydrogen generation by hangman metalloporphyrins. *J. Am. Chem. Soc.* **2011**, *133* (23), 8775−8777.

(54) Hammes-Schiffer, S. Proton-Coupled Electron Transfer: Moving Together and Charging Forward. *J. Am. Chem. Soc.* **2015**, *137* (28), 8860−8871.

(55) Solis, B. H.; Hammes-Schiffer, S. Proton-coupled electron transfer in molecular electrocatalysis: theoretical methods and design principles. *Inorg. Chem.* **2014**, *53* (13), 6427–6443.

(56) Henry, R. M.; Shoemaker, R. K.; DuBois, D. L.; DuBois, M. R. Pendant Bases as Proton Relays in Iron Hydride and Dihydrogen Complexes. *J. Am. Chem. Soc.* **2006**, *128* (9), 3002–3010.

(57) Lu, Y.-C.; He, Q.; Gasteiger, H. A. Probing the Lithium-Sulfur Redox Reactions: A Rotating-Ring Disk Electrode Study. *J. Phys. Chem. C* **2014**, *118* (11), 5733–5741.

(58) Frisch, M. J.; Trucks, G. W.; Schlegel, H. B.; Scuseria, G. E.; Robb, M. A.; Cheeseman, J. R.; Scalmani, G.; Barone, V.; Petersson, G. A.; Nakatsuji, H.; Li, X.; Caricato, M.; Marenich, A. V.; Bloino, J.; Janesko, B. G.; Gomperts, R.; Mennucci, B.; Hratchian, H. P.; Ortiz, J. V.; Izmaylov, A. F.; Sonnenberg, J. L.; Ding, F.; Lipparini, F.; Egidi, F.; Goings, J.; Peng, B.; Petrone, A.; Henderson, T.; Ranasinghe, D.; Zakrzewski, V. G.; Gao, J.; Rega, N.; Zheng, G.; Liang, W.; Hada, M.; Ehara, M.; Toyota, K.; Fukuda, R.; Hasegawa, J.; Ishida, M.; Nakajima, T.; Honda, Y.; Kitao, O.; Nakai, H.; Vreven, T.; Throssell, K.; Montgomery, J. A., Jr.; Peralta, J. E.; Ogliaro, F.; Bearpark, M. J.; Heyd, J. J.; Brothers, E. N.; Kudin, K. N.; Staroverov, V. N.; Keith, T. A.; Kobayashi, R.; Normand, J.; Raghavachari, K.; Rendell, A. P.; Burant, J. C.; Iyengar, S. S.; Tomasi, J.; Cossi, M.; Millam, J. M.; Klene, M.; Adamo, C.; Cammi, R.; Ochterski, J. W.; Martin, R. L.; Morokuma, K.; Farkas, O.; Foresman, J. B.; Fox, D. J. *Gaussian 16*, rev. C.01; Gaussian Inc.: Wallingford, CT, 2016.

(59) Yanai, T.; Tew, D. P.; Handy, N. C. A new hybrid exchange-correlation functional using the Coulomb-attenuating method (CAM-B3LYP). *Chem. Phys. Lett.* **2004**, *393* (1), 51–57.

(60) Hehre, W. J.; Ditchfield, R.; Pople, J. A. Self—Consistent Molecular Orbital Methods. XII. Further Extensions of Gaussian—Type Basis Sets for Use in Molecular Orbital Studies of Organic Molecules. *J. Chem. Phys.* **1972**, *56* (5), 2257–2261.

(61) Hariharan, P. C.; Pople, J. A. The influence of polarization functions on molecular orbital hydrogenation energies. *Theoret. Chim. Acta* **1973**, *28* (3), 213–222.

(62) Clark, T.; Chandrasekhar, J.; Spitznagel, G. W.; Schleyer, P. V. R. Efficient diffuse function-augmented basis sets for anion calculations. III. The 3-21+G basis set for first-row elements, Li-F. *J. Comput. Chem.* **1983**, *4* (3), 294–301.

(63) Hay, P. J.; Wadt, W. R. Ab initio effective core potentials for molecular calculations. Potentials for K to Au including the outermost core orbitals. *J. Chem. Phys.* **1985**, *82* (1), 299–310.

(64) Tomasi, J.; Mennucci, B.; Cammi, R. Quantum Mechanical Continuum Solvation Models. *Chem. Rev.* **2005**, *105* (8), 2999–3094.

(65) Neese, F. The ORCA program system. *Wiley Interdiscip. Rev.: Comput. Mol. Sci.* **2012**, *2* (1), 73–78.

(66) Neese, F. Approximate second-order SCF convergence for spin unrestricted wavefunctions. *Chem. Phys. Lett.* **2000**, *325* (1), 93–98.

(67) Lee, C.; Yang, W.; Parr, R. G. Development of the Colle-Salvetti correlation-energy formula into a functional of the electron density. *Phys. Rev. B: Condens. Matter Mater. Phys.* **1988**, *37* (2), 785–789.

(68) Becke, A. D. A new mixing of Hartree-Fock and local density-functional theories. *J. Chem. Phys.* **1993**, *98* (2), 1372–1377.

(69) Weigend, F.; Ahlrichs, R. Balanced basis sets of split valence, triple zeta valence and quadruple zeta valence quality for H to Rn: Design and assessment of accuracy. *Phys. Chem. Chem. Phys.* **2005**, *7* (18), 3297–3305.

(70) Rappoport, D.; Furche, F. Property-optimized Gaussian basis sets for molecular response calculations. *J. Chem. Phys.* **2010**, *133* (13), 134105.

(71) Hellweg, A.; Rappoport, D. Development of new auxiliary basis functions of the Karlsruhe segmented contracted basis sets including diffuse basis functions (def2-SVPD, def2-TZVPPD, and def2-QVPPD) for RI-MP2 and RI-CC calculations. *Phys. Chem. Chem. Phys.* **2015**, *17* (2), 1010–1017.

(72) Weigend, F. Hartree-Fock exchange fitting basis sets for H to Rn †. *J. Comput. Chem.* **2008**, *29* (2), 167–175.

(73) Weigend, F.; Kattannek, M.; Ahlrichs, R. Approximated electron repulsion integrals: Cholesky decomposition versus resolution of the identity methods. *J. Chem. Phys.* **2009**, *130* (16), 164106.

(74) Kossmann, S.; Neese, F. Comparison of two efficient approximate Hartee-Fock approaches. *Chem. Phys. Lett.* **2009**, *481* (4), 240–243.

(75) Barone, V.; Cossi, M. Quantum Calculation of Molecular Energies and Energy Gradients in Solution by a Conductor Solvent Model. *J. Phys. Chem. A* **1998**, *102* (11), 1995–2001.

(76) Neese, F. Importance of Direct Spin-Spin Coupling and Spin-Flip Excitations for the Zero-Field Splittings of Transition Metal Complexes: A Case Study. *J. Am. Chem. Soc.* **2006**, *128* (31), 10213–10222.

(77) Humphrey, W.; Dalke, A.; Schulten, K. VMD: Visual molecular dynamics. *J. Mol. Graphics* **1996**, *14* (1), 33–38.

Supporting Information

H₂ evolution from electrocatalysts with redox-active ligands: Mechanistic insights from theory and experiment vis-à-vis Co-Mabiq

G. Ceren Tok, ‖ ,† Sebastian Reiter, ‖ ,‡ Anna T. S. Freiberg, §,† Leonhard Reinschlüssel,†
Hubert A. Gasteiger,† Regina de Vivie-Riedle*,‡ and Corinna R. Hess*,†

† Department of Chemistry and Catalysis Research Center, Technical University of Munich,
Lichtenbergstr. 4, 85748 Garching, Germany

‡ Department of Chemistry, Ludwig-Maximilians-Universität München, Butenandtstr. 5-13,
81377 München, Germany

Corresponding authors: Regina de Vivie-Riedle (Regina.de_Vivie@cup.uni-muenchen.de),
Corinna R. Hess (corinna.hess@ch.tum.de)

Index

pH-dependent potential correction

The CV data of 0.2 mM Co_{Mbq} in the presence of 2 mM *para*-cyanoanilinium (pCA, pK_a:7.0 in acetonitrile) and *para*-Br-anilinium (pBrA, pK_a: 9.43 in acetonitrile) exhibit a 150 mV potential difference with respect to the onset of the pre-catalytic step. To determine the agreement between theoretical and experimental values, the pK_a values of pCA and pBrA were converted to pH (Table S1) and the potential shift determined according to Eq S1, Eq S2 and Eq 3.

$$E = E^0 + \frac{2.3RT}{zF} \log \frac{[ox]}{[red]} \qquad Eq\ S1$$

According to the Nernst equation given above, where:

R = gas constant, 8.314 J K^{-1} mol^{-1}

T = temperature in Kelvin, 298.15 K

Z = number of electrons transferred, 1 electron (assumed)

F = Faraday constant, 96485.33 C mol^{-1}

In the presence of pCA and pBrA:

$$\left(Co^{II}(Mabiq)\right)^+ + e^- + H^+ \underset{K_{eq}}{\longleftrightarrow} (Co^{II}(Mabiq) - H)^+$$

$$(Co^{II}(Mabiq) - H)^+ + e^- \rightarrow (Co(Mabiq) - H)^0$$
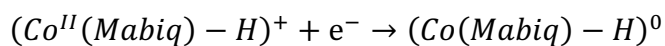
$$E = E^0 + \frac{2.3RT}{zF} \log \frac{[(Co^{II}(Mabiq) - H)^+]}{[(Co(Mabiq) - H)^0]}$$

$$K_{eq} = \frac{[(Co^{II}(Mabiq) - H)^+]}{[(Co^{II}(Mabiq))^+][H^+]}$$

$$HA \underset{K_a}{\longleftrightarrow} H^+ + A^-$$
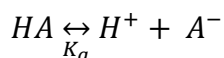
$$K_a = \frac{[H^+][A^-]}{[HA]}$$

$$E = E^0 + \frac{2.3RT}{zF} \log \frac{K_{eq}K_a[(Co^{II}(Mabiq))^+][HA]}{[A^-][(Co(Mabiq)-H)^0]} \qquad Eq\ S1.1$$

In the presence of *p*An:

$$\left(Co^{II}(Mabiq)\right)^+ + e^- \rightarrow (Co^{II}(Mabiq\ \bullet))^0$$

$$(Co^{II}(Mabiq\ \bullet))^0 + e^- + H^+ \underset{K_{eq}}{\longleftrightarrow} (Co(Mabiq\ \bullet)-H)^0$$

$$E = E^0 + \frac{2.3RT}{zF} \log \frac{[(Co^{II}(Mabiq))^+]}{[(Co^{II}(Mabiq\ \bullet))^0]}$$

$$K_{eq} = \frac{[(Co(Mabiq\ \bullet)-H)^0]}{[(Co^{II}(Mabiq\ \bullet))^0][H^+]}$$

$$E = E^0 + \frac{2.3RT}{zF} \log \frac{K_{eq}K_a[(Co^{II}(Mabiq))^+][HA]}{[A^-][((Co(Mabiq\ \bullet)-H)^0]}$$

The concentration of [Co^{II}(Mabiq)]$^+$ (*Co$_{Mbq}$*) is known, however, the protonation of the various sites is affected by the acid strength; i.e., the concentrations of the intermediates [Co^{II}(Mabiq)-H]$^+$, [Co^{II}(Mabiq$\bullet$)]^0 and [Co(Mabiq$\bullet$)-H]^0 are not the same in each acidic media, and the equilibrium constant in each acidic media is not known. The extended Nernst equation shown as *Eq S*1.1[1] can therefore not be solved.

If we assume the potential shift follows the Nernst law simply on the basis of a change in acid strength, then based on the Nernst Equation (Eq S1), the formal potential varies 59 mV with each pH unit at 25°C (Eq S2):

$$E = E^0 + \frac{2.3RT}{zF} \log[H^+], \qquad \frac{2.3RT}{zF} = 59\ mV \qquad Eq\ S2$$

$$K_a = 10^{-pKa} = \frac{[H^+][A^-]}{[HA]} \quad , \quad [HA] = 2mM, \quad [H^+] = [A^-] \qquad Eq\ S3$$

$$pH = -\log([H^+])$$

The pH difference corresponds to 1.21 pH units between pCA and pBrA, and between pBrA and pAn, leading to a ~70 mV theoretical potential shift between each pair of acidic media for the pre-catalytic step, if we assume the theoretical potential shift to be independent of the equilibrium constant, kinetic and solvent effect. This is seen to be a lower limit of the expected thermodynamic potential shift. When comparing the CV data of the Co_{Mbq} complex in the presence of pCA vs. pBrA, the equilibrium constant K_{eq} will be lower in the case of pBrA, which can be concluded from the formation enthalpies of the cationic (Co_{Mbq}-H^{DKI})$^+$ and (Co_{Mbq}-H^{Im})$^+$ intermediates shown in Table 1 of the main paper. However, we note that the equilibrium constant of the protonation reaction plays a significant role in the calculated theoretical potential difference.[1] Ligand protonation can occur at different ligand sites, and is dependent on the acid strength and basicity of the various ligand functionalities. Therefore, the equilibrium constant can change significantly for different acids, meaning that the exact theoretical potential shift cannot be calculated in our system. Potential-pK_a diagrams for non-aqueous systems[2] also offer an option to determine theoretical potentials. Since we do not know the pK_a values of the multiple intermediates, which are essential to this method, we instead used the approach described above.

Table S1. Calculated K_a, concentration ([H+]) and pH values of pCA, pBrA and pAn

	pCA	pBrA	pAn
K_a	$1x10^{-7}$	$3.72x10^{-10}$	$1.38x10^{-12}$
[H+]	$1.4x10^{-5}$	$8.62x10^{-7}$	$5.25x10^{-8}$
pH	4.85	6.06	7.28

Current response of the pre-catalytic step after the bulk electrolysis

The current magnitude of the pre-catalytic processes following bulk electrolysis differs for *p*CA and *p*BrA. The pre-catalytic steps in *p*CA and *p*BrA show the same initial current (25 μA), however, the remnant pre-catalytic current after bulk electrolysis is two times greater for the Co/*p*BrA solution (15 μA) than observed for the Co/*p*CA solution (8 μA). The remnant amount of ***Co$_{Mbq}$*** present after bulk electrolysis of the *p*CA or *p*BrA solutions (based on percent conversion), appears to correlate with the remaining pre-catalytic current, such that the pre-catalytic reactions appear to be predominantly available from ***Co$_{Mbq}$***; i.e. the conversion between ***Co$_{Mbq}$-H^2*** and ***Co$_{Mbq}$*** may not be fully reversible on the time scale of a CV.

*CVs of **Co$_{Mbq}$** with varied p-anisidinium concentrations*

The CV data for 0.2 mM ***Co$_{Mbq}$*** with 2 mM *p*-anisidinium (*p*An, pK_a:11.86 in acetonitrile) suggests a different mechanism (EEC) for the pre-catalytic step. In order to determine which reduction step is proton dependent, varied equivalents of *p*An were added. The recorded CV data show that the reduction potential matching the $[Co^{II}(Mabiq)]^+/[Co^{II}(Mabiq\bullet)]^0$ couple does not shift with increasing acid concentration, hence, this reduction event is not proton dependent. For the following reduction step, the potentials shift from -0.969 V$_{Fc}$ to -0.91 V$_{Fc}$ with increasing acid concentration from 2 mM to 16 mM *p*An (Figure S1). The theoretical potential shifts were further calculated based on the Nernst equation (Eq S4) to confirm the agreement between calculated and experimental results.
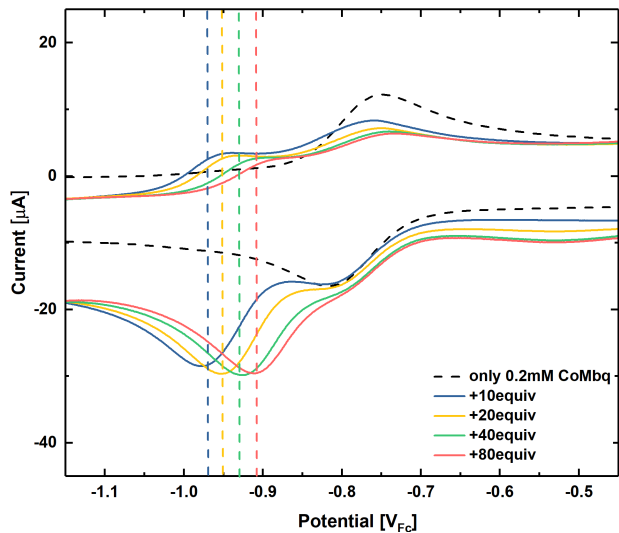
Figure S1: CVs of 0.2 mM **_Co_**_Mbq_ in the absence of acid (dashed black line) and with 2 mM (solid blue trace), 4 mM (solid yellow trace), 8 mM (solid green trace), and 16 mM (solid pink trace) _p_An in 0.1 M LiBF$_4$/MeCN; glassy carbon electrode; 100 mV/s scan rate, in a RDE set-up.

$$[Co^{II}(Mabiq \bullet)]^{0} + e^{-} + H^{+} \rightarrow [Co(Mabiq) - H]^{0}$$
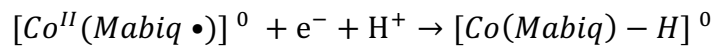
$$E = E^{0} - \frac{RT}{zF} \ln \frac{[red]}{[ox]} \qquad Eq\ S4$$

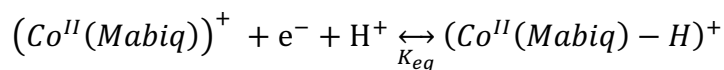According to the Nernst equation given above, where:

R = gas constant, 8.314 J K^{-1} mol^{-1}

T = temperature in Kelvin, 298.15 K

Z = number of electrons transferred, 1 electron (assumed)

F = Faraday constant, 96485.33 C mol^{-1}

The potential difference for a proton dependent process is given by:

$$\Delta E_{[p-anisidinium_2]-[p-anisidinium_1]} = -\frac{RT}{zF} \ln\left\{\frac{[red_2]}{[ox_2]}\frac{[ox_1]}{[red_1]}\right\},$$

$$[p - anisidinium_2] > [p - anisidinium_1]$$

$$[ox_1] = [p - anisidinium_1][[Co^{II}(Mabiq\bullet)]^0]$$

$$[ox_2] = [p - anisidinium_2][[Co^{II}(Mabiq\bullet)]^0]$$

$$[red_1] = [red_2] = [[Co(Mabiq) - H]^0]$$

The concentration of pAn is known and we assume that the concentration of $[Co^{II}(Mabiq\bullet)]^0$ and the reduced species also is the same at each acid concentration. Hence, the following equation applies:

$$\Delta E_{[p-anisidinium_2]-[p-anisidinium_1]} = -\frac{RT}{zF} \ln\left\{\frac{[ox_1]}{[ox_2]}\right\}$$

If all assumptions are correct, the potential shifts calculated between 2 mM and 4 mM p-anisidinium, 2 mM and 8 mM p-anisidinium, 2 mM and 16 mM p-anisidinium are ~18, 36 and 54 mV respectively.

In Figure S1, the reduction peak potential ($E_{p,c}$) in the presence of 2 mM p-anisidinium (vertical dashed blue line) represents the reference potential. The vertical dashed yellow, green and pink lines indicate the calculated potential differences between 2 mM and 4 mM pAn, 2 mM and 8 mM pAn, 2 mM and 16 mM pAn. The theoretical and experimental potential differences are in agreement, indicating that the second reduction is proton dependent. To summarize, the first reduction is only an electrochemical reaction (E) and the second reduction involves an electrochemical reduction followed by a chemical reaction (EC), thus the reaction mechanism prior to the HER is different than in the Co/pCA case.

Structural distortions upon protonation of [Co^{II}(Mabiq$^{\cdot}$)]^0
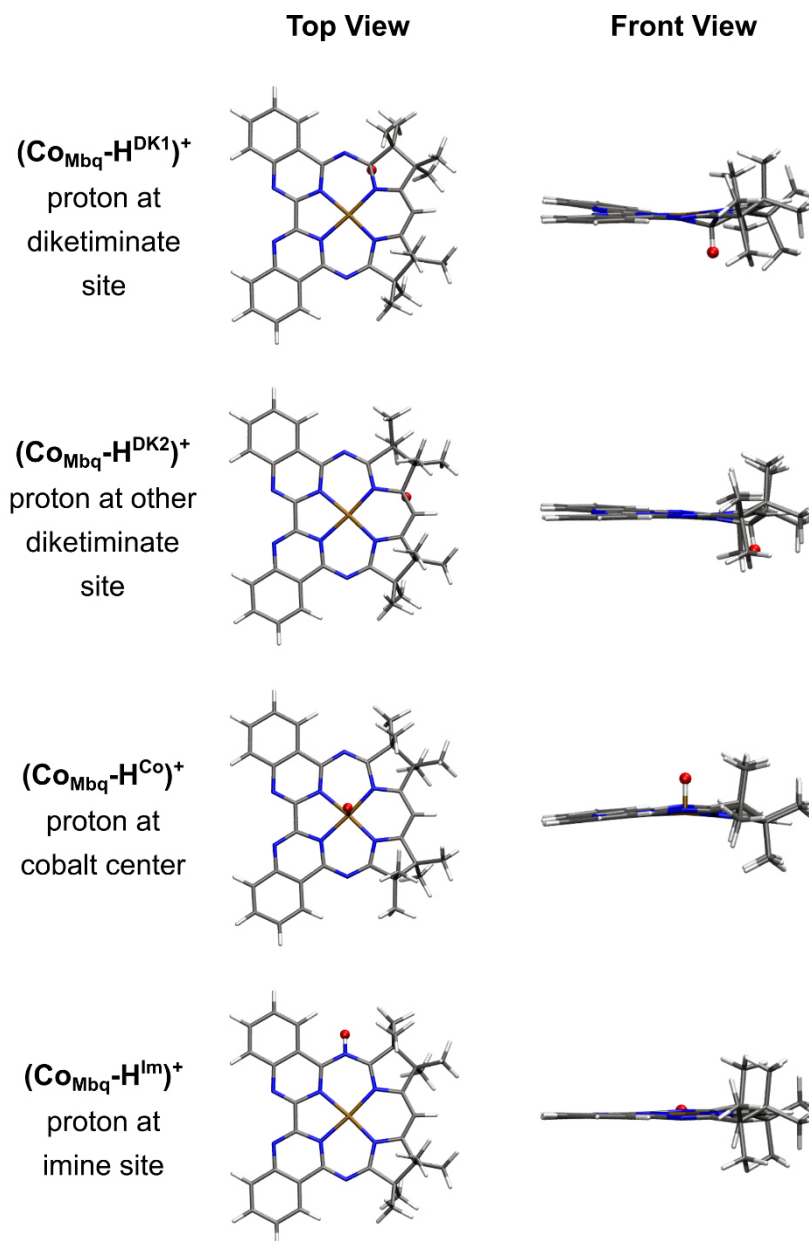
Figure S2: Optimized structures of possible intermediates after the protonation step, depicted in top and side views of the molecule. Cobalt is depicted in ocher, carbon in grey, nitrogen in blue, hydrogen in white. The added proton is marked in red. Protonation at both diketiminate sites leads to strong distortion from the planar geometry and breaking of ligand aromaticity. Protonation at the cobalt center only causes slight pyramidalization and the imine product remains planar.

TD-DFT absorption spectrum of [Co^{II}(Mabiq$^{\cdot}$)]^0

In our early tests, we calculated a TD-DFT absorption spectrum for the [Co^{II}(Mabiq$^{\cdot}$)] complex using the same level of theory that was used for optimization (see Computational Details in the main article). The only difference at this early stage was that both the geometry optimization and the TD-DFT calculation was conducted in the gas phase without solvation effects.
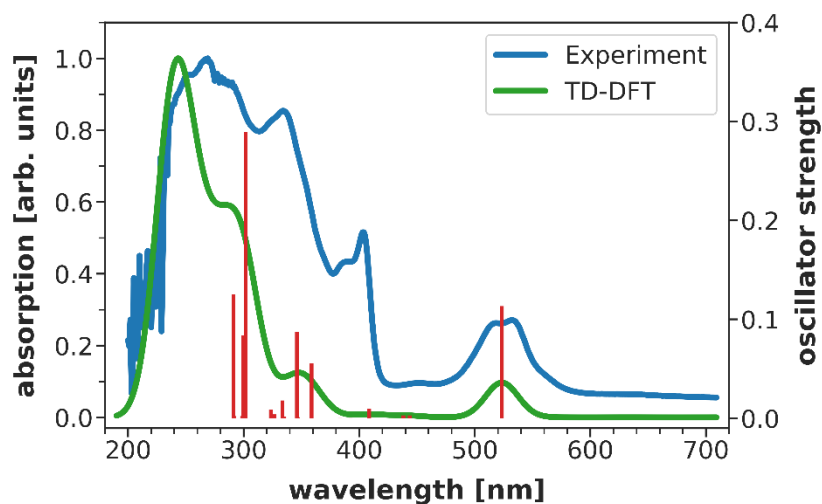
Figure S3: TD-DFT absorption spectrum of [Co^{II}(Mabiq$^{\cdot}$)] in comparison to the experimental spectrum. The line spectrum was convoluted with an FWHM of 0.24 eV and the convoluted spectrum was scaled such that the highest absorption is 1. Note that the experimental band at 411 nm cannot be assigned unambiguously in the TD-DFT spectrum. The double peak structure of the band around 520 nm is also not reproduced in the calculation.

DFT/MRCI spectrum of $(Co_{Mbq}\text{-}H^{Im})^+$
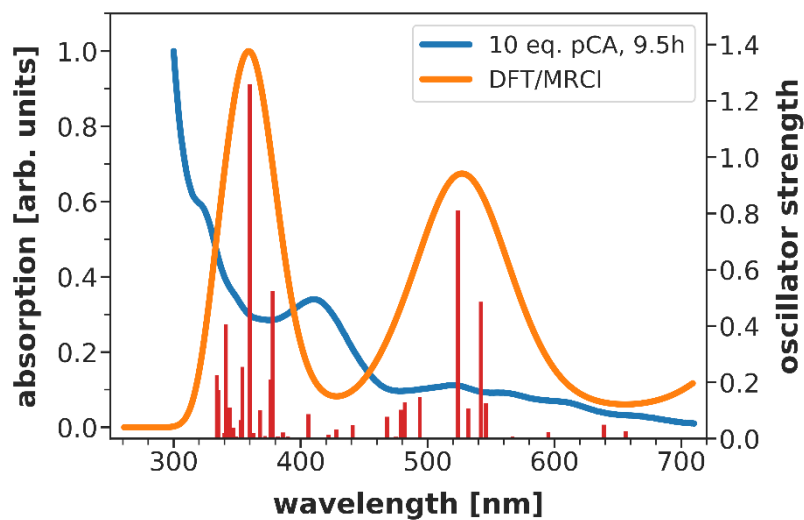
Figure S4: DFT/MRCI absorption spectrum for the cation $(Co_{Mbq}\text{-}H^{Im})^+$, where the proton attaches

to one of the imine sites of the ligand.

Spin densities of cationic and reduced intermediate species
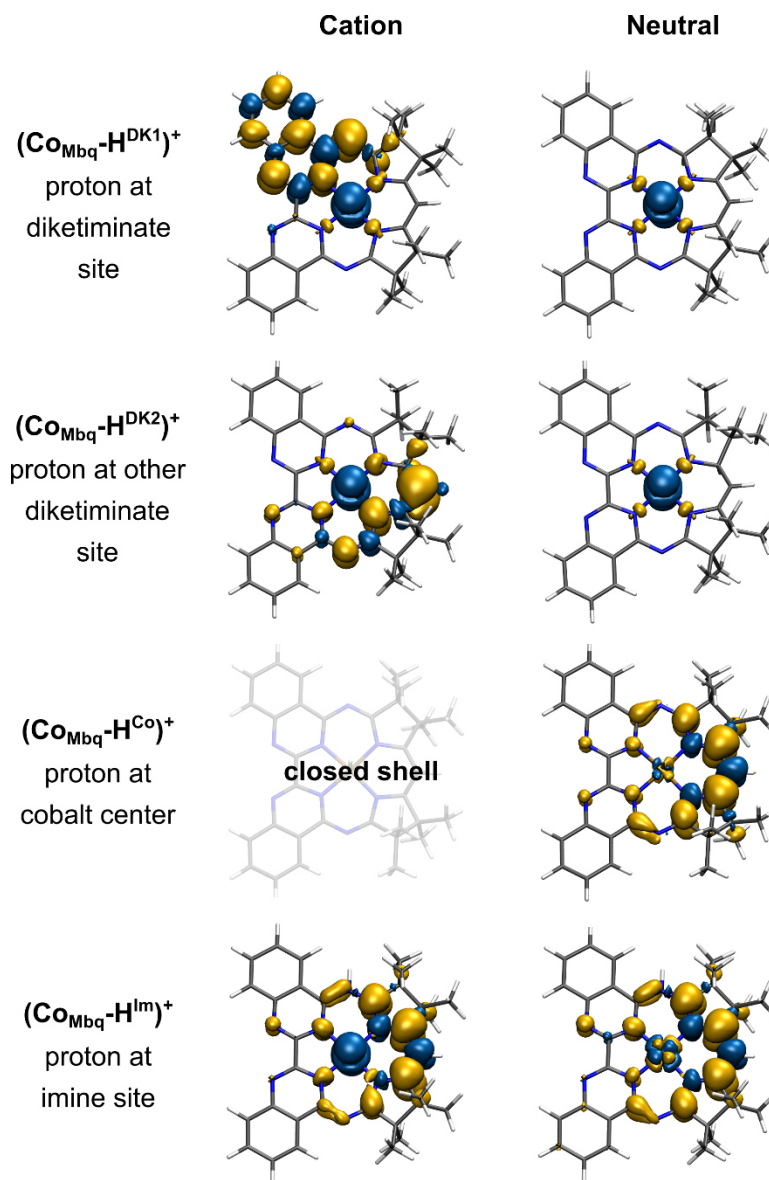
Figure S5: Broken-symmetry DFT spin densities, i.e. difference between alpha- and beta-electron densities, of the optimized cationic (1-electron-1-proton) and reduced (2-electron-1-proton) intermediates (Isovalue=0.002). Reduction happens where the unpaired spin-density changes from the cation to the neutral species. Thus, the second electron is added to the ligand, if the proton attaches to either of the diketiminate sites or the cobalt center, whereas reduction occurs on the metal if the proton attaches to the imine site.
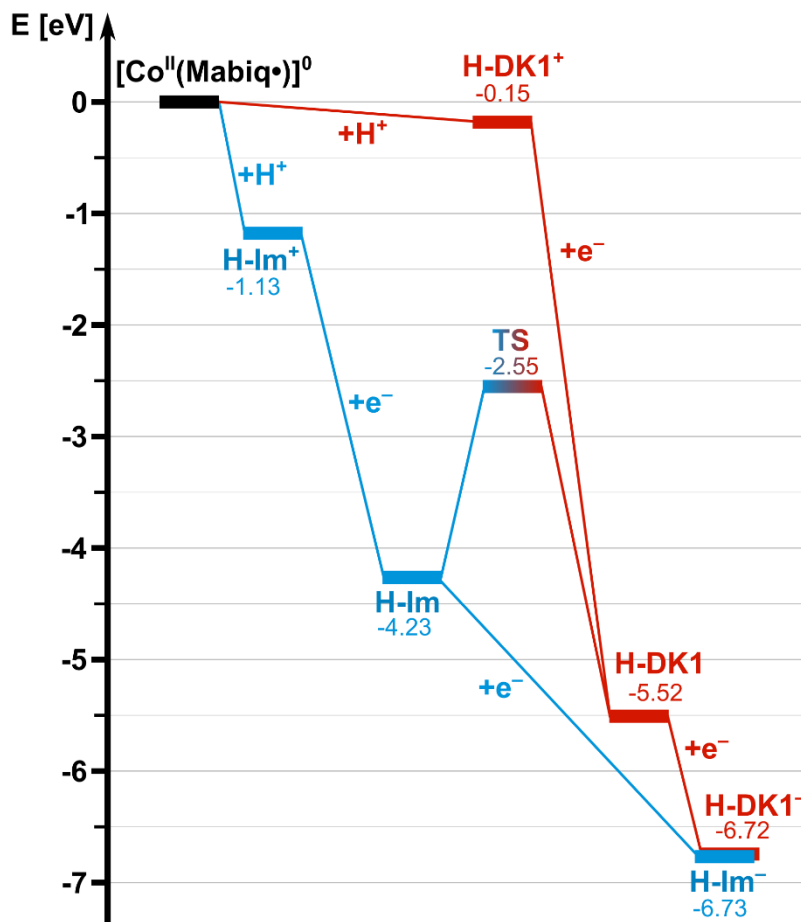
Figure S6: Calculated Gibbs free energy levels of DFT optimized intermediates, relative to $[Co^{II}(Mabiq^{\bullet})]^{0}$. Energies of protonation steps include the acid contributions (cf. Eq 2 in the main article). Reduction energies are given for the respective half-reaction. For brevity, the notations H-DK1 and H-Im are used to denote $\boldsymbol{Co_{Mbq}\text{-}H^{DK1}}$ and $\boldsymbol{Co_{Mbq}\text{-}H^{Im}}$. TS is the transition state for interconversion between the two species.

Electrostatic potentials and selected atomic charges of $(Co_{Mbq}\text{-}H_2^{Im,Co})^+$ and $Co_{Mbq}\text{-}H_2^{Im,Co}$

The charge distribution of the doubly protonated complexes can provide insights into the reactivity towards hydrogen evolution. There are different ways to obtain atomic charges from quantum chemical calculations. In this work, we chose to inspect the electrostatic potential (ESP) rather than common population analyses as it reflects the actual charge distribution in the complex without resorting to arbitrary electron localization schemes. Merz-Singh-Kollman charges[3] (Table S2) are derived from the ESP by fitting the potential at various points in space.
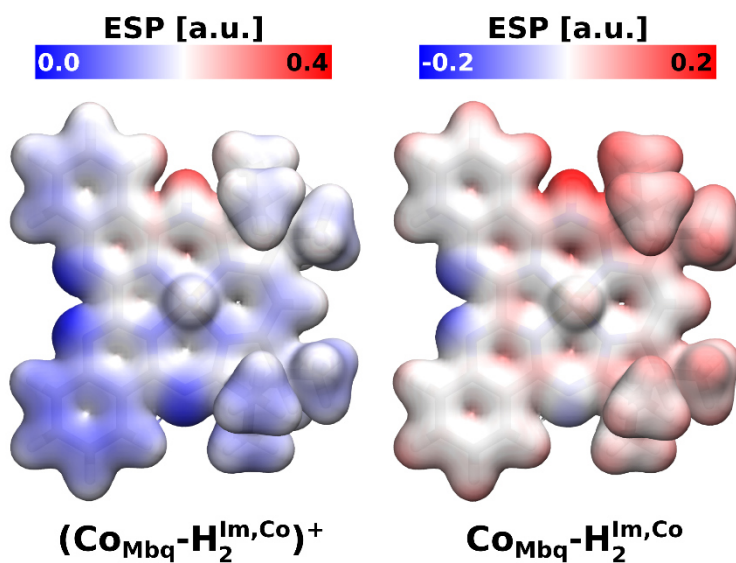
Figure S7: Broken-symmetry DFT derived Electrostatic potential (ESP) of *$(Co_{Mbq}\text{-}H_2^{Im,Co})^+$* and its reduced form *$Co_{Mbq}\text{-}H_2^{Im,Co}$*, mapped onto a surface plot of the electron density (Isovalue: 0.02). The Co-bound proton carries a visibly smaller positive charge than the other protons in the complex.

Table S2: Selected Merz-Singh-Kollman charges, derived from broken-symmetry DFT, for the intermediate species along the two possible pathways starting from *(Co$_{Mbq}$-H^{Im})$^+$* and *(Co$_{Mbq}$-H^{DK1})$^+$*.

	Co	*Co-bound H*
(Co$_{Mbq}$-H^{Im})$^+$	1.16	/
Co$_{Mbq}$-H^{Im}	0.18	/
(Co$_{Mbq}$-H^{Im})$^-$	0.01	/
(Co$_{Mbq}$-H$_2$^{Im,Co})$^+$	1.20	-0.14
Co$_{Mbq}$-H$_2$^{Im,Co}	1.21	-0.17
(Co$_{Mbq}$-H^{DK1})$^+$	1.18	/
Co$_{Mbq}$-H^{DK1}	1.15	/
(Co$_{Mbq}$-H^{DK1})$^-$	0.52	/
Co$_{Mbq}$-H$_2$^{DK1,Im}	0.53	/

Cartesian coordinates and energies of optimized geometries

Table S3 lists the SCF energies E^{SCF}, enthalpies H (Gaussian Output: *Sum of electronic and thermal Enthalpies*) and Gibbs free energies G (Gaussian Output: *Sum of electronic and thermal Free Energies*) of the DFT optimized geometries. The Cartesian coordinates are compiled on the following pages.

Table S3: Charge, spin multiplicity, SCF energies E^{SCF}, enthalpies H and Gibbs free energies G of optimized geometries.

Species	Charge	Multiplicity	E^{SCF} (E_h)	H (E_h)	G (E_h)
pCA	1	1	-380.091264	-379.949961	-379.990478
D-pCA	0	1	-379.671408	-379.545770	-379.586008
[Co^{II}(Mabiq•)]^0	0	1	-1859.692794	-1859.038305	-1859.136648
(Co$_{Mbq}$-H^{DK1})$^+$	1	1	-1860.114199	-1859.448828	-1859.546706
(Co$_{Mbq}$-H^{DK2})$^+$	1	1	-1860.119786	-1859.453626	-1859.551293
(Co$_{Mbq}$-H^{Co})$^+$	1	1	-1860.123039	-1859.458900	-1859.557196
(Co$_{Mbq}$-H^{Im})$^+$	1	1	-1860.150164	-1859.483461	-1859.582583
Co$_{Mbq}$-H^{DK1}	0	2	-1860.311779	-1859.645479	-1859.743799
Co$_{Mbq}$-H^{DK2}	0	2	-1860.319865	-1859.653614	-1859.752064
Co$_{Mbq}$-H^{Co}	0	2	-1860.255891	-1859.594802	-1859.694555
Co$_{Mbq}$-H^{Im}	0	2	-1860.262527	-1859.597357	-1859.696523
(Co$_{Mbq}$-H^{DK1})$^-$	-1	1	-1860.354755	-1859.690039	-1859.787915
(Co$_{Mbq}$-H^{Im})$^-$	-1	1	-1860.353736	-1859.688750	-1859.788357
(Co$_{Mbq}$-H$_2^{Im,Co}$)$^+$	1	2	-1860.698986	-1860.023402	-1860.122443
Co$_{Mbq}$-H$_2^{Im,Co}$	0	1	-1860.815777	-1860.143616	-1860.243379
Co$_{Mbq}$-H$_2^{DK1,Im}$	0	1	-1860.886272	-1860.208529	-1860.306596
Transition state Co$_{Mbq}$-H^{Im} → Co$_{Mbq}$-H^{DK1}	0	2	-1860.196014	-1859.536157	-1859.634925

D-pCA

atom	x [Å]	y [Å]	z [Å]
C	-1.711629	0.000016	-0.005293
C	-0.994899	-1.210620	-0.004719
C	0.386908	-1.210177	-0.002258
C	1.095969	0.000027	-0.000981
C	0.386928	1.210201	-0.002310
C	-0.994911	1.210641	-0.004698
H	-1.534467	-2.152957	-0.007751
H	0.925725	-2.152069	0.000320
H	0.925700	2.152119	0.000331
H	-1.534442	2.152996	-0.007763
C	2.524854	-0.000013	0.003913
N	3.684854	-0.000031	0.008117
H	-3.565502	-0.846059	0.222489
H	-3.565544	0.845882	0.222804
N	-3.086396	-0.000020	-0.055596
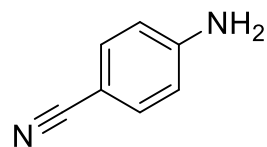
pCA

atom	x [Å]	y [Å]	z [Å]
C	1.603252	0.000229	-0.000073
C	0.939387	-1.214739	-0.000107
C	-0.449439	-1.214858	-0.000070
C	-1.138776	-0.000250	-0.000054
C	-0.447724	1.215923	-0.000094
C	0.939353	1.217923	-0.000097
H	1.483668	-2.153041	-0.000176
H	-0.991418	-2.153265	-0.000052
H	-0.991217	2.153495	-0.000099
H	1.484554	2.155815	-0.000075
C	-2.576320	-0.000199	0.000041
N	-3.733090	-0.000794	0.000162
H	3.453572	-0.955464	-0.000146
H	3.465153	0.470747	-0.826142
H	3.464817	0.470053	0.827050
N	3.077728	-0.000993	0.000175
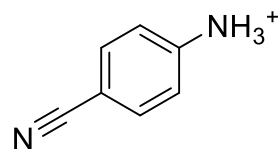
[Co^{II}(Mabiq•)]^0

atom	x [Å]	y [Å]	z [Å]
Co	0.000008	-0.105696	0.021013
N	-1.285423	1.309363	0.043200
N	1.285282	1.309531	0.043228
N	1.368126	-1.411774	-0.021733
N	-1.367933	-1.411937	-0.022404
N	-1.385538	3.695020	-0.070225
N	1.385120	3.695111	-0.071946
N	3.279561	0.028200	0.165989
N	-3.279595	0.027753	0.165216
C	-0.743114	2.571036	-0.018866
C	0.742823	2.571103	-0.019339
C	2.752783	3.637608	-0.063157
C	3.493959	4.837308	-0.126881
C	4.868834	4.793728	-0.115795
C	5.544345	3.556318	-0.039493
C	4.836234	2.377656	0.023772
C	3.425262	2.401894	0.011505
C	2.618921	1.209046	0.069153
C	2.700380	-1.132512	0.132394
C	3.512001	-2.399531	0.341080
C	2.560481	-3.460692	-0.294965
C	1.225006	-2.748006	-0.157641
C	0.000282	-3.389917	-0.236193
C	-1.224556	-2.748114	-0.158699
C	-2.559850	-3.460839	-0.297527
C	-3.511994	-2.400108	0.338282
C	-2.700300	-1.132890	0.131014
C	-2.619043	1.208729	0.069380
C	-3.425525	2.401554	0.012981
C	-4.836486	2.377173	0.025730
C	-5.544731	3.555831	-0.036191
C	-4.869367	4.793371	-0.111595
C	-3.494498	4.837088	-0.123148
C	-2.753194	3.637398	-0.060822
C	3.642664	-2.582410	1.868668
C	4.913290	-2.331269	-0.262436
C	2.607048	-4.839656	0.366851
C	2.824608	-3.635244	-1.806662
C	-2.606908	-4.840176	0.363469
C	-2.822647	-3.634575	-1.809561
C	-3.643953	-2.583885	1.865649
C	-4.912765	-2.331587	-0.266398
H	2.953742	5.776683	-0.183812
H	5.440997	5.715043	-0.165032
H	6.629579	3.537266	-0.030359
H	5.341510	1.421517	0.083267
H	0.000383	-4.465291	-0.362599
H	-5.341656	1.420936	0.084538
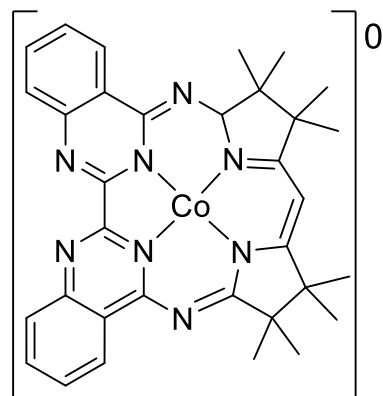
H	-6.629959	3.536668	-0.026687
H	-5.441631	5.714679	-0.159791
H	-2.954386	5.776562	-0.179442
H	2.668413	-2.665282	2.360372
H	4.222000	-3.481016	2.099694
H	4.166254	-1.721664	2.294578
H	4.901844	-2.051334	-1.318174
H	5.411320	-3.302382	-0.168155
H	5.513486	-1.590348	0.271212
H	3.631808	-5.225828	0.353211
H	1.986119	-5.554499	-0.181176
H	2.262491	-4.820837	1.403276
H	3.785528	-4.130619	-1.974207
H	2.042104	-4.257312	-2.251234
H	2.834042	-2.677224	-2.335537
H	-1.985425	-5.554660	-0.184395
H	-2.263311	-4.821925	1.400224
H	-3.631627	-5.226414	0.348664
H	-2.831772	-2.676255	-2.337899
H	-3.783345	-4.130003	-1.978212
H	-2.039661	-4.256269	-2.253807
H	-2.670113	-2.666945	2.358138
H	-4.223397	-3.482680	2.095665
H	-4.167985	-1.723433	2.291607
H	-5.513433	-1.590941	0.267103
H	-4.900432	-2.051131	-1.321989
H	-5.410851	-3.302760	-0.173031

(Co_{Mbq}-H^{DK1})⁺

(Co$_{Mbq}$-H^{DK1})$^{+}$

atom	x [Å]	y [Å]	z [Å]
Co	-0.019621	-0.124154	-0.114490
N	1.307317	1.307938	-0.136879
N	1.440578	3.663421	0.157548
N	3.300001	0.044627	-0.341735
N	1.319124	-1.470893	-0.223970
C	0.775255	2.536782	-0.001559
C	2.789205	3.601618	0.205425
C	3.525131	4.797722	0.398892
H	2.977581	5.727812	0.504010
C	4.894448	4.748505	0.449356
H	5.466629	5.658178	0.598604
C	5.573874	3.514889	0.306262
H	6.657901	3.496732	0.348029
C	4.878699	2.340531	0.113930
H	5.395083	1.395172	0.002812
C	3.475317	2.365405	0.063645
C	2.668464	1.180196	-0.137388
C	2.699836	-1.201754	-0.647766
H	2.722233	-1.232549	-1.752535
C	3.521445	-2.404069	-0.108157
C	2.459407	-3.541585	-0.255535
C	1.171789	-2.755483	-0.041032
C	-0.065983	-3.389283	0.257045
H	-0.051304	-4.454963	0.443575
C	3.878458	-2.150201	1.364355
H	4.443747	-2.990969	1.774754
H	2.992800	-2.000171	1.990002
H	4.504092	-1.256911	1.444002
C	4.807329	-2.617345	-0.902138
H	5.488454	-1.776345	-0.741131
H	4.629132	-2.702075	-1.977435
H	5.318667	-3.527019	-0.569376
C	2.639158	-4.698147	0.733193
H	3.651828	-5.104934	0.645890
H	1.944367	-5.513018	0.510750
H	2.482565	-4.393959	1.770643
C	2.405888	-4.126117	-1.683525
H	3.307790	-4.710221	-1.887223
H	2.316688	-3.355424	-2.455059
H	1.544991	-4.793947	-1.780940
N	-1.286794	1.328783	-0.071109
N	-1.325803	3.710141	-0.038548
N	-3.301468	0.070991	-0.133872
N	-1.417740	-1.397422	0.051256
C	-0.710958	2.573344	-0.036695
C	-2.695630	3.676975	-0.091279
C	-3.408931	4.892933	-0.108608
H	-2.849869	5.822044	-0.076985
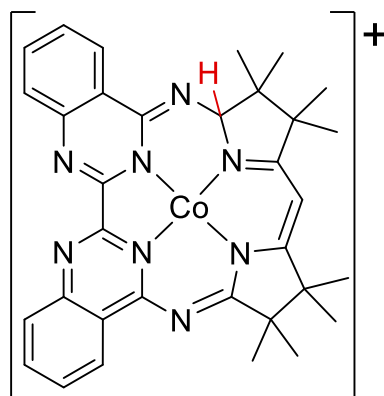
C	-4.783855	4.877061	-0.166531
H	-5.335245	5.811921	-0.181381
C	-5.485869	3.654094	-0.207720
H	-6.570010	3.659102	-0.254197
C	-4.804533	2.457740	-0.189519
H	-5.329105	1.510876	-0.220485
C	-3.396406	2.453671	-0.131709
C	-2.622898	1.235778	-0.111717
C	-2.733092	-1.103080	-0.037700
C	-3.575794	-2.365690	-0.081710
C	-2.602423	-3.390031	0.587641
C	-1.263184	-2.746460	0.272360
C	-3.801943	-2.677551	-1.577067
H	-4.417045	-3.574711	-1.689438
H	-2.861451	-2.836102	-2.113971
H	-4.328390	-1.843567	-2.049762
C	-4.933609	-2.212153	0.599435
H	-5.556172	-1.513234	0.035824
H	-4.850265	-1.834448	1.620845
H	-5.449468	-3.177735	0.628950
C	-2.740104	-4.826427	0.082362
H	-3.768545	-5.174596	0.223527
H	-2.090660	-5.499670	0.649648
H	-2.486265	-4.925496	-0.975339
C	-2.749548	-3.391275	2.125101
H	-3.709975	-3.825485	2.416551
H	-2.686122	-2.383480	2.546951
H	-1.955067	-3.995310	2.572415

Co_{Mbq}-H^{DK1}

Co$_{Mbq}$-H^{DK1}

atom	x [Å]	y [Å]	z [Å]
Co	-0.001966	-0.106515	-0.069857
N	1.285008	1.344210	-0.155109
N	1.332753	3.714041	0.158596
N	3.318166	0.115984	-0.245013
N	1.363561	-1.429604	-0.197633
C	0.731617	2.579632	-0.036044
C	2.706746	3.657908	0.306343
C	3.409430	4.851210	0.560367
H	2.846117	5.777298	0.622728
C	4.780594	4.832297	0.729236
H	5.314823	5.757095	0.926827
C	5.484625	3.620387	0.646796
H	6.562076	3.607410	0.780268
C	4.802965	2.443321	0.391762
H	5.329227	1.498602	0.316832
C	3.411808	2.447038	0.219676
C	2.661163	1.210737	-0.076331
C	2.721228	-1.096783	-0.697274
H	2.631274	-1.035372	-1.795186
C	3.566247	-2.348116	-0.336106
C	2.496948	-3.478913	-0.477610
C	1.236044	-2.717678	-0.087428
C	0.021938	-3.384229	0.274099
H	0.068254	-4.452005	0.445419
C	4.062932	-2.238890	1.112419
H	4.659683	-3.114515	1.384453
H	3.239444	-2.153969	1.829444
H	4.688483	-1.350253	1.217976
C	4.774801	-2.496556	-1.258270
H	5.474953	-1.673449	-1.084480
H	4.498762	-2.480386	-2.316540
H	5.307086	-3.434003	-1.060403
C	2.761443	-4.718789	0.382535
H	3.760831	-5.112625	0.168914
H	2.046112	-5.514427	0.152723
H	2.701546	-4.509783	1.453312
C	2.307094	-3.941065	-1.939190
H	3.182914	-4.504085	-2.275572
H	2.153353	-3.105861	-2.628698
H	1.436698	-4.600408	-2.013680
N	-1.309658	1.312634	-0.081727
N	-1.415203	3.686023	-0.218831
N	-3.293400	-0.000454	-0.052275
N	-1.375185	-1.418565	0.140084
C	-0.761570	2.572337	-0.123898
C	-2.782796	3.609045	-0.281995
C	-3.530911	4.799675	-0.399345
H	-2.997204	5.743514	-0.439334

22
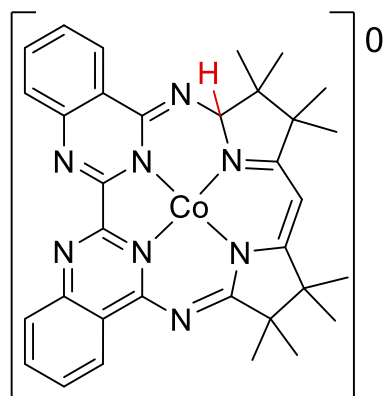
C	-4.904742	4.743815	-0.459323
H	-5.479978	5.660149	-0.549714
C	-5.574605	3.503418	-0.403514
H	-6.658488	3.474971	-0.451502
C	-4.859472	2.332453	-0.288987
H	-5.357377	1.371681	-0.245339
C	-3.451317	2.370368	-0.228322
C	-2.643038	1.178542	-0.116833
C	-2.692736	-1.158458	0.085701
C	-3.514567	-2.437856	0.121304
C	-2.489695	-3.427379	0.765468
C	-1.180713	-2.766869	0.366233
C	-3.816135	-2.796469	-1.349187
H	-4.419547	-3.707084	-1.404871
H	-2.902707	-2.953614	-1.931591
H	-4.382002	-1.984735	-1.815093
C	-4.836961	-2.287926	0.870439
H	-5.501548	-1.615382	0.322741
H	-4.705999	-1.880202	1.875374
H	-5.333392	-3.260693	0.955006
C	-2.626837	-4.878912	0.305766
H	-3.638469	-5.243772	0.512766
H	-1.932529	-5.523974	0.852668
H	-2.429609	-5.001677	-0.761567
C	-2.559983	-3.392698	2.307688
H	-3.497250	-3.832912	2.660185
H	-2.490375	-2.373684	2.700716
H	-1.733623	-3.973415	2.727651

(Co$_{\text{Mbq}}$-H$^{\text{DK1}}$)$^-$

atom	x [Å]	y [Å]	z [Å]
Co	-0.011469	-0.112095	-0.077268
N	1.287599	1.332334	-0.159123
N	1.338281	3.705285	0.159720
N	3.320282	0.109899	-0.247385
N	1.335076	-1.413773	-0.230086
C	0.740174	2.566431	-0.042474
C	2.708567	3.646766	0.310162
C	3.416267	4.836296	0.567305
H	2.852199	5.761251	0.633022
C	4.786248	4.815484	0.732619
H	5.321696	5.739099	0.931814
C	5.488674	3.604878	0.643196
H	6.566522	3.590712	0.771554
C	4.804345	2.431430	0.387047
H	5.325609	1.485082	0.303135
C	3.413910	2.436573	0.220665
C	2.661854	1.201533	-0.076389
C	2.707190	-1.098128	-0.693331
H	2.664108	-1.053056	-1.796554
C	3.544387	-2.343837	-0.298282
C	2.494103	-3.476306	-0.498444
C	1.213546	-2.733211	-0.129216
C	0.029419	-3.395328	0.204753
H	0.060339	-4.469429	0.335791
C	3.961629	-2.236835	1.174311
H	4.568383	-3.096587	1.473600
H	3.095682	-2.184014	1.842130
H	4.551499	-1.330256	1.320572
C	4.800721	-2.470217	-1.156098
H	5.469527	-1.628259	-0.953834
H	4.575648	-2.465052	-2.226359
H	5.345631	-3.393560	-0.928887
C	2.745815	-4.730772	0.343281
H	3.749778	-5.122352	0.146297
H	2.035126	-5.522128	0.085778
H	2.659861	-4.539027	1.415082
C	2.369945	-3.914405	-1.973181
H	3.262570	-4.460617	-2.293907
H	2.228263	-3.067647	-2.651018
H	1.508942	-4.579755	-2.088807
N	-1.286519	1.291730	-0.082255
N	-1.387132	3.677358	-0.238645
N	-3.300792	0.016457	0.010788
N	-1.371649	-1.429264	0.133679
C	-0.752118	2.553903	-0.136145
C	-2.768583	3.617395	-0.295534
C	-3.496929	4.808851	-0.425100
H	-2.944921	5.741483	-0.483337
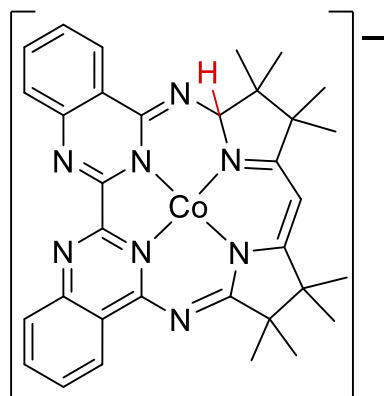
C	-4.878948	4.784306	-0.473728
H	-5.436417	5.710418	-0.573895
C	-5.558473	3.560759	-0.391651
H	-6.643444	3.541040	-0.428759
C	-4.853764	2.378675	-0.263858
H	-5.366738	1.426700	-0.200729
C	-3.448896	2.386382	-0.215760
C	-2.658589	1.178712	-0.090070
C	-2.712974	-1.150600	0.132354
C	-3.528537	-2.436042	0.144063
C	-2.486738	-3.434178	0.738240
C	-1.185881	-2.755843	0.326440
C	-3.861976	-2.765564	-1.324716
H	-4.452439	-3.683713	-1.404170
H	-2.956248	-2.888355	-1.927585
H	-4.446293	-1.946921	-1.754597
C	-4.835884	-2.321270	0.924663
H	-5.505958	-1.617226	0.425081
H	-4.681784	-1.962401	1.944798
H	-5.342407	-3.291770	0.974114
C	-2.629019	-4.875059	0.247697
H	-3.633074	-5.253655	0.467722
H	-1.917572	-5.529937	0.760028
H	-2.456059	-4.969737	-0.826680
C	-2.518292	-3.438538	2.280388
H	-3.439013	-3.896551	2.654364
H	-2.449861	-2.425187	2.688206
H	-1.672665	-4.015653	2.666174

(Co_{Mbq}-H^{DK2})⁺

$(Co_{Mbq}\text{-}H^{DK2})^+$

atom	x [Å]	y [Å]	z [Å]
Co	0.013952	-0.103081	-0.137365
N	-1.363375	3.719910	-0.026479
N	-1.287063	1.344713	-0.053814
N	-3.289778	0.056041	-0.071574
N	-1.396039	-1.425171	-0.075060
N	1.395003	-1.402060	-0.258388
N	3.296869	0.024267	-0.016390
N	1.307507	1.319636	-0.045172
N	1.406715	3.699768	0.076433
C	-0.720884	2.594253	-0.030635
C	-2.726059	3.670683	-0.041503
C	-3.460459	4.876581	-0.042471
H	-2.916182	5.814657	-0.033841
C	-4.833682	4.835169	-0.053646
H	-5.401885	5.759929	-0.054650
C	-5.520345	3.598770	-0.063340
H	-6.605254	3.589955	-0.071758
C	-4.825118	2.414046	-0.062700
H	-5.337201	1.460168	-0.070733
C	-3.412039	2.434250	-0.052912
C	-2.613504	1.248233	-0.059518
C	-2.750781	-1.109546	-0.065096
C	2.684683	-1.148438	-0.153200
C	2.649603	1.186590	0.007329
C	3.448964	2.394905	0.097309
C	4.854784	2.363640	0.155984
H	5.355773	1.403581	0.136489
C	5.567572	3.540997	0.236104
H	6.651632	3.516324	0.281234
C	4.895147	4.778832	0.259897
H	5.466722	5.699614	0.323137
C	3.519466	4.827165	0.204771
H	2.981763	5.769366	0.223561
C	2.778540	3.631437	0.123094
C	0.765995	2.580595	0.000553
C	3.543395	-2.404452	-0.259087
C	2.492820	-3.512324	0.071610
C	1.219735	-2.831026	-0.508742
C	-0.065758	-3.421206	-0.096605
H	-0.092731	-4.504334	-0.040351
C	-1.270839	-2.753585	0.065991
C	-2.583512	-3.427072	0.422656
C	-3.592431	-2.368563	-0.128341
C	4.751988	-2.371654	0.678019
H	5.264986	-3.339426	0.662468
H	4.476402	-2.144838	1.710309
H	5.459119	-1.607525	0.347366
C	4.058581	-2.479701	-1.711014
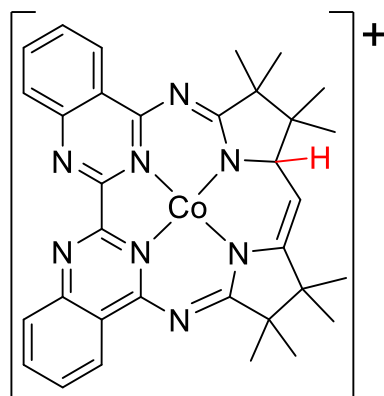
H	3.252633	-2.542112	-2.448953
H	4.707629	-3.350430	-1.841839
H	4.644954	-1.583729	-1.932808
C	2.773174	-4.868286	-0.573668
H	2.014994	-5.602798	-0.282058
H	3.740630	-5.256391	-0.238033
H	2.788002	-4.819763	-1.665584
C	2.332416	-3.701115	1.588556
H	1.508498	-4.388647	1.804755
H	2.127768	-2.758236	2.105158
H	3.237409	-4.134704	2.021757
C	-2.630218	-3.516691	1.964579
H	-3.563632	-3.986578	2.285568
H	-2.557470	-2.533021	2.438173
H	-1.801482	-4.129811	2.330362
C	-2.747034	-4.832124	-0.158520
H	-3.769889	-5.182974	0.009278
H	-2.080583	-5.540314	0.342404
H	-2.543602	-4.873265	-1.230950
C	-3.908538	-2.598365	-1.623612
H	-4.520644	-3.495551	-1.746660
H	-3.004631	-2.712476	-2.229826
H	-4.472533	-1.745282	-2.010251
C	-4.905069	-2.249517	0.642126
H	-5.551565	-1.511181	0.162249
H	-4.755516	-1.939413	1.678476
H	-5.428867	-3.210720	0.639412
H	1.235617	-2.991486	-1.605709

Co_{Mbq}-H^{DK2}

atom	x [Å]	y [Å]	z [Å]
Co	0.000469	-0.099939	-0.104553
N	-1.528306	3.658840	-0.080800
N	-1.353546	1.282106	-0.057354
N	-3.298155	-0.082725	-0.106108
N	-1.342647	-1.460936	-0.021734
N	1.439476	-1.349235	-0.262030
N	3.278208	0.164067	-0.011305
N	1.237978	1.378287	-0.013214
N	1.231354	3.755155	0.171185
C	-0.849825	2.556797	-0.035795
C	-2.895047	3.544106	-0.163539
C	-3.675504	4.716941	-0.228260
H	-3.168547	5.676240	-0.210771
C	-5.047417	4.627368	-0.312082
H	-5.646701	5.531353	-0.362540
C	-5.680648	3.368553	-0.332218
H	-6.762511	3.310528	-0.397974
C	-4.930773	2.213756	-0.267776
H	-5.400265	1.237670	-0.280245
C	-3.527087	2.286785	-0.184406
C	-2.688956	1.103559	-0.117430
C	-2.646131	-1.239558	-0.018565
C	2.710098	-1.036470	-0.200167
C	2.585321	1.293659	0.056837
C	3.329258	2.534808	0.208315
C	4.732951	2.563565	0.301879
H	5.274666	1.626474	0.259624
C	5.393712	3.765774	0.443427
H	6.476570	3.785151	0.515938
C	4.667053	4.971365	0.493687
H	5.194890	5.913687	0.605070
C	3.292222	4.960992	0.402131
H	2.713772	5.878508	0.438844
C	2.603880	3.738939	0.257982
C	0.640577	2.609804	0.047347
C	3.626620	-2.232711	-0.439492
C	2.648146	-3.414058	-0.140962
C	1.309687	-2.778602	-0.606567
C	0.069072	-3.437288	-0.089987
H	0.122158	-4.513953	0.038776
C	-1.100828	-2.844824	0.144069
C	-2.379579	-3.508105	0.636421
C	-3.444428	-2.536814	0.029558
C	4.884927	-2.200773	0.429778
H	5.439117	-3.140276	0.323893
H	4.659958	-2.053334	1.488654
H	5.538487	-1.384380	0.113061
C	4.064712	-2.175766	-1.917664
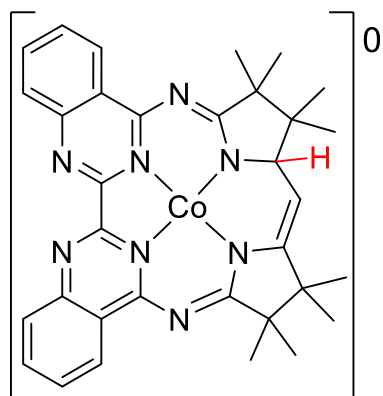
H	3.222186	-2.234914	-2.613342
H	4.752065	-2.996201	-2.145972
H	4.588568	-1.233737	-2.104761
C	2.965621	-4.703973	-0.897417
H	2.259035	-5.494993	-0.623242
H	3.969318	-5.065010	-0.646117
H	2.914254	-4.575216	-1.982136
C	2.602421	-3.722146	1.363709
H	1.833943	-4.469248	1.580491
H	2.378881	-2.832970	1.961842
H	3.558826	-4.128271	1.705139
C	-2.380570	-3.450104	2.177939
H	-3.298335	-3.882982	2.587673
H	-2.291451	-2.424755	2.551109
H	-1.533264	-4.023732	2.565519
C	-2.535590	-4.966187	0.207715
H	-3.528922	-5.338457	0.481750
H	-1.801868	-5.597940	0.718615
H	-2.402579	-5.102445	-0.868105
C	-3.785804	-2.893110	-1.431479
H	-4.384196	-3.808204	-1.474875
H	-2.886603	-3.042053	-2.037913
H	-4.370493	-2.084567	-1.880319
C	-4.744200	-2.420913	0.823293
H	-5.448276	-1.770604	0.298302
H	-4.589901	-2.005033	1.821751
H	-5.209075	-3.407400	0.929795
H	1.279766	-2.841730	-1.706761

(Co_{Mbq}-H^{Co})⁺

$(Co_{Mbq}\text{-}H^{Co})^+$

atom	x [Å]	y [Å]	z [Å]
Co	-0.000000	-0.102511	0.046801
N	-1.289347	1.318743	0.046513
N	1.289348	1.318741	0.046511
N	1.370485	-1.405465	-0.044500
N	-1.370487	-1.405463	-0.044496
N	-1.389302	3.691847	-0.115050
N	1.389306	3.691846	-0.115040
N	3.274954	0.025883	0.227079
N	-3.274954	0.025888	0.227085
C	-0.741173	2.575425	-0.044025
C	0.741176	2.575424	-0.044023
C	2.755041	3.630222	-0.089720
C	3.500376	4.824578	-0.173964
C	4.874275	4.772224	-0.140806
C	5.545866	3.535632	-0.019983
C	4.835453	2.361053	0.064418
C	3.425016	2.393863	0.027527
C	2.618705	1.208125	0.098950
C	2.701889	-1.129467	0.159605
C	3.493940	-2.404518	0.359851
C	2.556817	-3.441920	-0.336112
C	1.220521	-2.736207	-0.211625
C	-0.000003	-3.378502	-0.313341
C	-1.220525	-2.736205	-0.211620
C	-2.556823	-3.441918	-0.336099
C	-3.493941	-2.404513	0.359867
C	-2.701890	-1.129464	0.159613
C	-2.618704	1.208128	0.098950
C	-3.425013	2.393866	0.027520
C	-4.835451	2.361057	0.064408
C	-5.545862	3.535637	-0.020001
C	-4.874270	4.772227	-0.140829
C	-3.500371	4.824581	-0.173985
C	-2.755037	3.630224	-0.089732
C	3.566472	-2.627238	1.887299
C	4.914010	-2.326715	-0.195069
C	2.583559	-4.842709	0.278162
C	2.851469	-3.558403	-1.849364
C	-2.583563	-4.842705	0.278177
C	-2.851482	-3.558403	-1.849350
C	-3.566465	-2.627230	1.887315
C	-4.914014	-2.326710	-0.195047
H	2.966155	5.764307	-0.263562
H	5.451519	5.689068	-0.206133
H	6.630375	3.515599	0.006685
H	5.336048	1.405484	0.157996
H	-0.000004	-4.450344	-0.457778
H	-5.336046	1.405490	0.157991
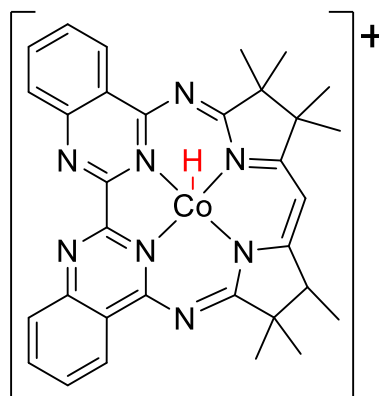
H	-6.630371	3.515605	0.006665
H	-5.451513	5.689072	-0.206163
H	-2.966149	5.764308	-0.263587
H	2.576045	-2.719360	2.343272
H	4.133230	-3.535297	2.109203
H	4.079900	-1.782533	2.354596
H	4.938726	-2.018104	-1.242240
H	5.402188	-3.302858	-0.109565
H	5.498771	-1.604774	0.379572
H	3.609907	-5.223021	0.281121
H	1.984060	-5.539077	-0.314667
H	2.208659	-4.860799	1.303660
H	3.814481	-4.051522	-2.006072
H	2.079990	-4.162114	-2.335313
H	2.878717	-2.582279	-2.342597
H	-1.984068	-5.539075	-0.314653
H	-2.208658	-4.860794	1.303674
H	-3.609912	-5.223016	0.281143
H	-2.878732	-2.582280	-2.342585
H	-3.814496	-4.051521	-2.006052
H	-2.080006	-4.162116	-2.335302
H	-2.576036	-2.719352	2.343284
H	-4.133223	-3.535288	2.109224
H	-4.079890	-1.782524	2.354613
H	-5.498771	-1.604768	0.379597
H	-4.938736	-2.018102	-1.242217
H	-5.402192	-3.302852	-0.109537
H	0.000001	-0.138125	1.463580

Co_{Mbq}-H^{Co}

atom	x [Å]	y [Å]	z [Å]
Co	0.000086	-0.113027	0.037777
N	-1.289983	1.312149	-0.001886
N	1.292471	1.310091	-0.003371
N	1.391735	-1.417102	-0.026875
N	-1.394196	-1.414867	-0.018680
N	-1.377900	3.690637	-0.157799
N	1.383518	3.689865	-0.136181
N	3.286530	0.040724	0.194887
N	-3.285685	0.046838	0.204550
C	-0.741913	2.565146	-0.092654
C	0.746185	2.564353	-0.086986
C	2.755429	3.635029	-0.083734
C	3.491476	4.835573	-0.141729
C	4.867593	4.802166	-0.078876
C	5.545964	3.573702	0.044936
C	4.838057	2.391769	0.102396
C	3.431968	2.408117	0.037023
C	2.637238	1.194520	0.080132
C	2.688409	-1.141005	0.137029
C	3.510502	-2.406942	0.326654
C	2.573247	-3.465527	-0.336554
C	1.227023	-2.789800	-0.151571
C	-0.003463	-3.412011	-0.208293
C	-1.232588	-2.788167	-0.139626
C	-2.581370	-3.463043	-0.308987
C	-3.511321	-2.399743	0.357039
C	-2.689370	-1.136027	0.152937
C	-2.635047	1.198832	0.079226
C	-3.428292	2.412760	0.021759
C	-4.834576	2.398563	0.083471
C	-5.541114	3.580430	0.010211
C	-4.861151	4.806648	-0.126491
C	-3.484826	4.837987	-0.185754
C	-2.750109	3.637541	-0.111158
C	3.627324	-2.613055	1.851766
C	4.915670	-2.319848	-0.264656
C	2.662173	-4.864292	0.276206
C	2.834360	-3.581658	-1.854529
C	-2.666325	-4.858363	0.312210
C	-2.856575	-3.586983	-1.823815
C	-3.614241	-2.597352	1.884318
C	-4.921784	-2.314283	-0.221661
H	2.949092	5.770871	-0.234568
H	5.434194	5.727223	-0.123933
H	6.630154	3.559469	0.094237
H	5.344143	1.438544	0.195399
H	-0.004731	-4.490213	-0.328599
H	-5.341910	1.447002	0.186260
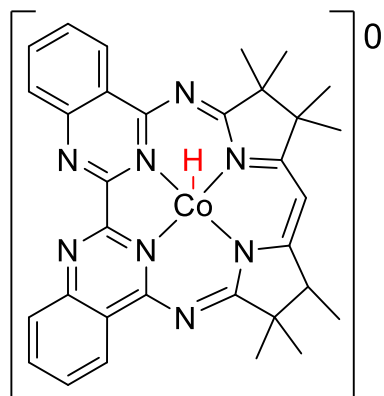
H	-6.625439	3.567869	0.056919
H	-5.426679	5.731669	-0.184026
H	-2.941265	5.771642	-0.287759
H	2.647246	-2.724425	2.326567
H	4.220434	-3.504782	2.076028
H	4.128582	-1.750550	2.301047
H	4.910514	-2.014712	-1.313641
H	5.415933	-3.291855	-0.191274
H	5.511365	-1.590631	0.289985
H	3.691070	-5.236945	0.222715
H	2.035127	-5.568939	-0.279084
H	2.343751	-4.884872	1.321103
H	3.808505	-4.039600	-2.053147
H	2.065510	-4.211638	-2.312241
H	2.807909	-2.605401	-2.349393
H	-2.044812	-5.566696	-0.244615
H	-2.338735	-4.873515	1.354362
H	-3.696012	-5.230273	0.269825
H	-2.833396	-2.613419	-2.324128
H	-3.833108	-4.044658	-2.010998
H	-2.092847	-4.220457	-2.285252
H	-2.629955	-2.707356	2.350637
H	-4.206336	-3.487081	2.118956
H	-4.110308	-1.731811	2.333565
H	-5.511442	-1.581193	0.334327
H	-4.926044	-2.015051	-1.272340
H	-5.422472	-3.285246	-0.138085
H	0.002896	-0.129805	1.457251

(Co_{Mbq}-H^{Im})⁺

(Co_{Mbq}-H^{Im})⁺

atom	x [Å]	y [Å]	z [Å]
Co	-0.012676	-0.120482	-0.001438
N	1.326360	1.314551	0.011446
N	1.434712	3.689134	0.000777
N	3.232975	-0.013026	0.051730
N	1.365789	-1.479326	-0.027994
C	0.778993	2.575590	0.007607
C	2.800562	3.623478	-0.017229
C	3.535350	4.826776	-0.037861
H	2.987233	5.762531	-0.034181
C	4.909118	4.792048	-0.064767
H	5.475542	5.717391	-0.081875
C	5.591762	3.558304	-0.074225
H	6.675840	3.541816	-0.101269
C	4.893309	2.373746	-0.051954
H	5.456194	1.447029	-0.068460
C	3.481455	2.386600	-0.018990
C	2.649837	1.215904	0.012075
C	2.654446	-1.248140	0.049877
C	3.487867	-2.494925	0.257517
C	2.485243	-3.560636	-0.305545
C	1.163753	-2.849026	-0.074117
C	-0.088254	-3.439640	0.006936
H	-0.114567	-4.523661	0.019654
C	3.683434	-2.638610	1.783999
H	4.267776	-3.535796	2.004735
H	2.727591	-2.710131	2.311000
H	4.228755	-1.778409	2.183637
C	4.858154	-2.466669	-0.422195
H	5.539743	-1.776277	0.087577
H	4.805331	-2.183168	-1.475607
H	5.320577	-3.456141	-0.358371
C	2.587296	-4.932616	0.360890
H	3.602213	-5.330840	0.258280
H	1.912901	-5.642384	-0.127294
H	2.333280	-4.904942	1.422783
C	2.651709	-3.739525	-1.830901
H	3.601904	-4.227743	-2.067316
H	2.614102	-2.783983	-2.363881
H	1.844370	-4.370003	-2.214028
N	-1.277463	1.341037	-0.009680
N	-1.324018	3.725518	0.037408
N	-3.300437	0.098633	-0.089236
N	-1.434107	-1.403493	0.019434
C	-0.708316	2.588971	0.015083
C	-2.696662	3.692534	0.038322
C	-3.410126	4.907423	0.071795
H	-2.850087	5.836339	0.097762
C	-4.787408	4.893324	0.070872

34
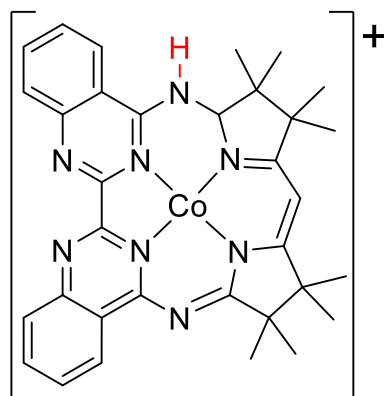
H	-5.338138	5.828487	0.096855
C	-5.489181	3.671622	0.035721
H	-6.574459	3.674503	0.035060
C	-4.804247	2.476117	0.001612
H	-5.328626	1.528877	-0.026111
C	-3.396120	2.471899	0.003102
C	-2.623271	1.246544	-0.029959
C	-2.731330	-1.093400	-0.074354
C	-3.592662	-2.334342	-0.255311
C	-2.644223	-3.438146	0.311905
C	-1.295061	-2.784255	0.080269
C	-3.807432	-2.483172	-1.776520
H	-4.434125	-3.353620	-1.991510
H	-2.861885	-2.599045	-2.315882
H	-4.315228	-1.595324	-2.164154
C	-4.956285	-2.231961	0.424794
H	-5.561296	-1.465218	-0.064995
H	-4.878756	-1.968851	1.482187
H	-5.488531	-3.186078	0.345229
C	-2.799091	-4.810720	-0.344589
H	-3.832478	-5.160287	-0.247431
H	-2.161828	-5.549564	0.151191
H	-2.538837	-4.800704	-1.405549
C	-2.817921	-3.605215	1.837937
H	-3.789829	-4.049373	2.073323
H	-2.740831	-2.649816	2.366651
H	-2.039870	-4.269221	2.226184
H	4.243407	-0.023869	0.076668

Co_Mbq-H^Im

atom	x [Å]	y [Å]	z [Å]
Co	-0.003315	-0.121371	-0.007143
N	1.326337	1.302681	-0.003836
N	1.454282	3.683214	-0.033425
N	3.228156	-0.027991	0.051362
N	1.345773	-1.483182	-0.009045
C	0.794613	2.567559	-0.011995
C	2.821064	3.610571	-0.056860
C	3.563597	4.809601	-0.093620
H	3.019668	5.748256	-0.100306
C	4.938004	4.771147	-0.121565
H	5.508067	5.694214	-0.150556
C	5.612989	3.534029	-0.115739
H	6.697270	3.509819	-0.142830
C	4.905636	2.353519	-0.078643
H	5.462853	1.422741	-0.083426
C	3.494017	2.370801	-0.045087
C	2.652706	1.203277	-0.001124
C	2.644349	-1.264225	0.061120
C	3.474301	-2.509052	0.295201
C	2.465070	-3.579875	-0.245113
C	1.146515	-2.849141	-0.039338
C	-0.108444	-3.437966	0.013701
H	-0.139452	-4.522498	0.027736
C	3.683841	-2.632617	1.820833
H	4.264978	-3.528608	2.057601
H	2.731272	-2.686870	2.356060
H	4.236093	-1.766945	2.199920
C	4.842256	-2.503161	-0.391604
H	5.527539	-1.801169	0.097682
H	4.784483	-2.241646	-1.450740
H	5.304892	-3.491698	-0.309009
C	2.553734	-4.936378	0.455352
H	3.566034	-5.346302	0.368453
H	1.875184	-5.653448	-0.016791
H	2.295123	-4.879923	1.515235
C	2.639243	-3.802712	-1.763385
H	3.586182	-4.305389	-1.984683
H	2.611407	-2.860489	-2.320141
H	1.827425	-4.435454	-2.134156
N	-1.262182	1.346042	-0.012931
N	-1.301707	3.737462	0.050364
N	-3.294821	0.119440	-0.090326
N	-1.435986	-1.399586	-0.000215
C	-0.695945	2.590072	0.011766
C	-2.674419	3.711358	0.070423
C	-3.381988	4.930665	0.126118
H	-2.814824	5.855755	0.152777
C	-4.759297	4.928918	0.145924
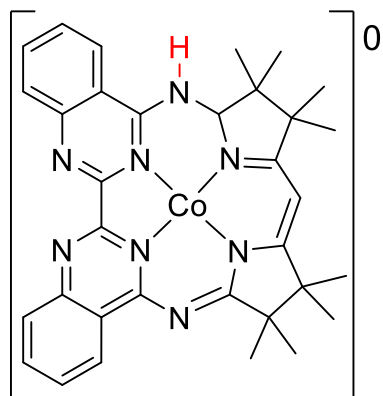
H	-5.302694	5.868016	0.189367
C	-5.468330	3.711376	0.109850
H	-6.553840	3.719382	0.126240
C	-4.789227	2.512672	0.054070
H	-5.320630	1.569122	0.026617
C	-3.380698	2.494704	0.033597
C	-2.612030	1.264202	-0.022018
C	-2.733827	-1.081227	-0.090727
C	-3.609276	-2.312195	-0.295336
C	-2.671132	-3.431632	0.257393
C	-1.316156	-2.773912	0.054767
C	-3.826787	-2.442139	-1.817303
H	-4.459934	-3.304598	-2.048457
H	-2.881296	-2.556230	-2.357390
H	-4.326550	-1.544310	-2.193214
C	-4.974859	-2.215401	0.382475
H	-5.576590	-1.439613	-0.097674
H	-4.899173	-1.965939	1.443545
H	-5.512489	-3.166060	0.290193
C	-2.824430	-4.789934	-0.429849
H	-3.859430	-5.140839	-0.350163
H	-2.191955	-5.541181	0.053968
H	-2.554787	-4.757506	-1.488231
C	-2.863871	-3.635139	1.776201
H	-3.839795	-4.081091	1.993464
H	-2.788008	-2.691973	2.326736
H	-2.091652	-4.310352	2.157755
H	4.237854	-0.043320	0.076715

(Co_{Mbq}-H^{Im})[−]

atom	x [Å]	y [Å]	z [Å]
Co	-0.021242	-0.125128	0.003577
N	1.335004	1.300438	0.011685
N	1.536068	3.678158	0.015657
N	3.224871	-0.093640	0.054584
N	1.319206	-1.518995	-0.008983
C	0.847133	2.552440	0.017480
C	2.901797	3.572312	-0.026670
C	3.682226	4.737804	-0.048070
H	3.158425	5.688167	-0.021966
C	5.074971	4.673839	-0.103613
H	5.658713	5.590765	-0.119019
C	5.714113	3.438667	-0.147103
H	6.798012	3.380549	-0.202238
C	4.959825	2.262638	-0.127692
H	5.491273	1.314614	-0.184238
C	3.555802	2.304242	-0.054260
C	2.684551	1.167427	0.004234
C	2.630613	-1.308753	0.044080
C	3.427758	-2.576988	0.288060
C	2.399171	-3.623576	-0.263162
C	1.092667	-2.869784	-0.040102
C	-0.177566	-3.441445	0.000763
H	-0.227089	-4.526961	0.011434
C	3.624619	-2.721505	1.813138
H	4.170496	-3.639093	2.061882
H	2.662252	-2.736507	2.333061
H	4.200178	-1.873391	2.199445
C	4.802258	-2.610696	-0.385267
H	5.494418	-1.908764	0.097457
H	4.755629	-2.359171	-1.447743
H	5.253401	-3.605273	-0.287459
C	2.471979	-4.992195	0.415702
H	3.475930	-5.425013	0.317240
H	1.773586	-5.689298	-0.059415
H	2.218912	-4.944886	1.477746
C	2.569368	-3.828579	-1.784164
H	3.507598	-4.343495	-2.025844
H	2.548642	-2.873501	-2.318448
H	1.742142	-4.437249	-2.162304
N	-1.240825	1.369363	0.004753
N	-1.233830	3.764045	0.057497
N	-3.299421	0.179854	-0.076291
N	-1.471275	-1.381507	0.003691
C	-0.640563	2.605514	0.029672
C	-2.601288	3.756559	0.060979
C	-3.291114	4.989664	0.100563
H	-2.696920	5.897771	0.129288
C	-4.667611	5.016946	0.101555
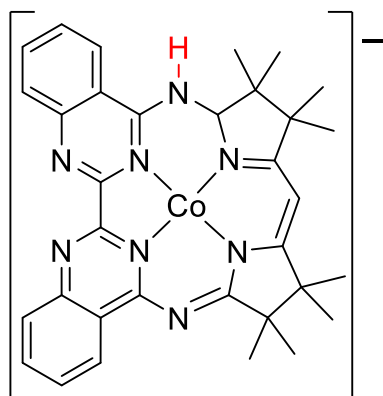
H	-5.192304	5.968743	0.132365
C	-5.401684	3.813439	0.062165
H	-6.488239	3.841945	0.063025
C	-4.743254	2.602669	0.022868
H	-5.282970	1.663171	-0.007420
C	-3.335598	2.556098	0.022312
C	-2.590035	1.311589	-0.014880
C	-2.756858	-1.029829	-0.074024
C	-3.661889	-2.244056	-0.278067
C	-2.743705	-3.386434	0.261628
C	-1.373347	-2.758727	0.043848
C	-3.897995	-2.360352	-1.797053
H	-4.559234	-3.202072	-2.035977
H	-2.957026	-2.493000	-2.340862
H	-4.368480	-1.440427	-2.157264
C	-5.018280	-2.111467	0.411619
H	-5.581938	-1.293820	-0.045030
H	-4.923807	-1.883122	1.475997
H	-5.600794	-3.036067	0.303987
C	-2.939977	-4.738817	-0.426802
H	-3.979809	-5.075147	-0.327075
H	-2.307721	-5.503692	0.038124
H	-2.690941	-4.704227	-1.490397
C	-2.930616	-3.591238	1.780431
H	-3.918233	-4.007225	2.013351
H	-2.814854	-2.650088	2.326660
H	-2.171248	-4.287261	2.152129
H	4.232098	-0.116959	0.103768

(Co$_{\text{Mbq}}$-H$_2^{\text{Im,Co}}$)$^+$

atom	x [Å]	y [Å]	z [Å]
Co	-0.017505	-0.117564	0.025168
N	-1.271385	1.327789	0.004507
N	1.318440	1.304337	0.001761
N	1.355262	-1.466181	-0.030890
N	-1.421660	-1.388719	-0.027606
N	-1.325995	3.707051	-0.164332
N	1.433017	3.675790	-0.136051
N	3.217690	-0.013271	0.206273
N	-3.285674	0.095628	0.230342
C	-0.706308	2.575795	-0.094739
C	0.776879	2.563717	-0.089162
C	2.797559	3.612307	-0.082022
C	3.535018	4.812488	-0.139660
C	4.907790	4.777207	-0.080430
C	5.586093	3.546546	0.037016
C	4.884600	2.365034	0.094563
C	3.473555	2.378835	0.037449
C	2.640360	1.210493	0.081571
C	2.638266	-1.243257	0.137920
C	3.456929	-2.498613	0.339870
C	2.497811	-3.531131	-0.346144
C	1.162396	-2.830638	-0.166994
C	-0.088311	-3.421154	-0.236642
C	-1.292607	-2.765684	-0.164865
C	-2.656965	-3.409396	-0.323655
C	-3.553545	-2.338549	0.374021
C	-2.714536	-1.088825	0.168643
C	-2.614018	1.240353	0.091932
C	-3.390225	2.460434	0.029343
C	-4.796917	2.463592	0.095882
C	-5.485299	3.654613	0.014323
C	-4.789588	4.871427	-0.134507
C	-3.413816	4.886467	-0.197615
C	-2.697081	3.676263	-0.115291
C	3.548946	-2.721026	1.866694
C	4.869631	-2.435677	-0.243347
C	2.555697	-4.934964	0.256886
C	2.768901	-3.632592	-1.863403
C	-2.760708	-4.812303	0.276613
C	-2.955678	-3.500287	-1.836462
C	-3.627608	-2.552791	1.901209
C	-4.972806	-2.216726	-0.175250
H	2.990382	5.745853	-0.230320
H	5.477138	5.699804	-0.125098
H	6.669640	3.529917	0.079699
H	5.444842	1.440393	0.177176
H	-0.115874	-4.497544	-0.363902
H	-5.317243	1.520408	0.208074
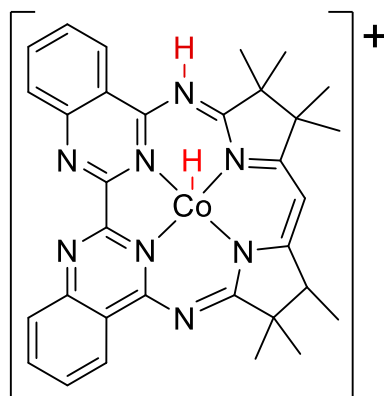
H	-6.569374	3.657938	0.063944
H	-5.344244	5.802392	-0.198058
H	-2.858251	5.811727	-0.308473
H	2.560262	-2.815579	2.324836
H	4.116957	-3.630495	2.079505
H	4.067155	-1.883947	2.343963
H	4.887501	-2.092392	-1.280087
H	5.327395	-3.428472	-0.205394
H	5.513769	-1.777127	0.350292
H	3.577381	-5.326441	0.209892
H	1.922355	-5.620372	-0.313863
H	2.224216	-4.959725	1.297199
H	3.734518	-4.108677	-2.058047
H	1.991990	-4.242732	-2.332629
H	2.764655	-2.651566	-2.349181
H	-2.171089	-5.526767	-0.305996
H	-2.411617	-4.852934	1.310910
H	-3.800219	-5.156167	0.250664
H	-2.922831	-2.519369	-2.321209
H	-3.943409	-3.936606	-2.012843
H	-2.212292	-4.140369	-2.320859
H	-2.637208	-2.689237	2.346776
H	-4.233188	-3.433407	2.134010
H	-4.097426	-1.684045	2.371489
H	-5.536238	-1.480612	0.403136
H	-4.991652	-1.902409	-1.221151
H	-5.489796	-3.178996	-0.094710
H	-0.014362	-0.140769	1.443260
H	4.224447	-0.026179	0.296940

Co$_{Mbq}$-H$_2$^{Im,Co}

atom	x [Å]	y [Å]	z [Å]
Co	-0.018115	-0.112904	0.033814
N	-1.270599	1.339363	-0.003164
N	1.303267	1.301011	-0.016010
N	1.345536	-1.472581	-0.005584
N	-1.439094	-1.384828	-0.045406
N	-1.305737	3.722269	-0.109844
N	1.458736	3.672213	-0.188008
N	3.221281	-0.046812	0.228831
N	-3.295224	0.117729	0.197765
C	-0.689953	2.582835	-0.083126
C	0.796273	2.548616	-0.109726
C	2.844160	3.598671	-0.162227
C	3.590659	4.772857	-0.259458
C	4.985079	4.739806	-0.227486
C	5.643272	3.518578	-0.100485
C	4.916621	2.334298	-0.005757
C	3.510208	2.350529	-0.028747
C	2.667085	1.195423	0.063471
C	2.642780	-1.252181	0.194848
C	3.424810	-2.522770	0.460924
C	2.482825	-3.547925	-0.258138
C	1.146313	-2.833867	-0.127425
C	-0.103303	-3.421034	-0.236042
C	-1.311346	-2.763988	-0.198144
C	-2.675231	-3.390880	-0.421769
C	-3.587341	-2.324554	0.263250
C	-2.727503	-1.077712	0.114191
C	-2.615763	1.256236	0.098043
C	-3.381697	2.489275	0.087024
C	-4.786372	2.506987	0.180383
C	-5.466159	3.706334	0.150946
C	-4.759700	4.918949	0.027510
C	-3.384674	4.918732	-0.061974
C	-2.676923	3.699809	-0.031929
C	3.440943	-2.734833	1.990570
C	4.865732	-2.500885	-0.051107
C	2.507417	-4.951329	0.348144
C	2.814289	-3.656919	-1.762232
C	-2.816758	-4.804289	0.145341
C	-2.922415	-3.451725	-1.945264
C	-3.722971	-2.569284	1.780823
C	-4.984014	-2.180577	-0.336900
H	3.055593	5.712358	-0.358707
H	5.552400	5.662224	-0.303790
H	6.728109	3.480683	-0.079995
H	5.468913	1.403035	0.076259
H	-0.130696	-4.497276	-0.370210
H	-5.314260	1.565657	0.272716
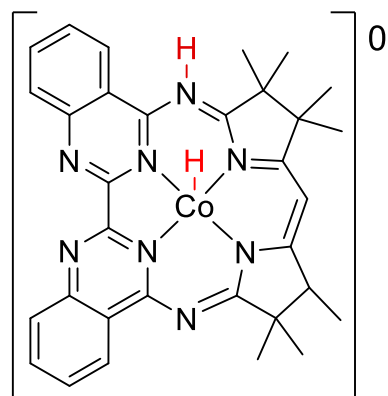
H	-6.549208	3.718083	0.222003
H	-5.303599	5.858406	0.003968
H	-2.821063	5.841483	-0.154676
H	2.428488	-2.795164	2.400942
H	3.971502	-3.656784	2.245809
H	3.958237	-1.904039	2.480460
H	4.940407	-2.184166	-1.094063
H	5.307047	-3.498863	0.034749
H	5.489913	-1.834178	0.554988
H	3.526082	-5.354617	0.338695
H	1.886375	-5.632326	-0.241928
H	2.139011	-4.970351	1.376394
H	3.781980	-4.143322	-1.921589
H	2.049152	-4.258306	-2.262021
H	2.839868	-2.675085	-2.246272
H	-2.203441	-5.510697	-0.423093
H	-2.514234	-4.866949	1.193308
H	-3.855729	-5.143058	0.066128
H	-2.858129	-2.462053	-2.409179
H	-3.908345	-3.871046	-2.169946
H	-2.168328	-4.091986	-2.413257
H	-2.750399	-2.724378	2.258829
H	-4.345011	-3.448152	1.975903
H	-4.200943	-1.704559	2.250813
H	-5.565256	-1.452634	0.234515
H	-4.960301	-1.843464	-1.375842
H	-5.511476	-3.140240	-0.298352
H	-0.020919	-0.127025	1.453804
H	4.222129	-0.060449	0.374414

Co_{Mbq}-H₂^{DK1,Im}

Co$_{Mbq}$-H$_2^{DK1,Im}$

atom	x [Å]	y [Å]	z [Å]
Co	-0.020209	-0.123045	-0.032599
N	1.340162	1.311406	-0.078806
N	1.440419	3.682753	0.118107
N	3.225653	-0.020627	0.016237
N	1.285933	-1.472578	-0.184635
C	0.798640	2.567571	-0.035025
C	2.798841	3.604843	0.278891
C	3.528352	4.798640	0.462434
H	2.983455	5.736731	0.464269
C	4.891899	4.755520	0.636667
H	5.450539	5.675145	0.779327
C	5.571412	3.521142	0.631380
H	6.647108	3.494794	0.769205
C	4.876380	2.346807	0.448831
H	5.432491	1.415445	0.449787
C	3.476520	2.369749	0.271394
C	2.661024	1.194642	0.057712
C	2.650256	-1.196516	-0.618833
H	2.647125	-1.016097	-1.704007
C	3.469224	-2.475048	-0.305538
C	2.369187	-3.556449	-0.572137
C	1.118863	-2.796262	-0.148647
C	-0.088033	-3.418319	0.166801
H	-0.100331	-4.496932	0.260872
C	3.904118	-2.499449	1.168858
H	4.418078	-3.437357	1.393544
H	3.054663	-2.402173	1.851226
H	4.607257	-1.693224	1.395888
C	4.708843	-2.600758	-1.193428
H	5.458715	-1.845650	-0.931007
H	4.476367	-2.480725	-2.254619
H	5.182445	-3.578895	-1.057566
C	2.581794	-4.872315	0.182014
H	3.572236	-5.283113	-0.042545
H	1.845528	-5.617526	-0.133932
H	2.496144	-4.755977	1.264765
C	2.229665	-3.889386	-2.074250
H	3.104725	-4.440770	-2.432655
H	2.110749	-2.996864	-2.695771
H	1.348925	-4.519690	-2.228616
N	-1.252185	1.327278	-0.068860
N	-1.292802	3.713369	-0.261002
N	-3.297637	0.110856	0.027096
N	-1.421362	-1.397687	0.148497
C	-0.688830	2.576931	-0.140176
C	-2.674588	3.692452	-0.318527
C	-3.368937	4.904141	-0.466803
H	-2.794889	5.822685	-0.541083
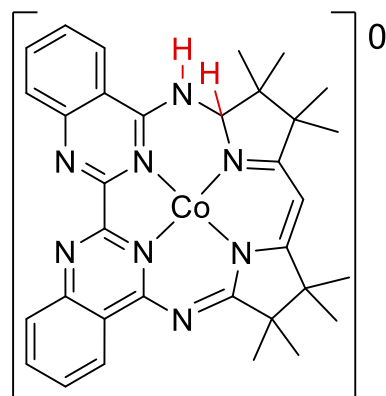
C	-4.751205	4.913144	-0.513064
H	-5.285777	5.851242	-0.627638
C	-5.463379	3.706680	-0.409298
H	-6.548724	3.715354	-0.443975
C	-4.790204	2.507491	-0.263805
H	-5.330973	1.572016	-0.184149
C	-3.384011	2.480453	-0.218714
C	-2.623489	1.252943	-0.079291
C	-2.747239	-1.077495	0.146398
C	-3.608605	-2.332452	0.156550
C	-2.598317	-3.372914	0.734615
C	-1.278860	-2.735618	0.321270
C	-3.966839	-2.638300	-1.312732
H	-4.591439	-3.534260	-1.387652
H	-3.073849	-2.791557	-1.927841
H	-4.527409	-1.797546	-1.732053
C	-4.905117	-2.178086	0.949524
H	-5.562918	-1.460829	0.451605
H	-4.733038	-1.818418	1.966917
H	-5.433973	-3.136388	1.007698
C	-2.795741	-4.803633	0.231970
H	-3.812956	-5.144568	0.454308
H	-2.107966	-5.489381	0.736801
H	-2.631783	-4.897168	-0.844252
C	-2.621268	-3.393225	2.278281
H	-3.556653	-3.823949	2.649232
H	-2.515563	-2.388946	2.700766
H	-1.795351	-4.006058	2.652339
H	4.233297	-0.032100	0.064621

Transition state between Co$_{Mbq}$-H^{Im} and Co$_{Mbq}$-H^{DK1}

atom	x [Å]	y [Å]	z [Å]
Co	-0.004184	-0.124891	-0.066073
N	1.393516	1.244773	-0.028531
N	1.623747	3.622343	-0.027272
N	3.307852	-0.139921	0.024758
N	1.273549	-1.569972	-0.159380
C	0.930480	2.522470	-0.033153
C	2.752711	1.056339	0.026065
C	2.659791	-1.380869	-0.241134
H	3.572970	-0.611645	-1.014122
C	3.341458	-2.647101	0.267752
C	2.281962	-3.697689	-0.204801
C	1.011366	-2.858896	-0.125310
C	-0.297091	-3.424078	-0.147004
H	-0.364221	-4.504742	-0.191102
C	3.424025	-2.582200	1.807684
H	3.882863	-3.485075	2.223007
H	2.436799	-2.462848	2.266336
H	4.038544	-1.725530	2.100483
C	4.749361	-2.868088	-0.281755
H	5.427429	-2.100928	0.106309
H	4.780267	-2.820441	-1.373631
H	5.142193	-3.841983	0.032194
C	2.237538	-4.974273	0.637971
H	3.228277	-5.441512	0.664884
H	1.548343	-5.705119	0.203351
H	1.921950	-4.786270	1.667227
C	2.474472	-4.088854	-1.684929
H	3.380279	-4.689914	-1.813010
H	2.553895	-3.207235	-2.328491
H	1.624938	-4.688765	-2.026457
N	-1.197680	1.402755	0.013233
N	-1.125615	3.782463	-0.083885
N	-3.279507	0.264900	0.163653
N	-1.506017	-1.329546	-0.060355
C	-0.559447	2.618612	-0.040359
C	-2.541754	1.378907	0.057755
C	-2.775566	-0.951761	0.126974
C	-3.687450	-2.143997	0.377733
C	-2.849234	-3.293142	-0.266310
C	-1.449232	-2.717076	-0.136436
C	3.000532	3.492002	-0.008836
C	3.618329	2.228017	0.025732
C	-2.496174	3.817490	-0.071768
C	-3.256156	2.635995	0.006514
C	3.796229	4.650019	-0.020750
C	5.018500	2.142568	0.053706
H	3.300622	5.615533	-0.048541
H	5.486416	1.164897	0.089698
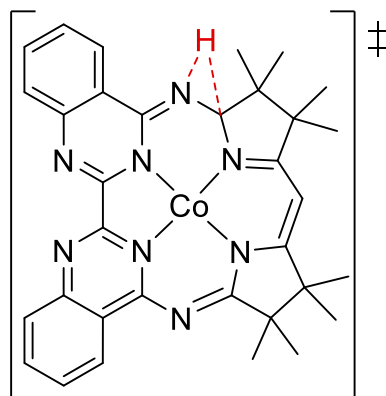
C	5.176372	4.551587	0.001542
H	5.783981	5.451528	-0.008258
C	5.791550	3.291718	0.040319
H	6.874332	3.216060	0.062454
C	-3.150970	5.065730	-0.133624
C	-4.663533	2.710811	0.024519
C	-4.526373	5.120550	-0.117815
H	-5.030314	6.081021	-0.166246
C	-5.288665	3.936535	-0.037914
H	-6.372430	3.994220	-0.025522
H	-2.546012	5.964574	-0.193143
H	-5.233531	1.791946	0.085684
C	-3.149616	-3.435009	-1.774290
H	-2.444203	-4.139576	-2.224489
H	-4.161534	-3.818927	-1.935068
H	-3.057312	-2.481129	-2.303283
C	-3.028996	-4.660810	0.393075
H	-4.084630	-4.952571	0.373811
H	-2.472157	-5.428502	-0.153034
H	-2.688232	-4.674025	1.430881
C	-5.094389	-1.964791	-0.188134
H	-5.667544	-2.891153	-0.071550
H	-5.616985	-1.172981	0.353967
H	-5.089161	-1.694889	-1.246617
C	-3.785681	-2.290629	1.910921
H	-4.208553	-1.377979	2.340936
H	-4.441649	-3.125398	2.174902
H	-2.807668	-2.463667	2.371226

References

1. Zhong, W.; Wu, L.; Jiang, W.; Li, Y.; Mookan, N.; Liu, X., Proton-coupled electron transfer in the reduction of diiron hexacarbonyl complexes and its enhancement on the electrocatalytic reduction of protons by a pendant basic group. *Dalton Trans.* ***2019,*** *48* (36), 13711-13718.
2. McCarthy, B. D.; Dempsey, J. L., Decoding Proton-Coupled Electron Transfer with Potential-pKa Diagrams. *Inorg. Chem.* ***2017,*** *56* (3), 1225-1231.
3. Singh, U. C.; Kollman, P. A., An approach to computing electrostatic charges for molecules. *J. Comp. Chem.* ***1984,*** *5* (2), 129-145.

_____

3.2.3 Utilization of operando transmission UV-Vis spectroscopy

While the previous section focuses on the characterization of the intermediate products via bulk electrolysis and UV-Vis spectroscopy, real-time monitoring of these new complexes would enable the identification of the intermediates at the precatalytic step at defined potentials. For this purpose, the operando spectroelectrochemical pouch-cell setup (section 2.3) was selected.

The experimental cell setup consisted of a 50% chemically delithiated LFP electrode (with an areal capacity of either 0.2 mAh/cm^2 or 0.6 mAh/cm^2) both as a counter and a reference electrode, a carbon paper (Freudenberg H1410) as a working electrode, and celgard (H2013) as a separator. 0.1 M LiBF$_4$ in MeCN was selected as an electrolyte, and *p*CA was used as a proton source. The LFP electrode was compressed at ~10 kN for 30 s, and prior to cell assembly, all the cell compartments and electrodes were dried under vacuum at elevated temperature. Co$_{Mbq}$ dissolved in the electrolyte and various *p*CA concentrations were added to the solution, and then the pouch-cell was sealed. The most crucial factor to be considered during cell assembly is that there should be no bubble accumulation in the slit (see Figure 2.4) during the sealing step. For this purpose, altered solution amounts and sealing pressures were tested as an initial step to determine the optimum values.
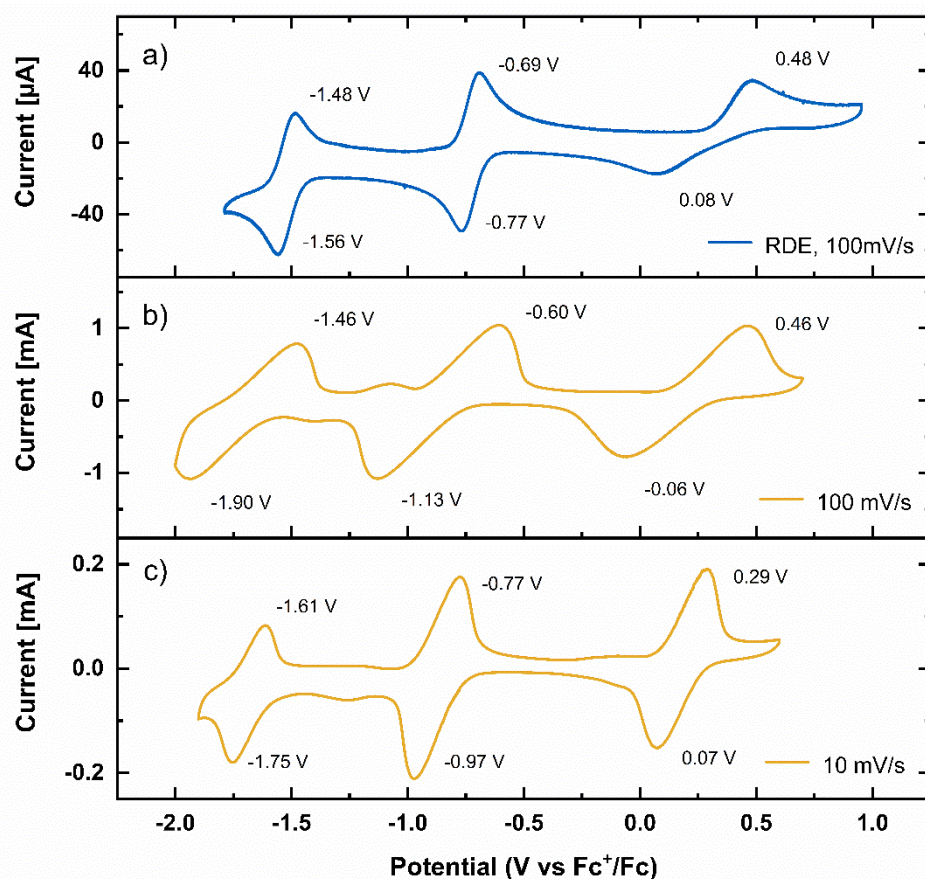
Figure 3.1: Cyclic voltammograms of 1 mM Co$_{Mbq}$ in 0.1 M LiBF$_4$/MeCN: a) conducted with a glassy carbon electrode in the RDE setup at 100 mV/s under Ar atmosphere (orange traces); b) and c) were conducted within the operando transmission UV-Vis spectroscopy pouch-cell setup with the compressed LFP electrodes (0.6 mAh/cm^2) at 100 mV/s (b) and at 10 mV/s (c).

Benchmark experiments with Co$_{Mbq}$ ([Co^{II}(Mabiq)(THF)](PF$_6$)]) containing solutions were conducted since the spectroscopic and electrochemical features of Co-Mabiq complexes are well established. The benchmark experiments included CVs at various scan rates as well as chronoamperometric stepping experiments, combined with UV-Vis spectroscopy. The peak potentials of the oxidation and reduction features are stated in Figure 3.1. Compared to the CVs conducted with the RDE cell setup at 0 rpm (Figure 3.1a), the redox features observed in the pouch-cell setup, especially the reduction features, are shifted up to 360 mV at 100 mV/s based on the peak potentials (Figure 3.1b). Interestingly, at the slower scan rates of 10 mV/s the potential shifts are substantially less (Figure 3.1c). The redox features at high scan rates are also tilted in comparison to the CV scan conducted with the RDE cell setup, which most likely originates from high ohmic resistances in the pouch-cell setup. Decreasing the scan rates below 10 mV/s causes the appearance

_____

of new redox features (not shown), which likely originate from some unidentified side reactions, which become relevant when the potential is applied for very long times. In comparison to the standard RDE cell setup (section 2.3), the pouch-cell setup includes the counter and working electrodes in the same solution. Therefore, side reactions might be taking place on the counter electrode that can influence the redox features at very slow scan rates. The next set of benchmark experiments involved acquiring operando UV-Vis spectra of the Co_{Mbq} solution in this cell setup. Different potential hold steps were applied, and UV-Vis spectra were monitored to investigate the change of spectroscopic features at oxidative and reductive potentials. Prior to the experiment, the absorption spectra of the solution were recorded at open circuit potential (OCV) to obtain the reference spectra of Co_{Mbq}. Firstly, Co_{Mbq} was reduced to Co^I–Mabiq by holding the potential at −1.16 V_{Fc}. Due to the small amount of the solution and the high area of the working electrode in the pouch-cell, the Co^I–Mabiq species was obtained in 0.2 h (Figure 3.2, blue trace). To examine whether Co^I–Mabiq could be subsequently oxidized to the starting complex (Co_{Mbq}), the potential was held at 0.14 V_{Fc}. The Co_{Mbq} was obtained within 0.2 h (Figure 3.2, green trace). Furthermore, Co_{Mbq} is reduced by two electrons to the "Co^0" form at −1.9 V_{Fc} (not shown); however, when the potential was held at 0.14 V_{Fc}, the "Co^0" form was partially oxidized back to the starting complex due to the poor solubility of the "Co^0" form leading to precipitation. Overall, the benchmark experiments suggest that the utilized cell setup involving Co_{Mbq} solution is suitable to further examine the real-time intermediate complexes in the presence of *p*CA.
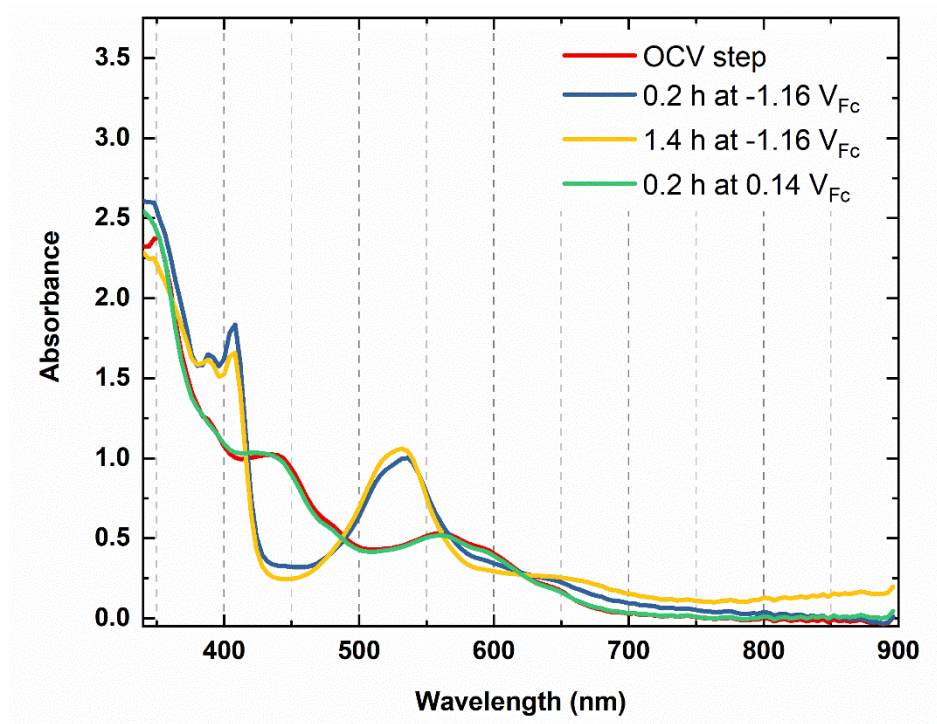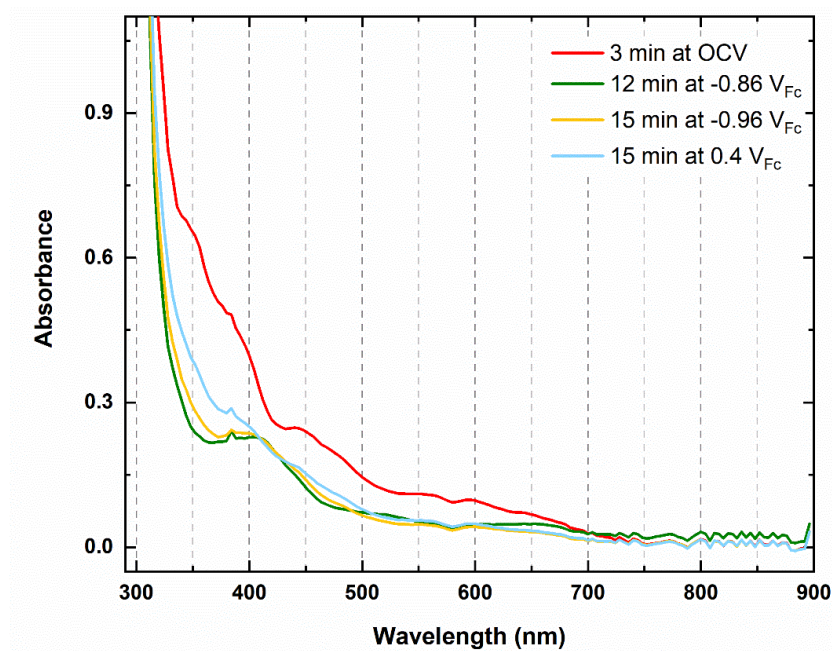
Figure 3.2: UV-Vis spectra of 1 mM Co_Mbq in 0.1 M LiBF$_4$/MeCN with 30 mM *p*CA using an LFP counter electrode (0.6 mAh/cm^2) and a spectral acquisition rate of 60 nm/min. Spectra were recorded at OCV (red line) and various applied potentials: at -1.16 V$_{Fc}$ for 0.2h and 1.4 h (blue and yellow line) and at 0.14 V$_{Fc}$ for 0.2 h (green line).

The next part of this section focuses on the *p*CA addition to the system to characterize the possible intermediates under applied potential. The same procedure as in the benchmark experiments was used. Firstly, the recorded CVs of Co_Mbq with *p*CA do not entirely agree with the redox features observed at the RDE cell setup with the same *p*CA concentration. The redox features of the precatalytic wave appear more broadened and shifted in the pouch-cell, while peak current potentials are more obscure, especially at high scan rates (data not shown). To understand the reasons for the sluggish features and the effect of *p*CA, the *p*CA concentration is increased in the system. Slight improvement in the redox features with the increasing *p*CA concentration (Figure 3.3) implies there might be a significant consumption of *p*CA resulting from a chemical reaction in the system, most likely at the LFP electrode. The formed side products from the chemical reaction, in combination with the low *p*CA (i.e., proton) concentration, might be the reasons for the change of the redox features on the CVs. Hence, a new set of experiments was conducted prior to operando UV-Vis experiments to validate this hypothesis.
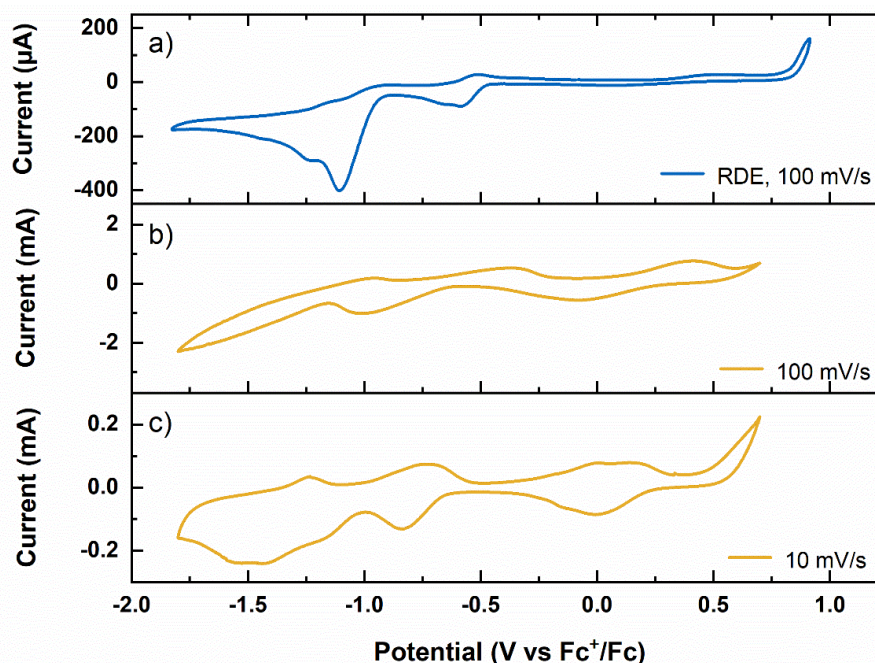
Figure 3.3: Cyclic voltammograms of 1 mM Co$_{Mbq}$ in 0.1 M LiBF$_4$/MeCN in the presence of *p*CA: a) conducted with a glassy carbon electrode in the RDE setup in the presence of 10 mM *p*CA at 100 mV/s; under Ar atmosphere (blue traces); b) and c) were conducted within the operando transmission UV-Vis spectroscopy pouch-cell setup with the compressed LFP electrodes (0.2 mAh/cm^2) in the presence of 30 mM *p*CA at 100 mV/s (b) and at 10 mV/s (c).

The new experiments were based on the assumption that there might be a significant consumption of *p*CA by the LFP counter electrode. Validation of this argument needs to be quantified by performing a UV-Vis calibration experiment and determining the proton consumption based on the change in absorbance of *p*CA. This is enabled by the fact that *p*CA protonated, as well as unprotonated, only shows one distinctive band at 271 nm; however, the intensity increases upon deprotonation, as electrons are more delocalized in this form. Hence, a concentration series of both protonated and unprotonated *p*CA in MeCN was measured by UV-Vis spectroscopy to obtain a calibration line (Figure 3.4).

LFP electrodes with different loadings were stored in solutions with various *p*CA concentrations for 4 h. If *p*CA does not react with the LFP electrodes, the extinction coefficient values of *p*CA should be around 8487 M^{-1}cm^{-1} (Figure 3.4, black line). After the storage experiment, the extinction coefficient values of *p*CA were around 9445 M^{-1}cm^{-1} and match the calibration line of unprotonated *p*CA (Figure 3.4, pink line), suggesting that the initially protonated *p*CA (Figure 3.4, black line) was

125

deprotonated. Hence, our initial assumption that there is a reaction of the LFP electrode with the protonated *p*CA is likely valid. Despite of this, we still pursued investigating the effect of the reaction to the intermediate complex formed during operando measurements.
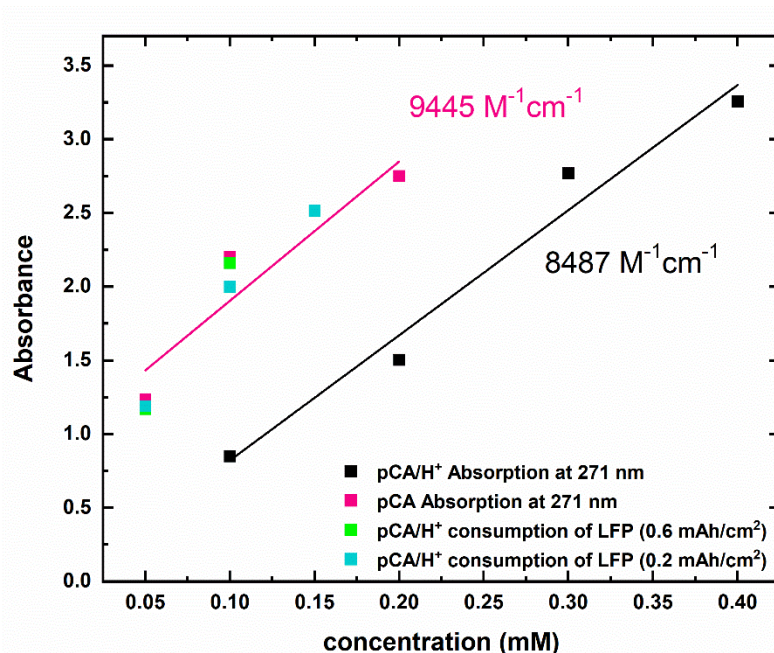
Figure 3.4: Linear fits of extinction coefficients for the protonated (black slope) and the unprotonated (purple slope) form of *p*-cyanoanilinium (*p*CA) in MeCN. Concentration dependent *p*CA consumption behavior of LFP electrodes with different areal capacities (0.6 mAh/cm^2: green; 0.2 mAh/cm^2: turquoise).

The last set of experiments aimed to characterize the intermediates by UV-Vis spectroscopy, although there is most likely an interference from the side products formed due to the reaction between LFP and *p*CA surface reaction. Even though the CV result of Co$_{Mbq}$ in the presence of varied *p*CA concentrations did not exhibit the exact expected redox features, chronoamperometric steps analogous to the benchmark experiments were applied. The applied time was kept short, since the benchmark experiments showed that the conversion between the redox couples occurs the most within 0.2 h. The applied potentials are set to the precatalytic wave because more negative potentials result in H$_2$ evolution, which causes the accumulation of bubbles within the slit. Thus, the selected holding time was limited to 15 min, and the potentials were selected as −0.86 V$_{Fc}$, −0.96 V$_{Fc}$, and 0.4 V$_{Fc}$, respectively. The UV-Vis spectra recorded at OCV matched the Co$_{Mbq}$ complex, and when the potential was held at −0.86 V$_{Fc}$ for 12 min, a prominent band around

_____

410 nm appeared (Figure 3.5, green line). Once the potential was switched to −0.96 V$_{Fc}$, the band shifted to 395 nm (i.e., to lower wavelengths). When oxidative potentials were applied, the band shifted to 385 nm (Figure 3.5, blue line). Notably, the broad band between 500–700 nm from the Co$_{Mbq}$ complex disappeared for all applied potentials.

Figure 3.5: UV-Vis spectra of 1 mM Co$_{Mbq}$ in 0.1 M LiBF$_4$/MeCN with 30 mM *p*CA using a LFP counter electrode (0.6 mAh/cm^2) and a spectral acquisition rate of 60 nm/min. Spectra were recorded at OCV (red line) and at various applied potentials: -0.86 V$_{Fc}$ for 12 min (green line), -0.96 V$_{Fc}$ for 15 min (orange line), and 0.4 V$_{Fc}$ for 15 min (blue line).

Even though the appearance of the 410 nm band coincides with the result obtained using the bulk electrolysis experiments, the disappearance of the band between 500–700 nm and the shift of the band at 410 nm over time do not agree with the results in section 3.2. Since the reaction between LFP and *p*CA might form products that could interfere with the absorbance spectra of the intermediates, the results obtained with this setup are, unfortunately, inconclusive. Therefore, this study is not being pursued further.

Real-time monitoring of the precatalytic species by operando transmission UV-Vis spectroscopy can be a very useful method; however, the optimization of the technique for the Co–Mabiq system is necessary to characterize the intermediates.

_____

The main problem is the reaction between the LFP counter electrode and protons. Since the counter electrode can not be separated from the acid containing solution, another counter electrode that is stable in the presence of protons should be selected. Since this technique was developed for the Li-ion battery systems, finding a suitable electrode combination for the HER catalyst systems can be challenging.

4 Conclusions

Redox-active ligands can enhance the H_2 evolution kinetics and activity due to their electron and proton storage and transfer features. However, redox non-innocent environments may also result in nonproductive pathways. Thus, this PhD thesis aimed to determine the H_2 evolution potential based on the Co-centered macrocyclic biquinazoline (Mabiq) redox-active ligand and investigate the underlying mechanisms of the HER. For this, different diagnostic tools were employed to examine these subjects, such as OEMS to quantify the gas evolution as well as RDE, RRDE, bulk electrolysis, UV-Vis spectroscopy, and theoretical calculations of absorption spectra to evaluate the underlying mechanisms.

In the first study of this thesis (section 3.1), the OEMS technique developed for the Li-ion battery studies is adapted to be able to record the catalyzed H_2 evolution as a function of applied potential. For this purpose, we utilize a two-compartment cell setup to record the gas evolution in the working electrode compartment, which contains the Co_{Mbq} solution in the presence of *para*-cyanoanilinium (*p*CA). By applying chronoamperometric steps, we observe that H_2 evolution starts at -0.9 V_{Fc} and increases exponentially after the onset potential, so that the redox feature prior to -0.9 V_{Fc} (named a precatalytic wave) is correlated with a modifying step on Co_{Mbq} complex. Different *p*CA concentrations are employed in the Co_{Mbq} solution to examine the maximum amount of H_2 release *via* OEMS, showing that 48-62% of the theoretical maximum amount of H_2 are produced. Noteworthy to mention is that the most amount of H_2 is generated within the first two hours of potential hold, suggesting that a deactivation step may take place over time. Further results reveal that holding the potential in the potential region of the precatalytic wave prior to the H_2 evolution potential decreases the amount of evolved H_2. Overall, these experiments imply that we have both active and inactive species in the reaction

system and that the active species initially lead to H$_2$ formation, but that over time, inactive species become more dominant. Based on these findings, the RRDE technique is employed to further analyze the precatalytic wave. Benchmark experiments give insightful information that two electrons and at least one proton are transferred to the complex at the precatalytic wave. Based on this result, we propose an ECE mechanism for the precatalytic step. The outcomes of the first study exhibit that redox-active ligands can result in nonproductive pathways, and further characterization of the formed complex at precatalytic wave is necessary to develop strategies to enhance the activity of the Co-centered Mabiq ligand.

The second part of the thesis (section 3.2.1) focuses on the underlying mechanisms and characterization of the formed intermediates prior to H$_2$ evolution, *i.e.*, on the precatalytic wave in Co$_{Mbq}$ solution in the presence of *p*CA, because the characterization of the intermediate products may assist the optimization and design of catalysts to improve the HER kinetics. In this respect, we conduct the bulk electrolysis technique and analyze the formed products by UV-Vis spectroscopy. Recorded CVs after the bulk electrolysis display a new H$_2$ evolution potential, implying the produced intermediate complex has a higher overpotential toward H$_2$ release instead of being inactive, as it is concluded in the first study. The formation of a species with absorption at 411 nm is correlated to the catalyst displaying higher overpotential towards H$_2$ evolution. Additionally, using acids with pK$_a$'s in the range of 7.0 to 9.43 confirms the presence of two different intermediates in the electrocatalytic H$_2$ evolution pathway, with lower acid strengths leading to the formation of the intermediate with a higher overpotential for the HER. Another outcome of proton sources with different pK$_a$ values is that the proton source influences the order of proton and electron transfer steps at the formation of precatalytic intermediates. However, attempts to characterize the intermediates by experimental methods are unsuccessful; thus, quantum chemical calculations are performed to study the relative energies and spectroscopic properties of possible protonation products. Calculations suggest that EC and ECE steps lead to two thermodynamically stable species, imine or diketiminate based products, respectively. Calculated absorption spectra of these two possible intermediates imply that the diketiminate site protonated intermediates display a band close to

411 nm. Interestingly, the band between 600 nm and 700 nm agrees with the imine site protonated intermediate. Combined experimental and calculated results suggest that protonation of the diketiminate site on the ligand results in higher HER overpotentials, and protonation of the imine site corresponds to the initially more active catalyst (Figure 4.1). At least three electrons are accumulated on the ligand in the pathway involving diketiminate site protonated species, and it follows the ligand-centered mechanism, while the imine site protonation involves metal-hydride generation and less proton and electron transfer steps compared to the ligand-centered mechanism to release H_2. Moreover, altering the acid strength affects the species generated at the precatalytic step. Stronger acids lead to imine site protonation, while weak acids favor the diketiminate site protonation. Our study highlights that the Co-Mabiq complex offers metal- and multiple ligand-protonation sites and that Mabiq can act as a "hydride" sink, causing higher HER overpotential. Due to the multiple protonation sites on the ligand, different possible precatalytic intermediates form that may inhibit the kinetics towards the HER. Moreover, conditions such as acid strength are crucial factors to be considered for effective HER, and this study reveals that weak acid strengths lead to stable intermediate formation with higher overpotentials toward H_2 release.
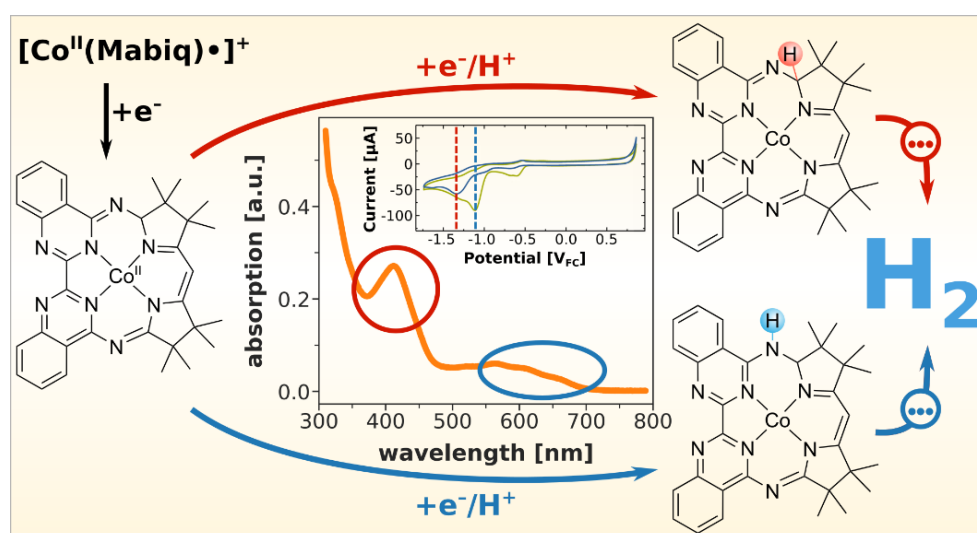
Figure 4.1: Illustration of the possible formed intermediates prior to H_2 evolution, displaying the characteristic features of absorption spectra and the H_2 evolution potentials indicated by cyclic voltammetry. The blue color representing the imine site protonated intermediate, and the red color representing the diketiminate site pronated intermediate. Reprinted with permission from Tok *et al* [81]. Copyright 2024 American Chemical Society.

The last section of this PhD thesis (section 3.2.2) focuses on the characterization of the precatalytic intermediates by operando transmission UV-Vis spectroscopy. The recorded CV on only the Co$_{Mbq}$ solution displays the redox couples in good agreement with the reported values. Furthermore, applied reductive potentials clearly produce the "Co^0" and "Co^I" forms. However, the CV result on Co$_{Mbq}$ in the presence of *p*CA shows shifted precatalytic redox features and indecipherable H$_2$ evolution potentials. Since the counter electrode and working electrode are in the same compartment and since *p*CA is the only new addition to the system, a reaction between the LFP counter electrode and *p*CA that leads to the consumption of protons and the formation of a side product is likely. For this purpose, extinction coefficients of protonated and unprotonated forms of *p*CA based on the absorption band at 271 nm are established, and the consumption of protons by the LFP counter electrode is confirmed by detecting the extinction coefficient of *p*CA solutions where LFP electrodes are stored in. Since the results in the presence of *p*CA in the system were not reliable, we did not pursue the use of the operando transmission technique any further.

Overall, the effect of the redox moiety within the ligand framework is often challenging to demonstrate conclusively, and it is difficult to draw relevant conclusions between different systems. However, the Mabiq system offers a great opportunity to study the advantages and disadvantages of redox-active ligands. Redox-active ligands disrupt the usual electron distribution within catalysts, and an increased electron density on the ligand may trigger redox events, which lead to new catalytic pathways, as in the Mabiq ligand system. In the Co-Mabiq system, in situ probing techniques and DFT calculations are coupled and they facilitate deciphering the catalytic dead ends and the truly active forms of the catalysts. The proton and electron storage by Mabiq can be advantageous for accessing the reduced forms, and coupling of a proton to the reduction process shifts the potential to more positive values compared to formal Co$^{II/I}$. However, Mabiq can also act as a hydride sink and accumulate electrons, which results in high HER overpotentials. Therefore, the catalyst design plays an important role in improving the HER kinetics and lowering its overpotential. Firstly, the ineffective pathways might be prevented by modifying the ligand part, which leads to higher overpotential, i.e., modifying the

diketiminate site for the Co-Mabiq system. Secondly, the nucleophilicity of the metal-center should be considered as one of the key aspects, while high Lewis basicity of the metal-center might promote the hydride generation that facilitates the HER. The Co-Mabiq system results in two different pathways, involving either the ligand-hydride or the metal-hydride formation; thus, different metal-centers might favor the metal-hydride formation that can decrease the HER overpotential. Lastly, the reaction conditions, such as the acid strength of the proton source, can influence the pathway without modifying the catalyst. In this work, the Mabiq redox-active ligand is investigated in detail, and the key aspects of the HER are determined based on this system. Since each redox-active ligand system differs, such as the rigidity of the ligand or the geometry adopted by the complex, a comparison with complexes bearing redox-active ligands should be systematically carried out to tune the HER activity.

References

1. European Parliment EU and the Paris agreement: towards climate neutrality. https://www.europarl.europa.eu/news/en/headlines/priorities/climate-change/20191115STO66603/eu-and-the-paris-agreement-towards-climate-neutrality (accessed July 7, 2022).

2. Eurostat Glossary:Fossil fuel. https://ec.europa.eu/eurostat/statistics-explained/index.php?title=Glossary:Fossil_fuel (accessed June 20, 2022).

3. International Energy Agency Total energy supply (TES) by source, World 1990-2019 https://www.iea.org/data-and-statistics/data-tables?country=WORLD&fuel=Energy%20supply&indicator=TESbySource (accessed June 20, 2022).

4. Hannah Ritchie, M. R. Energy Production and Consumption. https://ourworldindata.org/energy-production-consumption (accessed June 23, 2022).

5. International Energy Agency Hydrogen. https://www.iea.org/reports/hydrogen (accessed June 30, 2022).

6. Das, A.; Han, Z.; Brennessel, W. W.; Holland, P. L.; Eisenberg, R., Nickel Complexes for Robust Light-Driven and Electrocatalytic Hydrogen Production from Water. *ACS Catal.* **2015,** *5* (3), 1397-1406.

7. Fukuzumi, S.; Lee, Y.-M.; Nam, W., Thermal and Photocatalytic Production of Hydrogen with Earth-Abundant Metal Complexes. *Coord. Chem. Rev.* **2018,** *355*, 54-73.

8. Durst, J.; Simon, C.; Hasché, F.; Gasteiger, H. A., Hydrogen Oxidation and Evolution Reaction Kinetics on Carbon Supported Pt, Ir, Rh, and Pd Electrocatalysts in Acidic Media. *J. Electrochem. Soc.* **2014,** *162* (1), F190-F203.

9. Eftekhari, A., Electrocatalysts for Hydrogen Evolution Reaction. *Int. J. Hydrog. Energy* **2017,** *42* (16), 11053-11077.

10. Berardi, S.; Drouet, S.; Francas, L.; Gimbert-Surinach, C.; Guttentag, M.; Richmond, C.; Stoll, T.; Llobet, A., Molecular Artificial Photosynthesis. *Chem. Soc. Rev.* **2014,** *43* (22), 7501-19.

11. McKone, J. R.; Lewis, N. S.; Gray, H. B., Will Solar-Driven Water-Splitting Devices See the Light of Day? *Chem. Mater.* **2013,** *26* (1), 407-414.

12. Bullock, R. M., Reaction: Earth-Abundant Metal Catalysts for Energy Conversions. *Chem.* **2017,** *2* (4), 444-446.

13. Das, A.; Hessin, C.; Ren, Y.; Desage-El Murr, M., Biological Concepts for Catalysis and Reactivity: Empowering Bioinspiration. *Chem. Soc. Rev.* **2020,** *49* (23), 8840-8867.

14. Brazzolotto, D.; Gennari, M.; Queyriaux, N.; Simmons, T. R.; Pecaut, J.; Demeshko, S.; Meyer, F.; Orio, M.; Artero, V.; Duboc, C., Nickel-Centred Proton

_____

Reduction Catalysis in a Model of [NiFe] Hydrogenase. *Nat. Chem.* **2016,** *8* (11), 1054-1060.

15. Lubitz, W.; Ogata, H.; Rudiger, O.; Reijerse, E., Hydrogenases. *Chem. Rev.* **2014,** *114* (8), 4081-148.

16. Firpo, V.; Le, J. M.; Pavone, V.; Lombardi, A.; Bren, K. L., Hydrogen Evolution from Water Catalyzed by Cobalt-Mimochrome VI*a, a Synthetic Mini-Protein. *Chem. Sci.* **2018,** *9* (45), 8582-8589.

17. Stephenson, M.; Stickland, L. H., Hydrogenase: A Bacterial Enzyme Activating Molecular Hydrogen: The properties of the Enzyme. *Biochem. J.* **1931,** *25* (1), 205-214.

18. Fontecilla-Camps, J. C.; Volbeda, A.; Cavazza, C.; Nicolet, Y., Structure/Function Relationships of [NiFe]- and [FeFe]-Hydrogenases. *Chem.l Rev.* **2007,** *107* (10), 4273-4303.

19. Winkler, M.; Esselborn, J.; Happe, T., Molecular Basis of [FeFe]-Hydrogenase Function: An Insight into the Complex Interplay between Protein and Catalytic Cofactor. *Biochim. Biophys. Acta* **2013,** *1827* (8-9), 974-85.

20. Lubitz, W.; Reijerse, E.; van Gastel, M., [NiFe] and [FeFe] Hydrogenases Studied by Advanced Magnetic Resonance Techniques. *Chem. Rev.* **2007,** *107* (10), 4331-4365.

21. Léger, C.; Jones, A. K.; Roseboom, W.; Albracht, S. P. J.; Armstrong, F. A., Enzyme Electrokinetics: Hydrogen Evolution and Oxidation by Allochromatium Vinosum [NiFe]-Hydrogenase. *Biochem.* **2002,** *41* (52), 15736-15746.

22. Pandelia, M. E.; Ogata, H.; Lubitz, W., Intermediates in the Catalytic Cycle of [NiFe] Hydrogenase: Functional Spectroscopy of the Active Site. *Chemphyschem* **2010,** *11* (6), 1127-40.

23. Simmons, T. R.; Berggren, G.; Bacchi, M.; Fontecave, M.; Artero, V., Mimicking Hydrogenases: From Biomimetics to Artificial Enzymes. *Coord. Chem. Rev.* **2014,** *270-271*, 127-150.

24. Hidalgo, R.; Ash, P. A.; Healy, A. J.; Vincent, K. A., Infrared Spectroscopy During Electrocatalytic Turnover Reveals the Ni-L Active Site State During H_2 Oxidation by a NiFe Hydrogenase. *Angew. Chem. Int. Ed. Engl.* **2015,** *54* (24), 7110-3.

25. Sommer, C.; Adamska-Venkatesh, A.; Pawlak, K.; Birrell, J. A.; Rudiger, O.; Reijerse, E. J.; Lubitz, W., Proton Coupled Electronic Rearrangement within the H-Cluster as an Essential Step in the Catalytic Cycle of [FeFe] Hydrogenases. *J. Am. Chem. Soc.* **2017,** *139* (4), 1440-1443.

26. Tard, C.; Pickett, C. J., Structural and Functional Analogues of the Active Sites of the [Fe]-, [NiFe]-, and [FeFe]-Hydrogenases. *Chem. Rev.* **2009,** *109* (6), 2245-2274.

_____

27. Mulder, D. W.; Guo, Y.; Ratzloff, M. W.; King, P. W., Identification of a Catalytic Iron-Hydride at the H-Cluster of [FeFe]-Hydrogenase. *J. Am. Chem. Soc.* **2017,** *139* (1), 83-86.

28. Liu, Y.-C.; Chu, K.-T.; Huang, Y.-L.; Hsu, C.-H.; Lee, G.-H.; Tseng, M.-C.; Chiang, M.-H., Protonation/Reduction of Carbonyl-Rich Diiron Complexes and the Direct Observation of Triprotonated Species: Insights into the Electrocatalytic Mechanism of Hydrogen Formation. *ACS Catal.* **2016,** *6* (4), 2559-2576.

29. Coutard, N.; Kaeffer, N.; Artero, V., Molecular Engineered Nanomaterials for Catalytic Hydrogen Evolution and Oxidation. *Chem. Commun. (Camb.)* **2016,** *52* (95), 13728-13748.

30. McKone, J. R.; Marinescu, S. C.; Brunschwig, B. S.; Winkler, J. R.; Gray, H. B., Earth-Abundant Hydrogen Evolution Electrocatalysts. *Chem. Sci.* **2014,** *5* (3), 865-878.

31. Costentin, C.; Dridi, H.; Saveant, J. M., Molecular Catalysis of H_2 Evolution: Diagnosing Heterolytic versus Homolytic Pathways. *J. Am. Chem. Soc.* **2014,** *136* (39), 13727-34.

32. Solis, B. H.; Hammes-Schiffer, S., Substituent Effects on Cobalt Diglyoxime Catalysts for Hydrogen Evolution. *J. Am. Chem. Soc.* **2011,** *133* (47), 19036-9.

33. Muckerman, J. T.; Fujita, E., Theoretical Studies of the Mechanism of Catalytic Hydrogen Production by a Cobaloxime. *Chem. Commun. (Camb.)* **2011,** *47* (46), 12456-8.

34. Barton, B. E.; Rauchfuss, T. B., Terminal Hydride in [FeFe]-Hydrogenase Model Has Lower Potential for H_2 Production Than the Isomeric Bridging Hydride. *Inorg. Chem.* **2008,** *47* (7), 2261-2263.

35. Cheah, M. H.; Tard, C.; Borg, S. J.; Liu, X.; Ibrahim, S. K.; Pickett, C. J.; Best, S. P., Modeling [Fe–Fe] Hydrogenase: Evidence for Bridging Carbonyl and Distal Iron Coordination Vacancy in an Electrocatalytically Competent Proton Reduction by an Iron Thiolate Assembly That Operates through Fe(0)–Fe(II) Levels. *J. Am. Chem. Soc.* **2007,** *129* (36), 11085-11092.

36. Capon, J.-F.; Gloaguen, F.; Pétillon, F. Y.; Schollhammer, P.; Talarmin, J., Electron and Proton Transfers at Diiron Dithiolate Sites Relevant to the Catalysis of Proton Reduction by the [FeFe]-Hydrogenases. *Coord. Chem. Rev.* **2009,** *253* (9), 1476-1494.

37. Ogo, S.; Ichikawa, K.; Kishima, T.; Matsumoto, T.; Nakai, H.; Kusaka, K.; Ohhara, T., A Functional [NiFe] Hydrogenase Mimic That Catalyzes Electron and Hydride Transfer from H_2. *Science* **2013,** *339* (6120), 682-684.

38. Wiese, S.; Kilgore, U. J.; DuBois, D. L.; Bullock, R. M., [Ni(PMe$_2$NPh$_2$)$_2$](BF$_4$)$_2$ as an Electrocatalyst for H_2 Production. *ACS Catal.* **2012,** *2* (5), 720-727.

39. Wilson, A. D.; Newell, R. H.; McNevin, M. J.; Muckerman, J. T.; DuBois, M. R.; DuBois, D. L., Hydrogen Oxidation and Production Using Nickel-Based Molecular Catalysts with Positioned Proton Relays. *J. Am. Chem. Soc.* **2006,** *128* (1), 358-366.

_____

40. Shaw, W. J.; Helm, M. L.; DuBois, D. L., A Modular, Energy-Based Approach to the Development of Nickel Containing Molecular Electrocatalysts for Hydrogen Production and Oxidation. *Biochim. Biophys. Acta* **2013,** *1827* (8-9), 1123-39.

41. Liu, T.; Chen, S.; O'Hagan, M. J.; Rakowski DuBois, M.; Bullock, R. M.; DuBois, D. L., Synthesis, Characterization, and Reactivity of Fe Complexes Containing Cyclic Diazadiphosphine Ligands: The Role of the Pendant Base in Heterolytic Cleavage of H_2. *J. Am. Chem. Soc.* **2012,** *134* (14), 6257-72.

42. Kilgore, U. J.; Roberts, J. A.; Pool, D. H.; Appel, A. M.; Stewart, M. P.; DuBois, M. R.; Dougherty, W. G.; Kassel, W. S.; Bullock, R. M.; DuBois, D. L., $[Ni(P(Ph)_2N(C_6H_4X)_2)_2]^{2+}$ Complexes as Electrocatalysts for H_2 Production: Effect of Substituents, Acids, and Water on Catalytic Rates. *J. Am. Chem. Soc.* **2011,** *133* (15), 5861-72.

43. Helm, M. L.; Stewart, M. P.; Bullock, R. M.; DuBois, M. R.; DuBois, D. L., A Synthetic Nickel Electrocatalyst with a Turnover Frequency Above 100,000 s^{-1} for H_2 Production. *Science* **2011,** *333* (6044), 863-866.

44. Curtis, C. J.; Miedaner, A.; Ciancanelli, R.; Ellis, W. W.; Noll, B. C.; Rakowski DuBois, M.; DuBois, D. L., $[Ni(Et_2PCH_2NMeCH_2PEt_2)_2]^{2+}$ as a Functional Model for Hydrogenases. *Inorg. Chem.* **2003,** *42* (1), 216-227.

45. Appel, A. M.; Pool, D. H.; O'Hagan, M.; Shaw, W. J.; Yang, J. Y.; Rakowski DuBois, M.; DuBois, D. L.; Bullock, R. M., $[Ni(PPh_2NBn_2)_2(CH_3CN)]^{2+}$ as an Electrocatalyst for H_2 Production: Dependence on Acid Strength and Isomer Distribution. *ACS Catal.* **2011,** *1* (7), 777-785.

46. Rakowski DuBois, M.; DuBois, D. L., The Roles of the First and Second Coordination Spheres in the Design of Molecular Catalysts for H_2 Production and Oxidation. *Chem. Soc. Rev.* **2009,** *38* (1), 62-72.

47. DuBois, D. L., Development of Molecular Electrocatalysts for Energy Storage. *Inorg. Chem.* **2014,** *53* (8), 3935-60.

48. O'Hagan, M.; Shaw, W. J.; Raugei, S.; Chen, S.; Yang, J. Y.; Kilgore, U. J.; DuBois, D. L.; Bullock, R. M., Moving Protons with Pendant Amines: Proton Mobility in a Nickel Catalyst for Oxidation of Hydrogen. *J. Am. Chem. Soc.* **2011,** *133* (36), 14301-12.

49. Fraze, K.; Wilson, A. D.; Appel, A. M.; Rakowski DuBois, M.; DuBois, D. L., Thermodynamic Properties of the Ni–H Bond in Complexes of the Type $[HNi(P_2RN_2R')_2](BF_4)$ and Evaluation of Factors That Control Catalytic Activity for Hydrogen Oxidation/Production. *Organometallics* **2007,** *26* (16), 3918-3924.

50. Schrauzer, G. N., Organocobalt Chemistry of Vitamin B_{12} Model Compounds (Cobaloximes). *Acc. Chem. Res.* **1968,** *1* (4), 97-103.

51. Valdez, C. N.; Dempsey, J. L.; Brunschwig, B. S.; Winkler, J. R.; Gray, H. B., Catalytic Hydrogen Evolution from a Covalently Linked Dicobaloxime. *Proc. Natl. Acad. Sci. USA* **2012,** *109* (39), 15589-93.

52. Dempsey, J. L.; Winkler, J. R.; Gray, H. B., Mechanism of H$_2$ Evolution from a Photogenerated Hydridocobaloxime. *J. Am. Chem. Soc.* **2010,** *132* (47), 16774-16776.

53. Dempsey, J. L.; Brunschwig, B. S.; Winkler, J. R.; Gray, H. B., Hydrogen Evolution Catalyzed by Cobaloximes. *Acc. Chem. Res.* **2009,** *42* (12), 1995-2004.

54. Razavet, M.; Artero, V.; Fontecave, M., Proton Electroreduction Catalyzed by Cobaloximes: Functional Models for Hydrogenases. *Inorg. Chem.* **2005,** *44* (13), 4786-4795.

55. Jacques, P.-A.; Artero, V.; Pécaut, J.; Fontecave, M., Cobalt and Nickel Diimine-Dioxime Complexes as Molecular Electrocatalysts for Hydrogen Evolution with Low Overvoltages. *Proc. Natl. Acad. Sci. USA* **2009,** *106* (49), 20627-20632.

56. Bhattacharjee, A.; Andreiadis, E. S.; Chavarot-Kerlidou, M.; Fontecave, M.; Field, M. J.; Artero, V., A Computational Study of the Mechanism of Hydrogen Evolution by Cobalt(diimine-dioxime) Catalysts. *Chem.* **2013,** *19* (45), 15166-74.

57. Kaeffer, N.; Chavarot-Kerlidou, M.; Artero, V., Hydrogen Evolution Catalyzed by Cobalt Diimine-dioxime Complexes. *Acc. Chem. Res.* **2015,** *48* (5), 1286-95.

58. Baffert, C.; Artero, V.; Fontecave, M., Cobaloximes as Functional Models for Hydrogenases. 2. Proton Electroreduction Catalyzed by Difluoroborylbis(dimethylglyoximato)cobalt(II) Complexes in Organic Media. *Inorg. Chem.* **2007,** *46* (5), 1817-1824.

59. Hu, X. L.; Brunschwig, B. S.; Peters, J. C., Electrocatalytic Hydrogen Evolution at Low Overpotentials by Cobalt Macrocyclic Glyoxime and Tetraimine Complexes. *J. Am. Chem. Soc.* **2007,** *129* (29), 8988-8998.

60. Kaeffer, N.; Morozan, A.; Fize, J.; Martinez, E.; Guetaz, L.; Artero, V., The Dark Side of Molecular Catalysis: Diimine–Dioxime Cobalt Complexes Are Not the Actual Hydrogen Evolution Electrocatalyst in Acidic Aqueous Solutions. *ACS Catal.* **2016,** *6* (6), 3727-3737.

61. Artero, V.; Chavarot-Kerlidou, M.; Fontecave, M., Splitting Water with Cobalt. *Angew. Chem. Int. Ed.* **2011,** *50* (32), 7238-66.

62. Panagiotopoulos, A.; Ladomenou, K.; Sun, D.; Artero, V.; Coutsolelos, A. G., Photochemical Hydrogen Production and Cobaloximes: the Influence of the Cobalt Axial N-ligand on the System Stability. *Dalton Trans.* **2016,** *45* (15), 6732-8.

63. Dempsey, J. L.; Winkler, J. R.; Gray, H. B., Kinetics of Electron Transfer Reactions of H$_2$-Evolving Cobalt Diglyoxime Catalysts. *J. Am. Chem. Soc.* **2010,** *132* (3), 1060-1065.

64. Solis, B. H.; Hammes-Schiffer, S., Theoretical Analysis of Mechanistic Pathways for Hydrogen Evolution Catalyzed by Cobaloximes. *Inorg. Chem.* **2011,** *50* (21), 11252-62.

65. Lacy, D. C.; Roberts, G. M.; Peters, J. C., The Cobalt Hydride That Never Was: Revisiting Schrauzer's "Hydridocobaloxime". *J. Am. Chem. Soc.* **2015,** *137* (14), 4860-4.

66. Estes, D. P.; Grills, D. C.; Norton, J. R., The Reaction of Cobaloximes with Hydrogen: Products and Thermodynamics. *J. Am. Chem. Soc.* **2014,** *136* (50), 17362-5.

67. Chirik, P. J., Preface: Forum on Redox-Active Ligands. *Inorg. Chem.* **2011,** *50* (20), 9737-40.

68. Kaim, W.; Schwederski, B., Non-Innocent Ligands in Bioinorganic Chemistry—An Overview. *Coord. Chem. Rev.* **2010,** *254* (13), 1580-1588.

69. Kaim, W., Manifestations of Noninnocent Ligand Behavior. *Inorg. Chem.* **2011,** *50* (20), 9752-65.

70. Luca, O. R.; Crabtree, R. H., Redox-active Ligands in Catalysis. *Chem. Soc. Rev.* **2013,** *42* (4), 1440-59.

71. Luo, G.-G.; Zhang, H.-L.; Tao, Y.-W.; Wu, Q.-Y.; Tian, D.; Zhang, Q., Recent Progress in Ligand-Centered Homogeneous Electrocatalysts for Hydrogen Evolution Reaction. *Inorg. Chem. Front.* **2019,** *6* (2), 343-354.

72. Zarkadoulas, A.; Field, M. J.; Artero, V.; Mitsopoulou, C. A., Proton Reduction Reaction Catalyzed by Homoleptic Nickel Bis-1,2-Dithiolate Complexes: Experimental and Theoretical Mechanistic Investigations. *ChemCatChem* **2017,** *9* (12), 2308-2317.

73. Letko, C. S.; Panetier, J. A.; Head-Gordon, M.; Tilley, T. D., Mechanism of the Electrocatalytic Reduction of Protons with Diaryldithiolene Cobalt Complexes. *J. Am. Chem. Soc.* **2014,** *136* (26), 9364-76.

74. Rosenkoetter, K. E.; Wojnar, M. K.; Charette, B. J.; Ziller, J. W.; Heyduk, A. F., Hydrogen-Atom Noninnocence of a Tridentate [SNS] Pincer Ligand. *Inorg. Chem.* **2018,** *57* (16), 9728-9737.

75. Straistari, T.; Fize, J.; Shova, S.; Réglier, M.; Artero, V.; Orio, M., A Thiosemicarbazone-Nickel(II) Complex as Efficient Electrocatalyst for Hydrogen Evolution. *ChemCatChem* **2017,** *9* (12), 2262-2268.

76. Thompson, E. J.; Berben, L. A., Electrocatalytic Hydrogen Production by an Aluminum(III) Complex: Ligand-Based Proton and Electron Transfer. *Angew. Chem. Int. Ed.* **2015,** *54* (40), 11642-6.

77. Nippe, M.; Khnayzer, R. S.; Panetier, J. A.; Zee, D. Z.; Olaiya, B. S.; Head-Gordon, M.; Chang, C. J.; Castellano, F. N.; Long, J. R., Catalytic Proton Reduction with Transition Metal Complexes of the Redox-Active ligand bpy2PYMe. *Chem. Sci.* **2013,** *4* (10), 3934-3945.

78. Luca, O. R.; Konezny, S. J.; Blakemore, J. D.; Colosi, D. M.; Saha, S.; Brudvig, G. W.; Batista, V. S.; Crabtree, R. H., A tridentate Ni pincer for Aqueous Electrocatalytic Hydrogen Production. *New J. Chem.* **2012,** *36* (5), 1149-1152.

79. Haddad, A. Z.; Cronin, S. P.; Mashuta, M. S.; Buchanan, R. M.; Grapperhaus, C. A., Metal-Assisted Ligand-Centered Electrocatalytic Hydrogen Evolution upon Reduction of a Bis(thiosemicarbazonato)Cu(II) Complex. *Inorg. Chem.* **2017,** *56* (18), 11254-11265.

80. Queyriaux, N., Redox-Active Ligands in Electroassisted Catalytic H$^+$ and CO$_2$ Reductions: Benefits and Risks. *ACS Catal.* **2021,** *11* (7), 4024-4035.

81. Tok, G. C.; Reiter, S.; Freiberg, A. T. S.; Reinschlussel, L.; Gasteiger, H. A.; de Vivie-Riedle, R.; Hess, C. R., H$_2$ Evolution from Electrocatalysts with Redox-Active Ligands: Mechanistic Insights from Theory and Experiment vis-a-vis Co-Mabiq. *Inorg. Chem.* **2021**.

82. McNamara, W. R.; Han, Z.; Yin, C.-J.; Brennessel, W. W.; Holland, P. L.; Eisenberg, R., Cobalt-dithiolene Complexes for the Photocatalytic and Electrocatalytic Reduction of Protons in Aqueous Solutions. *Proc. Natl. Acad. Sci.* **2012,** *109* (39), 15594-15599.

83. Porcher, J.-P.; Fogeron, T.; Gomez-Mingot, M.; Derat, E.; Chamoreau, L.-M.; Li, Y.; Fontecave, M., A Bioinspired Molybdenum Complex as a Catalyst for the Photo- and Electroreduction of Protons. *Angew. Chem. Int. Ed.* **2015,** *54* (47), 14090-14093.

84. Solis, B. H.; Hammes-Schiffer, S., Computational Study of Anomalous Reduction Potentials for Hydrogen Evolution Catalyzed by Cobalt Dithiolene Complexes. *J. Am. Chem. Soc.* **2012,** *134* (37), 15253-6.

85. Zarkadoulas, A.; Field, M. J.; Papatriantafyllopoulou, C.; Fize, J.; Artero, V.; Mitsopoulou, C. A., Experimental and Theoretical Insight into Electrocatalytic Hydrogen Evolution with Nickel Bis(aryldithiolene) Complexes as Catalysts. *Inorg. Chem.* **2016,** *55* (2), 432-44.

86. Panetier, J. A.; Letko, C. S.; Tilley, T. D.; Head-Gordon, M., Computational Characterization of Redox Non-Innocence in Cobalt-Bis(Diaryldithiolene)-Catalyzed Proton Reduction. *J. Chem. Theory Comput.* **2016,** *12* (1), 223-30.

87. Koshiba, K.; Yamauchi, K.; Sakai, K., A Nickel Dithiolate Water Reduction Catalyst Providing Ligand-Based Proton-Coupled Electron-Transfer Pathways. *Angew. Chem. Int. Ed.* **2017,** *56* (15), 4247-4251.

88. Sherbow, T. J.; Fettinger, J. C.; Berben, L. A., Control of Ligand pK$_a$ Values Tunes the Electrocatalytic Dihydrogen Evolution Mechanism in a Redox-Active Aluminum(III) Complex. *Inorg. Chem.* **2017,** *56* (15), 8651-8660.

89. Haddad, A. Z.; Garabato, B. D.; Kozlowski, P. M.; Buchanan, R. M.; Grapperhaus, C. A., Beyond Metal-Hydrides: Non-Transition-Metal and Metal-Free Ligand-Centered Electrocatalytic Hydrogen Evolution and Hydrogen Oxidation. *J. Am. Chem. Soc.* **2016,** *138* (25), 7844-7.

90. Jain, R.; Mamun, A. A.; Buchanan, R. M.; Kozlowski, P. M.; Grapperhaus, C. A., Ligand-Assisted Metal-Centered Electrocatalytic Hydrogen Evolution upon Reduction of a Bis(thiosemicarbazonato)Ni(II) Complex. *Inorg. Chem.* **2018,** *57* (21), 13486-13493.

91. Straistari, T.; Hardre, R.; Fize, J.; Shova, S.; Giorgi, M.; Reglier, M.; Artero, V.; Orio, M., Hydrogen Evolution Reactions Catalyzed by a Bis(thiosemicarbazone) Cobalt Complex: An Experimental and Theoretical Study. *Chem.* **2018,** *24* (35), 8779-8786.

92. Lee, C. H.; Dogutan, D. K.; Nocera, D. G., Hydrogen Generation by Hangman Metalloporphyrins. *J. Am. Chem. Soc.* **2011,** *133* (23), 8775-7.

_____

93. Solis, B. H.; Maher, A. G.; Honda, T.; Powers, D. C.; Nocera, D. G.; Hammes-Schiffer, S., Theoretical Analysis of Cobalt Hangman Porphyrins: Ligand Dearomatization and Mechanistic Implications for Hydrogen Evolution. *ACS Catal.* **2014,** *4* (12), 4516-4526.

94. Solis, B. H.; Maher, A. G.; Dogutan, D. K.; Nocera, D. G.; Hammes-Schiffer, S., Nickel Phlorin Intermediate Formed by Proton-Coupled Electron Transfer in Hydrogen Evolution Mechanism. *Proc. Natl. Acad. Sci. USA* **2016,** *113* (3), 485-92.

95. Bediako, D. K.; Solis, B. H.; Dogutan, D. K.; Roubelakis, M. M.; Maher, A. G.; Lee, C. H.; Chambers, M. B.; Hammes-Schiffer, S.; Nocera, D. G., Role of Pendant Proton Relays and Proton-Coupled Electron Transfer on the Hydrogen Evolution Reaction by Nickel Hangman Porphyrins. *Proc. Natl. Acad. Sci. USA* **2014,** *111* (42), 15001-6.

96. Tok, G. C.; Freiberg, A. T. S.; Gasteiger, H. A.; Hess, C. R., Electrocatalytic H_2 Evolution by the Co-Mabiq Complex Requires Tempering of the Redox-Active Ligand. *ChemCatChem* **2019,** *11* (16), 3973-3981.

97. Stark, H. S.; Altmann, P. J.; Sproules, S.; Hess, C. R., Structural Characterization and Photochemical Properties of Mono- and Bimetallic Cu-Mabiq Complexes. *Inorg. Chem.* **2018,** *57* (11), 6401-6409.

98. Rickmeyer, K.; Niederegger, L.; Keilwerth, M.; Hess, C. R., Multifaceted Role of the Noninnocent Mabiq Ligand in Promoting Selective Reduction of CO_2 to CO. *ACS Catal.* **2022,** *12* (5), 3046-3057.

99. Grübel, M.; Bosque, I.; Altmann, P. J.; Bach, T.; Hess, C. R., Redox and Photocatalytic Properties of a NiII complex with a Macrocyclic Biquinazoline (Mabiq) Ligand. *Chem. Sci.* **2018,** *9* (13), 3313-3317.

100. Esezobor, O. Z.; Zeng, W.; Niederegger, L.; Grübel, M.; Hess, C. R., Co–Mabiq Flies Solo: Light-Driven Markovnikov-Selective C- and N-Alkylation of Indoles and Indazoles without a Cocatalyst. *J. Am. Chem. Soc.* **2022,** *144* (7), 2994-3004.

101. Puttock, E. V.; Banerjee, P.; Kaspar, M.; Drennen, L.; Yufit, D. S.; Bill, E.; Sproules, S.; Hess, C. R., A Series of [Co(Mabiq)Cl2-n] (n = 0, 1, 2) Compounds and Evidence for the Elusive Bimetallic Form. *Inorg. Chem.* **2015,** *54* (12), 5864-73.

102. Kaspar, M.; Altmann, P. J.; Pothig, A.; Sproules, S.; Hess, C. R., A Macrocyclic 'Co(0)' complex: The Relevance of Ligand Non-Innocence to Reactivity. *Chem. Commun.* **2017,** *53* (53), 7282-7285.

103. Banerjee, P.; Company, A.; Weyhermuller, T.; Bill, E.; Hess, C. R., Zn and Fe Complexes Containing a Redox Active Macrocyclic Biquinazoline Ligand. *Inorg. Chem.* **2009,** *48* (7), 2944-2955.

104. Muller, E.; Bernardinelli, G.; Vonzelewsky, A., A New Macrocyclic Ligand Combining 2 Different Coordination Sites - Macrocyclic Biquinazoline (Mabiq-) - Synthesis and Structure of the Free Ligand and of a Cobalt(III) Complex. *Inorg. Chem.* **1988,** *27* (25), 4645-4651.

_____

105. Elgrishi, N.; Rountree, K. J.; McCarthy, B. D.; Rountree, E. S.; Eisenhart, T. T.; Dempsey, J. L., A Practical Beginner's Guide to Cyclic Voltammetry. *J. Chem. Educ.* **2017,** *95* (2), 197-206.

106. Bard, A. J.; Faulkner, L. R.; Leddy, J.; Zoski, C. G., *Electrochemical Methods: Fundamentals and Applications.* Wiley New York: 1980; Vol. 2.

107. Rusling, J. F.; Suib, S. L., Characterizing Materials with Cyclic Voltammetry. *Adv. Mater.* **1994,** *6* (12), 922-930.

108. He, Q.; Gorlin, Y.; Patel, M. U. M.; Gasteiger, H. A.; Lu, Y.-C., Unraveling the Correlation between Solvent Properties and Sulfur Redox Behavior in Lithium-Sulfur Batteries. *J. Electrochem. Soc.* **2018,** *165* (16), A4027-A4033.

109. Lu, Y.-C.; He, Q.; Gasteiger, H. A., Probing the Lithium–Sulfur Redox Reactions: A Rotating-Ring Disk Electrode Study. *J. Phys. Chem. C* **2014,** *118* (11), 5733-5741.

110. Nikolic, J.; Expósito, E.; Iniesta, J.; González-Garcia, J.; Montiel, V., Theoretical Concepts and Applications of a Rotating Disk Electrode. *J. Chem. Educ.* **2000,** *77* (9), 1191.

111. Xing, W.; Yin, G.; Zhang, 5 - Rotating Disk Electrode Method. In Rotating Electrode Methods and Oxygen Reduction Electrocatalysts, *J. Eds. Elsevier: Amsterdam*, **2014**; pp 171-198.

112. Tsiouvaras, N.; Meini, S.; Buchberger, I.; Gasteiger, H. A., A Novel On-Line Mass Spectrometer Design for the Study of Multiple Charging Cycles of a Li-O2Battery. *J. Electrochem. Soc.* **2013,** *160* (3), A471-A477.

113. Metzger, M.; Strehle, B.; Solchenbach, S.; Gasteiger, H. A., Origin of H$_2$ Evolution in LIBs: H$_2$O Reduction vs. Electrolyte Oxidation. *J. Electrochem. Soc.* **2016,** *163* (5), A798-A809.

114. Metzger, M.; Marino, C.; Sicklinger, J.; Haering, D.; Gasteiger, H. A., Anodic Oxidation of Conductive Carbon and Ethylene Carbonate in High-Voltage Li-Ion Batteries Quantified by On-Line Electrochemical Mass Spectrometry. *J. Electrochem. Soc.* **2015,** *162* (7), A1123-A1134.

115. Förster, H., UV/VIS Spectroscopy. In Characterization I: -/-, *J. Eds. Springer Berlin Heidelberg* **2004**; pp 337-426.

116. Perkampus, H.-H., UV-VIS Spectroscopy and its Applications. *Springer Science & Business Media* 1992.

117. He, Q.; Freiberg, A. T. S.; Patel, M. U. M.; Qian, S.; Gasteiger, H. A., Operando Identification of Liquid Intermediates in Lithium–Sulfur Batteries via Transmission UV–vis Spectroscopy. *J. Electrochem. Soc.* **2020,** *167* (8), 080508.

List of Figures

_____

Acknowledgements

Lastly, I would like to express my gratitude to my family. You always support and encourage me; I could not have done this without you. I further thank Dilan and Yousef for your support; you are true friends.

Scientific Contributions

Articles

- **Tok, G. C.**, Reiter, S., Freiberg, A. T., Reinschlüssel, L., Gasteiger, H. A., de Vivie-Riedle, R., & Hess, C. R. (2021). H_2 Evolution from Electrocatalysts with Redox-Active Ligands: Mechanistic Insights from Theory and Experiment vis-à-vis Co-Mabiq. Inorganic Chemistry, 60(18), 13888-13902.

- **Tok, G. C.**, Freiberg, A. T., Gasteiger, H. A., & Hess, C. R. (2019). Electrocatalytic H_2 Evolution by the Co-Mabiq Complex Requires Tempering of the Redox-Active Ligand. ChemCatChem, 11(16), 3973-3981.

- Fominykh, K., **Tok, G. C.**, Zeller, P., Hajiyani, H., Miller, T., Döblinger, M., Pentcheva R., Bein, T. & Fattakhova-Rohlfing, D. (2017). Rock salt Ni/Co oxides with unusual nanoscale-stabilized composition as water splitting electrocatalysts. Advanced Functional Materials, 27(8), 1605121.

Articles in preparation

- Reinschlüssel, L.[=], **Tok, G. C.**[=], Berger, A., & Gasteiger, H. A. Spatially Resolved Operando X-Ray Absorption Spectroscopy in NCA/Graphite to Quantify the Potential-Dependent Transition Metal Dissolution and its Effect on Capacity Fading.

Conference Presentations

- **Tok, G. C.**, Reinschlüssel, L., Berger, A., & Gasteiger, H. A., Spatially Resolved Operando X-Ray Absorption Spectroscopy in NCA/Graphite to Quantify the Potential-Dependent Transition Metal Dissolution and its Effect on Capacity Fading, oral presentation, 241th Meeting of the Electrochemical Society (May 2022), Vancouver, Canada (due to the delay on the travel visa of the presenter, the work was presented by Anne Berger).

- **Tok, G. C.**, Reiter, S., Freiberg, A. T., Reinschlüssel, L., Gasteiger, H. A., de Vivie-Riedle, R., & Hess, C. R., Role of Redox-active Ligand of a Cobalt-Mabiq

Complex in the Hydrogen Evolution Reaction, oral presentation, 240th Meeting of the Electrochemical Society (2021), online meeting.

- **Tok, G. C.,** Freiberg, A. T., Gasteiger, H. A., & Hess, C. R., Employing Cobalt Molecular Catalyst for Electrochemical H_2 Evolution in Aprotic Media, poster presentation, 69th Annual Meeting of the International Society of Electrochemistry (2018), Bologna, Italy.